DUAL ACTIVE GALACTIC NUCLEI FROM RAINBOWS TO RADIO: TESTING THE RADIO-SELECTION METHOD WITH OPTICAL SPECTROSCOPY IN THE STRIPE 82 FIELD

by

Arran Gross

A thesis submitted in partial fulfillment of the
requirements for the Doctor of Philosophy
degree in Physics (Astronomy)
in the Graduate College of
The University of Iowa

May 2022

Committee: Hai Fu, Thesis Supervisor
Casey DeRoo
Keri Hoadley
Andrea Prestwich
Adam Myers

For Grammy, who taught me to see beauty in all things.

"A philosopher once asked, 'Are we human because we gaze at the stars, or do we gaze at them because we are human?' Pointless, really... 'Do the stars gaze back?' Now, that's a question." – Neil Gaiman, *Stardust*

ACKNOWLEDGEMENTS

Many people supported me in the completion of this work. I would like to thank my family who encouraged me the whole way through graduate school. Whether it was the 4 a.m. coffee and rides to the airport with my dad, nighttime Mario Kart with my brothers online, my mom's invariable stir fry dinners, or the regular cadence of phone call catch-ups with my grandmother, you all made me feel very loved and included from half a country away. I would also like to thank the many friends that I have made while at Iowa. Older graduate students like Dan, Gian, and Jorge made me feel like one of the gang since my first semester, making sure I did not feel lost at sea. Countless movie nights with Sarah, Collin, Cecilia, and Jake always kept things spirited (read: "peace be the journey"). I would also like to thank Jeanne Mullen for the countless pep talks, and always having my back. I owe a special thank you to my office-mates Dylan, Josh, and Sanjay who created an environment of camaraderie and support that made the study astronomy into a team effort (even when the color of the day was black). Most importantly, I would like to thank my mentor, Hai, who has taught me so much over five years. I hope that this thesis reflects the passion for astronomy that you have instilled in me; we truly are the lucky ones for getting to explore these frontiers.

ABSTRACT

Simulations of galactic mergers predict that tidally-induced gas inflows can trigger synchronized accretion onto the supermassive black holes at the center of each galaxy. These should be observable as dual active galactic nuclei (dAGN) at kpc-scale separations. We test this prediction using a carefully selected sample of 35 radio galaxy pairs from the Stripe 82 field. Using optical spectroscopy from the Keck LRIS instrument, we confirm that 21 of these pairs have consistent redshifts, and thus are kinematic pairs in mergers; the remaining 14 are found to be isolated galaxies. We further classify the optical spectral signatures of the kinematic pairs via emission line ratios, equivalent widths, and excess of radio power above star-formation predicted outputs. We find 6 galaxies are classified as low ionization LINER-type AGN, and 7 are AGN/starburst composites. Most of the LINERs are found to be retired galaxies, while the composite types are more likely to have some AGN contribution to their ionizing spectra. All our kinematic pairs show evidence of radio power more than 1 dex above the level expected just from star-formation, suggestive of a radio AGN contribution. To rule out the possibility of radio emission from one galaxy overlapping with its companion, we analyze high resolution ($0.3''$) imaging from the *Very Large Array* for 17 of the kinematic pairs. We find that 6 pairs host two separate radio cores thus confirming their status as dAGNs. The remaining 11 are single AGNs in each pair, with most exhibiting prominent jets/lobes overlapping their companion. Our final census will allow us to compute a corrected dAGN duty cycle, and test whether it is higher than predictions of stochastic fueling. While dAGNs are themselves rare, the merger process likely plays some part in their evolution.

PUBLIC ABSTRACT

Throughout the nearby Universe, there are stunning examples of galaxies in the process of colliding and merging together. Computer simulations predict that these violent events disrupt gas in the galactic disk, funneling it to the central nucleus where it can fuel black hole accretion in both galaxies involved. We search for evidence of these dual active galactic nuclei (dAGN) in closely separated galaxy pairs. Our sample consists of 35 radio galaxy pairs selected as having radio and optical detections. We analyze optical spectra and confirm that 21 of these pairs contain two galaxies at the same redshift, and thus are at the same cosmic distance and genuinely in a pair. The remaining 14 contain galaxies with wildly different redshifts and are thus isolated galaxies. We further investigate the source of the ionized emission lines in the spectra of the true pairs via emission line ratios, equivalent widths, and excess of radio power above star-formation predicted outputs. None of the galaxy pairs shows unambiguous evidence of an optical dAGN, and many have at least some starburst contributions. All of our true pairs do show evidence of radio power well above the level expected just from star-formation, suggestive of a radio AGN contribution. To rule out the possibility of radio emission from one galaxy overlapping with its companion, we analyze high-resolution radio images for 17 of the true pairs. We find that 6 pairs host two separate radio cores thus confirming their status as dAGNs. The remaining 11 contain a single AGN in each pair, with most exhibiting prominent radio jets overlapping their companion. We give optical preselection cuts to further boost the success rate of finding dAGNs in future all-sky surveys.

TABLE OF CONTENTS

LIST OF TABLES

Table

LIST OF FIGURES

Figure

CHAPTER 1

INTRODUCTION

1.1 Active Galactic Nuclei

Our current understanding of the galaxies in our present day Universe involves a history of mass assembly via major and minor galaxy mergers. This hierarchical model of galaxy formation leads to a dynamic and ever-changing landscape of high mass luminous elliptical galaxies, well structured spiral galaxies, and transitory irregular galaxies with sweeping tails of gas and dust left in the wake of tidal interactions. For galaxies like our Milky Way, cosmological hydrodynamical simulations have shown that large components of their stellar material have originally come from several other galaxies via mergers throughout their evolution (e.g., Rodriguez-Gomez et al., 2016; Pillepich et al., 2017). Aside from facilitating the ex-situ acquisition of mass, gravitational torques from mergers can disrupt gas in the galactic disk, driving massive flows of material toward the central region (Di Matteo, Springel, and Hernquist, 2005). The consequences of gravitational torques can also be seen in the form of inducing stellar bars in the bulge which further funnel large amounts of interstellar gas from the built up reservoir to the central kiloparsec on short timescales (Barnes and Hernquist, 1991). Inflowing gas from outer regions of the galaxy can supply the pristine raw material needed to induce an intense burst of star-formation, while also diluting the metallicity of the surrounding interstellar medium (Torrey et al., 2012). Most dramatically, the influx of gas streaming towards the nuclear region can trigger supermassive black hole (SMBH) accretion in the central parsec of a galaxy, initiating an active galactic nucleus (AGN) (e.g., Capelo and Dotti, 2016a). These active black holes are the most powerful and luminous engines in

the universe, at times dominating the luminosity of the host galaxy.

1.1.1 AGN: a Brief Historical Context

The study of active galactic nuclei began just over a century ago, and has since blossomed into one of the major fields of investigation in astronomy, encompassing every wavelength of light in the electromagnetic spectrum. Optical spectroscopy has been a crucial tool in this endeavor since the very beginning, as the first indications of an active galaxy were gleaned from nebular emission lines superimposed on a stellar absorption continuum in the spiral "nebula" (now known as a galaxy), NGC 1068 (Fath, 1909; Slipher, 1917). Further studies by Seyfert (1943) of galaxies with high-ionization emission lines reminiscent of planetary nebulae revealed a class of galaxies (now known as Seyfert galaxies) with highly Doppler-broadened lines originating from a bright nucleus. Similar emission spectra were subsequently observed in the galaxies hosting the recently discovered strong radio sources Cygnus A and Cassiopeia A (Baade and Minkowski, 1954), revealing a possible connection between powerful extragalactic optical and radio sources. Greater study of radio sources revealed objects which were optically point-like and star-like in appearance, but with spectra hosting unknown broad emission lines and a lack of absorption lines quite unlike the spectra of stars, earning these objects the monicker of being quasi-stellar radio sources, or quasars for short (Burbidge, 1967). The landmark study of the radio star 3C 273 by Schmidt (1963) revealed that the hitherto puzzling broad emission lines were actually the well known Balmer series of Hydrogen that had been redshifted well beyond its usual optical rest wavelengths. The high redshift of these apparently distant galaxies ($z = 0.367$ for the galaxy 3C 48) implied that they must be incredibly luminous (Greenstein and Schmidt, 1964), outshining

the fainter underlying host galaxy to give the nucleus the appearance of a stellar source. Similar radio-quiet but optically brighter sources with strong ultraviolet emission were soon after dubbed quasi-stellar objects, or QSOs, although the term quasar is generically also used (Burbidge, 1967).

Substantial efforts to categorize the growing population of active galactic nuclei resulted in a plethora of classification schemes. Chief among these is the separation of emission line-emitting nuclei by the degree of Doppler broadening in their permitted line profiles of Hydrogen and Helium (as well as in their forbidden lines, though to a lesser degree) (Khachikian and Weedman, 1974), where Type I exhibit broadened wings and Type II generally only show the narrower component. Models of photoinization as the main mechanism for the emission lines then led to the interpretation of two distinct physical regions around the nucleus: a dense region of clouds with high levels of orbital motion around the nucleus responsible for broadening the lines, and a lower density region further from the nucleus with less motion producing the narrow cores of the lines (Shields, 1974). These became known as the broad line region (BLR) and narrow line region (NLR), respectively. Concurrently, the vast radio lobes emitted by some radio galaxies, such as Cygnus A, were explained as outflows from the nuclear region by the "twin-exhaust" model of magnetized and collimated relativistic plasma (Blandford and Rees, 1974). The source powering these highly energetic effects was proposed to be a compact object surrounded by an accretion disk (Salpeter, 1964), characterized as a dead stellar remnant or black hole (Lynden-Bell, 1969). The accretion disk itself was originally thought to radiate due to viscous instabilities (Pringle, 1976), but the role of magnetic field lines threading the disk has since gained importance (Balbus and Hawley, 1991). The

discovery of lower-ionization nuclear emission regions (LINERs) with weak emission lines (Heckman, 1980) revealed a new population of so-called low luminosity active galactic nuclei (LLAGN; see Ho, 2008, for a review) perhaps fueled by a lower level of accretion. The puzzling variety of AGN and whether they are preferentially observed with broad lines (or without), beamed jets, or only radio emission was finally woven together in a coherent picture of observation angle effects in the so-called unified model of AGN, where some sight-lines are blocked by an obscuring dusty torus (Urry and Padovani, 1995). The evolving picture seems to indicate a continuum of AGN along an evolutionary sequence where accretion is a primary driver of the physical processes around the central black hole and the resulting luminous output (Heckman and Best, 2014). This brief historical overview serves to motivate the multiwavelength signatures (especially in optical and radio) investigated throughout the rest of this work.

1.1.2 AGN: a Phenomenological Sketch

The effects resulting from SMBH accretion are observable across the entire electromagnetic spectrum, offering clues about the physical structures surrounding the central black hole. We briefly describe these structures and their emission mechanisms to give context for our sample selection strategy later on. The accretion disk is traditionally modeled as a geometrically-thin optically-thick disk of hot gas (Shakura and Sunyaev, 1973), whose thermal blackbody emission contributes to the featureless underlying optical and UV continuum (O'Dell, 1986). This continuum emission illuminates the clouds in the closely held BLR, and further out in the NLR (which itself might indicate outflowing winds), generating the nebular emission lines characteristic of AGN (Osterbrock and Ferland, 2006, sec. 14.8). The

thin disk model is thought to be the dominant mechanism at higher accretion rates. At lower levels of accretion (*e.g.*, in LLAGN), the disk might truncate and puff up due to thermal trapping to form a radiatively inefficient accretion flow (Narayan and Yi, 1994). This accretion flow is thought to be advection dominated, transferring energy directly onto the black hole (Yuan, F. et al., 2002). Jets of plasma glowing in radio frequencies are prominent in radio-loud AGNs, caused by the synchrotron emission of relativistic electrons forced helically outwards away from the black hole along intense polar poloidal magnetic field lines via the Blandford-Znajek process (Blandford and Znajek, 1977). While jets are ubiquitous in the aptly-named jet-mode of low activity (Falcke, Körding, and Markoff, 2004), some quasar-mode AGN also display jets as powerful radio-loud sources while others might only produce weak jets, if any at all (Heckman and Best, 2014). A corona of hot particles evaporated from the surface of the accretion disk surrounds the immediate vicinity of the disk, and might be responsible for X-ray emission via Inverse-Compton upscattering of disk photons off these hotter particles (Liang and Price, 1977; Haardt and Maraschi, 1993). The exact geometry and distance from the black hole (i.e., the "lamppost" model) is a current matter of debate (Ursini et al., 2020). For instance, perhaps X-rays are generated by synchrotron self-Compton emission from shocks at the base of the jet (Yuan, F. et al., 2002). Optical, UV, and X-ray emission can be absorbed and blocked from the observer's view by the shroud of a dusty torus, which would reprocess the light and emit strongly at infrared (IR) wavelengths (Bannikova et al., 2021). While there is some evidence that the dust might actually be patchy, direct imaging of the torus surrounding NGC 4261 using *HST* strongly suggests a torus structure for at least some AGN (Jaffe et al., 1996). In this scenario, the viewing angle

dictates which wavelengths the observer will see and what the system as a whole will look like, as suggested in the AGN unification scheme of Urry and Padovani (1995). Searching for the presence of AGN then requires several lines of evidence over multiple wavelengths to rigorously confirm or rule out nuclear activity. In this text, we focus primarily on the signatures of optical emission lines and radio jets. We illustrate the quasar mode and radio mode frameworks with schematic sketches in Figures 1.1 and 1.2, respectively. Which of these modes of activity dominates during galactic mergers is still a matter of debate, and a question of concern in our current investigation.

1.1.3 dual AGN

A question naturally arises: if SMBHs can be fueled by gas inflows, and inflows can be triggered via tidal interactions during a galactic merger, then should we expect there to be AGNs triggered in both merging galaxies at the same time? Closely related and more generally, should we expect to see more AGNs in mergers? Simulations of major galaxy mergers indicate that simultaneous SMBH accretion could occur if prompted by strong tidal forces during the close approach of a merger (galactic separations $\lesssim$10 kpc) (e.g., Wassenhove et al., 2012; Blecha et al., 2012; Rosas-Guevara et al., 2019). It is difficult to predict when both of the SMBHs could be active (Blecha, Loeb, and Narayan, 2013), and the observability timescale likely depends on the mass ratio between the two galaxies (e.g., Martini, 2004; Hopkins et al., 2005). However, for a major merger, simulations suggest a window of dual activity of $\sim$100 Myr (Capelo et al., 2017), which becomes shorter with increasing mass disparity between the two galaxies. This activity appears to be at its highest levels during late pericenter passages (Capelo et al., 2017), when tidal torques and ram-pressure shocks

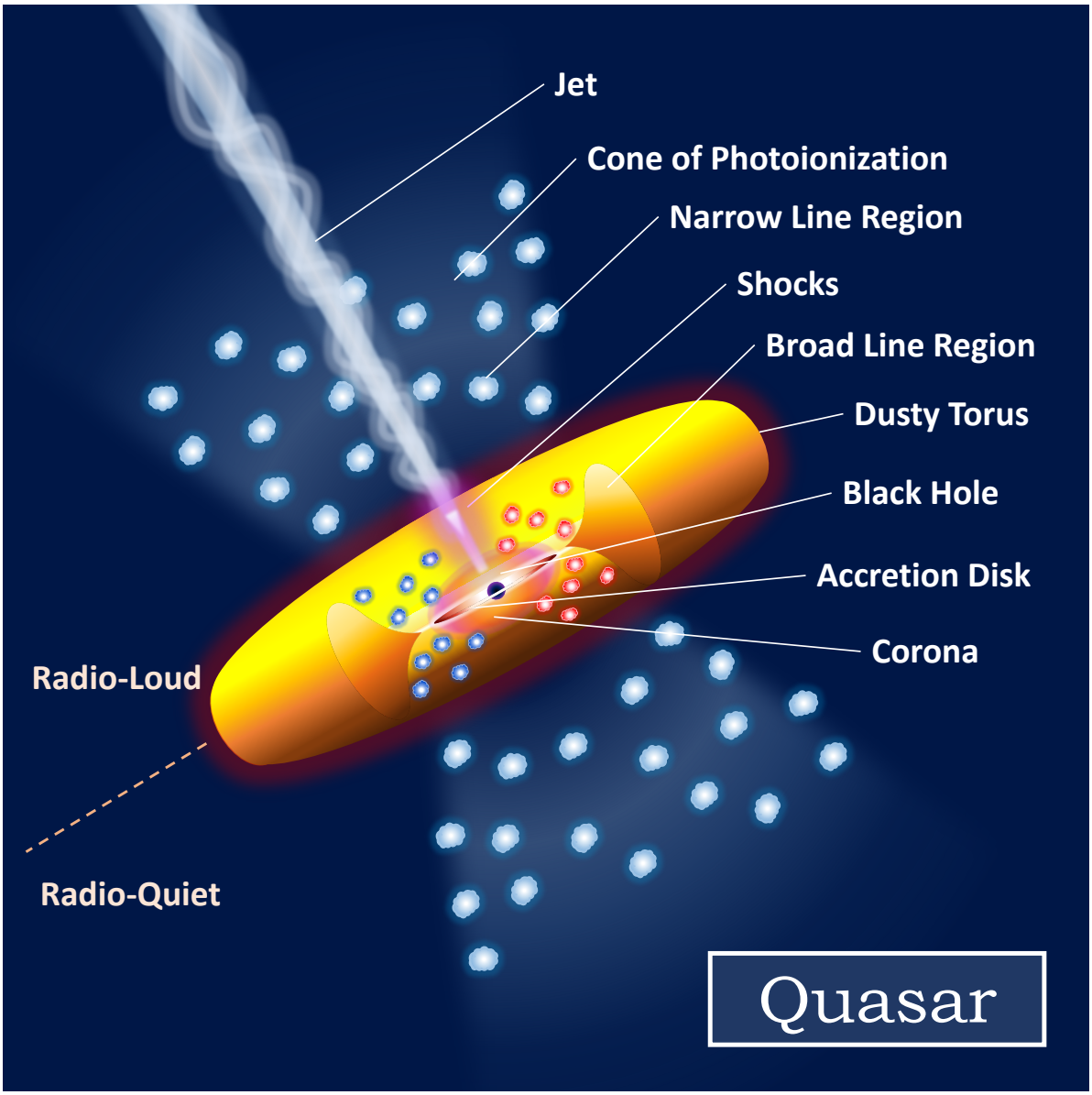

Figure 1.1. Sketch of Quasar-type AGN in radiative/quasar mode. Scaling is exaggerated for readability. The dusty torus (shown in cross-section) extends out ∼1−100 pc, and might actually be patchy. The accretion disk extends from the dust sublimation radius down to the inner most stable orbit around the black hole (r ∼3 Schwarzchild radii). The thermal continuum UV emission of the disk (exiting the torus in a bipolar cone of light) photoionizes the close in dense region of rapidly rotating clouds (leading to Doppler broadening) in the BLR, and further out in the less dense NLR (extending several hundred parsecs out), giving rise to the observed nebular emission lines. A haze of evaporated electrons surrounds the disk in a corona that might be responsible for X-ray emission through inverse-Compton upscattering of photons from the disk. Synchrotron emission, generated by jets of outflowing relativistic electrons ensnared in a powerful poloidal magnetic field, is present for radio-loud AGN, but may be weak or absent for radio-quiet AGN. Sketch drawn by the author based on modified figures by Urry and Padovani (1995) and Heckman and Best (2014).

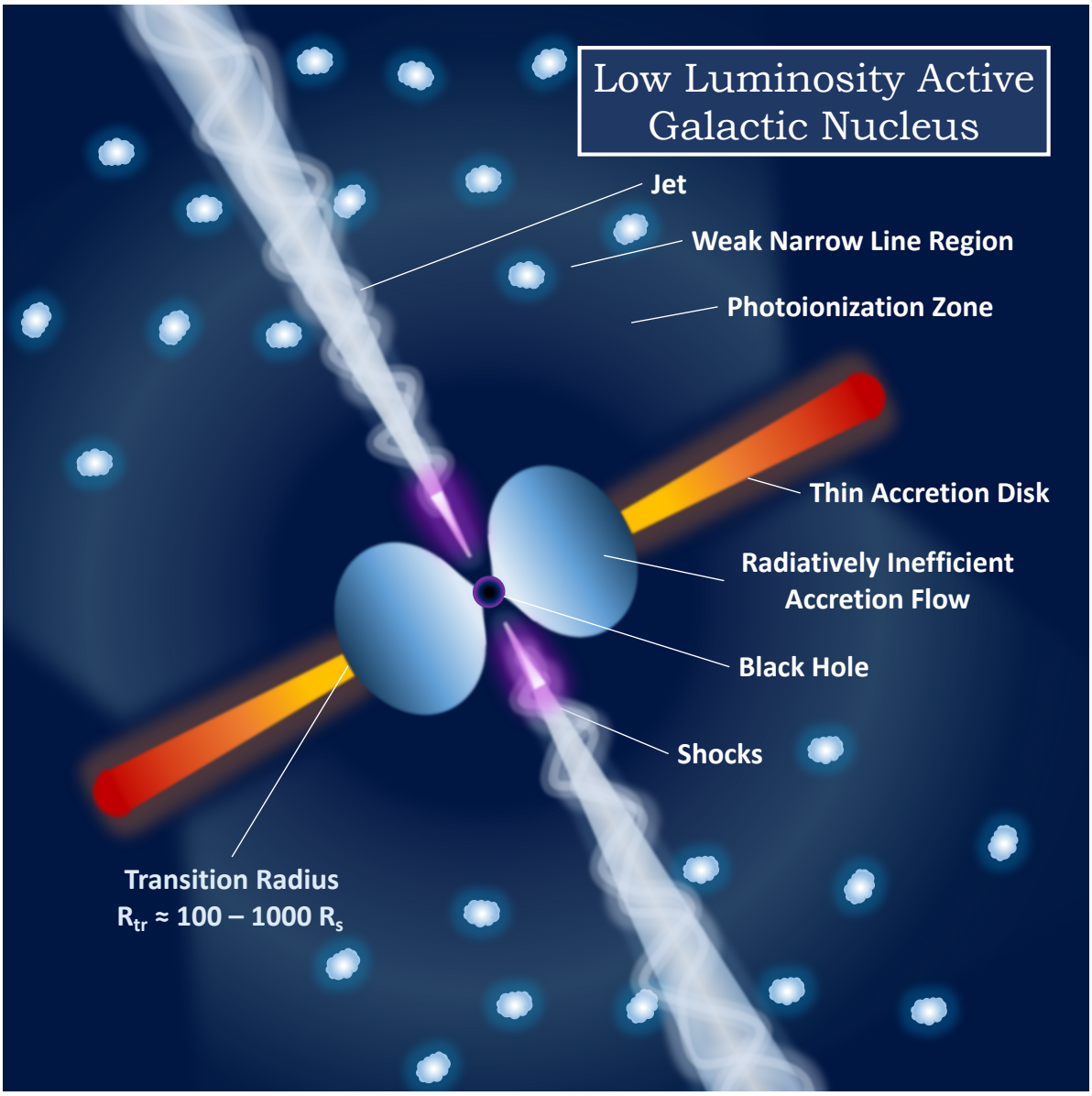

Figure 1.2. Sketch of Low Luminosity AGN in jet/radio mode. This figure (not to scale) is significantly zoomed in compared to Figure 1.1 to focus on the innermost parsec inhabited by the accretion disk. While similar to quasars, LLAGN likely have a truncated accretion disk that transitions to a radiatively inefficient accretion flow around a radius of several hundred Schwartzschild radii. Energy from the flow is advected directly onto the black hole. It is thought that at lower accretion rate ($< 10^{-2}$ times the Eddington limit), the dusty torus is no longer supported. While still capable of lower levels of photoionization in a weak NLR (shown here much closer in than its actual distance of several hundred parsecs), most of the energy transported outward is in the form of mechanical feedback from powerful radio synchrotron jets. Shocks at the base of the jets might be responsible for the low levels of observed X-rays. Sketch drawn by the author based on figures by Ho (2008) and Heckman and Best (2014).

are able to efficiently transport gas to the central parsecs (Capelo and Dotti, 2016b). Recent semi-analytical simulations by Li, Ballantyne, and Bogdanović (2021) similarly indicate that scales of $\sim$0.3$-$0.5 kpc are the most likely separations at which to find dAGNs. At this stage, the merging galaxies should each exhibit an AGN before the final coalescence of the two galaxies.

There is a complication within this idealized scheme of merger-fueled activity. AGN have also been observed in isolated galaxies which show no evidence of gravitational disturbances (Villforth et al., 2014; Hopkins, Kocevski, and Bundy, 2014; Kocevski et al., 2015). In these cases, it is suspected that chance accretion of small pockets of gas through random stochastic processes may be responsible for triggering an AGN phase (Hopkins et al., 2006; Hopkins, Kocevski, and Bundy, 2014). These small-scale instabilities might be due to cloud-cloud interactions (Genzel, Hollenbach, and Townes, 1994), minor mergers between a high-mass galaxy and its low-mass companion (Hernquist and Mihos, 1995), or instabilities within the galactic disk or bar (Norman and Silk, 1983). Generally, it is thought that major mergers are typically responsible for the massive gas inflows necessary for high luminosity AGN, while secular stochastic processes trigger longer-lived periods of LLAGN activity (Pierce et al., 2022; Zhao et al., 2022), especially in gas-rich spiral galaxies (Storchi-Bergmann and Schnorr-Müller, 2019). However, whether or not stochastic processes contribute to or dominate over the effects of merger interactions to trigger a phase of synchronized activity in dual systems (not isolated) is still a matter of open debate.

1.2 The Search For Dual Active Galactic Nuclei

With predictions from simulations suggesting the existence of a population of dAGNs, is there any observational evidence to support synchronous SMBH accretion? Telltale signs of kpc-scale dAGN activity were first discovered in the radio galaxy 3C 75 (Owen et al., 1985), which shows a pair of radio jets originating from a pair of stellar nuclei separated by 7.7 kpc, in line with simulation predictions. Many campaigns over the past several decades have uncovered a scant population of dAGNs. Optical and X-ray observations have identified a number of other kpc-scale dAGNs, including LBQS 0103−2753 (Junkkarinen et al., 2001), NGC 6240 (Komossa et al., 2003), 3C 294 (Stockton et al., 2004), Arp 299 (Ballo et al., 2004), Mrk 463 (Bianchi et al., 2008), NGC 3393 (Fabbiano et al., 2011), Mrk 266 (Mazzarella et al., 2012), PSO J308-21.23 (Connor et al., 2019). High resolution radio imaging has likewise revealed a dearth of dAGNs, including J1010+1413 (Goulding et al., 2019) and Mrk 739 (Tubín et al., 2021). Recently, a triple AGN system has even been discovered at $z = 0.077$ (Pfeifle et al., 2019). A recent study by Yue et al. (2021) gives evidence of kiloparsec-scale dual quasars at extremely high redshift of 5.66 using the Dark Energy Survey. However, these serendipitous "one-off" discoveries do not offer a statistically large enough sample necessary to properly address the question of dAGN triggering. The situation is further complicated by the inhomogeneous methodologies which obstruct a true "apples-to-apples" comparison.

To procure a large enough sample, a multi-step strategy must be employed. Starting with simply identifying potential dAGN candidates efficiently requires lower-resolution observations of larger samples. This has been done optically using double-peaked [O III] AGNs in the DEEP2 Galaxy Redshift Survey (Gerke et al., 2007; Comerford et al., 2009) and in

the Sloan Digital Sky Survey (SDSS; Wang et al., 2009; Liu et al., 2010; Smith et al., 2010; Kim et al., 2020; Zhang et al., 2021b), as well as through BPT-selection in spectroscopic galaxy pairs in SDSS (Ellison et al., 2011; Liu, Shen, and Strauss, 2012; Fu et al., 2018) and the Yunnan Faint Object Spectrograph (Zhang et al., 2021a), and astrometric jitters in Gaia imaging (Shen et al., 2021). Many nearby AGNs have been detected in hard X-rays in the Swift Burst Alert Telescope (BAT) survey (Koss et al., 2010) as well as the *Chandra* survey of merging galaxies (Brassington, Ponman, and Read, 2007; Teng et al., 2012). Wide-area radio campaigns such as the VLA Stripe 82 survey have revealed radio AGN pairs (Fu et al., 2015b). Selection by mid-IR has more recently gained favor using WISE to isolate AGN by their colors (Satyapal et al., 2014; Satyapal et al., 2017). Many of these pre-selection strategies suffer from one of two weaknesses, however: either they rely on higher sensitivity observations which are not practical to obtain in the large quantities needed, or they are large area surveys that lack the resolution required to discern two separate emission sources.

Once a sample of candidates has been identified, confirmation of dAGN presence requires high-resolution observations at wavelengths that trace AGN activity. This has been done in optical and near-IR with adaptive optics imaging (Fu et al., 2011b; Rosario et al., 2011; Imanishi et al., 2020), *HST* imaging (Liu et al., 2012; Comerford et al., 2015; Liu et al., 2018a), *Large Binocular Telescope* spectroscopy (Husemann et al., 2020), and integral-field spectroscopy (McGurk et al., 2011; Fu et al., 2011). Dedicated follow-ups in X-ray with *Chandra* (Comerford et al., 2011; Koss et al., 2011; Koss et al., 2012; Teng et al., 2012; Liu et al., 2013; Comerford et al., 2015; Ellison et al., 2017; Hou et al., 2019; Foord et al., 2020; Iwasawa et al., 2020) and NuStar (Ptak et al., 2015; Koss et al., 2016), and in radio with the

VeryLargeArray (Fu et al., 2011a; Fu et al., 2015a; Müller-Sánchez et al., 2015) and the *VeryLongBaselineArray* (Tingay and Wayth, 2011; Deane et al., 2014; Wrobel, Walker, and Fu, 2014; Bondi, M. et al., 2016; Liu et al., 2018b) have confirmed a small population of *bonafide* dAGNs, with overall modest success rates. Recently, Hou, Li, and Liu (2020) confirmed an astounding 21 dAGNs using archival *Chandra* X-ray data of optically-selected AGN pairs, albeit at separations >10 kpc, illustrating the success of following such a sample selection strategy as outlined above. Identifying and rigorously confirming dAGNs is a slow process since multi-wavelength evidence is necessary. Currently there are $\lesssim$50 dAGNs with projected separations less than $\sim$10 kpc in the literature (see Satyapal et al., 2017; De Rosa et al., 2019, for recent compilations). Despite the modest and inhomogeneous sample, it seems clear that the AGN duty cycle is higher in mergers than in isolated systems. Further progress in understanding the triggering and nature of dAGN systems will require a statistical sample compiled using a consistent strategy.

1.3 The Sample

This thesis seeks to address the identification and nature of a population of dAGN using a complete and uniformly treated sample. The identification of the original sample was done in Fu et al. (2015b), with the primary goal of identifying pairs of galaxies which have coincident regions of bright optical nuclei and radio emission. Once a list of potential targets was culled from the overall sample, a follow-up campaign was conducted as a pilot study on a small subset of the most promising candidates in Fu et al. (2015a). The resulting 4 pairs of galaxies with strong evidence for dAGN were then further characterized using proprietary X-ray data in Gross et al. (2019). We motivate this thesis by first discussing these previous

works and justifying the merit in further exploring the vast remainder of the original sample.

1.3.1 Paper I: Sample Selection

In the quest for a sample of dAGNs with known selection biases, we start with a moderate-resolution wide-area survey in the hopes of identifying a large number of potential candidates. The Stripe 82 region is an approximately 300 deg^2 narrow swath of sky (centered on the vernal equinox with 20 hr $<$ R.A. $<$ 4 hr, $-1.26 <$ Dec. $< +1.26$) targeted by the Sloan Digital Sky Survey (SDSS) (Abazajian et al., 2009). Because of its equatorial position, the region has been fully scanned many times ($\geq$70) in the optical range by SDSS between 2000 and 2008 (Jiang et al., 2014). The deep co-added *ugriz* images resulted in a catalog of point source detections down to 5σ detection limits for the filters of 25.1$-$22.8 AB (Jiang et al., 2014). Approximately 92 deg^2 of this region has also been scanned at 1.4 GHz (resolution $\sim$1.8$''$) by the *Very Large Array* (VLA) between 2007 and 2009 in two discontiguous regions, resulting in a catalog of nearly 18,000 sources (Hodge et al., 2011). This combination of wide and deep, relatively sharp observations in multiple wavelengths opens up the possibility of identifying many faint sources.

The first step of the sample selection strategy done in Fu et al. (2015b) is to cross-reference the optical and radio catalogs. Within a search radius of 1.8$''$, a total of 11,203 VLA sources were found to have matching SDSS counterparts in at least one of the optical photometric bands from the catalogs of Jiang et al. (2014) and Ahn et al. (2014). The search radius choice was guided by not only the resolution of the radio survey, but also the possibility that sources in close proximity may not have been deblended well when extracting radio photometry from extended regions, while also being mindful of astrometric

offsets between the the optical and radio catalogs. This large set of individual galaxies is then whittled down to a catalog of galaxy pairs by requiring that galaxy pairs contain 2 radio centroids (each having an optical ID) with angular separations $\leq 5''$, which corresponds to a physical separation of 10 kpc at z = 0.11 (assuming that both galaxies are at the same redshift). Misidentified pairs are then removed by visual inspection to avoid cases of optical cross-band astrometry errors or cases where the optical counterparts are clearly positioned within the radio lobes of a nearby radio galaxy.

83 galaxies pairs remain after these selection criteria, which are then qualitatively graded into four categories based on the degree of alignment between the radio and optical sources. Grades A and B are considered promising dAGN candidates because there are clear associations between the locations and position angles of the paired optical and radio sources. The distinction between the two categories is done by eye, where grade B pairs show some evidence of extended radio structure that might indicate radio lobes or ionized gas outflows from one source giving the impression of a secondary source (an issue which we shall return to in great detail). Grades C and D show large offsets between one of the optical components and the corresponding radio component or even misalignment between the optical and radio position angles, and are thus excluded from further analysis. The final census includes 22 strong cases of optical/radio galaxy pairs (grade A), and 30 well aligned and promising pairs (grade B). We refer the reader to Fu et al. (2015b) figures 3 and 4 for the original optical/radio stamp images for the grade A and B pairs.

Several subsequent steps of the sample selection are then conducted using archival optical spectra from SDSS for 6 pairs, and Keck observations for 2 other pairs. Emission

line fitting rejected 2 of the pairs as being at different redshifts and thus at different cosmic distances and not true mergers (Fu et al., 2015b). For 8 of the remaining individual galaxies with detectable emission lines, evidence of AGN activity was inferred by the observed radio emission being a factor of ten in excess of what would be predicted for pure star-forming regions based on Hα luminosity. Most of the sources also showed optical ionization signatures of AGN/star-forming composite regions when placed on the BPT diagram (discussed further in §2.4.1). These sources were thus considered persuasive identifications of dAGNs.

1.3.2 Paper II: Follow-up Pilot Study

The resolution of the VS82 survey is fine enough to resolve radio emission coincident with two galaxies in a pair down to 1.8″. However, actually verifying whether the emission constitutes two separate radio cores requires resolution on the sub-arcsecond scale. In fact, the premise of this dAGN optical/radio selection was conceived through the verification of a previous dAGN by Fu et al. (2011a) via high-resolution radio imaging follow-up of a spectroscopically double-peaked [O III] optical target. Pinpointing separate radio cores in this 1.4″ (7.4 kpc) separated pair (SDSS J150243.1+111557) was necessary in this case to refute the possibility that the optical signature originated from the gas kinematics of a singular accreting source.

Follow-up high resolution VLA observations of 6 of the final suspected dAGN pairs in the parent sample above were conducted by Fu et al. (2015a). At a frequency of 6 GHz , the greatly improved resolution (∼0.3″) revealed that 4 of the pairs did indeed contain bright compact cores with spectral index values indicating synchrotron radiation from AGN jets. The other two candidate systems were resolved as individual cores with strong jets/lobes

giving the false impression of dual cores at lower resolution. Altogether, 4 pairs of dAGNs (8 individual sources) were yielded from the original ∼11,000 radio and optical sources. The success of the sample selection motivates replicating the strategy beyond the pilot sample to address the rest of the sample.

1.3.3 Paper III: X-ray Follow-up on the Pilot Study

In order to better characterize the nature of the confirmed 4 dAGN pairs from the pilot study, follow-up X-ray observations using the *Chandra X-ray Observatory* were conducted in Gross et al. (2019). Briefly, the sample of dAGNs yielded a surprising mix of results in the X-ray data. With *Chandra's* resolution of $\sim 0.5''$, the dual systems were able to be spatially resolved. One pair did indeed contain 2 obvious bright cores. Two pairs showed a setup where one source is clearly detected, and its companion is marginally detected. The last pair contains two sources where neither is significantly detected in X-ray, but we were able to put upper limits on their fluxes. The resulting K-corrected 2−10 keV luminosities ranged between $39.8 < \log(L_{\rm X}\ /{\rm erg\ s^{-1}}) < 42.0$, characterizing the sources as Low Luminosity AGN or Seyferts when taken together with their radio and Hα properties. While spectral fitting was generally not possible for such low count data, the hardness ratios indicated that several sources were only mildly obscured by neutral Hydrogen in the vicinity of the nucleus ($21.2 < \log(N_{\rm H}/{\rm cm^{-2}}) < 22.7$), and the remaining sources were unobscured and thus intrinsically low luminosity. These pieces of evidence suggested that dAGN activity may not be triggered by major gas inflows induced by the merger, but instead by a combination of small scale stochastic accretion processes assisted by minor tidal disturbances. The small number of sources in this subset of the overall sample does, however, limit the scope of

these conclusions. A larger statistical sample size is needed to more concretely constrain the observed trends and draw more firm conclusions about the mechanism that triggers synchronized AGN activity in galaxy mergers.

1.4 The Scope of this Thesis: the Remaining Sample

Out of the total set of 52 grade A and B galaxies pairs from Fu et al. (2015b), only 8 pairs have been rigorously confirmed/refuted thus far. In this thesis we analyze the remainder of this sample in a similar fashion. We aim to confirm additional dAGN pairs using a combination of optical spectroscopy, emission line diagnostics, and 6 GHz high resolution radio imaging.

One of the major roadblocks in the original study was the lack of complete spectroscopic coverage. To confirm whether a given galaxy pair is indeed a spectroscopic binary (step 1 of the selection strategy), we require observations of *both* nuclei in the pair. Archival coverage of the Stripe 82 sample is far from complete, with SDSS redshifts usually only available for one source in a given pair, if at all. Through 3 observing campaigns with the Keck telescope, we have obtained optical data to analyze both targets in most of the remaining sample of Grade A and B candidate pairs. We begin in §2 by detailing the acquisition, reduction, and analysis of the new spectral data. We confirm a subsample of the pairs are indeed in mergers where the redshifts are consistent. We use the reduced spectra to extract emission line fluxes from the galaxies, and then apply these to a potpourri of well established metrics to assess whether the ionization state of each source is consistent with hosting an AGN (step 2 of the selection strategy). The spectra will lastly allow us to infer properties of the central black holes, namely their masses.

We further analyze the spectroscopic binaries in §3 using 6 GHz radio data obtained through 3 observing campaigns with the *VLA*. We have coverage for 17 of the most promising pairs. The high-resolution imaging data (step 3 of the selection strategy) will allow us to definitively pinpoint the cores of radio emission expected for AGN, and separate out imposters that are the effect of radio jets from one galaxy interacting with its companion. The synthesis of this multiwavelength data will finally allow us to estimate properties of the putative SMBHs fueling in the confirmed AGNs, including the accretion rate and duty cycle of activity.

Our primary aim for this thesis is to more completely constrain the rate of synchronous supermassive black hole activity in merging galaxies. By identifying and confirming additional dAGN systems, we can then address whether the AGN duty cycle is enhanced during major galaxy mergers, as is predicted by simulations. Secondarily, we seek to characterize the properties of the dAGN systems found within our sample to draw conclusions about the effects of such synchronous accretion. For example, are dAGN more likely to be found in a state of higher accretion as in quasars, or lower accretion as in LLAGN? Unraveling the nature of dAGN triggering and its effects may better inform the broader astronomical community in discussions of AGN fueling and feedback, and their significance as it relates to the galactic evolution across cosmic time. We also explore ways to optimize the efficiency of our selection method to inform future searches of dAGN with the *VLA* Sky Survey. Note that throughout this text, we adopt a concordance Λ cold dark matter cosmology based on the *WMAP* mission, with energy density values of $\Omega_{\rm m} = 0.3,\ \Omega_{\Lambda} = 0.7,$ and $\Omega_{\rm b} = 0.0455$; we also assume a Hubble constant value of $H_0 = 70$ km s^{-1} Mpc^{-1} (or, a reduced parameter

of $h = 0.7$) (Komatsu et al., 2011).

CHAPTER 2

OPTICAL SPECTROSCOPY

Analysis of optical spectra serves two main purposes: to obtain redshift values for the galaxies, and to extract emission line fluxes. The former is a critical step in separating true merging pairs from those whose on-sky positions allow them to merely masquerade as mergers. *Bona fide* mergers will have redshift values that are broadly consistent with small differences due to the orbital motions of the galaxies during the merging process. The latter step is useful for identifying whether a galactic nucleus is in fact actively accreting. The relative brightness of certain nebular emission lines allow us to ascertain whether the ionized gas in the central region (if there is an appreciable amount) is due to the hard ionizing spectrum of an AGN impinging on the BLR and NLR gas, or if a burst of star formation is causing lower levels of ionization through creation of extensive H II regions around clusters of O and B type stars. Since we will already have the optical spectra necessary for redshift estimation, optical emission line analysis follows naturally as the first tool in the identification of AGN.

2.1 Observations

The spectroscopic data were acquired over three observational campaigns between 2015 and 2017. All observations were carried out using the Low Resolution Imaging Spectrometer (LRIS) at the Keck I Observatory (Oke et al., 1995). A 1.5″wide (175″ length) long slit was used for all observations, as well as the 560 Dichroic to separate the incoming light into the blue and red channels at 5600Å (50% transmission at 5696Å) to minimize overlap

of diffraction orders. Both the red and blue CCD detectors have a scaling of 0.135″per pixel. The nominal wavelength range for LRIS is 3200−10,000Å, although this is not achieved for all of our observations. Over the eight different nights of observations, we used the B600 blue grism paired with either the R400 or R600 red grating, although the same setup is used consistently throughout a given night. This leads to varying amounts of overlap between the red and blue sides of the spectra from one night to the next, but in general the majority of observations avoid any gaps in wavelength coverage. The details of the optical observations are separated by night and given in Table 2.1.

The original sample was selected based on the *ugriz* optical imaging, and the Petrosian magnitude of the fainter galaxy in each pair guided the proposed observation times. We restate the r-band magnitudes for the two galaxies in each pair to illustrate the range of optical faintness across the sample. Seeing conditions varied widely by night, necessitating the last couple observations added on to additional nights. In some cases this was caused by fog that intervened during nights that started out clear. As well, some of the optically fainter targets were found to require longer exposure times than obtained during the first round of observations. This is the case for the pair in 2242+0030, where one of the galaxies has an r-band magnitude of 23.3AB. In general, out of the total 52 grade A and B target pairs, 13 pairs were dropped from the proposed observations since they would have required over one hour of integration time to achieve a modest S/N$\sim$3 per resolution element. We also note that five of the observed pairs had calibration issues during the observations, and thus cannot be properly analyzed. In total, the spectroscopic sample is then composed of 14 grade A pairs, 20 grade B pairs, and one grade D pair (which is included despite its lowered

grade because of obvious evidence of an ongoing galactic merger), yielding 35 galactic pairs with spectroscopic information.

We also note that the resolution possible for the instrument results in limitations during our analysis. The dimensionless resolution can be characterized by $R = \frac{\lambda}{\Delta\lambda}$, where λ is the operational wavelength and $\Delta\lambda$ is the separation between two spectral peaks that can be individually resolved (Appenzeller, 2012). This is equivalent to the inverse of a dimensionless FWHM scaled by the speed of light, such that $R = \frac{c}{\Delta v}$. As an estimate, the highest resolution is achieved for our observations utilizing the 600 lines/mm grating in the red channel and $1.5''$ slit, which results in R$\sim$1595, or $\Delta v \sim 188$ km/s. The poorest resolution is achieved for the blue grism (B600/4000 used in all cases), with a minimum resolvable FWHM of $\sim$300 km/s. We return to these constraints in our discussion of the measured velocity dispersions of our galaxies in §5.2

2.2 Data Reduction

To clean the optical spectra, we utilize a data reduction pipeline tailor-made for single-slit observations from LRIS: LPIPE (Perley, 2019). Briefly, the program first conducts bias subtraction from the 2D image from the CCD, and mask known "bad pixels." The normalized dome, Halogen, and sky flats are median combined and then divided out of the science spectra to remove pixel-to-pixel nonuniform responses along the slit. Cosmic ray cleaning (known informally as "zapping") to remove trailing saturated pixels is then done by modeling the signal and sky, then checking for pixels (and their surrounding neighbors) with bright deviations which are subsequently removed and replaced with median-model estimates of the pixel value. While this algorithm manages to robustly percolate through

Table 2.1. Observation Log for the Keck/LRIS targets

Designation	r_1 ; r_2	Obs.	Time (UT)	ExpT (s)
2011-10-23		B600/4000	R400/8500	
0152−0010	16.1 ; 19.0		11:31	600
2220+0058	18.5 ; 19.5		06:32	600
2232+0012	19.8 ; 19.1		11:31	900
2252+0106	... ; ...		11:31	600
2300−0005	17.4 ; 17.2		07:47	600
2302−0003	21.3 ; 20.6		08:05	1800
2318+0045	23.1 ; 20.6		09:00	900
2014-09-27		B600/4000	R400/8500	
2235+0003	21.6 ; 22.7		05:49	1800
2242+0030	23.3 ; 19.9		06:26	1800
2015-09-14		B600/4000	R600/7500	
0135+0119	18.4 ; 22.0		12:26	2400
0144−0042	22.4 ; 19.7		13:13	2400
0152−0010	16.1 ; 19.0		14:00	1200
0210−0051	19.6 ; 21.5		14:26	2100
2235+0003	21.6 ; 22.7		07:14	3600
2258+0030	18.4 ; ...		08:22	2400
2305+0024	21.1 ; 20.0		09:10	2400
2319+0038	22.0 ; 20.8		11:08	1200
2015-10-16		B600/4000	R600/7500	
0111−0000	22.9 ; 21.0		11:41	1800
0147−0008	20.7 ; 20.1		12:18	1800
0149−0014	19.1 ; 20.0		12:55	1700
2244+0010	22.1 ; 22.6		07:45	1820
2305+0024	21.1 ; 20.0		06:58	1200
2016-09-07		B600/4000	R600/7500	
0120−0046	23.3 ; 21.0		13:49	2400
0142−0001	22.5 ; 21.9		12:58	1800
0203−0033	22.9 ; 22.0		14:37	1200
2211+0027	24.0 ; 19.6		07:10	1200
2213+0048	23.9 ; 21.6		07:36	1200
2218+0045	... ; 22.3		08:04	2400
2229−0004	... ; 23.0		08:49	2400
2245+0058	20.4 ; ...		09:36	2400
2250+0011	23.3 ; 21.9		10:24	2400
2303−0117	21.7 ; 20.3		11:12	1200
2308+0025	23.4 ; 20.9		11:42	2400
2017-05-31		B600/4000	R400/8500	
2242+0030	23.3 ; 19.9		13:32	3600
2017-06-23		B600/4000	R400/8500	
2304−0109	... ; ...		12:52	4800
2017-10-15		B600/4000	R400/8500	
0116+0058	23.0 ; ...		08:07	2400

Observations are grouped by night (in bold), where we also specify the blue grism and red grating used for that night. We give the designation for the target galaxy pair, the SDSS r-band AB magnitudes for the 2 targets in each pair, start time of observation (hour : min), and exposure time.

the trails of most cosmic rays, it does fail occasionally in cases of vertical trails which are usually not removed for risk of confusion with genuine emission lines in the spectra (as is the case for a few of our final spectra). Vertical emission lines from atmospheric air glow are then corrected for via sky-subtraction. Because of the tilt of the sky lines, medians of the sky flux are calculated in blocks of wavelength columns, interpolated, and then fit with a simple polynomial least squares fit. The resulting model of the sky lines is then subtracted out of the science data. Multiple exposures of the same observation are then shifted to account for dithering, and stacked via a simple summation.

The targets are then extracted from the cleaned 2D spectra using apertures that account for the curvature of the dispersed signal across the CCD. To calculate this curvature (the "trace"), bright sources on the slit are identified and their spectra are binned into blocks along the wavelength axis to generate a series of spatial profiles for each column. The centroids of the profiles are cross-correlated to find wavelength-dependent offsets, which are then fit with a polynomial to determine a generic trace function. At this point, a user-interface is used to specify the centroid of the extraction region for a given object, which is necessary for our dual sources where the pipeline would normally default to identifying and extracting the brighter source only. The astrometric offset for each observation is determined by cross-correlating the spatial profiles from the red and blue channels to ensure that the centroid of the extraction region is consistent to within a few pixels. The width of the extraction regions is $2\sqrt{2 \times \ln(2)} \times \sigma$, where σ is the Gaussian width of the profile. In practice, this is tweaked manually in cases where the extraction regions of the sources in a pair might overlap. Simple extraction is then done to collapse the 2D spectrum along

the y-pixel dimension (while accounting for the trace) to give a 1D spectrum in terms of wavelength (still in pixels) and brightness.

To obtain the wavelength-calibrated science spectrum, 1D spectra are extracted from concurrent observations taken of the calibration lamps ("arcs"). The typical array of lamps used in our LRIS observations are Hg, Cd+Zn, Ne, and Ar. A pattern-matching algorithm is used to find potential matches of trios of bright lines by comparing the wavelengths of the lines from a reference list to the x-pixel positions of the observed lines such that a possible matching triplet has $\frac{\lambda_3-\lambda_2}{\lambda_2-\lambda_1} \sim \frac{x_3-x_2}{x_2-x_1}$. A high-order polynomial is used to fit the wavelength solution, which is subsequently refined by dropping lines that are poor matches. The final polynomial gives the conversion from pixel to wavelength. The higher order terms of the polynomial must be corrected for flexure within the spectrograph due to varying orientation with respect to gravity between the arc and science observations. This is done by matching the spectrum's observed sky lines (stored separately after subtraction from the science frame) with a catalog of sky lines to find a small linear offset which is used to "nudge" the wavelength solution. This final solution is then applied to the science spectrum. In Figure 2.1, we show an example of the intermediate data products up to this point for one of our pairs. This includes the 2D spectrum, with the traced extraction regions overlaid, as well as the resulting wavelength-calibrated 1D spectra for each extraction. At this point, the spectra are still in separate red and blue channels. We show the diagnostic plots for all 35 pairs in the Appendix §B.

2.2.1 Redshift Estimates

Once we have wavelength-calibrated 1D spectra, we can obtain estimates of the redshifts. This step is essential to verify whether both galaxies in a pair are at close separations and thus truly in the process of merging. If the redshifts between the two components differ substantially, then the objects only constitute a pair due to projection along the line of sight axis, such that the galaxies are actually widely separated along the line of sight. These "projected pairs" are thus disqualified from our further analysis in the context of genuine galaxy mergers hosting dAGNs, although there is no reason why the individual galaxies themselves might not each host an AGN in isolation.

The diagnostic panels in the suites like that of Figure 2.1 are indispensable in obtaining an estimate of each source's redshift since the former is useful in pinpointing uncleaned cosmics that might masquerade as emission lines and the latter is used for identifying the patterns of known emission lines. We estimate the redshift values by eye as a first pass, to be later fine tuned using spectral fitting (which itself requires a decent guess of the redshift). At this stage, we do not require flux calibration. In fact, the non-flux calibrated spectra prove to be easier to work with since telltale features tend to be greatly exaggerated. We use a suite of emission lines and absorption features taken from SDSS (who in turn obtain the values from the National Institute of Standards and Technology (NIST) atomic spectra database). We show these as labeled vertical blue and red lines, respectively, in the lower panels of Figure 2.1. In most cases, there is a clearly identifiable emission or absorption marker in both objects in a given pair, in both red and blue portions of the spectrum. Generally speaking, on the blue side of the spectrum we can nearly always spot the dramatic

"fang-shaped" Ca II absorption complex (so-called H and K lines), even in the absence of the nearby [O II]λ3727 emission line. On the red side, some targets exhibit clear Hα and [N II] emission line complexes. Where those are lacking, we can usually spot the deep absorption feature due to the Na I doublet (so-called D1 and D2 lines), or the pairing of Hβ and [O III]λ5007 emission lines.

Complications with the by-eye estimate arise in cases of low S/N spectra. The most likely issue seen is that the blue side of the spectrum is faint to the point of being barely perceptible (peak source counts <150 per spectral bin), even if the red side is very bright. This is not surprising given that many of our targets are intrinsically red in their SDSS optical co-add images. This is certainly the case in Figure 2.1 where source B is clearly redder in color in the region measured by the slit, yielding only a faint 2D spectrum on the blue side. We can still obtain a redshift estimate, although we flag the less certain measurements to denote complications. The majority of our sample has easily discernible redshifts, and hence are not assigned a flag. Our qualitative demarcations for the redshift flags are: (Moderate) the blue side may be faint, but obvious markers can still be seen in the red side of the spectrum, giving a reliable redshift estimate; (Fair) both sides of the spectrum might be faint or noisy or contain an uncleaned cosmic, but there is still somewhat obvious complexes of features that match up; (Poor) the spectrum is so faint or noisy that we resort to template matching on a binned version of the spectrum to find potential match-ups. We note that in all instances of pairs with consistent redshifts, we were able to find reasonable evidence for the redshift values even if template matching was necessary. Of the 9 individual sources for which template matching was done, only one (221331.87+004836.1)

required any rigorous treatment. The other 8 sources were double-checked with template matching because of particularly noisy spectra (due to imperfect sky-subtraction), or stray uncleaned cosmics adding imposter emission spikes; however, the template matches were obvious in all cases. We also note that among the pairs with consistent redshifts, only one source (221142.42+002731.2) has a quality flag of Poor. Even with these complications, our by-eye estimates yield redshift values to within $z \pm 0.00005$, which is more than sufficient for the purposes of identifying mergers.

These redshift estimates are listed in Tables 2.2 and 2.3, for pairs with contemporary redshifts and for the projected pairs with opposing redshifts, respectively. Even with our by-eye estimates, cases of projected pairs are easily spotted. In total, we find 21 confirmed spectroscopic binaries and 14 projected pairs. For confirmed spectroscopic binaries, we calculate the velocity difference between each component galaxy. Since the observed redshift is a combination of the intrinsic (Doppler) motions of the co-orbiting galaxies and also the cosmological expansion of intervening space due to the Hubble flow, we use a relativistic approximation: $\Delta V = \frac{\Delta z}{1+z_{\rm sys}} \times c$, where $z_{\rm sys}$ is the redshift of the system (from our estimates) in which the galaxies reside at the same scale factor. In practice, at the low redshifts of our sample, and where $\Delta z = z_{\rm obs} - z_{\rm sys}$ is small, it does not make much difference which of the galaxies in a pair that we designate as having $z_{\rm sys}$. Traditionally, an arbitrary cut for the velocity difference between two galaxies is used to discern those in a genuine pair: ≤ 500 km s^{-1}. In Table 2.2, there are 2 pairs which are above this threshold, but which merit inclusion. The pair in 2258+0030 is within 100 km/s of the loose threshold used in the literature. The pair in 0147−0008 is found to be at a ΔV higher than the threshold, but is

also at a fairly low physical separation (∼14 kpc). These spectroscopic binaries constitute "kinematic pairs" of galaxies at kiloparsec-scale separations, which are likely in the process of merging.

2.2.2 Flux Calibration

While flux calibration is not necessary for determining spectroscopic binaries, it is a necessary procedure if one wants to extract emission line fluxes. For each night of Keck observations, a standard star was observed and reduced in identical fashion to the other science spectra in §2.2. At this point, the spectra are still in units of counts, which must be translated to flux units. The standard stars observed are well known in the literature, and well calibrated versions of their spectra are obtained from the CALSPEC database.[1] For most nights, either the standard star BD+28_4211 or G191−B2B was observed. The only exception to this is for observations on 150914 when the star Hiltner600 was observed (reference spectrum obtained from the ESO archive).[2]

The standard stars' spectra contain some prominent stellar absorption features and even bands of telluric lines from Earth's atmosphere that have not been well corrected for. Most notably, the atmospheric A and B bands of O_2 and the duo of H_2O bands between 6800Å$< \lambda <$8400Å can deprecate the flux received by ground-based observatories by up to 80%. Because of this, we interpolate over these known regions using line lists from LPIPE (Perley, 2019). The interpolation is also done for the reference spectrum for each standard,

[1]CALSPEC database: https://archive.stsci.edu/hlsps/reference-atlases/cdbs/current_calspec.

[2]ESO database: https://www.eso.org/sci/observing/tools/standards/spectra/hilt600.html.

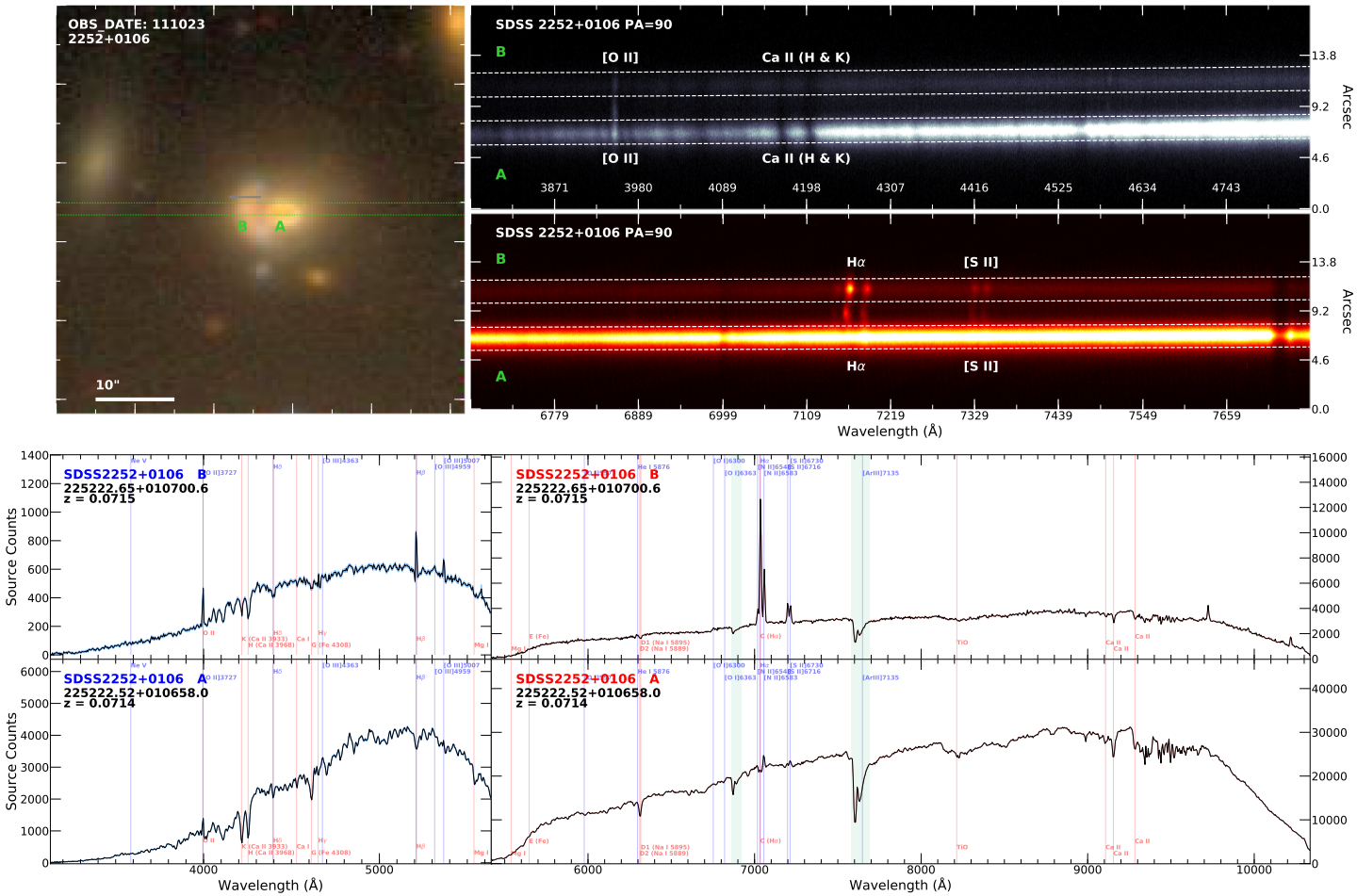

Figure 2.1. Example of optical spectra reduction and redshift estimate for the pair in 2252+0106. We show: **Top left:** the optical image with sources labeled A and B. The slit is overlaid (dashed green lines) with the gray arrow indicating its orientation. **Top right:** 2D optical spectra for the blue (upper panel) and red regions of the spectrum (lower panel). The extraction regions are shown with dashed lines. We also indicate useful "landmark" spectral features. **Bottom:** the 1D spectra for each extracted source in the pair before flux calibration. The obsID, source name, and redshift are given in the top left of each panel. Source B is shown on top, and is composed of the separate blue and red sides of the spectrum (left and right panels, respectively). Emission and absorption lines are indicated with blue and red vertical lines, respectively. Strong telluric bands are shown as green shaded regions.

Table 2.2. Properties of Kinematic Pairs

Optical ID J2000 (1)	Obs Date YYMMDD (2)	Grade (3)	$z_{\rm spec}$ (4)	$z-$flag (5)	Instru (6)	Sep (arcsec) (7)	Sep (kpc) (8)	ΔV (km s^{-1}) (9)	AGN class (10)
005113.93+002047.2	011113	A	0.1124	...	SDSS	3.4	7.0	64.5	1C, 2AS, 3, 4S, 5
005114.11+002049.4	000925	A	0.1126	...	SDSS				1C, 2AS, 3, 4S, 5
013412.78−010729.5	001003	A	0.0789	...	SDSS	4.6	6.8	136.9	1L, 2R, 3, 4F
013412.84−010725.0	030104	A	0.0784	...	SDSS				1C, 2R, 3
014203.08−000150.3	160907	B	0.7136	M	LRIS	2.5	18.0	350.3	...
014203.24−000151.0	160907	B	0.7116	...	LRIS				4F
014715.86−000819.5	151016	A	0.4725	...	LRIS	2.4	14.1	1226.6	4F
014715.94−000817.4	151016	A	0.4665	...	LRIS				...
014928.39−001445.7	151016	B	0.0897	...	LRIS	2.1	3.5	0.0	1S, 2S, 3
014928.41−001447.8	151016	B	0.0897	F	LRIS				1S, 2S, 3
015253.79−001005.6	150914	B	0.0821	...	LRIS	2.3	3.6	41.6	2R, 3, 4F
015253.92−001004.3	150914	B	0.0819	...	LRIS				1L, 2R, 3
020301.40−003341.7	160907	B	0.6946	F	LRIS	2.4	15.0	88.5	...
020301.43−003339.3	160907	B	0.6951	F	LRIS				4S
021021.00−005124.2	150914	A	0.2910	F	LRIS	3.2	14.0	92.9	2R, 3
021021.13−005126.7	150914	A	0.2914	F	LRIS				1C, 2S, 3
220634.97+000327.6	030921	A	0.0466	...	SDSS	4.6	4.2	124.5	1C, 2AS, 3, 4S
220635.08+000323.3	031025	A	0.0461	...	SDSS				1L, 2AS, 3, 4S
221142.42+002731.2	160907	B	0.7365	P	LRIS	3.1	22.6	86.3	5
221142.51+002728.5	160907	B	0.7360	...	LRIS				5
222051.55+005815.5	111023	B	0.3181	...	LRIS	2.6	12.1	68.2	1L, 2R, 3, 4F
222051.70+005816.7	111023	B	0.3178	...	LRIS				2R, 3
222907.53−000411.1	160907	B	0.5935	...	LRIS	3.6	23.9	470.3	4F
222907.77−000410.9	160907	B	0.5960	M	LRIS				...
223222.41+001226.3	111023	A	0.2200	...	LRIS	3.2	11.4	122.9	1C, 2AS, 3, 4S, 5
223222.60+001224.7	111023	A	0.2205	...	LRIS				1C, 2AS, 3, 4S, 5
223546.28+000358.8	150914	A	0.7925	F	LRIS	1.8	13.5	334.9	4F
223546.40+000358.7	150914	A	0.7905	F	LRIS				...
224426.44+001051.3	151016	B	0.6890	M	LRIS	2.6	18.5	408.3	4S
224426.61+001051.9	151016	B	0.6913	M	LRIS				4S
224532.53+005857.9	160907	B	0.6478	...	LRIS	3.1	21.5	0.0	5
224532.68+005855.8	160907	B	0.6478	...	LRIS				5
225222.52+010658.0	111023	D	0.0714	...	LRIS	3.2	4.4	28.0	1L, 2R, 3, 4F
225222.65+010700.6	111023	D	0.0715	...	LRIS				1S, 2AS, 3, 4F
225817.73+003007.7	150914	B	0.2553	...	LRIS	5.1	20.3	596.8	4S, 5
225817.97+003011.5	150914	B	0.2578	...	LRIS				1S, 2S, 3, 5
230010.18−000531.7	111023	A	0.1797	...	LRIS	2.5	7.6	25.4	1L, 2R, 3, 4F
230010.24−000534.0	111023	A	0.1798	...	LRIS				3, 4S
230342.74−011712.7	160907	A	0.5665	...	LRIS	2.7	17.6	19.1	4F
230342.91−011711.9	160907	A	0.5656	...	LRIS				...
231953.31+003816.7	150914	B	0.9045	F	LRIS	3.7	28.9	314.8	4S
231953.43+003813.4	150914	B	0.9025	F	LRIS				4S

Every two rows is a pair, and sources are sorted in ascending R.A. (1) J2000 coordinate of the optical source; (2) Observation date; (3) Grade of the dual candidate (Fu et al., 2015b); (4) Spectroscopic redshift; (5) Redshift estimate quality flag (M=moderate, F=fair, P=poor); (6) Instrument; (7) Angular separation; (8) Projected separation; (9) Radial velocity separation; (10) AGN classification flags: 1 = BPT [N II] class (A=AGN/Seyfert, L=LINER, C=Composite, S=Star-forming), 2 = WHAN diagram class (AS=Strong AGN, AW=Weak AGN, S=Star forming, R=Retired), 3 = Radio Excess, 4 = flat (F) or steep (S) radio spectrum in the 6 GHz core, and 5 = MIR color excess.

Table 2.3. Properties of Spectroscopically Determined Projected Pairs

Optical ID J2000 (1)	Obs Date YYMMDD (2)	Grade (3)	$z_{\rm spec}$ (4)	$z-$flag (5)	Sep (arcsec) (6)
011156.44−000015.1	151016	A	0.2530	M	2.5
011156.52−000017.3	151016	A	1.8190	M	
011613.73+005807.3	171015	B	1.0520	...	5.4
011613.77+005801.9	171015	B	0.9402	...	
012050.37−004656.6	160907	B	0.8340	...	3.3
012050.55−004658.4	160907	B	0.4824	M	
013505.89+011911.5	150914	B	0.7842	...	3.2
013505.88+011908.4	150914	B	0.3570	...	
014457.10−004216.6	150914	B	0.6535	...	2.5
014457.17−004218.8	150914	B	0.3193	...	
221331.60+004834.6	160907	B	0.8120	P	4.3
221331.87+004836.1	160907	B	0.9068	F	
221806.92+004515.9	160907	B	1.0988	...	2.2
221806.98+004517.9	160907	B	0.8360	...	
224204.25+003029.4	170531	A	0.7621	F	3.1
224204.45+003028.1	170531	A	0.5104	...	
225002.04+001131.9	160907	B	0.9880	M	4.5
225002.10+001136.3	160907	B	0.5295	P	
230223.28−000301.2	111023	B	0.3105	...	3.3
230223.46−000259.4	111023	B	0.5450	...	
230453.04−010946.6	170623	A	0.7448	M	1.7
230453.13−010945.5	170623	A	1.4339	M	
230559.17+002409.0	150914	A	0.5560	...	1.6
230559.19+002407.4	150914	A	0.3450	...	
230858.68+002527.8	160907	A	0.9410	P	3.7
230858.75+002531.4	160907	A	1.4150	...	
231843.30+004527.2	111023	B	0.2744	...	4.3
231843.55+004525.0	111023	B	0.9587	...	

Every two rows is a pair, and sources are sorted in ascending R.A. All spectra were obtained from Keck/LRIS. (1) J2000 coordinate of the optical source; (2) Observation date; (3) Grade of the dual candidate (Fu et al., 2015b); (4) Spectroscopic redshift; (5) Flag for grade of the redshift estimate where less certain (M=moderate, F=fair, P=poor, as described in the text), no tag indicates secure estimate; (6) Angular separation in arcsec between the optical counterparts in each candidate pair.

as they suffer from the same absorption features. For the telluric bands, a correction factor is calculated as the ratio between the observed over the interpolated count rate at a given wavelength, and stored for later use. The standard and reference spectra are interpolated to the same wavelength grid, and the throughput at each point is calculated as the ratio of the count rate over the flux. This array is then interpolated back to the resolution of the observed data using a cubic spline, and stored as the response function for the given night. This is done independently for the red and blue sides.

Before applying the response function to the science spectra, corrections must be made to account for varying amounts of optical depth due to observations at different altitudes, and thus differing amounts of atmospheric attenuation. We use the mean Mauna Kea atmospheric extinction curve drawn from Buton et al. (2013). Fitting a high-order polynomial to their data gives a generic function of the optical depth as a function of wavelength, $\tau(\lambda)$. The response function for a given science target is then given by: $R_{cont,sci} = R_{cont,std} \times \exp(-\Delta A \times \tau(\lambda))$, where $\Delta A = A_{std} - A_{sci}$ is the difference in airmass values measured for the standard star observation and the science target due to differing altitudes. For each science spectrum, the count rate is then divided by the corresponding attenuated response curve to obtain the flux in units of ergs/s/cm^2/Å. At this point, the telluric correction is also scaled by the airmasses, such that $f_{tel,sci} = f_{tel,std}^{(1+\Delta A/A_{std})}$, which is then divided into the science spectrum to recover the unabsorbed flux in the telluric bands (the array is set to unity everywhere outside the known telluric bands). Finally, the red and blue sides of the spectra are stitched together. Because the two channels overlap in wavelength, the exact point of the junction is determined to be the wavelength at which there is minimum difference between the throughputs for the

red and blue sides. The result is a fully wavelength and flux-calibrated science spectrum for each galaxy in our pairs observed with LRIS. We note that the archival SDSS spectra (3 pairs) are likewise properly calibrated through the pipeline of the SDSS collaboration. For the few cases where we have both SDSS and LRIS spectra, we obtain consistent results through our pipeline, and opt for the LRIS data for consistency.

2.3 Spectral Fitting

With the fully calibrated optical spectra in hand, we are able to analyze the relative strengths of important emission lines via spectral fitting. We use the IDL-based spectral fitting package SPFIT that was developed and introduced in Fu et al. (2018). The program simultaneously fits the stellar continuum and emission lines of a spectrum using the Penalized Pixel-Fitting (PPXF) method of Cappellari and Emsellem (2004). First, the spectrum is de-redshifted to rest-frame, thus our redshift estimates from §2.2.1 serve as necessary priors. The spectrum is then modeled as a superposition of common emission lines and a weighted sum of simple stellar populations (SSPs). The SSP templates used in the fitting routine are drawn from the MIUSCAT library (Vazdekis et al., 2012). Using the empirical stellar spectral libraries MILES (Sánchez-Blázquez et al., 2006), CaT (Cenarro et al., 2001), and Indo-U.S. for stellar population synthesis modeling (Valdes et al., 2004), these SEDs for single-age, single-metallicity stellar populations encompasses a spectral range of 3465−9469Å, sufficient for the de-redshifted wavelength ranges of our sample, at a resolution of 2.51Å.

The SSPs are corrected for foreground Galactic extinction (Cardelli, Clayton, and Mathis, 1989), and matched to the wavelength-dependent resolution of each target spectrum. The SSPs are convolved with the line-of-sight velocity distribution (LOSVD, $\mathcal{L}(v)$),

which itself is parametrized as a Gaussian line profile modified by a series of Gauss-Hermite polynomials to the fourth order (van der Marel and Franx, 1993):

$$\mathcal{L}(v) = \frac{e^{-(1/2)y^2}}{\sigma\sqrt{2\pi}} \left[1 + \sum_{m=3}^{M} h_m H_m(y)\right], \tag{2.1}$$

where and $y = (v - V)/\sigma$, and H_m are the Hermite polynomials with M parameters (V (mean radial velocity), σ (velocity dispersion), h_3, h_4). The total model for the underlying stellar continuum is then a weighted sum of the templates convolved with the LOSVD with an additive sum of weighted Legendre polynomials. The reddening of the stellar continuum by the target galaxy itself can be calculated using a Calzetti extinction law (Calzetti et al., 2000). In practice however, we run the fitting using a 6th-degree polynomial multiplicative corrective term which encapsulates the effects of reddening between the template and observed spectra, but also accounts for an ad-hoc aperture-loss correction. As in PPXF, the free parameter h_3 and h_4 terms of the Gauss-Hermite series are penalized such that in the case of noisier data where these higher moments cannot be well constrained, the terms will be contribute less and the fit will tend toward Gaussian yielding better minimized residuals and thus better minimized χ^2 for the fit.

The fit itself is conducted in several stages, using PPXF to solve for the weights of the SSPs using the bounded variable least squares nonlinear algorithm (Lawson and Hanson, 1974), while independently using the Levenberg-Marquardt nonlinear least-squares minimization in the MPFIT package to solve the Gauss-Hermite LOSVD (Markwardt, 2009). To obtain a reliable fit result for the complex composite spectral model, we break the total fitting routine into a series of three simpler fitting routines, obtaining reasonable guess values for the stellar continuum and emission lines separately. We begin by masking out regions of

the spectrum around emission lines, and fit only the stellar continuum with SSPs. The best-fit continuum model is then subtracted out from the spectrum, leaving an emission line-only residual spectrum which is then fit with Gaussian templates to obtain guess values for the emission lines-only model. To reduce the number of free parameters in the fit, we opt to tie the kinematics of all emission lines. The guess values for the stellar continuum and emission lines are then used in a final simultaneous and nonlinear fit of the full spectrum using MPFIT. An advantage of this multi-step approach is that the kinematics of the stellar populations and the gas producing emission lines need not be tied together. We show an example of the spectral fitting for one of our sources in Figure 2.2, where the lower inset panels highlight three regions of the spectrum important for ionization diagnostics. The fitted spectra for the majority of the optical sample are given in §B. We note that two individual sources out of the 35 pairs could not be fit with SPFIT: 011156.44−000015.1 is at such a high redshift ($z = 1.8$) that there is no wavelength overlap with the SSP templates; 230858.75+002531.4 is a QSO with broad lines that cannot be fit with the current implementation of SPFIT. However, neither of these galaxies is within a kinematic pair, and so are not necessary to test for dAGN.

We calculate the uncertainties on the best-fit line fluxes separately from those computed by MPFIT. Because many of the parameters in the fitting are tied together, the formal errors calculated by evaluating the covariance matrix with the Jacobian matrix within MPFIT are often underestimates. The fractional error of the line flux ($\delta f/f$, the inverse S/N) is mostly driven by the amplitude-to-noise ratio (A/N) and the observed line width in pixels (intrinsic + instrumental dispersion). Using a suite of Monte Carlo simulations of Gaussian

emission lines covering a range of these two parameters, we compute a two-dimensional polynomial describing $\delta f/f$. The best-fit width and A/N of the emission lines observed in the data are then used to compute their corresponding 1-σ line flux error. We also fit the 3 pairs of galaxies with spectra from SDSS to update the previous emission line measurements from Fu et al. (2015b), which had been obtained by the Portsmouth group (Thomas et al., 2013) using a similar procedure using pPXF and the GANDALF line fitting code (Sarzi et al., 2006). In total, this results in spectral fits for 68 of the full set of 70 galaxies, with varying degrees of spectral coverage and therefore varying access to observable emission lines.

2.4 Optical Emission Line Diagnostics

For the remainder of the analysis, we focus primarily on the kinematic pair subsample. The resulting best-fit spectral measurements allow us to probe the optical emission mechanisms in each galaxy. Does a given galaxy display evidence of nuclear-region ionization due to an AGN, or is it merely due to ongoing star-formation? Optical emission lines allow us to delineate between these two possibilities to characterize the nature of each galactic nucleus. In the following subsections, we utilize a cadre of well known optical emission line diagnostics to piece together a picture of each galactic nucleus. We start by assessing the relative strengths of emission lines produced through various ionization mechanisms. The broadening of specific emission lines can also inform us about the state of the central engine. A final comparison against the known radio flux allows us to rule out the predominance of interfering star formation signatures. We search for evidence of AGN activity in our kinematic pairs, and tabulate instances where it appears that both galaxies in a pair display optical signatures resulting in dAGN.

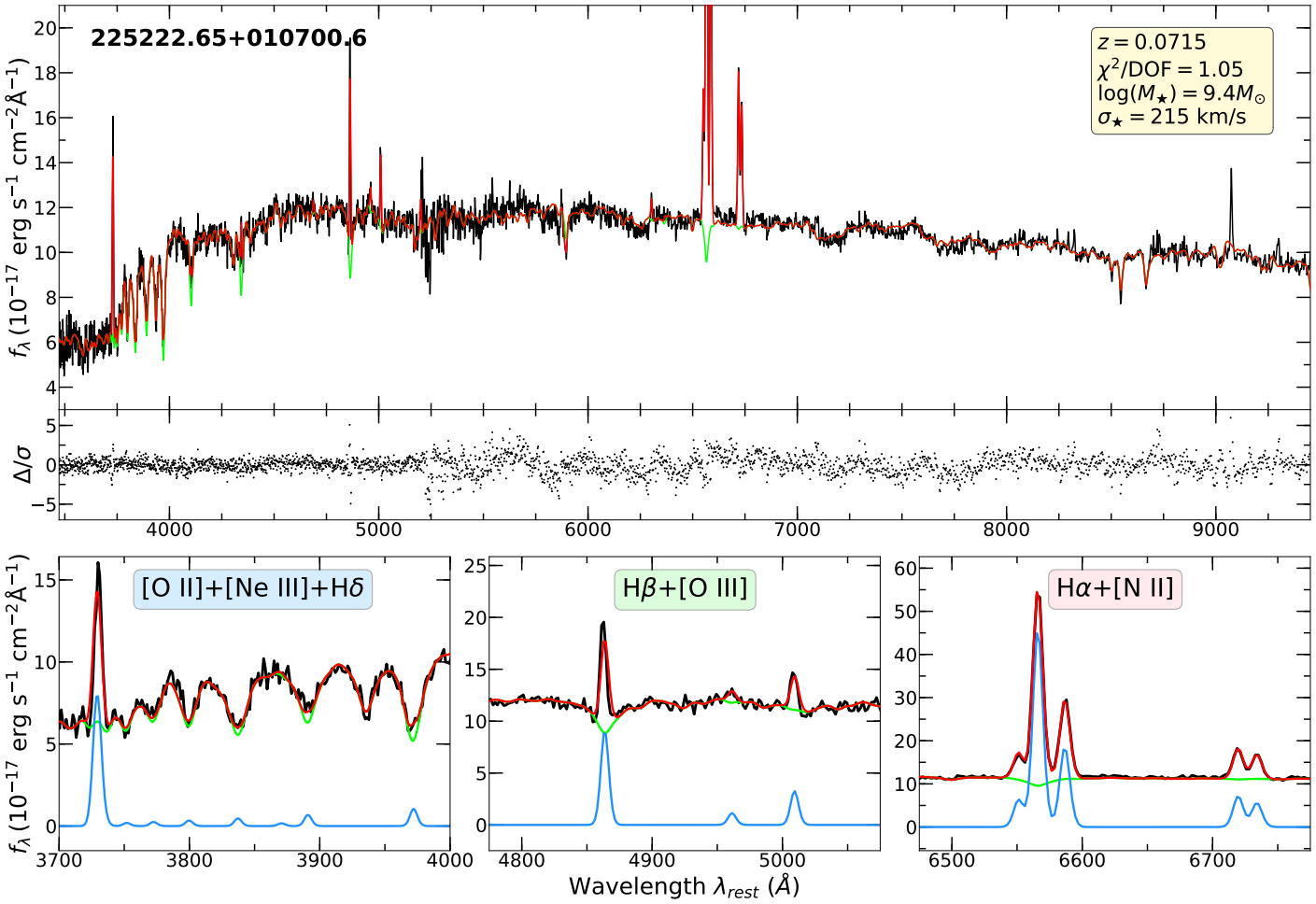

Figure 2.2. Example of the final fluxed spectrum for a source in the kinematic pairs sample with the results of spectral fitting using SPFIT. The top panel shows the full region of the de-redshifted spectrum that is covered by the SSP templates (source name in bold). The lower sub-panels show zoom-ins of important nebular emission line regions. The black line is the data, the underlying green line shows the best fit stellar continuum model, the blue line gives the continuum-subtracted emission line model, and the red line is the total resulting best-fit. We give some of the relevant output quantities in the inset box. The residuals (normalized by the error) are given in the lower portion the top panel.

Table 2.4. Emission Line Properties of the Kinematic Pairs

Optical Designation J2000 (1)	z (2)	log([O III]/Hβ) (3)	log([N II]/Hα) (4)	log([S II]/Hα) (5)	log([O I]/Hα) (6)	$L_{\rm H\alpha}$ log(erg s^{-1}) (7)	$W_{\rm H\alpha}$ log(Å) (8)	$L_{\rm [O\ III]}$ log(erg s^{-1}) (9)	$P^{\rm int}_{\rm 1.4\ GHz}$ log(W Hz^{-1}) (10)
005113.93+002047.2	0.1124	0.1 ± 0.03	-0.18 ± 0.03	-0.39 ± 0.05	-1.16 ± 1.25	41.1	1.5 ± 0.0	40.4	22.3
005114.11+002049.4	0.1126	-0.36 ± 0.26	-0.23 ± 0.0	-0.42 ± 0.0	-1.35 ± 0.72	41.4	1.8 ± 0.0	40.1	23.1
013412.78−010729.5	0.0789	0.56 ± 0.02	0.42 ± 0.04	0.13 ± 0.09	...± ...	40.1	0.1 ± 0.5	40.1	23.1
013412.84−010725.0	0.0784	0.09 ± 0.0	-0.1 ± 0.0	0.39 ± 0.0	-0.7 ± 0.02	39.0	-0.5 ± 0.0	38.8	23.0
014203.08−000150.3	0.7136	...± ...	...± ...	...± ...	...± ...	...	...± ...	...	24.0
014203.24−000151.0	0.7116	0.4 ± 0.03	...± ...	...± ...	...± ...	...	...± ...	41.0	25.0
014715.86−000819.5	0.4725	-0.18 ± 0.0	...± ...	...± ...	...± ...	...	...± ...	40.5	24.1
014715.94−000817.4	0.4665	0.22 ± 0.07	...± ...	...± ...	...± ...	...	...± ...	41.9	24.2
014928.38−001446.0	0.0897	0.35 ± 0.08	-0.84 ± 0.25	-0.29 ± 0.07	-1.14 ± 0.49	39.5	1.4 ± 0.0	39.2	22.6
014928.41−001447.8	0.0897	0.19 ± 0.13	-1.62 ± 1.88	-0.33 ± 0.1	-0.8 ± 0.25	39.2	1.1 ± 0.0	38.9	22.4
015253.79−001005.6	0.0821	...± ...	0.2 ± 0.03	0.11 ± 0.03	-1.24 ± 0.68	39.9	0.1 ± 0.1	39.1	22.7
015253.92−001004.3	0.0819	-0.27 ± 0.01	0.05 ± 0.11	0.04 ± 0.11	-0.4 ± 0.22	39.0	-0.0 ± 0.2	38.3	21.9
020301.40−003341.7	0.6946	-0.34 ± 0.25	...± ...	...± ...	...± ...	...	...± ...	40.3	24.7
020301.43−003339.3	0.6951	0.37 ± 0.13	...± ...	...± ...	...± ...	...	...± ...	40.9	24.5
021021.00−005124.2	0.291	...± ...	0.08 ± 0.0	0.52 ± 0.0	...± ...	39.6	-0.5 ± 0.0	39.6	23.8
021021.13−005126.7	0.2914	0.48 ± 0.0	-0.68 ± 0.79	-0.1 ± 0.21	-1.08 ± 2.0	40.2	0.9 ± 0.0	39.7	23.8
220634.97+000327.6	0.0466	-0.05 ± 0.07	-0.13 ± 0.02	-0.16 ± 0.03	-1.05 ± 0.97	40.4	1.1 ± 0.0	39.8	22.0
220635.08+000323.3	0.0461	0.22 ± 0.02	0.13 ± 0.0	0.12 ± 0.0	-0.5 ± 0.05	40.7	1.3 ± 0.0	40.3	22.1
221142.42+002731.2	0.7365	-0.56 ± 0.16	...± ...	...± ...	...± ...	...	...± ...	39.4	25.3
221142.51+002728.5	0.736	-0.54 ± 0.14	...± ...	...± ...	...± ...	...	...± ...	41.9	25.5
222051.55+005815.5	0.3181	-0.28 ± 0.0	0.75 ± 0.02	0.37 ± 0.05	...± ...	40.0	-0.2 ± 0.0	40.0	24.7
222051.70+005816.7	0.3178	...± ...	1.01 ± 0.0	1.02 ± 0.0	...± ...	38.9	-0.9 ± 0.0	39.7	25.1
222907.53−000411.1	0.5935	0.43 ± 0.0	...± ...	...± ...	...± ...	...	...± ...	40.8	25.2
222907.77−000410.9	0.596	...± ...	...± ...	...± ...	...± ...	...	...± ...	36.9	24.9
223222.41+001226.3	0.22	0.08 ± 0.14	-0.25 ± 0.04	-0.36 ± 0.05	-1.12 ± 1.48	41.2	1.5 ± 0.0	39.9	22.9
223222.60+001224.7	0.2205	-0.21 ± 0.27	-0.35 ± 0.0	-0.38 ± 0.0	-1.31 ± 3.37	41.2	1.6 ± 0.0	39.8	23.2
223546.28+000358.8	0.7925	...± ...	...± ...	...± ...	...± ...	...	...± ...	...	25.0
223546.40+000358.7	0.7905	...± ...	...± ...	...± ...	...± ...	...	...± ...	...	24.2
224426.44+001051.3	0.689	0.26 ± 0.0	...± ...	...± ...	...± ...	...	...± ...	40.6	24.6
224426.61+001051.9	0.6913	0.16 ± 0.11	...± ...	...± ...	...± ...	...	...± ...	40.8	25.0
224532.53+005857.9	0.6478	0.66 ± 0.01	...± ...	...± ...	...± ...	...	...± ...	41.2	24.5
224532.68+005855.8	0.6478	0.48 ± 0.03	...± ...	...± ...	...± ...	...	...± ...	41.6	24.1
225222.52+010658.0	0.0714	0.08 ± 0.05	0.54 ± 0.04	0.48 ± 0.04	-0.21 ± 0.24	40.1	0.1 ± 0.4	40.7	22.4
225222.65+010700.6	0.0715	-0.44 ± 0.21	-0.39 ± 0.0	-0.55 ± 0.0	-1.67 ± 7.7	40.7	1.7 ± 0.0	39.5	21.9
225817.73+003007.7	0.2553	...± ...	...± ...	...± ...	...± ...	...	...± ...	39.2	23.4
225817.97+003011.5	0.2578	-0.15 ± 0.16	-0.69 ± 0.9	-0.52 ± 0.62	-1.45 ± 2.43	40.6	1.3 ± 0.0	39.8	24.3
230010.18−000531.7	0.1797	-0.4 ± 0.0	0.38 ± 0.04	-0.03 ± 0.09	...± ...	40.2	0.1 ± 0.3	39.8	23.2
230010.24−000534.0	0.1798	-0.59 ± 0.37	...± ...	...± ...	...± ...	...	...± ...	39.9	23.0
230342.74−011712.7	0.5665	-0.37 ± 0.39	...± ...	...± ...	...± ...	...	...± ...	40.1	24.4
230342.91−011711.9	0.5666	-0.07 ± 0.0	...± ...	...± ...	...± ...	...	...± ...	40.5	24.6
231953.31+003816.7	0.9045	...± ...	...± ...	...± ...	...± ...	...	...± ...	...	25.3
231953.43+003813.4	0.9025	...± ...	...± ...	...± ...	...± ...	...	...± ...	...	24.6

Every two rows is a pair, and sources are sorted in ascending R.A. and computed values are logarithmic with 1-σ uncertainties. (1) J2000 coordinate of the optical source; (2) redshift; (3)−(6) emission line ratios; (7) Hα luminosity; (8) Hα equivalent width; (9) [O III] luminosity; (10) radio power computed from integrated source flux at 1.4 GHz.

2.4.1 BPT Diagnostic

We use the optical line fluxes to diagnose the origin of ionization in each galaxy. The widely used BPT diagrams (Baldwin, Phillips, and Terlevich, 1981) use ratios of strong optical emission lines to discriminate between two main sources of ionizing flux: 1) hot young populations of O and B stars from recent star formation; 2) the ionizing spectrum of an AGN (Kewley et al., 2006). The harder ionizing field of an AGN is expected to lead to an enhancement of low-ionization forbidden lines over Balmer recombination lines, while also boosting the rate of collisionally ionized lines (Ho, 2008). This is because the harder radiation field (extending well into the UV and X-ray) of an AGN is able to penetrate further into surrounding optically thick nebular gas than can be done by the field generated by hot O and B type stars in active star-forming regions, causing a deeper layer of partially ionized gas populated by free electrons as well as both neutral and ionized atoms. This low density region then facilitates the forbidden transitions preferentially, such as [N II], over the collisional de-excitation cooling mechanism that dominates in the inner H II region of higher density gas. Additionally, the increase in temperature of the surrounding gas from the higher ionizing photon flux of the AGN enhances the generation of collisionally excited forbidden lines like [O III]. Specifically, the BPT diagrams compare the ratio of [O III]/Hβ in three plots against, [N II]/Hα, [S II]/Hα, and [O I]/Hα. The ratios themselves are each composed of two lines that are close together in wavelength, and therefore do not suffer from an appreciable amount of differential reddening even without an attenuation correction. In Table 2.4, we give the numerical values for the line ratios utilized in the BPT diagrams for the kinematic pairs which have detectable emission lines. We also give the luminosities for

several emission lines that are important to our subsequent analysis. Our redshift estimates allow us to compute luminosity distances to the targets to scale the fluxes to luminosities.

A substantial complication in utilizing the BPT diagram as a tool is readily apparent: not all of the 42 galaxies in kinematic pairs have all four emission lines necessary for plotting on a BPT diagram. This is a combination of two independent factors. Firstly, if the galaxy does not host an AGN or is not actively producing stars at a substantial scale, then there likely will not be any optical emission lines in the spectrum at detectable levels. In this case, the spectrum is well characterized by the existing stellar populations in the galaxy, many of which are likely evolved and whose chemically enriched atmospheres contribute to the absorption features like Ca and Na. Secondly, the redshift range of the sample prevents us from obtaining emission line fluxes for much of the sample. For the entire set of 68 galaxies that could be fit (kinematic and projected pairs), 39 galaxies are at high enough redshift ($z \gtrsim 0.47$) that the Hα complex is not covered within the range of of the SSP templates after de-redshifting (if within the range of LRIS at all). Thirteen of these galaxies are at high enough redshift to likewise exclude coverage of the [O III] complex. As seen in Table 2.4, out of the 42 galaxies in the kinematic pairs, only 17 have all four emission lines necessary for plotting on the BPT diagrams. The situation is even more restrictive for the projected pairs sub-sample, where only 5 of the 28 galaxies have BPT diagnostic information, given in the Appendix §A.1.

In Figure 2.3, we plot the most commonly used BPT diagram, [O III]/Hβ vs. [N II]/Hα, for our kinematic pairs, where the forbidden lines are at λ5007Å and λ6584Å, respectively. Note that we use the same convention to label sources in all of the plots throughout

this work. Kinematic pairs are marked with circles and the select few rigorously confirmed dual AGNs (as demonstrated in later sections via radio imaging) are marked with stars. Objects in a pair are linked together with a thin line so long as both constituent galaxies appear on that plot. For comparison, we show the full distribution of SDSS DR8 galaxies with optical emission lines values from the Portsmouth group as the gray-scaled background (Thomas et al., 2013). We also plot the relations commonly used to categorize objects on the BPT diagram. Based on ionization models of starburst regions, the theoretical maximum starburst line from Kewley et al. (2001) gives a hard cutoff for the ionization signature that can be attributed to H II regions supported by O and B type stars:

$$\log([\text{O III}]/\text{H}\beta) = \frac{0.61}{\log([\text{N II}]/\text{H}\alpha) - 0.47} + 1.19. \tag{2.2}$$

In practice, there is known to be offsets from this trend as a function of galactic metallicity and redshift. For lower redshift galaxies, the empirical separation between AGN and star forming galaxies, found by Kauffmann et al. (2003) using SDSS spectra from over 22,000 galaxies, has the form:

$$\log([\text{O III}]/\text{H}\beta) = \frac{0.61}{\log([\text{N II}]/\text{H}\alpha) - 0.05} + 1.30. \tag{2.3}$$

The region between these two demarcations is thought to be populated with galaxies where the ionization budget has contributions from both starbursts and low levels of AGN activity, and are thus classified composite types. Kewley et al. (2006) note that these composite galaxies tend to contain metal-rich stellar populations since $\log([\text{N II}]/\text{H}\alpha)$ is a linear function of the nebular metallicity which saturates at high metallicities leading to the saturated nearly vertical distribution around $\log([\text{N II}]/\text{H}\alpha)$ = -0.5 seen in the star-forming branch of the

SDSS galaxies. Beyond this saturation point, even low levels of additional ionization from an AGN will push the value further to the right of the diagram. The objects which fall above the AGN demarcation can be further classified into Seyferts or LINERs using the relation from Kewley et al. (2006) for the [S II] diagram adopted for the [N II] diagram as done by Schawinski et al. (2007):

$$\log([\text{O III}]/\text{H}\beta) = 1.05 \times \log([\text{N II}]/\text{H}\alpha) + 0.45. \tag{2.4}$$

The distribution of the SDSS galaxies on the diagram gives rise to its nickname as the "seagull" diagram, where distinctive sequences are immediately obvious along the starburst line and extending into the AGN region. The branch in the AGN region is less well defined though, and as noted by Kewley et al. (2006), the transition from low ionized LINERs to higher ionized Seyferts likely represents a continuous sequence of corresponding accretion strengths.

In plotting our kinematic pair galaxies, we find that 4 are classified as starburst galaxies, 6 are LINERs, and 7 are starburst/AGN composites that fall within the intermediate region. We do not detect any Seyfert type AGNs in our sample, which would be a more straightforward identification of true AGN ionization. We use the color-coding based on this classification scheme for the remainder of this work. In later plots, we denote objects in pink which did not have enough information for a full [N II] BPT classification. We note that the ratios which have intrinsically low values in linear-space yield large uncertainties as a result of the error propagation to log-space regardless of the well constrained the errors on individual line fluxes. It not surprising that so many of our kinematic pairs fall in the composite region since the same ongoing merger effects which stimulate inflowing gas that fuels AGN likely also contribute to reinvigorated star-formation. It is perhaps also not surprising that

the AGNs found through this method are preferentially LINERs, which could be a sample selection effect insofar as that our sample is comprised of radio galaxies. Assessing whether they are actually operating in the low/radio/jet mode is addressed in our later discussion.

To further investigate the emission line trends, in Figure 2.3 we plot the [O III]/Hβ vs. [S II]/Hα BPT diagram. Unlike with [N II], the [S II] diagram requires measurements of both Sulfur lines in the doublet ($\lambda\lambda 6716, 6731$Å). We once again show the theoretical maximum starburst line from Kewley et al. (2001):

$$\log([\text{O III}]/\text{H}\beta) = \frac{0.72}{\log([\text{S II}]/\text{H}\alpha) - 0.32} + 1.30, \tag{2.5}$$

as well as the empirical division between Seyferts and LINERs from Kewley et al. (2006):

$$\log([\text{O III}]/\text{H}\beta) = 1.89 \times \log([\text{S II}]/\text{H}\alpha) + 0.76. \tag{2.6}$$

While we do not rely on the [S II]/Hα classification for diagnosing AGN, we do note that the classifications are largely consist with those found using [N II]/Hα. The most noticeable discrepancy is that one galaxy (014928.38−001446.0) moves from a classification as purely star-forming to that of a Seyfert. The underlying SDSS galaxies show a similar distribution as in Figure 2.3, but with a star-forming branch that veers away strongly from the dividing line. As has been shown for SDSS galaxies, composite types from the [N II] predominantly fall within the star-forming region of the [S II]. This is the case for more than half of the composites in our sample.

The [O III]/Hβ vs. [O I]/Hα BPT diagram is sometimes used as an additional cross-check for classification consistency. We show this diagram in Figure 2.5. Only 14 of the kinematic pair galaxies have [O I]λ6302Å detections, and these values are consistently

poorly constrained. This is not surprising given the lack of Seyfert-type strong AGNs seen in the main BPT diagram, which thus indicates only weak levels of emission lines above the stellar continuum for even the stronger lines like Hα. Here, the theoretical maximum starburst line from Kewley et al. (2001) is given by:

$$\log([\text{O III}]/\text{H}\beta) = \frac{0.73}{\log([\text{O I}]/\text{H}\alpha) + 0.59} + 1.33, \tag{2.7}$$

and the division between Seyferts and LINERs from Kewley et al. (2006) is:

$$\begin{aligned} &\log([\text{O I}]/\text{H}\alpha) > -0.59, \\ &\log([\text{O III}]/\text{H}\beta) = 1.18 \times \log([\text{O I}]/\text{H}\alpha) + 1.30 \end{aligned} \tag{2.8}$$

Several of the measurements are wholly unconstrained (shown with arrow error bars), and we thus do not rely on the classifications from this diagram. We give the resulting BPT classifications for each galaxy using the three diagrams in Table 4.1. However, we note that our final diagnosis of optical AGN signatures given in Table 2.2 is based solely on the [O III]/Hβ vs. [N II]/Hα diagram.

2.4.2 WHAN

The aforementioned BPT diagram is perhaps the most widely-used AGN diagnostic tool in optical astronomy, but it has obvious limitations. Most notably, to use the BPT diagram one needs four separate emission lines from a given galaxy. For faint galaxies which may not exhibit the entire suite of lines, this is not a practical option. The BPT diagram also suffers from potentially mis-diagnosing the LINER sub-category of AGN, such that weakly active galactic nuclei (wAGN) are lumped together with retired galaxies. These retired galaxies exhibit similar emission line ratios as the wAGN, even though their ionization comes from populations of hot low-mass evolved (post-asymptotic giant branch) stars. To

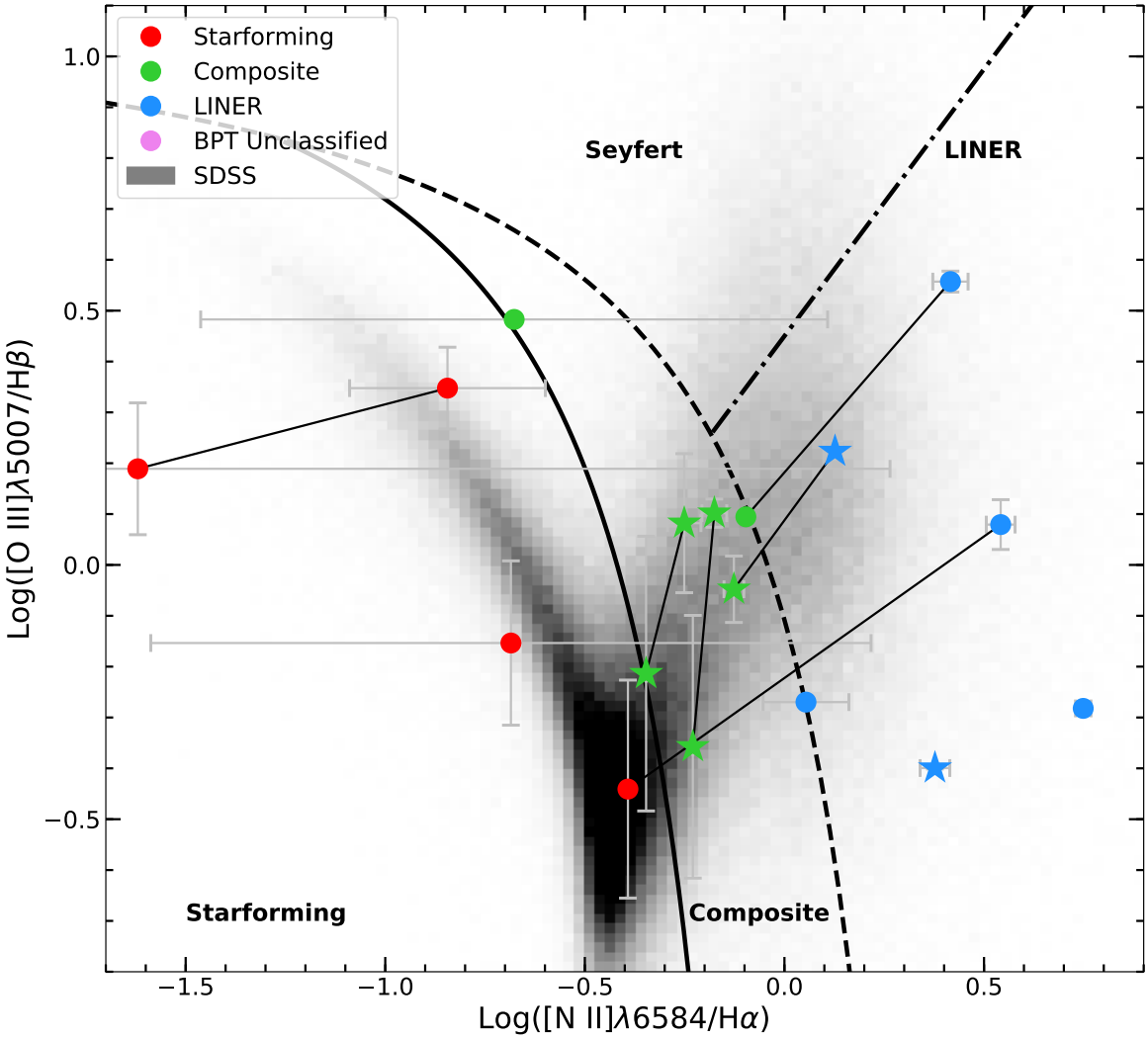

Figure 2.3. BPT plot for the kinematic pair subsample using the [N II] emission line. Color-coding for all subsequent plots is taken from this plot, and described by the legend. The 6 pairs with dual radio cores are shown with stars, and the remainder of the kinematic pairs with circles. Lines connect pairs where both galaxies have sufficient information to be plotted. We maintain this same scheme in subsequent plots. The underlying gray-scaled distribution is drawn from the SDSS DR8 sample of galaxies. Cases where error bars are large are usually due to low observed [N II] flux. Most of the confirmed dAGNs (marked with stars) are classified as AGN/star-forming composites bracketed by the theoretical maximum starburst relation of Kewley et al. (2001) (dashed line) and the empirical distribution of star-forming galaxies of Kauffmann et al. (2003). The remaining few show low levels of ionization due to AGN (LINERs), as separated from classical Seyfert AGN by the relation of Schawinski et al. (2007).

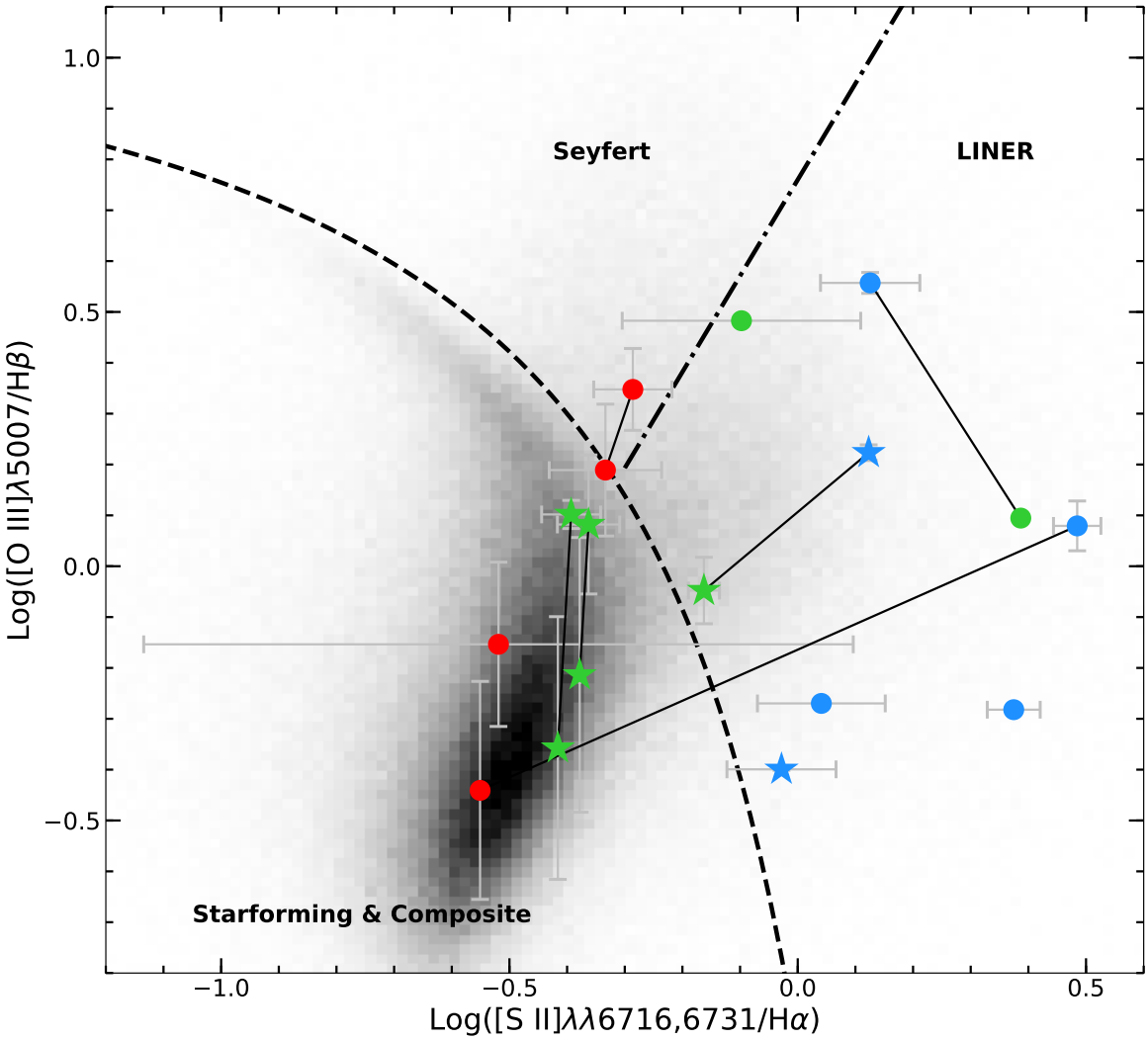

Figure 2.4. BPT plot using the [S II] emission line doublet. The labeling conventions are the same as in Figure 2.3. The LINER/Seyfert demarcation (dot-dashed line) is from Kewley et al. (2006). Notice that since some sources switch category from the most widely-used [N II] plot, the BPT diagrams cannot be unilaterally trusted as the only metric for diagnosing AGN activity. Interestingly, our radio-selection method seems to target a higher number of LINERs (and even a Seyfert) than would be expected based on the background parent distribution of SDSS galaxies.

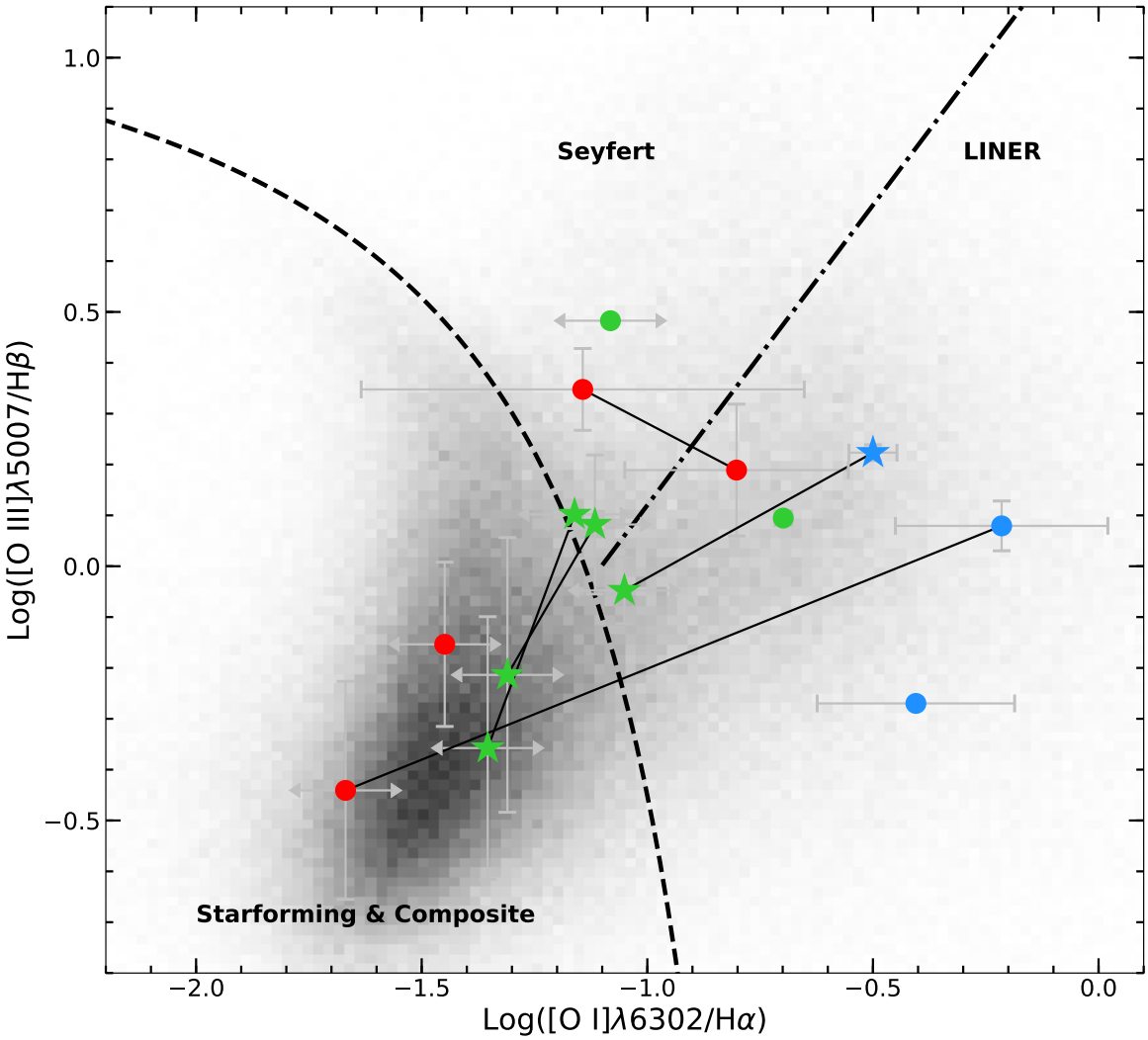

Figure 2.5. BPT plot using the [O I] emission line. The labeling conventions are the same as in Figure 2.3. The LINER/Seyfert demarcation (dot-dashed line) is from Kewley et al. (2006). Many of the x-axis uncertainties are unconstrained (arrows) since the emission line measurements of [O I] are incredibly faint, propagating to large errors. We therefore do not rely on this diagnostic in our classification scheme. It is interesting however that this metric yields the largest number of Seyfert and LINER classifications, capturing 4/6 of the dAGN galaxies with all emission lines observed.

distinguish the two conflicting scenarios for our sample, we supplement our BPT analysis above with the more recent WHAN diagram of Cid Fernandes et al. (2011). Their scheme separates wAGN from retired galaxies using the empirical bimodal distribution of ε, the ratio of extinction-corrected Hα luminosity with respect to the modeled Hα luminosity expected from photoionization due to older stellar populations ($>10^8$ yr). In practice, a reasonable observational proxy for ε is the Hα equivalent width, $W_{\mathrm{H}\alpha}$, which exhibits a similar bimodality separating the two populations at $W_{\mathrm{H}\alpha} = 3$Å. The equivalent width is defined by summing the strength of the wavelength-dependent line flux $F(\lambda)$ relative to the underlying continuum, such that $W_\lambda = \int(1 - F_{\mathrm{l+c}}/F_{\mathrm{c}})d\lambda$, where $F_{\mathrm{l+c}}$ is the full flux composed of emission line plus continuum. Aside from $W_{\mathrm{H}\alpha}$ being a readily observable quantity without needing theoretical modeling, it is directly related to ε through the same numerator, since $W_{\mathrm{H}\alpha}$ is then ratio of extinction-corrected Hα luminosity to the observed continuum luminosity around Hα, such that the line strength is the driving parameter of the equivalent width. Plotting $W_{\mathrm{H}\alpha}$ against the same x-axis of the BPT diagram in Figure 2.3, the WHAN diagram then only requires measurements of Hα and [N II]. This "cheaper" prescription allows us to diagnose an additional 2 galaxies that lack detectable emission in [O III] or Hβ, while also identifying imposter LINERs that are not AGN. The values for $W_{\mathrm{H}\alpha}$ are given in Table 2.4. We plot the WHAN diagram for our kinematic pair sample in Figure 2.6. The divisions

between the multiple categories from Cid Fernandes et al. (2011) are given by:

$$\begin{aligned}
&\text{(i) } \log([\text{N II}]/\text{H}\alpha) < -0.40 \text{ and } W_{\text{H}\alpha} > 3\text{Å} : \text{star forming galaxies,} \\
&\text{(ii) } \log([\text{N II}]/\text{H}\alpha) > -0.40 \text{ and } W_{\text{H}\alpha} > 6\text{Å} : \text{strong AGN (Seyfert),} \\
&\text{(iii) } \log([\text{N II}]/\text{H}\alpha) < -0.40 \text{ and } 6\text{Å} > W_{\text{H}\alpha} > 3\text{Å} : \text{weak AGN(“true” LINER),} \\
&\text{(iv) } W_{\text{H}\alpha} > 3\text{Å} : \text{retired galaxies.}
\end{aligned} \tag{2.9}$$

There are several interesting trends of which to take note here. First, nearly all of the galaxies classified as LINERs via the BPT diagram are shown to be retired galaxies. In fact, their nominal positions are not even near the demarcation in criterion (iv), although the uncertainties on several do overlap with the weak AGN region. Second, many of the composite type galaxies fall definitively in the strong AGN zone. Interestingly, all but one of the confirmed dAGN sources with emission line measurements fall within this category; however, none of these galaxies actually has a high enough [O III]/Hβ value to suggest that they are genuinely “strong” Seyfert AGNs. This raises an important point regarding the utility of the WHAN diagram: it is not a tool meant to diagnose AGN activity versus starbursts, but instead only serves to vindicate the LINERs which are suspect due to their low ionization. We therefore disqualify the 5 LINERs and composite galaxies in the retired region from having an AGN as their sources of ionizing photons. The WHAN classifications are also listed using tags in the last column of Table 2.2.

2.4.3 Radio Excess

A final diagnostic check for AGN activity relies on the bare minimum of observable emission lines. By comparing the radio power versus the Hα luminosity, we can surmise the presence of AGN if they show radio emission above the luminosity output by star-formation.

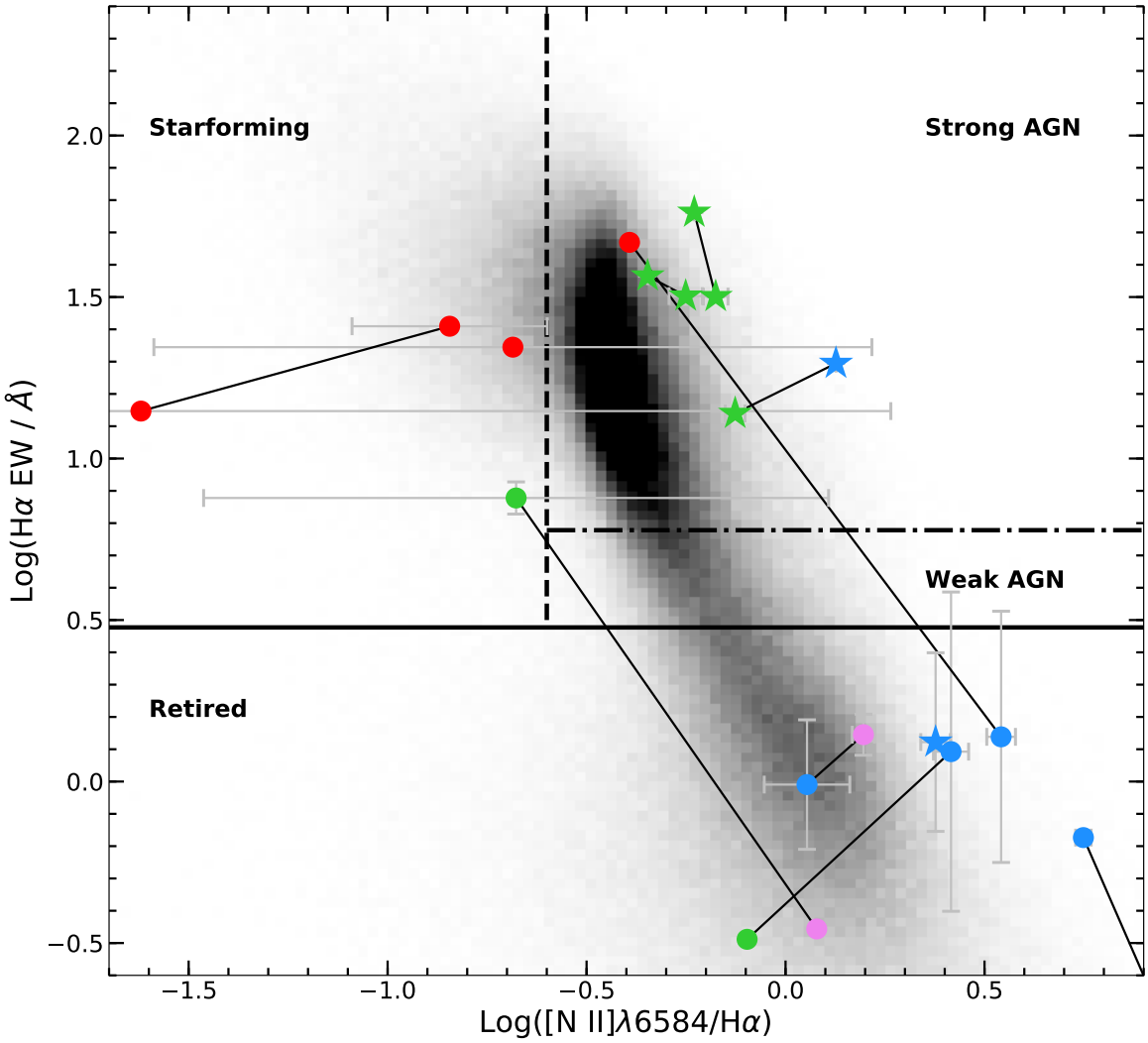

Figure 2.6. Hα equivalent width diagnostic plot for the kinematic pair sample. The labeling conventions are the same as in Figure 2.3. Pink points are objects which do not have all the necessary emission line measurements to be plotted in Figure 2.3, but do have sufficient data to be plotted here. The demarcations from Cid Fernandes et al. (2011) separate true AGN ionization from hot old stellar populations. Most of the weakly-ionized LINERs are found to be retired galaxies, and thus their optical signatures likely do not have an AGN origin. All of the composite-type dAGNs are securely placed in the strong AGN category. The underlying gray-scaled distribution is once again drawn from the SDSS DR8 sample of galaxies.

We estimate the star formation rate via the Hα luminosity using the relation from Murphy et al. (2011):

$$\log(\mathrm{SFR}/\mathrm{M}_\odot\ \mathrm{yr}^{-1}) = \log(L^{\mathrm{SF}}_{\mathrm{H}\alpha}/\mathrm{erg\ s}^{-1}) - 41.3. \tag{2.10}$$

An analogous SFR prediction using IR luminosity can be used in conjunction with the empirical IR-radio correlation of star-forming galaxies to similarly estimate the expected radio power at 1.4 GHz (Yun, Reddy, and Condon, 2001; Murphy et al., 2011). We invert this to solve for the radio power output by star formation alone using the Hα SFR:

$$\log(P^{\mathrm{SF}}_{1.4}(\mathrm{W\ Hz}^{-1})) = \log((\mathrm{SFR}_{\mathrm{H}\alpha}/\mathrm{M}_\odot\ \mathrm{yr}^{-1})/(6.35 \times 10^{-22})). \tag{2.11}$$

This relation is plotted as a dashed line in Figure 2.7, and represents a one-to-one relationship between the Hα luminosity and radio power at 1.4 GHz output by a starburst galaxy. Galaxies around this relation are classified as "radio-normal." We likewise plot this relation with a dotted line scaled in a way that represents a starburst region that could emit an order of magnitude higher radio power than what one would expect from the one-to-one relation. A galaxy plotted above this dotted line would then be producing over ten times the amount of radio power that what star formation alone can contribute, making the galaxy extremely "radio-excess." It is in this scenario where an additional explanation for the excess radio power is needed, which is most naturally explained by radio AGN. The solid line from Kauffmann and Heckman (2009) splits the known bimodal distribution of radio galaxies (as seen in the gray-scaled background histogram of SDSS galaxies with matches to VS82 radio sources), and is roughly analogous to the 10×radio-excess relation.

Using the redshifts to scale the archival integrated fluxes from Hodge et al. (2011) to luminosities, we plot the radio power at 1.4 GHz for our kinematic pair sample in Figure 2.7.

The uncertainties of $P_{1.4\mathrm{GHz}}$ are estimated as: $P_{1.4\mathrm{GHz}} \times \frac{RMS}{F_{\mathrm{peak}}} \times \sqrt{F_{\mathrm{int}}/F_{\mathrm{peak}}}$, where the peak and integrated fluxes are at 1.4 GHz. This is plotted against the observed Hα luminosity. In cases where Hα is not observable due to high redshift but Hβ is, we estimate the value of Hα via Hβ by assuming a Balmer decrement for case B recombination at T=10^4 K and $n_{\mathrm{e}} \sim 10^2 - 10^4$ cm^{-3}. We use a value of Hα/Hβ=2.8, appropriate for galaxies dominated by star formation (Osterbrock and Ferland, 2006), since we are probing the SFR in our sample assuming the upper limit scenario where all Hα photons are resulting from star formation. As noted by Kewley et al. (2006), observed Balmer decrements below the theoretical value are possible as a result of errors in the line fitting routine, but also for intrinsically low reddening. Using this method, we are able to plot 16 additional kinematic pair galaxies (shown as triangles), including one of the dAGN constituents. A caveat, however, is that our method for spectral fitting did not explicitly account for reddening using an extinction curve, and could thus be underestimating the more extincted Hβ flux resulting in an underestimated value for Hα. The corrective polynomial term incorporated in SPFIT should account for this, as well as the aperture-loss correction. We note that as a check, we did in fact re-run SPFIT adopting the Calzetti reddening curve, but the subtle adjustments to $L_{\mathrm{H}\alpha}$ did not result in a change in the radio-excess/radio-normal categorization of *any* of our sources (similarly, no appreciable change in BPT classification was observed either).

We see that all of the galaxies in the kinematic sample display radio-excess, which is perhaps not surprising since they were pre-selected based on their strong radio signatures. This suggests that all of these galaxies *contain* radio emission beyond what can be supplied by star formation alone. The caveat here is that this does not necessarily indicate that

the observed radio excess is in fact *generated by* that galaxy. As we shall see in §3, higher resolution radio imaging is necessary to positionally pinpoint whether the radio emission is native to the galaxy in question, or if it is actually a superposition of the radio emission of a strong jet or lobe being emitted by its neighboring galaxy. At the spatial resolution of the 1.4 GHz observations, it is not possible to definitively rule out the latter scenario.

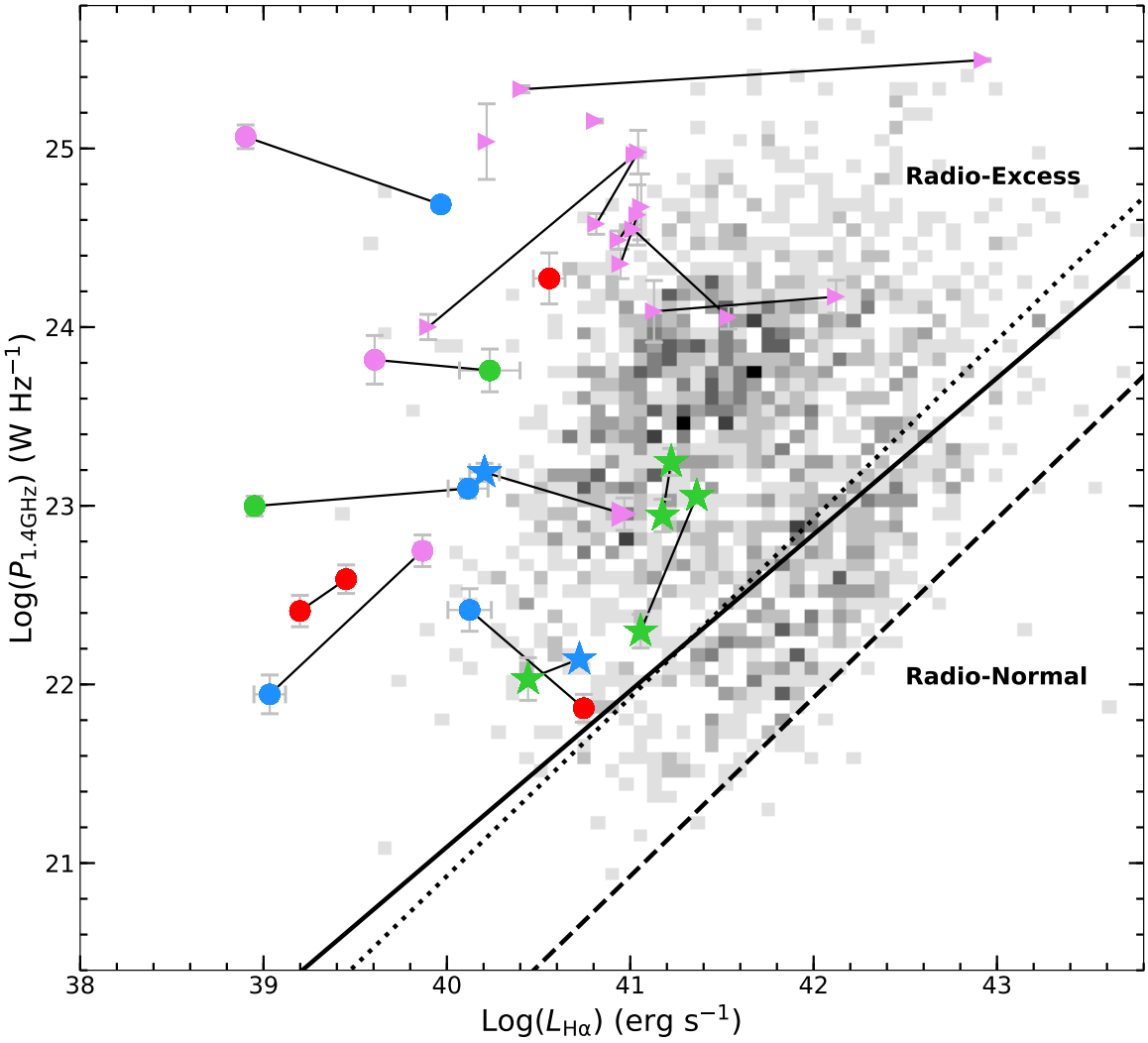

Figure 2.7. Radio excess plot of the kinematic pairs. The labeling conventions are the same as in Figure 2.3. The Hα luminosity is converted to a star formation rate via the relation of Murphy et al. (2011), and then translated to a predicted radio power emitted by that star forming population. The dashed line shows the one-to-one relation for SFR between Hα and the 1.4 GHz radio power. The dotted line shows a radio power that is 10$\times$ higher than that predicted for star formation. The solid line is the empirical relation given by Kauffmann and Heckman (2009) that splits the known bimodal distribution of radio galaxies, which is similar to the dotted relation. We find that all of the objects in the kinematic sample are above the solid line, implying a higher observed radio power than can be explained by star-formation alone, suggestive of AGN activity. We also plot the higher redshift galaxies which do not have measured Hα, but do have Hβ marked with (triangles). The underlying gray-scaled distribution is once again drawn from the SDSS DR8 sample of galaxies.

CHAPTER 3

RADIO INTERFEROMETRY IMAGING

Having confirmed that both nuclei in a given pair are at coincident redshifts, we must follow up with high-spatial resolution imaging to check whether both optical centers actually contain bright radio cores. This is the final step of our dAGN confirmation strategy. Radio imaging can robustly confirm whether both stellar nuclei in a merger are actively accreting since radio is a generic tracer of the the nonthermal synchrotron emission that seems to be a ubiquitous by-product of accretion-driven jets. Importantly, radio emissions are not extincted or obscured by intervening gaseous media or dust, and so do not have the same observability issues as optical techniques. Radio interferometry has the spatial resolution necessary to hone in on the cores of any putative AGN. Ideally for *bona fide* dAGN, we would observe two distinct, compact, bright cores which have spectral indices suggesting synchrotron radiation from SMBH jets, or synchrotron self-absorption from an obscured nuclear region. Two other outcomes are possible if both sources are not true AGNs: only one source in the pair is detectable, or one source is clearly responsible for the radio signature in both galaxies. The latter scenario is due to jets from one AGN impacting on the companion galaxy, giving the impression that there are two active cores when in fact there is only one. To fully diagnose each pair within the three scenarios above, we need both positional and spectral information. While the archival VS82 survey at 1.4 GHz managed a resolution of $1.8''$, our new observations at 6 GHz manage to achieve resolutions down to $0.3''$which is necessary to isolate radio emission of one galaxy from the other in a pair.

3.1 Observations

As with the optical spectroscopy above, the radio observations were conducted over three campaigns, between 2015 and 2018. All observations were conducted using the *Very Large Array* interferometer in Socorro, New Mexico. All observations were taken in the A-configuration (25 antennas), utilizing the C-band (central wavelength of 6 cm) which has a frequency range of 4−8 GHz. This configuration uses the widest spacings between the antennae to achieve longer baselines. The combination of this configuration and band is chosen specifically to achieve the sub-arcsecond resolution necessary to accurately separate the dual sources in our sample. The details of the observations are given in Table 3.1.

At the time of the original *VLA* proposal, not all of our sources had been fully analyzed. Thus, not all targets determined to be spectroscopic binaries in Table 2.2 are included in the follow-up radio observations. Generally, the targets which were not included tend to be those with redshift flags indicating marginal quality due to low signal.

3.2 Data Reduction

Of the 16 pairs listed in Table 3.1, six have been previously analyzed in Fu et al. (2015a). In what follows, we re-analyze these sources alongside the newer data for consistency. We utilize the Common Astronomical Software Applications (CASA) package v. 5.6 with VLA-specific procedures to perform data calibration and flagging to generate the measurement sets for each observation. The data for each observation is comprised of 2 basebands with width of ∼2 GHz, which each contain 8 spectral windows with widths of 128 MHz, which in turn are composed of 8 channels with width of 16 MHz.

Flagging is necessary to excise measurements (in time and frequency channels) that

Table 3.1. VLA Observations

Target	UT date	Int Time (min)	rms (μJy/bm)	Beam (arcsec)	PA (deg)
0051+0020	2015 Jul 06	60.0	4.8	0.28×0.26	+153.0
0134−0107	2015 Jul 06	20.8	22.7	0.32×0.25	−24.0
0142−0001	2018 Mar 03	59.3	46.8	0.52×0.39	+36.6
0147−0008	2016 Oct 04	59.1	13.4	0.37×0.30	+41.7
0152−0010	2016 Oct 04	59.0	32.3	0.38×0.30	+44.5
0203−0033	2018 Mar 03	59.5	19.3	0.51×0.39	+34.6
2206+0003	2015 Jun 30	58.0	4.5	0.28×0.24	+22.0
2220+0058	2015 Jun 30	16.4	9.9	0.28×0.24	+13.0
2229−0004	2018 Mar 06	31.2	60.7	0.46×0.35	−14.9
2232+0012	2015 Jun 30	57.6	4.2	0.27×0.25	+17.7
2235+0003	2016 Nov 01	58.6	6.4	0.38×0.28	+34.4
2244+0010	2016 Nov 01	58.1	8.1	0.38×0.28	+34.9
2252+0106	2015 Jul 05	56.9	4.9	0.31×0.25	+34.4
2258+0030	2016 Nov 06	57.9	26.0	0.40×0.28	+40.0
2300−0005	2015 Jul 05	57.6	5.0	0.32×0.25	+35.8
2303−0117	2018 Mar 06	60.0	32.2	0.48×0.35	−23.8
2319+0038	2016 Nov 04	58.6	23.8	0.39×0.27	+38.4

A-configuration C-band Observations for 17 of the Kinematic pairs. The integration time is roughly 1 hour for each observation. The resulting cleaned image rms noise levels are given in microJanskies per beam. We give the dimensions (major×minor axis) of the clean beams for each image, and the orientation (position angle, PA, in degrees from North).

are spuriously noisy due to radio frequency interference (RFI; *e.g.*, from passing satellites). In practice, only ∼3.4 GHz total bandwidth is used, since the component basebands do not fully sample out to 4 and 8 GHz, but also because the edge channels of the spectral windows are not included due to low sensitivity. These measurement sets consists of the uv-plane visibilities over the course of an observation, which in turn are dictated by the spatial separation of the antennae and the observed set of frequencies. Analogously to the calibration processes for the optical spectra above, the radio data are calibrated using a well constrained known source. During each observation, the nearby source 3C 48 was observed for 10 minutes for bandpass and flux calibration. The basic calibration procedure for CASA prunes out specific channels and time intervals during the observation which are affected by RFI and spurious "birdies."

We use the CASA routine `tclean` to perform synthesis imaging and deconvolution. We first generate a "dirty" image and "dirty beam" (PSF) for each observation by running the cleaning algorithm with zero iterations of cleaning. Because the uv-coverage is not fully sampled, regridding is done using a weighting scheme. The gridded data is then Fourier transformed to change the set of visibilities into an image of the sky. This "dirty" image contains radial and ring-shaped artifacts, called sidelobes, as a result of the incomplete sampling of the uv-plane. This is true for the PSF as well, but can be corrected for through iterative cleanings. At this point we run the cleaning algorithm on the dirty image in an iterative fashion. For each iteration, the brightest pixel is identified and a scaled (10% level) PSF is subtracted from the the image, leaving the remaining image to be further cleaned. This will reduce some of the effects of the sidelobes without going overboard in subtracting

and creating nonphysical negative "wells." The remaining brightest pixel on the image then becomes the focus of the next iteration. The amplitude and position of the subtracted PSF is retained in a list, which is concatenated over each successive iteration. The finalized list then represents a model image mapping the brightness on the sky. By convolving this list of clean components with the idealized PSF ("clean beam/restoring beam"), we recover a cleaned image of the sky brightness.

More precisely, we use the `tclean` routine with the following settings. The weighting scheme is set to Briggs weighting, with a robustness of 0.0. This type of weighting is a compromise between natural weighting, which weights each visibility based on the inverse square of the noise, and uniform weighting, which boosts lower-weighted visibilities proportionally so that all visibilities have the same weight. The choice of robust = 0.0 achieves a balance between resolving small scale structure while preserving the image fidelity by not boosting the rms noise of the image too much. The average restoring beam size has a FWHM of $0.43'' \times 0.32''$, with the specific values for each image given in Table 3.1. We choose a pixel scale of $0.05''$ for the images such that $\leq$5 pixels fit within the restoring beam. Cleaning is run iteratively until one of two criteria are met: either the residuals drop below a threshold of $\sim 12 \mu$Jy beam^{-1}, or 5000 iterations are performed.

We use the multi-term multi-frequency synthesis method, assuming that the spectrum of the source behaves like a power law such that the flux is related to the frequency and spectral index (slope) by $S_\nu \propto \nu^{-\alpha}$. We set the number of Taylor terms to two so that the power law is modeled as a linear polynomial. The ratio of the first and zeroth Taylor terms then gives a map of the spectral index.

In Figures 3.1, 3.2, and 3.3 we show a montage of multiwavelength imaging for the 17 pairs of galaxies observed with the *VLA* at 6 GHz. In some cases, the optical images from Jiang et al. (2014) show dramatic tidal tail structures indicative of mergers. We confirm the stellar cores with near-IR imaging from UKIDSS (UKIRT (United Kingdom Infrared Telescope) Infrared Deep Sky Survey (Lawrence et al., 2007)). The presence of radio emission coincident with both the optical and IR stellar nuclei is shown by the blue contours of the low-resolution VS82 radio imaging campaign at 1.4 GHz (Hodge et al., 2011). The red contours illustrate the results of the 6 GHz radio imaging in this section, illuminating the true morphological structures embedded in each region with higher resolution imaging. The restoring beam from the cleaning process is given in the lower right corner of each of the 6 GHz Stokes *I* images in the fourth column. Lastly, we show the spectral index maps for each region, where pixels outside the contours are masked. As we will discuss on a case by case basis in §4, the confirmed dAGNs in Figure 3.1 show strong evidence supporting a radio core in each stellar nucleus, while the remainder of the sample does not.

3.2.1 Image Decomposition

In order to estimate the spatial extent of the 6 GHz radio emission in each core, we utilize the CASA task `imfit`, which uses 2D least-squares fitting. We input a "guess" for the model elliptical Gaussian for each source. This is done interactively through CASA where we identify the location of the brightest pixel in the region of the suspected source. In all cases, we give a basic guess value of a $0.5'' \times 0.5''$ Gaussian with no positional angle (with the exception of 0134−0107 and 0152−0010, for which we use length values of $1''$). In the case of dAGNs, two Gaussian ellipses are fit simultaneously. The best-fit ellipses are

deconvolved from the restoring beam to give the intrinsic dimensions and orientations of the source. Since the errors on a given pixel in a cleaned image are correlated with those of the surrounding pixels, error estimates are given by the prescription of Condon (1997). The sources are found to have a range of compactness, with spatial axes from 0.69″down to 0.07″, or 14 kpc down to 0.18 kpc at the corresponding redshifts of those sources. Note that for the set of imposters, the regions fitted encompass only the central core regions, and any obvious jets are excluded using region masks. We give the results of the image fitting and extraction in Table 3.2. These regions are then used to extract the integrated flux density at 6 GHz, $S^{\rm tot}_{\rm 6GHz}$, in mJy. The fitted sources are not especially bright at 6 GHz, with only one deconvolved source (222051.54+005815.5) at a level above 1 mJy. However, this source's radio brightness is unsurprising given its obvious morphology as a powerful FR II type AGN with a radio lobe extending ∼50 kpc to the East.

In some cases, `imfit` fails to deconvolve the best-fit ellipse from the restoring beam, and no deconvolved estimate can be obtained. This is the case for sources whose spatial extent contains a number of pixels of equal or less amount than the beam, such that the source is only marginally resolved, as would be the case for a point source. For these cases, we give upper limit estimates of the integrated flux based on the un-deconvolved fits, though these should not be taken as the final values since the un-convolved regions encompass more pixels than the true extent of the sources. A strict upper limit on the size of these unresolved sources can be taken as the corresponding beam size in Table 3.1, although for consistency we estimate the upper limit of the integrated flux using the un-deconvolved best-fit source sizes. Of our 6 confirmed sets of dAGNs, all were able to be deconvolved from the beam

except for 014203.25−000150.8, 231953.31+003816.6, and both sources in 2300−0005 (which is consistent with Fu et al. (2015a)). Of all targets with detected sources above the rms noise, we were able to at least obtain a best-fit region, even if it is unable to be deconvolved. This is the case for 11 of the total 24 fitted regions.

3.2.2 Spectral Index

In addition to the integrated flux for the sources, we also wish to characterize the underlying spectrum to probe what type of emission process is responsible for the observed flux. This is done qualitatively using the spectral index, $\alpha_{4-8\mathrm{GHz}}$, which is the spectral energy distribution's power law slope such that the source's flux density $F_\nu = C \times E^{-\alpha}$, where C is some constant. This is sometimes recast when plotting the AGN continuum as $\log(\nu F_\nu)$ vs. $log(\nu)$ such that the power law is then of the form: $\nu F_\nu \propto \nu^{1-\alpha}$. The spectral index is then: $\alpha(\nu) = -\frac{\partial log(F(\nu))}{\partial log(\nu)}$. In radio astronomy, it is conventional to retain the negative in front of α, but characterize steep positive slopes with increasingly more negative values of α ($n.b.$, in X-ray astronomy, the photon index $\Gamma = \alpha + 1$). For a distribution of relativistic electrons in an optically thin medium ($\tau < 1$), the spectral energy distribution is a superposition of the spectra of the individual electrons. For synchrotron sources, this composite spectrum cannot rise faster than $\nu^{1/3}$, such that $\alpha < -1/3$ (Condon and Ransom, 2016). Many known (optically thin) synchrotron sources have $\alpha \sim -0.75$, so we consider sources in our sample with $\alpha < -0.5$ to be likely sources of non-thermal synchrotron radiation (O'Dea and Saikia, 2021). This could suggest SMBH activity as the source of the flux in the case of very young jets which have not permeated far outside the nuclear region. Counter to this scenario, an evolved radio AGN would be expected to exhibit jets or lobes with steep spectral index, while

Table 3.2. 6 GHz Radio Properties of Sample

Radio Designation J2000 (1)	$S^{\rm tot}_{6\,\rm GHz}$ (mJy) (2)	$\alpha_{4-8\,\rm GHz}$ (3)	Maj (arcsec) (4)	Min (arcsec) (5)	PA (deg) (6)
005114.11+002049.5	0.933±0.011	−0.85	0.206±0.006	0.189±0.005	+153±18
005113.93+002047.2	0.297±0.008	−0.96	0.073±0.024	0.038±0.036	+39±59
013412.78−010729.4	≤10.017±0.015	+0.27	≤0.316±0.000	≤0.250±0.000	≤+157±0
014203.25−000150.8	≤0.655±0.008	−0.47	≤0.344±0.003	≤0.264±0.002	≤+20±1
014715.86 −000819.4	0.311±0.007	−0.14	0.067±0.026	0.043±0.029	+95±50
015253.79−001005.5	≤0.330±0.003	+0.10	≤0.264±0.001	≤0.159±0.000	≤+63±0
020301.43−003339.1	≤0.330±0.007	−1.01	≤0.325±0.004	≤0.240±0.002	≤+45±1
220635.08+000323.2	0.588±0.010	−0.84	0.175±0.009	0.112±0.013	+111±58
220634.98+000327.6	0.069±0.013	−1.21	0.314±0.088	0.155±0.145	+66±31
222051.54+005815.5	1.107±0.025	−0.01	0.281±0.010	0.165±0.012	+75 ±4
222907.55−000410.9	≤0.719±0.010	−0.15	≤0.291±0.025	≤0.284±0.024	≤+165±14
223222.60+001224.7	0.244±0.008	−1.13	0.129±0.019	0.044±0.038	+103±48
223222.44+001225.9	0.133±0.011	−1.40	0.245±0.043	0.181±0.044	+128±32
223546.27+000358.8	0.140±0.009	−0.23	0.339±0.033	0.039±0.063	+84 ±6
224426.45+001051.1	0.136±0.019	−0.66	0.512±0.092	0.121±0.071	+35±5
224426.60+001052.3	0.089±0.038	−2.49	0.688±0.362	0.519±0.267	+120±78
225222.35+0010659.9	≤0.017±0.007	+0.49	≤0.343±0.097	≤0.183±0.026	≤+52±0
225222.65+0010700.7	≤0.092±0.009	−0.36	≤0.350±0.024	≤0.244±0.012	≤+14±5
225817.74+003007.5	≤0.735±0.008	−0.85	≤0.364±0.003	≤0.294±0.002	≤+83±1
230010.18−000531.6	≤0.498±0.009	−0.38	≤0.316±0.003	≤0.253±0.002	≤+120±2
230010.24−000533.9	≤0.063±0.009	−1.19	≤0.344±0.034	≤0.254±0.019	≤+6±10
230342.74−011712.7	0.632±0.008	−0.05	0.173±0.008	0.053±0.017	+4 ±4
231953.31+003816.6	≤0.594±0.008	−0.74	≤0.315±0.003	≤0.279±0.002	≤+16±3
231953.43+003813.4	0.143±0.015	−0.99	0.565±0.071	0.214±0.039	+22 ±5

Sources are sorted in ascending R.A. For observations where 2 cores are confirmed, the dual cores are listed together. (1) J2000 coordinate of the identified 6 GHz radio source core; (2) Total flux density at 6 GHz within the source extent in mJy; (3) Flux-weighted spectral index within the 4 GHz bandwidth contained within the source region (yet to be calculated); (4−6) Beam-deconvolved source sizes (FWHMs in arcsec) along the major and minor axes and the position angle of the major axis (degrees East of North). In cases of unresolved point sources (denoted with ≤), the values for column 7 are for the un-deconvolved regions, and are given as upper limits. The 1σ errors in Columns 9-11 are calculated by `imfit` using the procedure outlined in (Condon, 1997). The error of the 6 GHz photometry does not include the 3% uncertainty in the VLA flux density scale (Perley and Butler, 2013).

the core would have a flatter value due to synchrotron self-absorption in the obscured central region. We certainly see this arrangement in some of the single AGNs in our sample, most notably 2220+0058. However, thermal bremsstrahlung (free-free) emission from H II regions would also have a noticeably flat spectrum ($\alpha \sim -0.1$), and could suggest that nuclear star formation is dominating over any putative AGN. The spatial compactness of the central region is therefore an important distinguishing factor in weeding out this latter possibility.

We use the best-fit spatial regions from `imfit` to extract the flux-weighted spectral index values, $\alpha_{4-8\mathrm{GHz}}$. This is done by computing the weighted average of the pixel values enclosed within the fitted region on the spectral index map. We report the spectral index values for the fitted sources in Table 3.2. The maps themselves are plotted in the last column of Figures 3.1, 3.2, and 3.3. For readability, we only display the pixels within the lowest contours (3-σ above the rms noise) and set the rest of the map to NaNs. For the cases where the source is unresolved and `imfit` cannot properly ascertain the region's extent, we can still estimate the average spectral index in a similar fashion as for the integrated flux above, using the clean beam size as an upper limit for the source's physical extent.

The bulk result shows some interesting patterns. By eye, the cores of most of our confirmed dAGNs appear to meet the criterion for synchrotron emission. We note that for the 4 confirmed dAGNs originally discussed in Fu et al. (2015b), all 8 individual sources had $\alpha_{4-8\mathrm{GHz}} < -0.5$, broadly consistent with the results from the reanalyzed images presented here. The two new dAGNs match this pattern with one important distinction: these pairs show morphological evidence of evolved radio jet structures in one of their component galaxies. The galaxy producing the jets follows the pattern stated above where the core in both

instances is close to the nominal transition from synchrotron to synchrotron self-absorption. Therefore, these two systems might constitute a scenario wherein one galaxy first experiences a bout of accretion and produces a jet soon after the first pericenter passage, allowing enough time for the structure to expand outwards and age before the companion AGN switches on to produce a jet with a "younger" signature. For the rest of the sample where only one galaxy shows evidence of a radio AGN, we see that many show the same pattern of a flatter spectral index core with a progressively steeper spectrum outwards in the jets. Not all of these cores are strictly beyond the demarcation for nonthermal emission; 020301.43−003339.1 shows an interesting morphology of a synchrotron core with fragmented jets. However, every other single AGN does have a definitively flat spectral index.

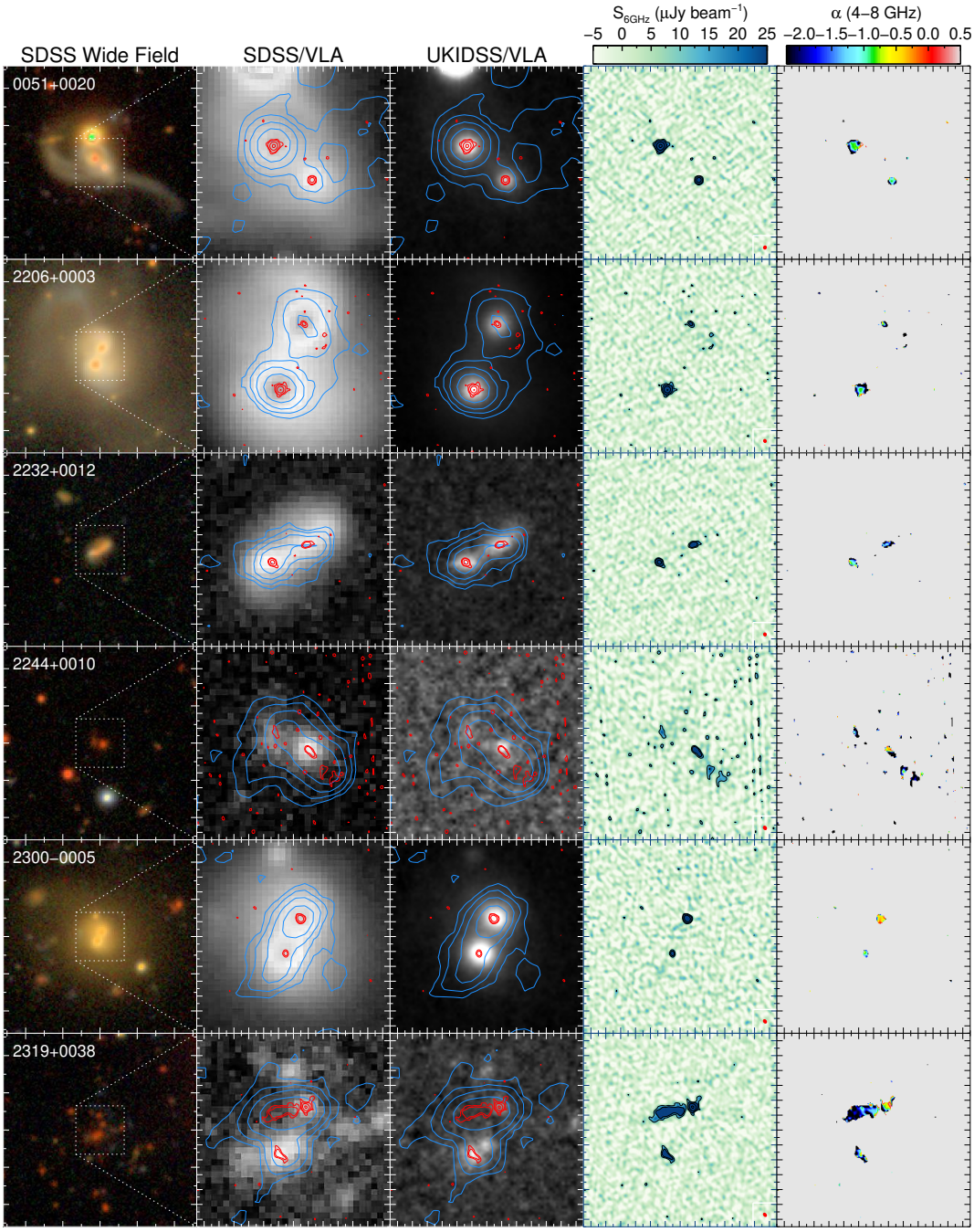

Figure 3.1. Montage of bona fide dual AGN systems. 1) Wide-field deep SDSS Stripe82 coadded optical images with source designation; 2) 4-times zoom-in of the optical images (in gray-scale for ease of viewing), with cyan contours from the VS82 1.4 GHz radio images and red contours from the 6 GHz VLA radio images; 3) UKIDSS IR images with the same contours as in column 2 ; 4) VLA 6 GHz intensity map, with corresponding contours; 5) 4-8 GHz spectral index map determined from the 6 GHz data. In all cases, the lowest contour level is at 3σ, and increase exponentially to the peak value. Major tick marks are spaced in $10''$ intervals in column 1, and $1''$ intervals in all other panels. N is up and E is left in all panels.

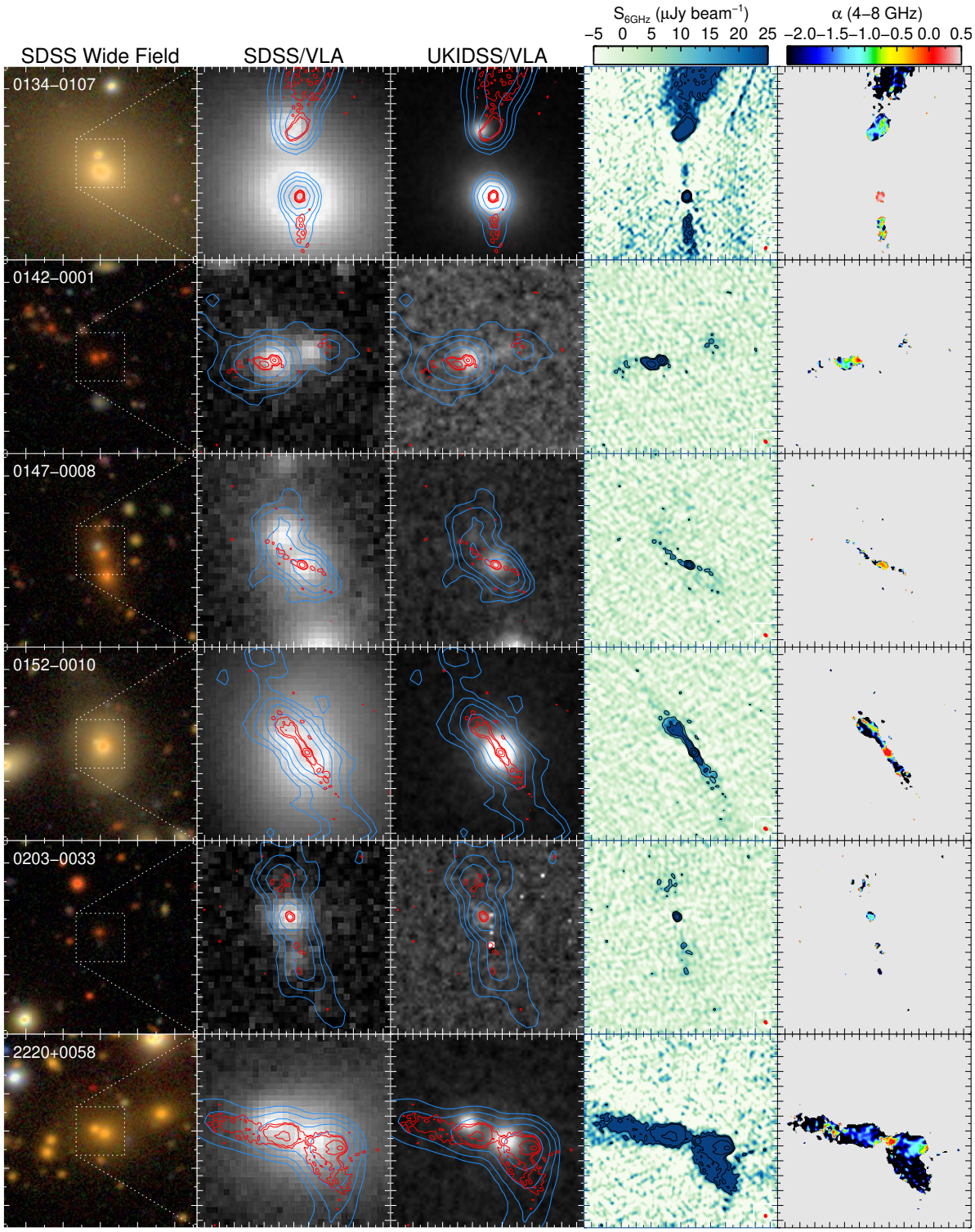

Figure 3.2. Montage of single AGN imposters. The panels are the same as for Figure 3.1. These pairs all show evidence of a single AGN with varying degrees of radio jets/lobes which are overlapping with the companion galaxy. This chance alignment gives the false impression of two separate radio sources at lower resolution.

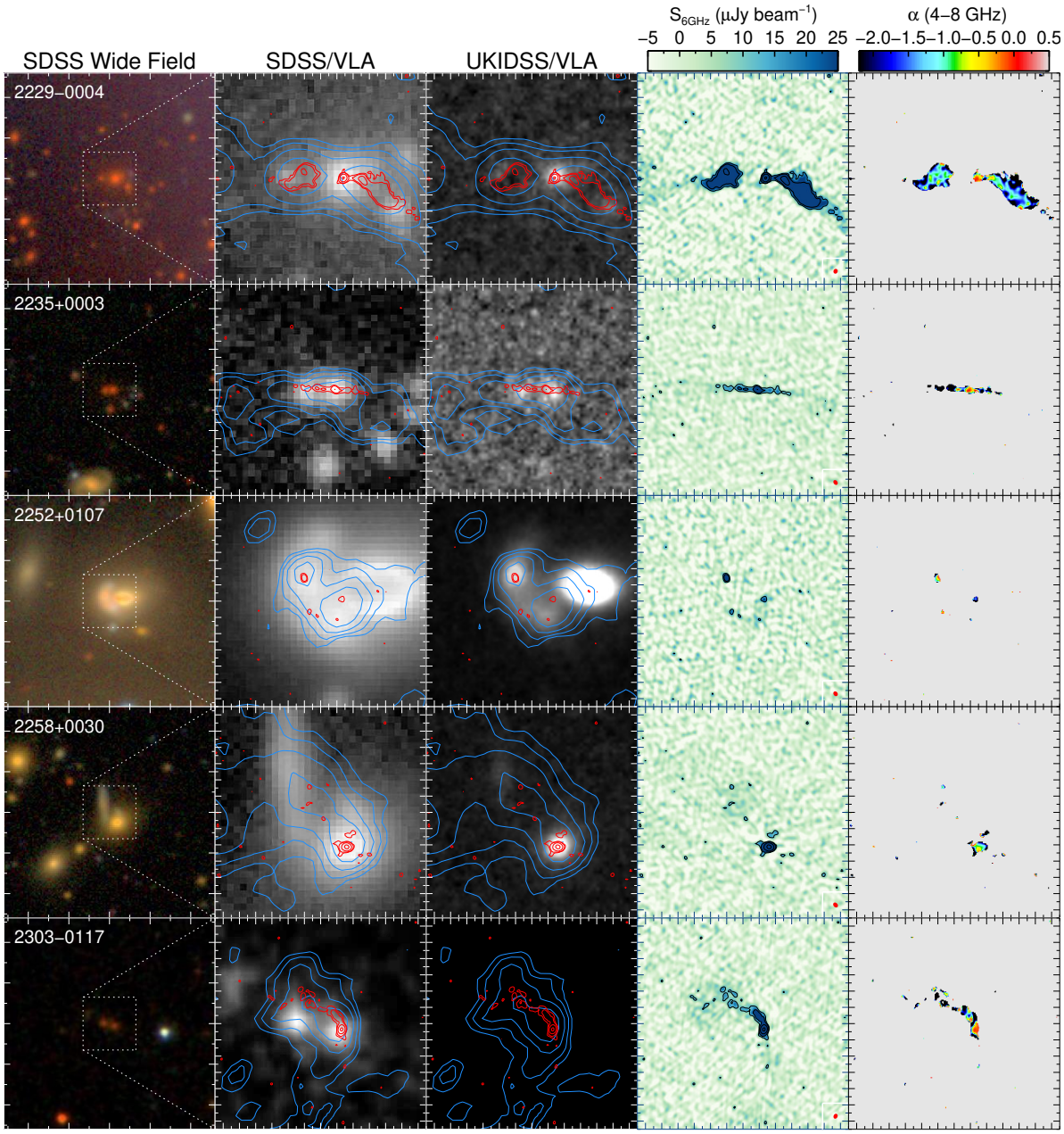

Figure 3.3. Montage of single AGN imposters (continued). The panels are the same as for Figure 3.1.

CHAPTER 4

THE FINAL SAMPLE

As has been shown in the previous chapters, our sample of radio-selected dAGN candidates shows a wide array of multi-wavelength properties. In this chapter, we weave together the multiple lines of evidence to paint a picture of what is physically going on in each pair. In this way, we rigorously confirm or reject each candidate for dual AGN status. We begin by examining each of the dual systems presented in Figure 3.1 and explaining the criteria they satisfy to achieve dAGN status. We synthesize similar arguments for why each of the remaining systems in the kinematic pairs sample do not qualify as a dAGN. Several of the candidates present tantalizing, albeit ambiguous, evidence suggestive of dAGN activity. We deem these few hold outs as tentative dAGN.

Our final census of dAGNs in the sample is predominantly guided by several criteria that we have thoroughly explored in this text. We show these scenarios for confirmation of dAGN schematically in Figure 4.1. We base our classification primarily on the 6 GHz radio imaging, where a dAGN system will exhibit two separate compact regions of high radio brightness above the background. As noted above, cases where one AGN is producing extended jets complicate this classification. For scenarios where a jet or radio lobe from one galactic nucleus overlaps with its companion galaxy, we consider optical emission line diagnostics of AGN activity in the companion to be strong evidence for a separate but synchronized AGN, and thus the pair constitutes a dAGN system. While not shown explicitly in the schematic, in cases where overlapping jets are not an issue, we also consider the 1.4

GHz radio excess as a potential indicator of AGN activity. For several pairs in the kinematic sample without 6 GHz radio imaging, we rely on the optical properties and radio excess as signatures suggesting dAGN activity, but do not consider these as robust confirmations compared to dual radio cores.

In addition to these confirmation methods, we investigate several other criteria common in the literature to either confirm or categorize AGN. As has been noted in §1.1.2, the unified model of AGN suggests that an appreciable fraction of AGN may be oriented in such a way that the dusty torus might block the sightline to the central engine; however, the AGN may still be detectable by its bevy of IR radiation reprocessed by the dust. One widely-used technique to preselect AGN involves making color cuts using mid-IR magnitudes from the Wide-field Infrared Survey Explorer (WISE) mission (Wright et al., 2010). Of the four WISE bands, the traditional MIR color diagram uses the W1−W2 and W2−W3 colors, where the effective wavelengths of the W1, W2, and W3 bands are 3.4μm, 4.6μm, and 12μm, respectively. In Figure 4.2, we show the mid-IR colors from WISE for our kinematic pairs. Of the 21 kinematic pairs, 12 pairs have WISE coverage. The color selection criteria of Jarrett et al. (2011) constrains a region of the plot to reliably select dAGN in advanced mergers (sep<10 kpc):

$$\begin{aligned} &\mathrm{W2}-\mathrm{W3} > 2.2 \text{ and } \mathrm{W2}-\mathrm{W3} > 4.2, \\ &\mathrm{W1}-\mathrm{W2} > (0.1 \times (\mathrm{W2}-\mathrm{W3}) + 0.38) \\ &\text{and } \mathrm{W1}-\mathrm{W2} < 1.7. \end{aligned} \tag{4.1}$$

However, Satyapal et al. (2017) note that this strict cut misses a substantial fraction of known dAGNs in the literature, and that a more relaxed cut of W1−W2>0.5 captures $\sim 2/3$ of known dAGNs. Since $\sim 66\%$ of our kinematic pairs have separations >10 kpc, we

adopt the less stringent cut from Satyapal et al. (2017) as an additional diagnostic for AGN activity. However, it is important to note that the resolution of WISE ($\sim 6'' - 12''$) is larger than the angular separation of any of our kinematic pairs, therefore the WISE photometric magnitudes encompass both galaxies within a given pair. We thus plot the color of the *combined* dAGN system in Figure 4.2, and therefore cannot say definitively which of the galaxies (or whether both in a pair) satisfy the AGN color cut. While this method cannot be used to diagnose dual AGN, it is still interesting to see which pairs exhibit the presence of IR AGN. We note that 5 of our dAGN systems are above the generous color cut, including the systems 0051+0020 and 2232+0012. Intriguingly, the two systems which pass the more strict color cut (2211+0027 and 2245+0058) are pairs for which we have no other diagnostic evidence of dAGN activity. While we do not take this as definitive evidence of dAGN, it does highlight the breadth of galaxy pair properties in our radio-selected sample.

A qualitative assessment of AGN type compares the radio and radiative outputs. In Figure 4.3, we plot the radio power versus the [O III] luminosity for the kinematic sample. As noted in §2.3 many of our galaxies our at redshifts high enough to exclude the possibility of measuring Hα; however, we do have [O III] measurements for most of the kinematic pair galaxies, giving us some additional insight into the properties of these galaxies. The methodology is similar to that of the radio-excess plot of Figure 2.7; however, instead of trying to compare against star formation output, here we are strictly comparing against the presumed radiative output of the putative AGN. Radio galaxies have been found to follow a bimodal distribution in this luminosity space. Galaxies with radio power above the empirical relation of Xu, Livio, and Baum (1999) shown in the figure are categorized as "radio-loud."

This is similar to the definition of radio loudness based on the optical to radio luminosity ratio of Kellermann et al. (1989) as employed by Roy et al. (2021) where $R > 1$ is classified as "radio-loud":

$$R = 0.4(m_i - t), \tag{4.2}$$

where m_i is the Petrosian i-band apparent magnitude (values from the SDSS co-added catalog of Jiang et al., 2014), and t is the AB radio magnitude:

$$t = -2.5 \log \left(\frac{S_{1.4\mathrm{GHz}}}{3631\mathrm{Jy}} \right). \tag{4.3}$$

While this demarcation does not constrain AGN or dAGN status, it does provide some context for the other classifications presented. At a glance, it highlights the bifurcation in our sample suggesting that the radio-preselection does allow for some less luminous radio galaxies to make it into the sample. Interestingly, most of the *bona fide* dAGNs lie on or below the demarcation, with optical emission suggesting either star-forming, composite, or LINER type using the BPT diagram. While the usual explanation would be that the optical emission of the LINERs is being produced by quasar/radiative mode AGN, we know from our WHAN analysis that it is instead produced via retired stellar populations. Conversely, most of the composite class dAGNs were shown to be strong AGNs in the WHAN diagram, so the former explanation for their boosted [O III] is likely the correct interpretation. It is also worth noting that many of these composite types are also radio-excess. While this may seem to be in tension with their categorization as radio-quiet, these dAGNs in particular were closer to the Seyfert region of the BPT diagram and thus would be expected to have lower Hα emission than forbidden emission. While we cannot rule out the possibility of retired stellar populations in many of the galaxies in the"radio-loud" population lacking Hα (pink

points), it is possible that their enhanced radio power is due to radio/kinetic mode AGN. It is again not surprising that 63% of the radio-selected galaxies are found to be radio-loud, since the selection criteria makes no presumption about the ionized emission of the galaxies.

We investigate one final method for assessing the nature of the central engines in our sources via their excitation states as a proxy for their accretion modes. Combining with the optical line fluxes from §2.4 with the radio properties, the individual AGN components can be classified as high excitation or low excitation radio galaxies (HERGs or LERGs) based on the multi-step system of Best and Heckman (2012). Generally, the higher degree of optical excitation in HERGs correspond to the higher mode of accretion which triggers radiative outflows (quasar mode AGN), whereas LERGs are associated with AGN emitting jets in radio mode (Hine and Longair, 1979; Laing et al., 1994). As with several of the previous radio galaxy trends employed in this text, this classification method is primarily based on a known bimodal distribution. The radio galaxy population is split by the Excitation Index (EI $\geq$0.95 for HERGs) of Buttiglione, S. et al. (2010):

$$\mathrm{EI} = \log\left(\frac{[\mathrm{O\ III}]}{\mathrm{H}\beta}\right) - \frac{1}{3}\left[\log\left(\frac{[\mathrm{N\ II}]}{\mathrm{H}\alpha}\right) + \log\left(\frac{[\mathrm{S\ II}]}{\mathrm{H}\alpha}\right) + \log\left(\frac{[\mathrm{O\ I}]}{\mathrm{H}\alpha}\right)\right]. \tag{4.4}$$

We use additional criteria for classification in cases where not all emission lines are observed. As done by Singha et al. (2021), we also classify based on the individual demarcations of Buttiglione, S. et al. (2010) for [NII] and [SII] when [OI] is not available:

$$\begin{aligned} \log\left(\frac{[\mathrm{O\ III}]}{\mathrm{H}\beta}\right) - \log\left(\frac{[\mathrm{N\ II}]}{\mathrm{H}\alpha}\right) &\lesssim 0.7, \\ \log\left(\frac{[\mathrm{O\ III}]}{\mathrm{H}\beta}\right) - \log\left(\frac{[\mathrm{S\ II}]}{\mathrm{H}\alpha}\right) &\lesssim 0.9 \end{aligned} \tag{4.5}$$

As with the BPT diagnostics, we may not have data on all emission lines necessary for these calculations. In these circumstances, we rely on measurement of the [O III] equivalent width

(EW $>$ 5 Å for HERGs) (Best and Heckman, 2012). We explore the various classification schemes and check for agreement in our sources, noting the final classification in Table 4.1. An interesting facet to this analysis is investigating whether both components in the confirmed duals are of the same class, or if there is a mix of excitation states. Interestingly, all but one of the six confirmed dAGNs have correlated states, all of which are LERGs. The exception is the pair in 2244+0010, where the more obvious radio source is in the low state, and the fainter source is in the high state.

As a means of tabulating, in Table 4.1 we report the results of our various classification metrics. The summary of the more reliable AGN classifications are also given via the tags in the last column of Table 2.2.

4.1 Bona fide dual AGN

We now focus on the kinematic pairs which show definitive evidence of dAGN activity. We find that 5 of our kinematic pairs show clear evidence of dual compact radio cores. One additional pair (2244+0107) shows tentative evidence of a second region of activity. We thus conclude that our sample contains 6 dAGN systems. These pairs are shown together in Figure 3.1.

4.1.1 0051+0020

This pair exhibits two well defined small-scale radio cores. The radio centroids coincide with a pair of BPT star-forming/AGN composite nuclei. The WHAN diagram shows that the optical nuclei are due to strong AGN (not retired galaxies), which are likely the source of the mechanical power driving the radio excess above the Hα-predicted levels. While we cannot resolve which nucleus in the pair is responsible for the WISE IR AGN signature,

Table 4.1. Classifications of Kinematic Pairs

Optical Designation J2000 (1)	BPT1 class (2)	BPT2 class (3)	BPT3 class (4)	Radio Excess (5)	Radio Loud (6)	MIR color (7)	Mode (8)
005113.93+002047.2	Comp	SF	Seyfert	Y	N	Y	L
005114.11+002049.4	Comp	SF	SF	Y	N	Y	L
013412.78−010729.5	LINER	LINER	...	Y	N	N	L
013412.84−010725.0	Comp	LINER	LINER	Y	Y	N	L
014203.08−000150.3	...	...	...	<	Y	N	L
014203.24−000151.0	...	...	...	<	Y	N	L
014715.86−000819.5	...	...	...	<	Y	N	L
014715.94−000817.4	...	...	...	<	N	N	H
014928.38−001446.0	SF	Seyfert	Seyfert	Y	N	N	H
014928.41−001447.8	SF	SF	LINER	Y	N	N	H
015253.79−001005.6	...	...	...	Y	N	N	L
015253.92−001004.3	LINER	LINER	LINER	Y	N	N	L
020301.40−003341.7	...	...	...	<	Y	N	H
020301.43−003339.3	...	...	...	<	Y	N	H
021021.00−005124.2	...	...	...	Y	Y	N	L
021021.13−005126.7	Comp	LINER	Seyfert	Y	Y	N	H
220634.97+000327.6	Comp	LINER	LINER	Y	N	N	L
220635.08+000323.3	LINER	LINER	LINER	Y	N	N	L
221142.42+002731.2	...	...	...	<	Y	Y	L
221142.51+002728.5	...	...	...	<	Y	Y	H
222051.55+005815.5	LINER	LINER	...	Y	Y	N	L
222051.70+005816.7	...	...	...	Y	Y	N	L
222907.53−000411.1	...	...	...	<	Y	N	H
222907.77−000410.9	...	...	...	N	N	N	L
223222.41+001226.3	Comp	SF	Seyfert	Y	N	Y	L
223222.60+001224.7	Comp	SF	SF	Y	Y	Y	L
223546.28+000358.8	...	...	...	<	N	N	...
223546.40+000358.7	...	...	...	N	N	N	...
224426.44+001051.3	...	...	...	<	Y	N	L
224426.61+001051.9	...	...	...	<	Y	N	H
224532.53+005857.9	...	...	...	<	Y	Y	H
224532.68+005855.8	...	...	...	<	N	Y	H
225222.52+010658.0	LINER	LINER	LINER	Y	N	N	L
225222.65+010700.6	SF	SF	SF	Y	N	N	L
225817.73+003007.7	...	...	...	N	Y	Y	L
225817.97+003011.5	SF	SF	SF	Y	Y	Y	L
230010.18−000531.7	LINER	LINER	...	Y	Y	N	L
230010.24−000534.0	...	...	...	<	N	N	L
230342.74−011712.7	...	...	...	<	Y	N	L
230342.91−011711.9	...	...	...	<	Y	N	L
231953.31+003816.7	...	...	...	N	N	N	...
231953.43+003813.4	...	...	...	N	N	N	...

Every two rows is a pair, and sources are sorted in ascending R.A. (1) J2000 coordinate of the optical source; (2) − (4) BPT diagnostic classifications (in order of Figures 2.3, 2.4, 2.5); (5) Radio excess determined via Hα SFR (< denotes excess via Hβ); (6) Radio loudness determined via $L_{[OIII]}$; (7) mid-IR color AGN status based on criteria of Satyapal et al. (2017); (8) mode of AGN activity (HERG/LERG).

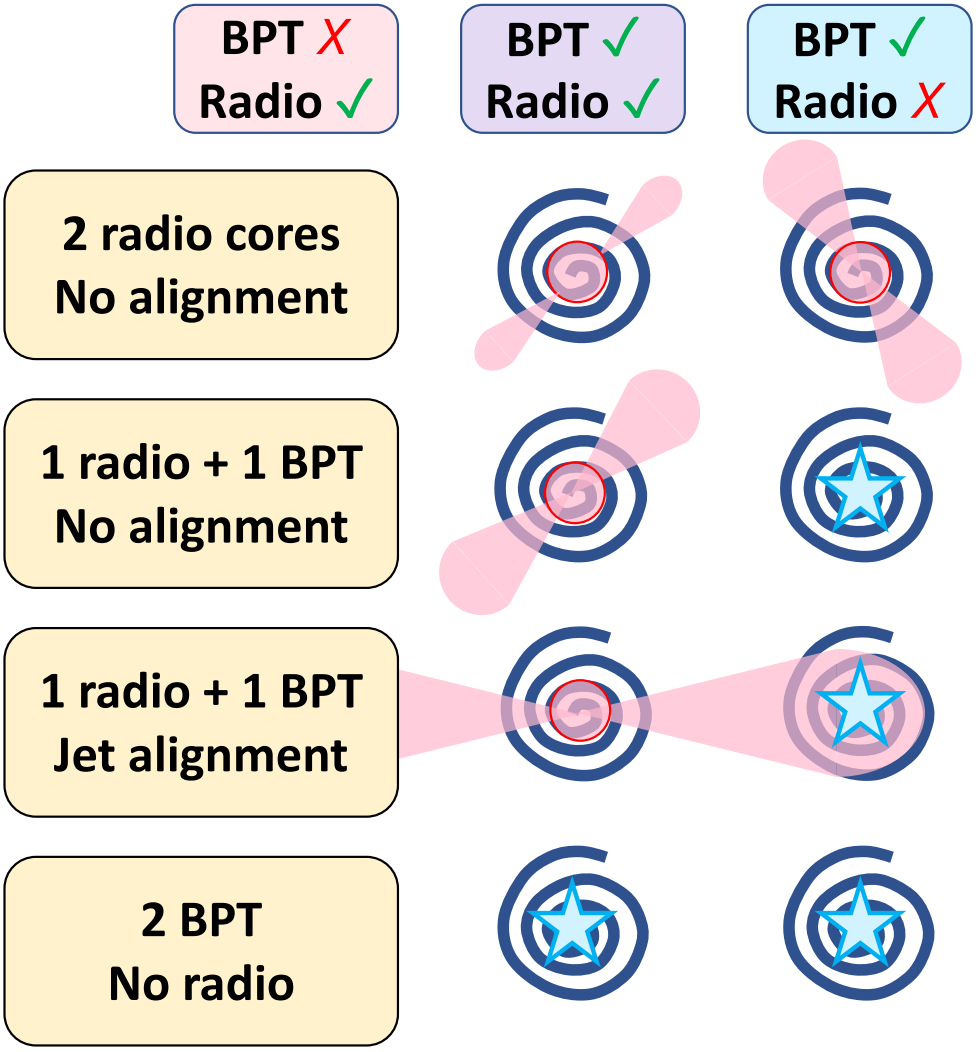

Figure 4.1. 4 scenarios for dual AGN classification in our sample. Radio emission is color-coded in pink and optical BPT classification as AGN (Seyfert/LINER) is coded as a blue star in the nucleus. Some of the jetted imposters may have BPT optical AGN signatures, and thus constitute a dAGN system. However, jetted imposter systems cannot be granted dAGN status based on the radio-excess diagnostic since the provenance of the excess observed for a galaxy without a radio core is likely the companion galaxy from which the jets originate. We do not use the MIR color diagnostic as a means of verifying dAGN since the resolution of the WISE encompasses both galaxies in a given pair such that the observed magnitude is actually a blend of both components.

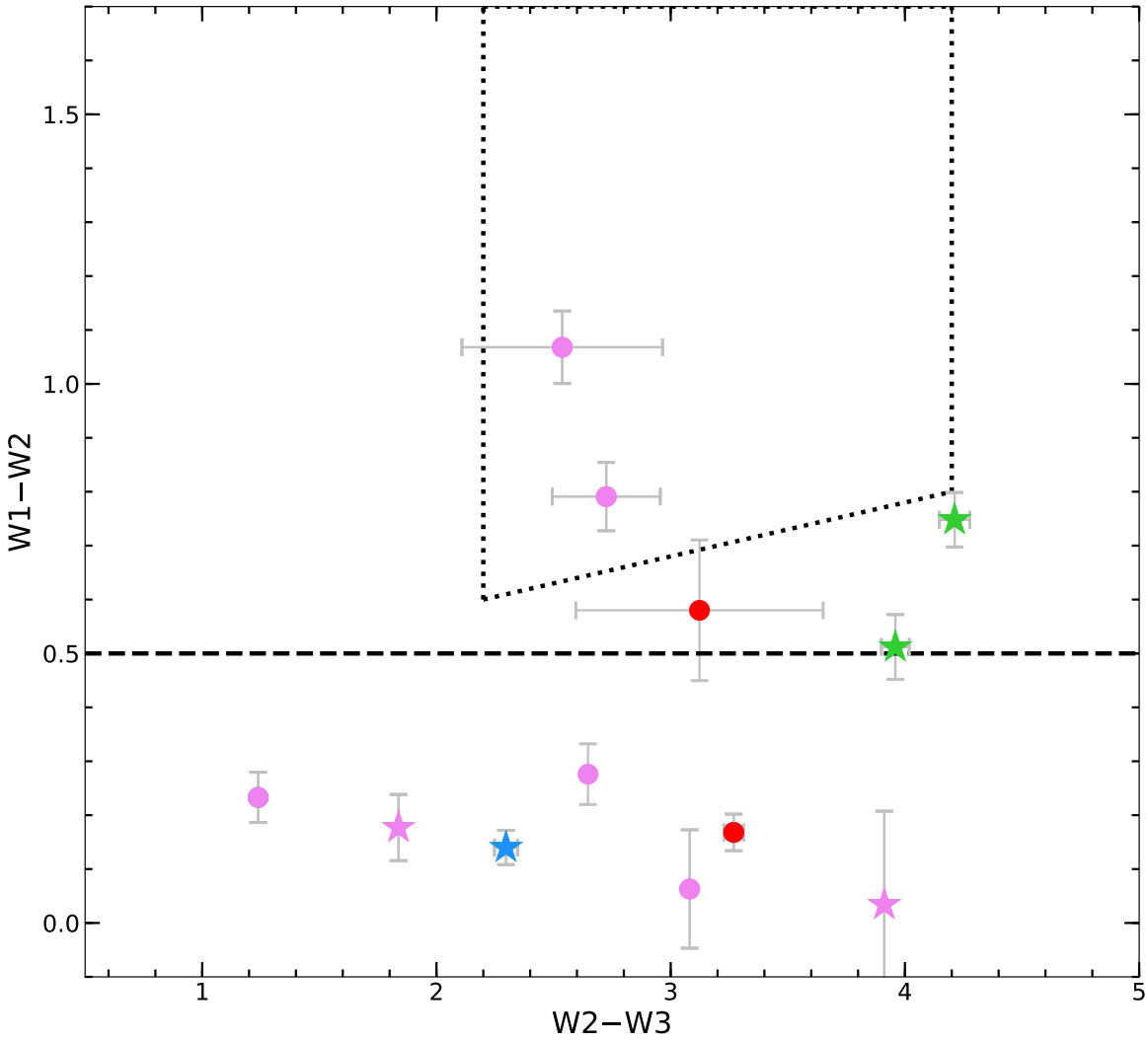

Figure 4.2. WISE IR colors for the kinematic pairs. Note that the finest angular resolution of WISE (∼6″for W1) is greater than the separation of any of our kinematic pairs. Thus, only one point is plotted for each pair and represents the composite color of the system. A total of 5 of our kinematic pairs lie above the empirical color cut at W1−W2 = 0.5 from Satyapal et al. (2017), suggesting that at least 1 galaxy in the pair is exhibiting AGN activity. A more stringent cut for AGN within box based on Jarrett et al. (2011), for which 2 of our pairs qualify. Note that these two pairs lack any AGN detections from the BPT diagnostics or radio follow-up.

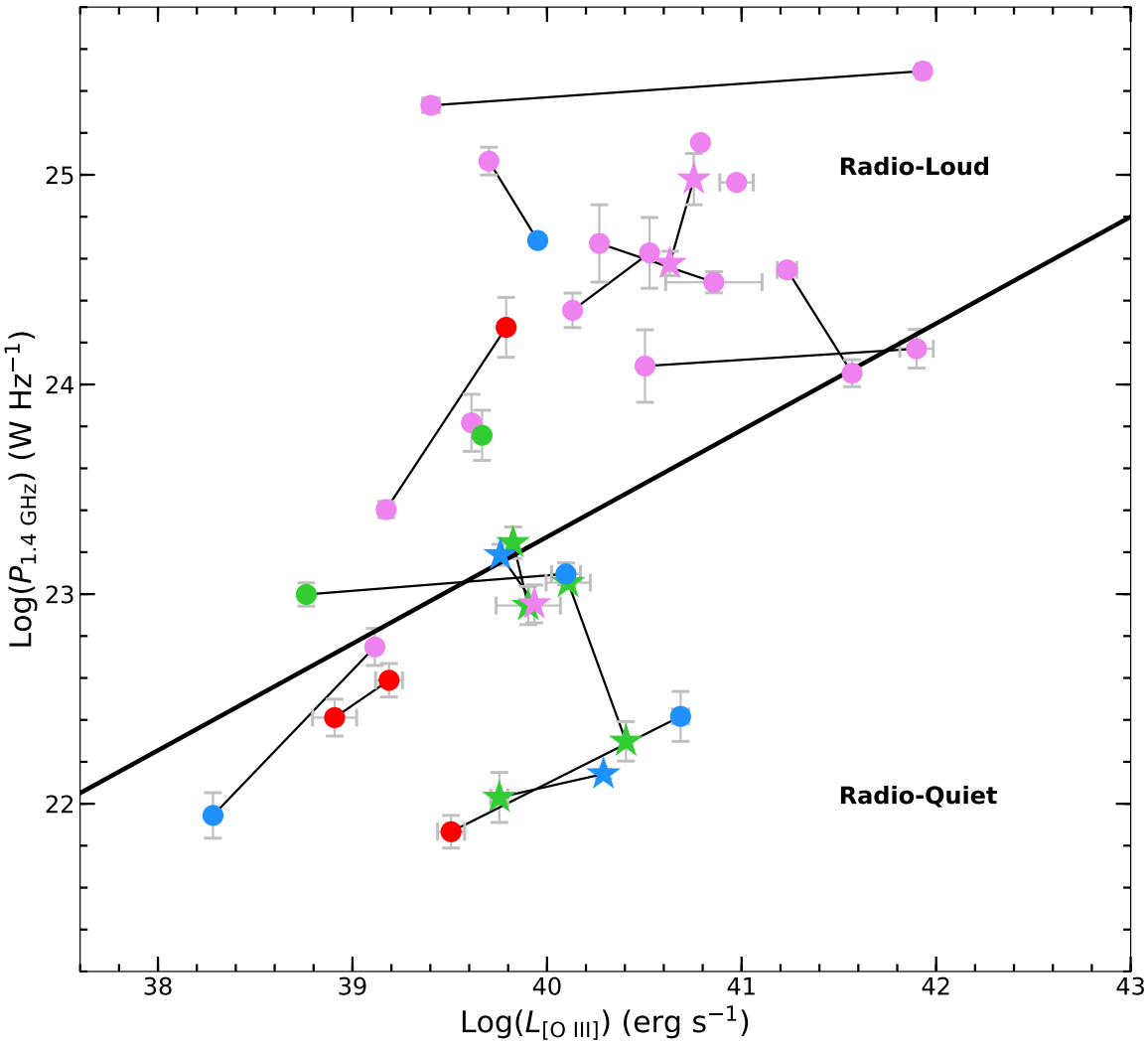

Figure 4.3. Radio Loudness based on Roy et al. (2021) and Xu, Livio, and Baum (1999), comparing radio luminosity against [O III] luminosity. As in the radio-excess plot, the empirical demarcation is based on the known bimodal distribution of active galaxies, similar to the relation of Kellermann et al. (1989). Galaxies above the relation are deemed radio-loud, and might be operating via the LERG/jet mode of low accretion instead of the HERG/quasar mode.

the detection of dual AGN in both optical and radio suggests that perhaps both galaxies contribute to this IR classification. We also note that Gross et al. (2019) found this pair to have X-ray detections for both nuclei with luminosities in the low luminosity AGN regime. Taken together, these traits make this pair the most concretely identified dAGN in our sample. We also note that neither galaxy is classified as radio-loud by the empirical relation of Xu, Livio, and Baum (1999) or the R parameter of Kellermann et al. (1989), suggesting that both nuclei are operating in radiative/quasar mode. However, both sources are classified as LERGs, implying that the observed cores are actually emitting unresolved small scale jets in radio mode activity, consistent with the steep spectral index values for both sources and lower Eddington ratios, consistent with the LLAGN status.

4.1.2 2206+0003

While both sources in this pair are well constrained to steep spectrum radio cores smaller than $\sim 0.3''$ similar to those in 0051+0020, we see differences between the optical nuclei in this pair. The NW galactic nucleus is a SF/AGN composite, while the SE nucleus is a LINER. Both are classified as strong AGN by the WHAN diagram, confirming that the nebular emission of at least the SE source is not due to old stellar populations. The radio excess in both components further implies the presence of dual AGN. Neither source is found to be radio-loud; however, both components are LERGs with modest levels of accretion.

4.1.3 2232+0012

This pair shows nearly identical evidence of dAGN activity as seen in the 0051+0020 pair. The system is classified as AGN by its WISE colors. Distinct from 0051+0020 is the classification of the SE nucleus as radio-loud, while the NW component is radio-quiet.

The SE nucleus does appear slightly more spatially extended in the 1.4 GHz radio imaging implying more substantial jet activity, although extended jets are not seen in the higher resolution 6 GHz image. This might imply that we are seeing the beginning of the jet mode feedback as low-level accretion begins.

4.1.4 2244+0107

At a substantial redshift ($\sim$0.7), [O III]/Hβ is the only emission line ratio detectable in the range of LRIS, making BPT or WHAN classification unattainable. We do note, however, that the SW nucleus is clearly coincident with a steep spectrum radio core, and there is tentative evidence of an unresolved radio source coincident with the optical and IR images of the NE galaxy. Importantly, the NE source *does not* appear to be well aligned with the radio lobe remnants to the SW of the companion galaxy, with a minimum angular difference in the alignment of $\sim 20^{\circ}$. The spatial extent ($\sim$ 14 kpc) and flatness of the intensity distribution at 6 GHz suggests that a jetted AGN in the NE component cannot be ruled out at the resolution of our VLA analysis. Two separate nuclei is further supported by the Hβ-propagated radio excess and radio-loudness seen in both components. We note that the HERG classification of the NE nucleus is based on the [O III] EW ($\sim$9Å) due to the lack of observable emission lines, and thus should not be treated as conclusive. As well, there is significant uncertainty in the estimate of the higher accretion rate ($\log(\lambda) \sim -0.9$), although this would corroborate the HERG nature of a putative AGN in the NE galaxy.

4.1.5 2300−0005

Only the NW galaxy exhibits detectable emission lines for classification as a LINER, though the WHAN diagram shows the nuclear ionization to be due to old stellar populations.

Both nuclei do show radio excess beyond the levels expected for stellar populations. Both sources have well constrained compact radio cores. The flat spectral index of the NW core suggests synchrotron self-absorption of small-scale AGN jets by the galactic media. Both sources are tentatively classified as LERGs via [O III] EW, consistent with the observed low level of accretion and radio excess.

4.1.6 2319+0038

Interestingly, the high redshift of this pair prevents any optical classification, yet both sources exhibit steep spectrum compact radio cores coincident with the optical and IR stellar nuclei. The unresolved point source in the NW galaxy is emitting a synchrotron jet which is not aligned with the companion nucleus. The SE source is more spatially compact and steeper spectrum; it is likely emitting young radio jets that are not spatially resolved at the high redshift. While we cannot classify either source as radio-excess, we note that their high radio-loudness ($R \geq 1.6$) is suggestive of radio mode accretion, although quasar mode accretion can still produce powerful jets. This pair is at the highest physical separation of any of our kinematic pairs ($\sim$ 104 kpc), and while not strictly in the kiloparsec-scale regime, we include it in our final sample. This system may have been triggered via tidal torques during its first pericenter passage, leading to the developed Fanaroff-Riley I morphology seen in the NW galaxy (Fanaroff and Riley, 1974). The definitive radio morphology of this pair offers the most conclusive new addition to the dAGN population in our sample.

4.2 Tentative Additional dAGN

The following kinematic pairs show a mix of optical evidence of AGN or radio excess, but some lack 6 GHz radio imaging follow-up. Therefore we cannot say definitively if the ob-

served radio excess is from two separate sources or one with jets overlapping the companion. Additional radio observations could elucidate any putative cores.

4.2.1 0149+0014

While this pair consists of two star-forming galaxies, both exhibit radio excess suggesting an additional source of radio power beyond star formation alone. While not well constrained, we note that the NE blue disk galaxy exhibits Seyfert BPT line ratios in the [N III]/Hα and [O I]/Hα diagnostics, and is classified as a HERG by all selection criteria, suggesting that it may be transitioning to radiative/quasar mode activity.

4.2.2 0210−0053

The NW galaxy shows only weak optical emission lines, likely due to older stellar populations. The optical signature of the SE galaxy is dominated by star-formation. However, both galaxies exhibit radio excess, with good positional alignment between the 1.4 GHz radio images and the optical nuclei.

4.2.3 2252+0106

This galaxy pair shows clear morphological evidence of tidal interactions due to an ongoing merger. The blue eastern galaxy is definitively classified as an ongoing starburst, perhaps prompted by the merger. The optically brighter yellow western galaxy is classified as a LINER by all BPT diagnostics; however, its nebular emission is shown to be due to retired stellar populations by the WHAN classification. Both galaxies do show radio excess, and the 1.4 GHz imaging shows a complex morphology where the brightness of the eastern source traces the warped galactic disk, and is not particularly aligned with the western galaxy. This pair does have 6 GHz imaging, which shows a flat spectrum compact radio core coincident

with each stellar nucleus. However, both cores are barely detected above the background and thus could not be deconvolved in our imaging analysis. If these are unresolved radio point sources, they must be intrinsically low luminosity. We therefore cannot concretely designate this pair as dAGN. Interestingly, the eastern galaxy does show some faint evidence a second radio detection, perhaps a relic from a previous radio jet which is not aligned with the western galaxy.

4.2.4 2258+0030

This pair also has 6 GHz observations, clearly showing a compact steep spectrum core in the SW galaxy. While there is some scant hints of fragmented radio emission aligned between the two galaxies, there is no overlap with the NE galaxy. We cannot rule out that the radio excess observed for both components is not due to remnants of jets from the SW component; however, we note that the star-forming class NE galaxy shows one of the highest degrees of radio excess (>2 dex) among the kinematic pair sample, which would be unlikely to have been generated by the faint tail end of the nearby jet. In this case, the pair might constitute a dAGN where one pair is confirmed by a resolved radio core and the other is inferred by radio-excess. Interestingly, this pair is one of the few which pass the WISE AGN color selection, although we cannot discern if this is due solely to the one well detected radio core.

4.3 Imposters

In the remaining kinematic pairs, we discuss the evidence suggesting that one galaxy contains an AGN, and why we rule out the companion. It should be noted that all of our kinematic pairs contain at least one AGN, so our radio-selection technique does at least

yield a robust sample of single AGNs. In general, these pairs either show only one radio core, or are jetted imposters. After propagating the Hβ luminosities to estimate SFR, we note that 2229−0004NE and 2235+0003SE are the only galaxies in the remaining kinematic pairs to not exhibit radio excess, making high resolution radio imaging crucial to avoiding misdiagnosing the origin of the radio power. These pairs serve as an interesting comparison against the duals, especially in the incidence of prominent jets.

The systems 0142−0001, 0147−0008, 2235+0003, and 2303−0117 all exhibit one flat spectrum compact radio core, but without any radio detection for the companion galaxies. None of the galaxies in these pairs exhibit optical evidence of AGN, although this is an artifact of their high redshifts ($z > 0.45$). Each pair shows evidence of fragmented jet structure originating from the active nucleus, with positional alignment with their companion galaxies that gives the false impression of a secondary radio source at lower resolution. The seemingly one-sided jet in 2303−0117 appears to curve around, but not intersect with, its companion galaxy, perhaps as a relic of the orbital velocity as the galaxies make their first pericenter passage. In 0142−0001, there is a suspicious weakly-detected clump of pixels $\sim 3\sigma$ above the noise in the vicinity of the NW galaxy, but it does not have good degree of overlap with the stellar nucleus. We suspect that this weak signal is the back side of the luminous jet clearly seen protruding from the SE galaxy.

The pair in 0203−0033 is similar to the four jetted single AGNs discussed above, with the exception that the radio core in the NE galaxy shows a markedly steep spectral index, similar to those seen in the confirmed dAGN sample.

The galaxies in 2211+0027 and 2245+0058 do not have follow-up radio observations

at 6 GHz, and their high redshift puts the diagnostic optical emission lines out of observable range. However, these two pairs pass the WISE color selections of both Satyapal et al. (2017) and Jarrett et al. (2011), giving them the most convincing evidence in our sample of each harboring at least one IR AGN. High resolution radio imaging might reveal dAGN in these systems. We note that the lower resolution 1.4 GHz observations suggest two separate radio cores in 2211+0027, while there is obvious evidence of a large scale (>500 kpc) FR II jet aligned with the companion galaxy in 2245+0058.

As discussed in Fu et al. (2015a) only one galaxy in 0134−0107 is confirmed to have a radio core. While the northern galaxy does exhibit a prominent radio hotspot coincident with the optical and IR nuclei, it is most likely due to a FR II lobe emanating from the southern source, in line with the southern facing jet. Moreover, the northern hotspot is not spatially compact, and shows a spectral index similar to the southern jet. The optical properties of the sources do not conclusively suggest dAGN either. While the southern galaxy is definitively classified as a LINER, the northern galaxy is on the cusp of the composite-LINER division on the [N II] BPT diagram (and firmly within the LINER category on the [S II] diagram), which might suggest that it harbors a separate optical AGN despite the radio lobe overlap. However, both are well below the $EW_{H\alpha}$ cut as retired galaxies, discounting AGN origin of their nebular ionization. We therefore rule out this pair as a dAGN.

The remaining sources all show clear signs of well evolved FR II radio lobes from one flat spectrum core that overlap the nuclear region of their companion galaxy. We therefore cannot argue that the observed radio excess for the companion is due to a potential AGN therein. The high redshift of the 2229−0004 system prevents any emission-line analysis. The

2220+0058 system contains a LINER, but the WHAN designation of both galaxies as retired suggests against optical AGN classification. Similar evidence is seen for the 0152−0010 pair, although in this case the radio core and retired LINER nucleus are in different galaxies.

As is seen for these single AGNs in kinematic pairs, high redshift becomes a restriction not only on the availability of optical emission line information, but also the spatial scale of prominent radio jets in the lower resolution images during sample selection. We suggest strategies to mitigate these challenges moving forward in §6.

CHAPTER 5

PROPERTIES OF THE FINAL SAMPLE

We supplement our discussion of the full kinematic sample by examining the properties of the active nuclei and how they relate to their host galaxies. There are several outstanding questions in the field regarding AGN triggering and fueling. Chiefly, do mergers instigate higher levels of accretion onto the central black hole via tidal torques? For an "apples to apples" comparison, we look to the Eddington ratio, which gives a mass-scaled accretion rate. Similarly, how does the accretion rate for dual AGN compare to that of single AGN that are also in mergers?

The results from spectral fitting allow us to estimate several useful quantities: the stellar mass, the black hole mass, and thus the Eddington-scaled accretion rate for each galaxy, where there is sufficient data. In Table 5.1 we give the properties of the central SMBH in each galaxy.

5.1 Galactic Properties

Our sample contains 35 kinematic pairs totaling 70 galaxies. All of the confirmed dAGNs occur at separations below ∼10 kpc except for 2319+0038 which is much more widely separated. Spectral fitting was able to fit 68 of these galaxies, yielding several important galactic properties: the stellar mass and the stellar velocity dispersion. It is well established that there seems to be a connection between the growth of galactic bulges and the supermassive black holes within them in the local Universe (McConnell and Ma, 2013). Zheng et al. (2009) note that, while it appears that episodes of star formation occur in iso-

Table 5.1. Derived Optical Properties of the Kinematic Pairs

Optical Designation J2000 (5)	$M_\star$ $\log(M_\odot)$	$\sigma_\star$ (km(1)	$M_{\rm BH}$ (2)	$\log(\lambda)$ (3)	(4)
005113.93+002047.2	10.3	150.0*	7.9	-2.0	
005114.11+002049.4	10.5	173.78*	8.1	-2.4	
013412.78−010729.5	11.3	278.48	9.0	-3.3	
013412.84−010725.0	10.6	225.26	8.2	-3.1	
014203.08−000150.3	10.9	...	8.6	-2.8	
014203.24−000151.0	11.4	234.13	9.2	-2.4	
014715.86−000819.5	11.4	...	9.1	-2.9	
014715.94−000817.4	10.4	646.26	8.0	-0.6	
014928.38−001446.0	9.1	...	6.5	-1.5	
014928.41−001447.8	9.0	...	6.4	-1.6	
015253.79−001005.6	10.9	...	8.6	-3.5	
015253.92−001004.3	10.2	...	7.7	-3.3	
020301.40−003341.7	10.1	...	7.7	-1.3	
020301.43−003339.3	10.0	...	7.6	-1.0	
021021.00−005124.2	11.2	...	9.0	-3.2	
021021.13−005126.7	10.2	...	7.7	-2.0	
220634.97+000327.6	10.1	124.45*	7.6	-2.3	
220635.08+000323.3	10.4	180.03*	7.9	-2.2	
221142.42+002731.2	10.9	...	8.6	-1.9	
221142.51+002728.5	12.1	202.3	9.9	-2.5	
222051.55+005815.5	11.2	357.58	8.9	-2.6	
222051.70+005816.7	10.9	350.46	8.6	-2.1	
222907.53−000411.1	11.6	250.83	9.4	-2.7	
222907.77−000410.9	10.9	...	8.6	-2.2	
223222.41+001226.3	10.0	195.63*	7.5	-2.0	
223222.60+001224.7	10.2	170.51*	7.7	-2.2	
223546.28+000358.8	11.8	235.34	9.6	...	
223546.40+000358.7	11.4	280.15	9.2	...	
224426.44+001051.3	11.1	...	8.9	-2.4	
224426.61+001051.9	10.0	...	7.5	-0.9	
224532.53+005857.9	10.2	274.69	7.7	-0.9	
224532.68+005855.8	11.0	...	8.6	-1.6	
225222.52+010658.0	10.8	258.57	8.4	-2.3	
225222.65+010700.6	9.4	214.67	6.9	-1.8	
225817.73+003007.7	11.3	...	9.1	-3.7	
225817.97+003011.5	9.8	450.88	7.3	-1.3	
230010.18−000531.7	11.3	318.78*	9.1	-3.6	
230010.24−000534.0	11.4	347.85*	9.2	-3.6	
230342.74−011712.7	11.5	283.87	9.3	-3.1	
230342.91−011711.9	11.5	234.26	9.3	-2.9	
231953.31+003816.7	11.9	...	9.7	...	
231953.43+003813.4	12.0	...	9.8	...	

Every two rows is a pair, and sources are sorted in ascending R.A. (1) J2000 coordinate of the optical source; (2) merger component or isolated galaxy in a projected pair; (3) total stellar mass measured from modeling the optical spectrum with simple stellar populations; (4) intrinsic stellar velocity dispersion of the stellar populations, where the higher resolution SDSS spectra are marked with * (LRIS has a maximum resolution of ∼200 km s^{-1}, so we do not report values below this); (5) black hole mass inferred from the $M_{\rm BH} - M_\star$ relation of Kormendy and Ho (2013), which has an intrinsic scatter of ∼0.29 dex; (6) Eddington ratio, $\lambda = (L_{\rm rad} + L_{\rm mech})/L_{\rm Edd}$.

lated disks whereas black hole growth occurs in major mergers, there is a global coevolution observed between the two over cosmic time. It is therefore interesting to compare the stellar mass of the galaxies in our sample, especially those with confirmed AGN. We show the range of stellar masses in the middle panel of Figure 5.1.

The kinematic pairs are all hosted by massive galaxies ($9.0 < \log(M_\star/\mathrm{M}_\odot) < 12.0$), where there is a slight preference for the confirmed dAGNs to be at $\log(M_\star/\mathrm{M}_\odot) \sim 10$. In section §2.4.3 we calculated the SFR for the galaxies based on their Hα emission. We find that the dAGN hosting galaxies show modest SFR approaching (and in some cases just exceeding) Milky Way level ($0.08 < \mathrm{SFR}/\mathrm{M}_\odot\mathrm{yr}^{-1} < 1.26$), where H$\alpha$ is detectable. So even the composite type galaxies hosting dAGNs are not found to be at starburst levels of star formation. The rest of the kinematic pairs show a similar trend, although it is perhaps surprising that the range of SFR is even lower ($0.09 < \mathrm{SFR}/\mathrm{M}_\odot\mathrm{yr}^{-1} < 0.54$) considering that this subsample contains the majority of the star-forming type galaxies. Of course, slit-based spectroscopy does not isolate only the bulge of the galaxy, and so it is impossible to pinpoint where the active star-forming regions may reside, if even near the nuclear region at all. To address this, spatially-resolved spectroscopy utilizing integral field units would be necessary, although this would only be practical for the lowest redshift portion of the same due to spaxel angular-size constraints.

5.2 Black Hole Properties

With the derived stellar, radio, and optical properties of our kinematic sample, we re now able to address the question of accretion rate with some caveats. We begin by estimating the black hole mass for each galactic nucleus. Fu et al. (2015a) used the empirical relation of

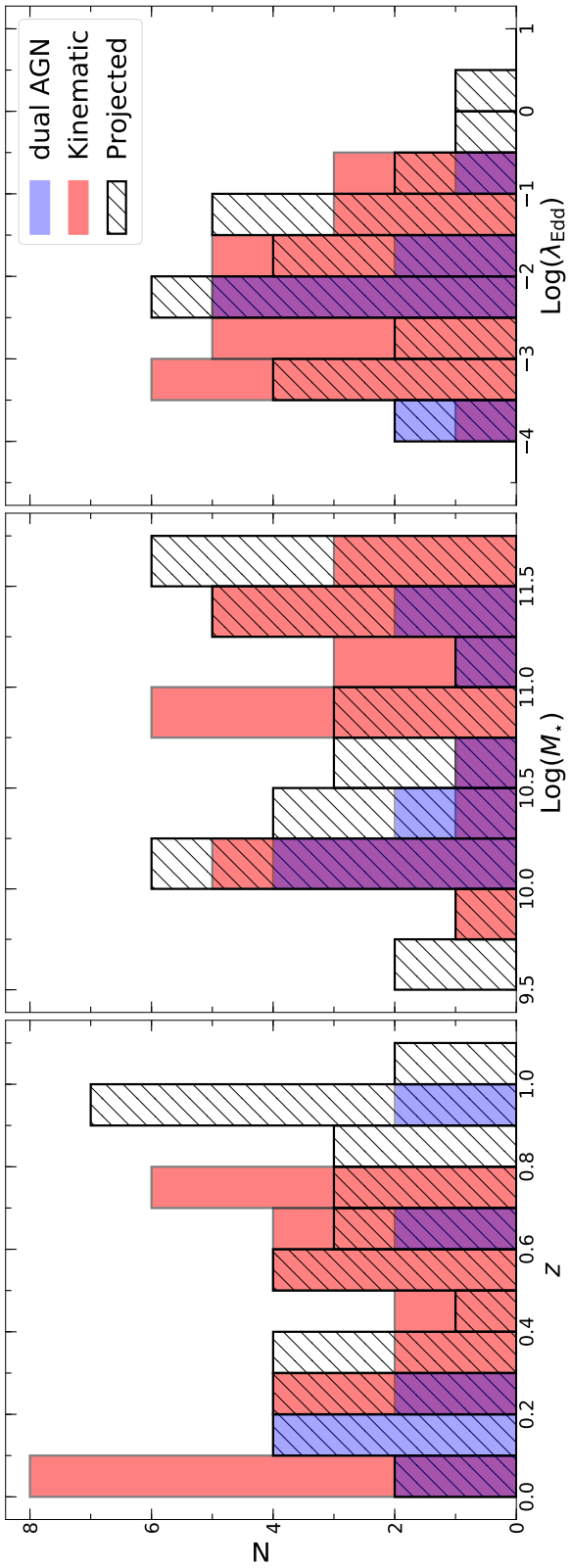

Figure 5.1. Histograms of redshift, stellar mass, and Eddington ratio. The kinematic pairs are presumed to be in galactic mergers, while the projected pairs are isolated galaxies. The confirmed dAGNs are not included in the tally of kinematic pairs for display purposes. The stellar masses are in units of $M_\odot$.

Kormendy and Ho (2013) between the black hole mass, $M_\bullet$, and the stellar velocity dispersion of the galactic bulge, $\sigma_\star$:

$$M_\bullet = 3.1 \times 10^8 \mathrm{M}_\odot (\sigma_\star / 200\,\mathrm{km\,s^{-1}})^{4.38}. \tag{5.1}$$

However, the pilot study utilized primarily archival spectra from SDSS. Our final kinematic sample is composed 86% of spectra from Keck LRIS, and as we noted above it has a resolution that limits our measurements of the velocity dispersion to $\sigma_\star \geq 200$ km s^{-1}. This in turn limits our ability to reliably measure $\sigma_\star$ for $\sim$43% of our galaxies in kinematic pairs, as can be seen by the swath of values we have excised from the third column of Table 5.1 due to artificially low measurements. The stellar velocity dispersion is measured by SPFIT by the widths of the absorption features of the composites spectral model. But because the estimate of the stellar mass is done using weighted sums of several spectral templates, it yields a more robust measurement of $M_\star$ than is achieved for $\sigma_\star$. We therefore choose to use the nearly flat stellar bulge mass relation of Kormendy and Ho (2013) (intrinsic scatter of 0.29 dex) to estimate the black hole mass:

$$\frac{M_\bullet}{10^9 \mathrm{M}_\odot} = (0.49^{+0.06}_{-0.05}) \left(\frac{M_{\mathrm{bulge}}}{10^{11} \mathrm{M}_\odot} \right)^{1.16 \pm 0.08}, \tag{5.2}$$

where we take the measured $M_\star$ as M_{bulge}.

To illustrate the difference in these two estimators, in Figure 5.2 we plot the results of one versus the other. For completeness, we include the galaxies in projected pairs (square points). It is immediately obvious that while the bulk of our galaxies yield $M_\bullet$ values around the one-to-one relation between the two techniques (dashed line), there is a substantial fraction of the population that falls below the minimum $M_\bullet$ measurable by the resolution

constraint (solid line) and is inaccessible using the $M_\bullet - \sigma_\star$ relation. Most of the confirmed dAGNs do follow the relation astoundingly well, but this is not really a fair comparison since the targets with higher resolution SDSS spectra have $\sigma_\star$ values that are predominantly lower than the LRIS limit. While only a few of the kinematic pair galaxies are above the dashed line, the few dAGNs below the relation would yield a gross underestimation of the black hole mass if we relied on the $M_\bullet - \sigma_\star$ relation.

A caveat to the $M_\star$-derived values is that the relation presumes that we are strictly using the stellar mass of the galactic bulge, and while the light profiles in the slit spectroscopy of our galaxies are dominated by their bulge components, we undoubtedly also capture some of the light from the stellar disk. While this is the prefered method for the sake of completeness, the choice to use $M_\bullet - \sigma_\star$ thus introduces some degree of overestimation. It is important to note that both of these techniques above are indirect inferences of the black hole mass through the stellar populations outside the black hole sphere of influence. The more direct and common approach would be a virial mass estimate via reverberation mapping based on the kinetic energy of the gas immediately around the black hole in the broad line region (typically by measuring Hβ) as it moves through the potential well of the central mass (Yong, Webster, and King, 2016). Generally, $M_\bullet = f\left(\frac{\Delta V^2 R}{G}\right)$, where ΔV is the velocity dispersion, $R = c\tau$ is the distance of the broad line region to the black hole (where τ is the time delay between changes in continuum emission and responses in line emission), G is the gravitational constant, and f is the virial coefficient that accounts for the geometry and kinematics of the system (Peterson and Wandel, 1999). Since our sample is almost exclusively composed of narrow-line (Type II) emission line systems, a virial estimate

of the black hole mass is not physically possible. We therefore adopt the $M_\bullet - M_{\rm bulge}$ relation values going forward.

We estimate the bolometric luminosity of each galactic nucleus as the sum of the radiative luminosity from nebular emission and the jet mechanical power. The jets and outflows caused by accretion onto compact objects like black holes generates mechanical feedback comparable to the radiative luminosity (Gallo et al., 2005; Justham and Schawinski, 2012). From the 1.4 GHz radio luminosity, we compute the luminosity supplied by the AGN jets using the relation from Cavagnolo et al. (2010):

$$L_{\rm mech} = 10^{43} {\rm erg\,s^{-1}} (L_{\rm 1.4GHz}/10^{24} {\rm W\,Hz^{-1}})^{0.7}. \tag{5.3}$$

Provided that the galaxy has observable [O III]λ5007 emission, we can similarly estimate the bolometric radiative luminosity of the AGN via an empirical scaling factor found by Heckman et al. (2004): $L_{\rm rad} = 3500 L_{\rm [O\,III]}$. We note that 5 galaxies in the kinematic pairs do not have observable [O III] emission, and thus cannot be used to infer a bolometric luminosity in this way. With the black hole mass estimates, the Eddington luminosity is:

$$L_{\rm Edd} = \frac{4\pi c G M_\bullet \mu m_p}{\sigma_T} = 1.26 \times 10^{38} M_\bullet / {\rm M_\odot\,erg\,s^{-1}}, \tag{5.4}$$

where c is the speed of light, G is the gravitational constant, μ is the mean molecular weight of the gas, m_p is the proton mass, and σ_T is the Thompson scattering cross section for electrons (Frank, King, and Raine, 2002). This reduces to the right hand side where the multiplicative factor assumes pure Hydrogen gas. We calculate the Eddington-scaled black hole accretion via the Eddington ratio, λ:

$$\lambda = (L_{\rm rad} + L_{\rm mech})/L_{\rm Edd}. \tag{5.5}$$

The accretion rate $\dot{M}$ required to reach the Eddington limit is then:

$$\dot{M}_{\rm Edd} = (L_{\rm Edd}/(\eta c^2), \tag{5.6}$$

where η is the efficiency of converting mass to luminosity, usually taken to be $\sim$10% (Netzer, 2013). The mass accretion rate can likewise be scaled per unit mass of the black hole, such that the normalized accretion rate:

$$\dot{m} = \frac{\dot{M}}{\dot{M}_{\rm Edd}} = \frac{\eta \dot{M} c^2}{L_{\rm Edd}}, \tag{5.7}$$

however, the Eddington ratio is more commonly quoted as a proxy for the accretion rate.

We calculate the Eddington ratios for our sample and find the range for the dAGNs to be $-3.6 < \log(\lambda) < -0.9$, although all but one of these (2244+0010 NE) have $\log(\lambda) < -2.0$ implying low levels of accretion. This is consistent with the picture found by Gross et al. (2019) that the majority of these dAGNs host LLAGNs. This also fits with the observed pattern of radio-LLAGNs in LERGs (Best and Heckman, 2012). The single AGNs in kinematic pairs (ignoring those with misattributed radio power) run a similarly wide range of accretion rates ($-3.7 < \log(\lambda) < -0.9$), with considerably more scatter. The upper range of the singles is seen to approach $\sim$10% of the Eddington limit, as expected for quasars, and indeed the majority of the HERGS are found to have values > -2.0. We see a similar distribution among the black holes in the projected pair sample, with a median value of $\log(\lambda) \sim -2.0$; however, without follow-up radio imaging of these pairs, it is impossible to say which sources are producing radio lobes that overlap their projected counterpart galaxies. We can conclude, however, that there appears to be no bias towards higher levels of accretion for dAGNs in mergers as compared to AGNs in isolated galaxies.

We can also use the redshift and black hole masses of our sample to estimate the level of X-ray activity expected for AGN. Merloni, Heinz, and Matteo (2005) found that active black holes follow a fundamental plane across many orders of magnitude relating X-ray luminosity, mass, and radio luminosity:

$$L_{\rm R} = (0.60^{+0.11}_{-0.11}) \log(L_{\rm X}) + (0.78^{+0.11}_{-0.09}) \log(M) + 7.33^{+4.05}_{-4.07}, \tag{5.8}$$

where the monochromatic radio luminosity is taken at 5 GHz, and the X-ray luminosity is taken in the band of 2−10 keV. The relation has a substantial degree of scatter ($\sigma_{\rm R} = 0.88$), and so our estimates here are purely speculative. What's more, the scatter in this relation has recently been shown to be dependent not just on redshift, but also on the degree of radio-loudness or -quietness of the AGN (Bariuan et al., 2022). We scale the radio luminosity at 5 GHz from 1.4 GHz assuming a power law relation and a spectral index $\alpha = -0.7$, typical for radio AGN and representative of the synchrotron dominated sources in our dAGN sample. Plotting our kinematic pair galaxies along this relation, we find that the would be expected to emit a range of X-ray luminosities, $41 < \log(L_{2-10\ \rm keV}/\rm ergs^{-1}) < 48$. The archival data points from Kellermann et al. (1989) and Merloni, Heinz, and Matteo (2005) give context that our sample indeed covers a broad range of activity, from LLAGNs to quasars. It is interesting to note that the two new pairs of dAGNs are at the upper range of the relation, counter to the trend of the previously confirmed dAGNs, perhaps reflective of higher accretion state at the higher redshift. As suggested by (Bariuan et al., 2022), we would expect the majority of our sample to a slight offset above this relation, such that our $L_{\rm X}$ is likely overestimated.

We overlay the observed $L_{\rm X}$ values from Gross et al. (2019) for the pilot sample of

dAGNs in Fu et al. (2015a), shown with the cyan symbols. Several of these sources were only marginally detected, yielding upper-limit estimates of the $L_{\rm X}$. As noted above, the small sample of dAGNs was found to exhibit low column density, and thus the low level of X-ray flux is intrinsic to those AGNs, categorizing them as LLAGN. We do see that 5/8 lie above the fundamental plane, indicating a slight enhancement of the radio activity, although all points are within the scatter of the relation. The newly confirmed dAGNs are comparatively more powerful objects, occupying the upper range of the relation among the archival QSOs. We would expect these objects to exhibit strong X-ray signatures if they were to be observed with *Chandra*, placing them at the higher ends of the $L_{12\mu\rm m}$ and $L_{\rm [OIII]}$ X-ray relations shown in Gross et al. (2019). Many of the single AGNs in kinematic pairs should also be imminently observable in X-ray, although their higher degree of activity might be masked by greater amounts of obscuration.

5.3 Sample Success Rate

With our final sample of rigorously confirmed AGN in kinematic pairs, we examine the success rate of our rigorous sample selection strategy via the fraction of dual AGN out of the kinematic sample. Note that this is not the same as a calculation of the dAGN duty cycle, which we address in §6.3. We find conclusive evidence for dAGNs in 24% (5/21) of the pairs based primarily on the radio morphology. If we include the compelling multi-wavelength evidence for 2244+0107, this becomes 29%. If we further include the 4 tentative pairs in §4.2, this fraction increases to nearly half the sample (10/21). We further note that for the 17 pairs observed at 6 GHz, every single pair shows evidence of at least one radio AGN core. Of these individual high resolution galaxies then, 68% (23/34) harbor an AGN, with 12/34

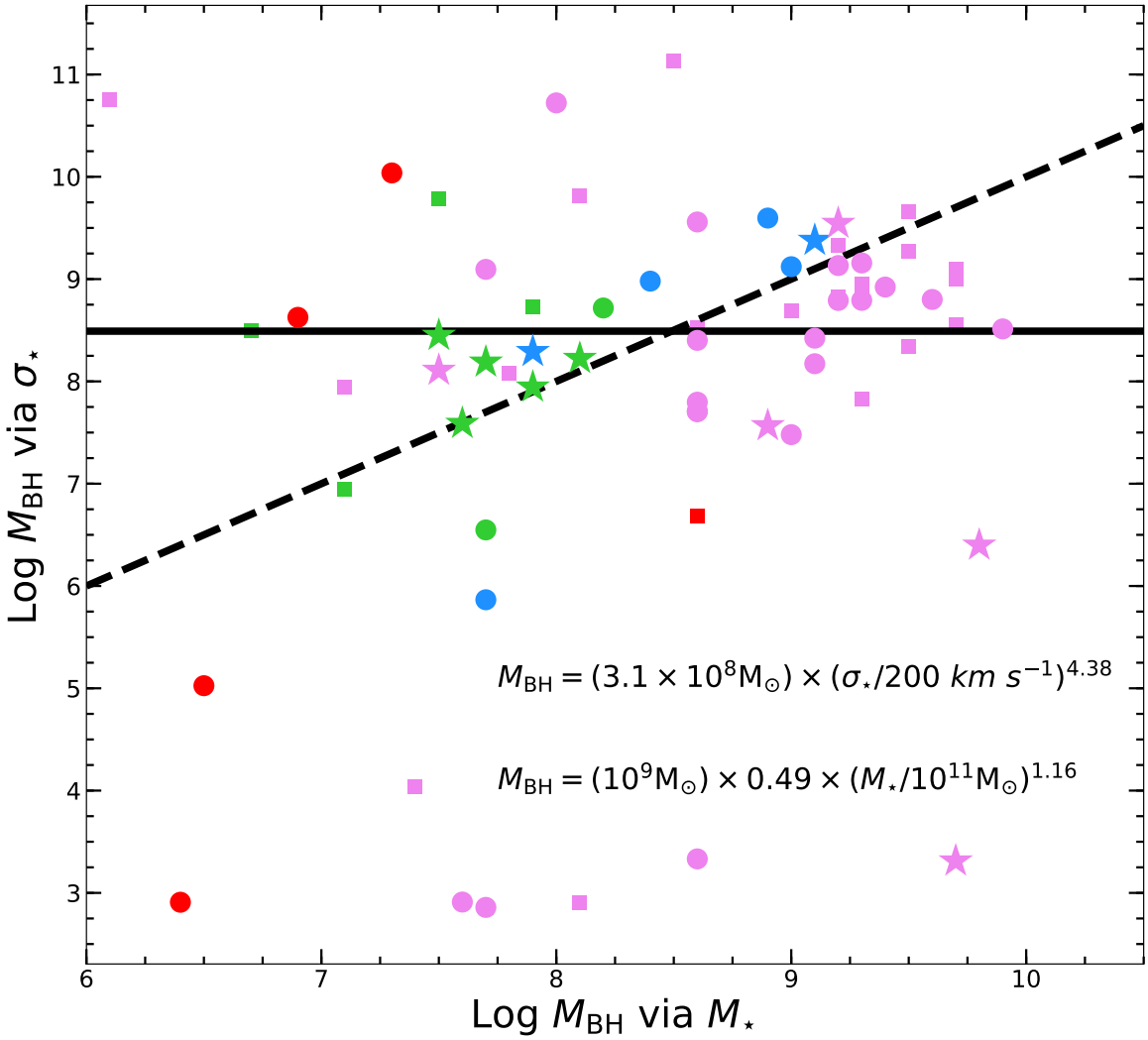

Figure 5.2. Black Hole Mass Estimators from (Kormendy and Ho, 2013). The equations for for both scalings are given. A one-to-one relation is shown with a dashed line. The solid line gives the cutoff for the resolution limit of LRIS, below which $\sigma_\star$ is oversampled and thus unreliable. Projected pairs are given by squares.

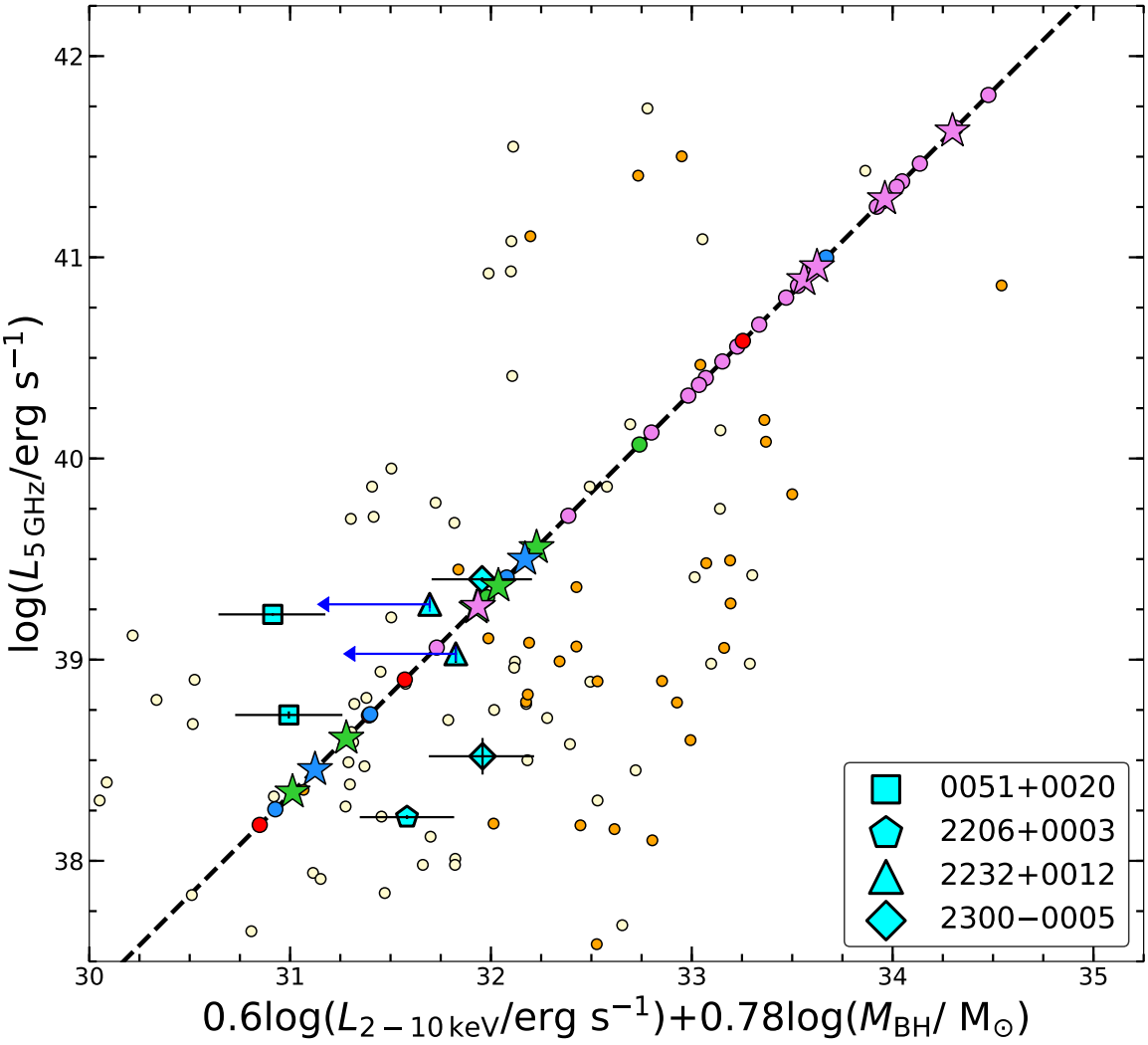

Figure 5.3. Black hole fundamental plane of activity of Merloni, Heinz, and Matteo (2005). We estimate the expected X-ray luminosity of our kinematic pair sample using the relation in equation 5.8. Determining whether our galaxies lie directly on the plane given by the dashed line requires direct measurements of the X-ray flux. However, the actual positions of the points could suggest which mode of activity our AGN are in. We show archival samples of AGN in yellow points from Merloni, Heinz, and Matteo (2005) and orange points from Kellermann et al. (1989) for a comparison. We expect that most of our sample would lie above the relation since the majority are classified as radio-loud. We plot the data for the 4 confirmed dAGNs from Gross et al. (2019), shown with the cyan symbols where arrows indicate upper limits due to X-ray non-detections. 5 of these AGNs (one is below the range shown here) are indeed above the fundamental plane as a result of their intrinsically low L_{X}.

being part of dual systems and 11/34 being single AGNs in galaxies belonging to kinematic pairs. Gathering together all of these lines of evidence (conservatively counting the two systems with only WISE AGN status as containing one AGN each), the total tally of AGN, single or dual, in galaxies undergoing mergers is then 69% (29/42) (or 74% depending on whether the two radio pairs in §4.2 are considered dAGNs). Of these, ∼31% likely are single AGN in mergers (13/42), or in the context of galaxy pairs, 62% (13/21) of the kinematic pairs host only one AGN. We quote our final dual AGN success rate as 6 dual systems out of 21 kinematic pairs, or a success rate of 29%. The success rate implies that given a similarly selected sample, with similar depth and spectroscopic data availability, we would expect nearly one third of the subsequent kinematic pairs to harbor dAGNs. This success rate can be improved using additional pre-selection criteria, which we investigate in the following chapter.

CHAPTER 6

PROSPECTS FOR FUTURE SAMPLES

Finally, we finish our discussion with perspectives on our sample selection technique. We address the shortcomings of the original selection strategy, focusing on the optical magnitudes from the VS82 survey. We then propose guidance for future large surveys of dAGNs to more efficiently preselect dAGN at a higher success rate.

6.1 Optical Colors

In selecting which sources from our parent sample would be observed to obtain optical spectroscopy, we employed a magnitude cut of $r < 23.4$ AB. This was done to ensure that observations of faint sources could achieve a minimum $S/N_{cont} \geq 3$ during a maximum observation time of 60 minutes, given the large number of targets in the observing program. While this magnitude cut is motivated by feasibility concerns, it also helps to select brighter galaxies that might be nearer by in the Universe. Closer proximity is desirable because at higher redshifts the signatures of radio hot spots from lobes and jets are less resolved and thus more easily confused with actual galactic cores, leading to a higher rate of projected pairs being observed in the initial sample selection phase. As we found in §2.2.1, our sample shows a wide range of redshifts, and as we have noted throughout the text this hampers our ability to comprehensively evaluate our sample.

We give the redshift distribution for the various sub-samples in the first panel of Figure 5.1. The distribution is illustrated more continuously in Figures 6.1 and 6.2, which plot the optical colors and r-band apparent magnitudes, m_r, of the sources. In these plots

we show the full sample from the optical spectroscopy including the projected pairs, the redshifts of which were hitherto unknown. The sample shows a wide range of $g-r$ and $r-i$ colors an m_r. At a glance, we see that all but one kinematic pair galaxy at $z < 0.4$ has $m_r < 20$ in Figure 6.1, which essentilly tells us lower redshift correlates to brighter fluxes and thus lower apparent magnitude. This is true for 3 of the 4 dAGNs in that redshift range (*n.b.*, 231953.31+003816.7 does not have g-band data, and so is not able to be plotted). The color magnitude diagram has traditionally been used as a valuable diagnostic tool to separate the galaxies belonging to the so-called blue cloud of star-forming galaxies from the quenched population along the red sequence, while a distinctive region between them (the green valley) has been shown to be heavily populated by AGN (Bell et al., 2004). The usual form of the color magnitude diagram samples the bluer color-space of NUV, and uses absolute magnitudes. However, for diagnostic purposes it is more relevant to determine patterns based on the readily available optical bands from SDSS, and use the apparent magnitudes which do not require prior knowledge of the redshifts of potential targets. Within this modified color-magnitude plot, we can still see that the dAGN are relatively isolated toward higher apparent magnitude and tend toward bluer color. While not shown, we did also plot against absolute magnitude. As expected the dAGNs occupy a region that straddles the red and blue loci in what would be the green valley equivalent for this color-space tending toward the blue cloud, which is unsurprising given that most of these galaxies are BPT composite types. Note also that the two new dAGNs at much higher redshift would fall in this bluer region after applying a K-correction to the optical bandpasses to account for the redshift. For the color-color diagram in Figure 6.2, lower redshift ($z < 0.5$) pairs appear to cluster blueward

of $r - i \sim 1.0$. In both diagrams there is a much larger spread in the $g - r$ color dimension, though nearly all lower z galaxies have $g - r < 2.0$. This is consistent with the distribution seen in the full parent sample from the VS82 radio and optical cross-matched catalog, shown as the underlying gray points. A distinctive break between two separate vertical branches apparently splits the the sample into two stellar populations around $r - i \sim 1.0$.

We investigate the redshift evolution of galaxy colors to illuminate possible trends using known spectral energy distributions (SEDs). We use the template spectra of Ilbert et al. (2008) and Salvato et al. (2008) which are a subset of the library from Polletta et al. (2007) of *XMM Newton* SEDs of sources in the COSMOS field. These templates cover a wide wavelength range from UV to IR. The SEDs give a full suite of galaxy types including QSOs, Which we show in Figure 6.3. The flux is rescaled to arbitrary units to show the full compliment of templates. We highlight three archetypal diagnostic SEDs which have the most extreme changes in slope for a given type: elliptical, starburst, and QSO. We smooth the templates (overlying black lines) to a resolution of 200Å. This is done as an *ad hoc* correction to account for the ∼1000Å width of the photometric bands. We sample the magnitudes of the smoothed SEDs at the nominal locations of the photometric bands (vertical dashed lines) at redshift intervals of 0.1 and compute the colors for each. The resulting trends are shown in Figure 6.4. The same diagnostic SEDs are shown highlighted, where the individual points give the colors at each redshift interval. We also do this for the rest of the SEDs (shown in fainter colors) to illustrate the fairly smooth evolution between the various classes of galaxies. In general, the red-orange templates are for QSO and extreme starburst SEDs, which connect to the star-forming and elliptical SEDs shown green-blue.

It is well known that QSOs occupy bluer color spaces than elliptical and starburst galaxies (e.g., Richards et al., 2002, and references therein); however the wide range of redshifts of QSOs, as well as potential broad emission line contribution, introduces variations in the observed colors that begin to mimic the latter (Siemiginowska et al., 1995). The QSO colors do not change much as a function of redshift, tending towards a locus of $g - r \sim 0.0$ and $r - i \sim 0.2$. The elliptical galaxies show a more dramatic redshift evolution, reddening substantially in both colors by $z \sim 0.5$. A similar, but less dramatic trend is seen in the starburst galaxies. This sharp horizontal shift corresponds to the apparent gap in the SDSS sample in Figure 6.2. This pattern is thus informative as to the behavior of higher redshift galaxies. To obtain a promising sample of potential active galaxy pairs, we suggest a selection cut at $r-i < 0.8$, which should drastically limit the sample to $z \leq 0.5$, regardless of whether the galaxies are star-forming or elliptical. Employing this cut on the full sample, we recover 62% (18/29) of the galaxies below the redshift threshold, excluding the four galaxies which are at low redshift but lack $r - i$ color data. Out of the full sample with $r - i$ data, this represents 30% (18/60). A more lenient cut of $r-i < 0.9$ only adds one additional low-redshift source while also including 4 additional high-redshift sources, thus lowering the success rate. As noted by Peters et al. (2015), no color-color cut can efficiently include all AGN while simultaneously excluding star-forming galaxies. Based on the SED trends, this color cut will have a slight bias towards selecting lower redshift ellipticals than starbursts. However, the cut does not constrain the redshift of QSOs, which tend to get bluer at higher redshift. This is not especially an issue for a similarly radio-selected sample, however, which we would expect to be dominated by radio-mode AGN as opposed to quasar-mode as shown in our sample.

We do note, however, that the color cut misses our most well-established dAGN, 0051+0020, which has $r-i$ colors significantly redder than any of our mock SED trends. This is an effect of the redshifted strong emission lines in its spectra, which cross into the i-band and yield a noticeably redder color index. We therefore suggest that $1.50 \lesssim r-i \lesssim 2.13$ is occupied by galaxies with strong emission lines that have been redshifted to $0.095 \lesssim z \lesssim 0.248$, and so would also be worthwhile to preselect.

Similar to the color cut above, we can suggest a cut for the r-band apparent magnitude at $m_r < 20$, which would give a selection rate of 31% for the galaxies in our full sample which have r-band data (19/61), where all but one of these galaxies is at $z < 0.5$. Note that this cut misses the 11 galaxies in the sample that are at $z < 0.5$, but lack r-band data. Combining the two cuts would only yield 11 galaxies at low redshift that have r and i-band data. By number, the two cuts yield comparable success rates for selecting low-z galaxies.

6.2 VLASS

Our suggested color cut can be used as a preselection criterion for forthcoming large-area surveys. For example, the Very Large Array Sky Survey (VLASS) began observations in 2017 and will finish its third and final pass in 2024 (Lacy et al., 2020). With observations covering the entire sky north of $\delta > 40^\circ$, the 33,885 deg^2 coverage will overlap entirely with the 14,555 deg^2 of the SDSS imaging survey, including the $\sim$ 300 deg^2 region of Stripe 82. Only 92 deg^2 of Stripe 82 was covered by the VS82 radio imaging campaign, thus the imaging provided by VLASS can fill in the remaining $\sim$210 deg^2 of Stripe 82. We note that this additional 200% area of overlap increase from VLASS will not have equivalent sensitivity ($\sim 70\mu$Jy/beam) or resolution ($2.5''$) to the VS82 survey (52 μJy/beam; $1.8''$). However, this

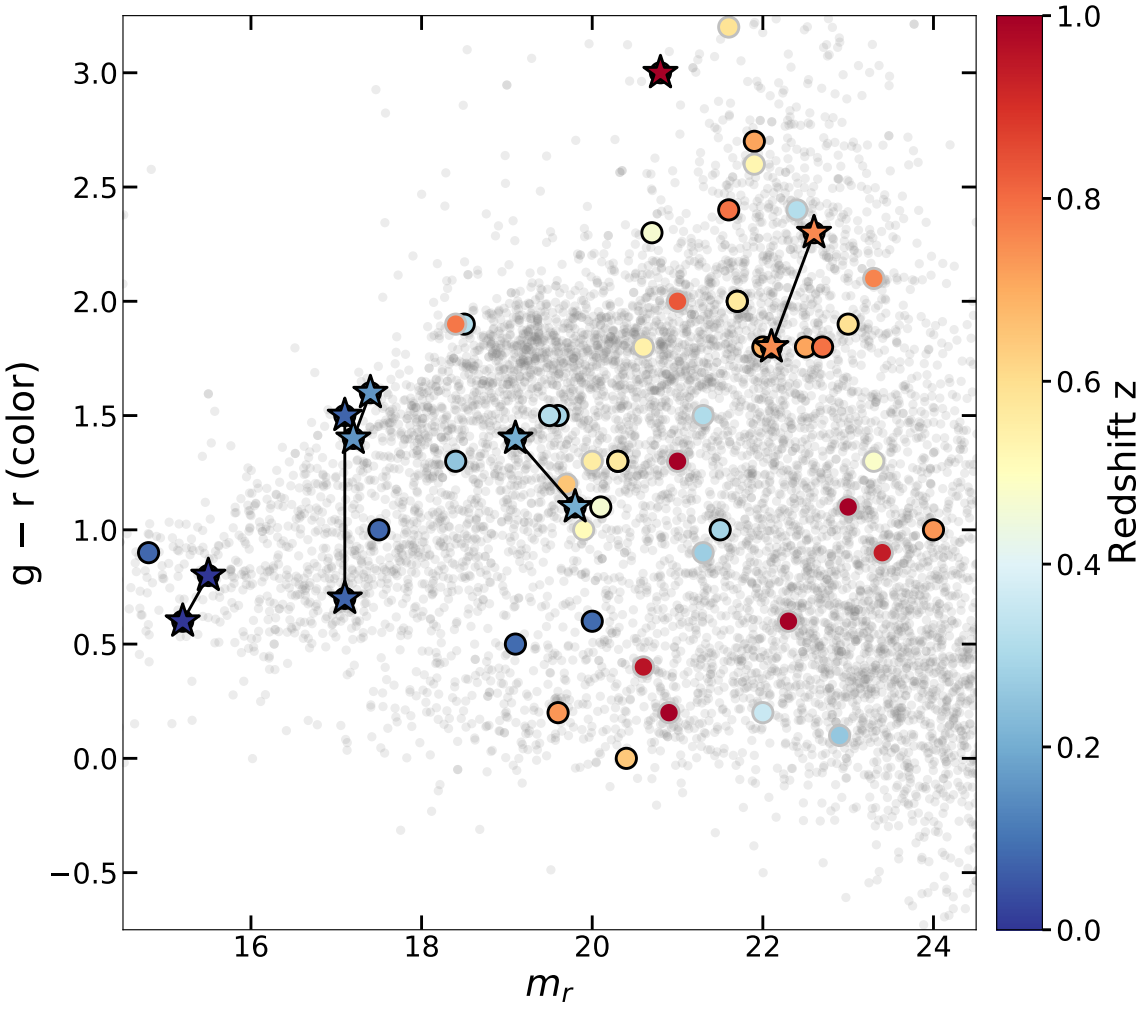

Figure 6.1. Optical color-magnitude diagram for the spectroscopically confirmed pair sample using optical magnitudes from (Jiang et al., 2014). Lines connect the confirmed dAGNs (stars), and the rest of the kinematic pairs have black outlines. Since we use this plot as a pre-selection strategy, we also plot the projected pairs (gray outlines) since we would not know their redshifts *a priori*. A cut at apparent magnitude $m_r < 20.0$ would preferentially select galaxies at redshift $z < 0.5$.

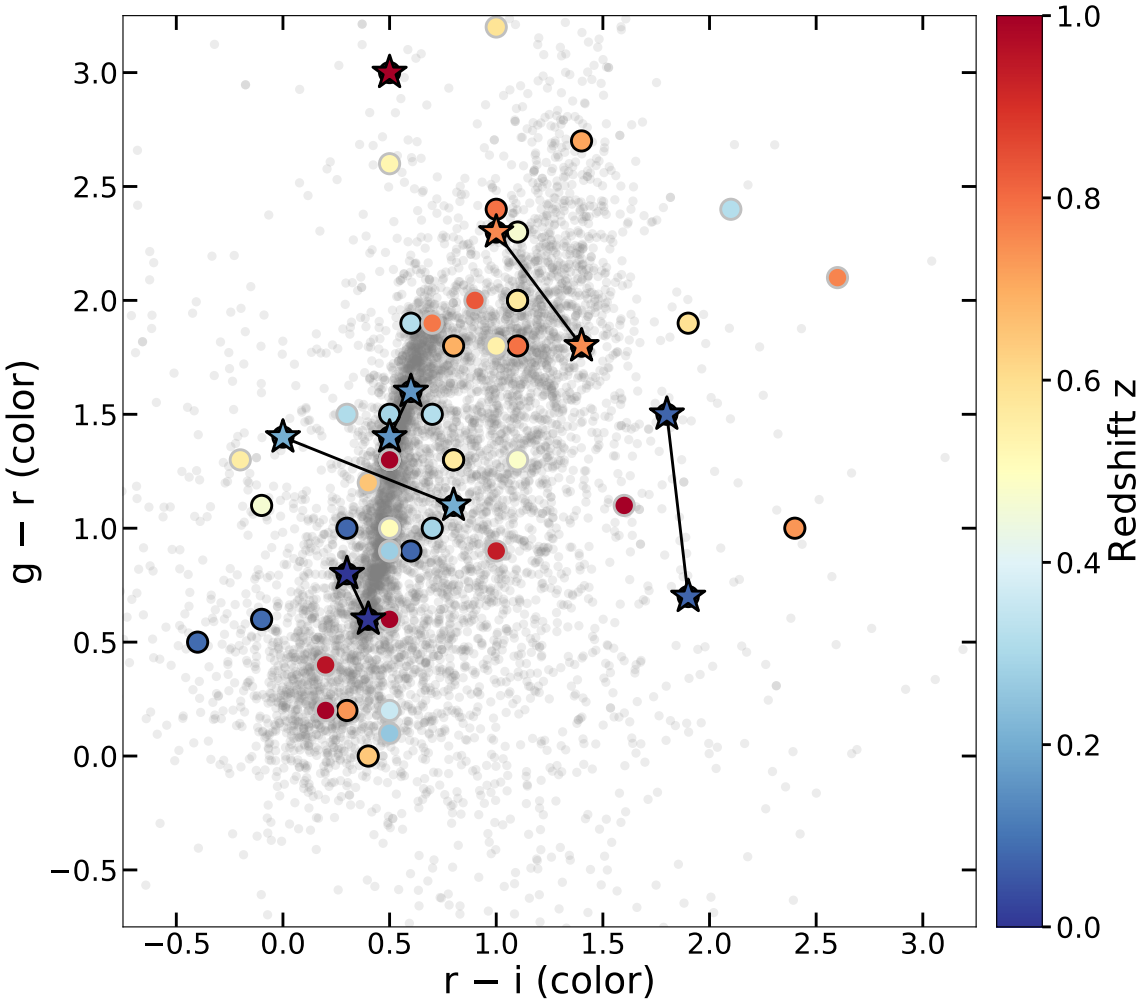

Figure 6.2. Optical color-color diagram for the spectroscopically confirmed pair sample. The same labelling convention is used as in Figure 6.1. Although there are exceptions, a pre-selection strategy employing a color cut drawn at $r - i = 0.8$ would yield predominantly low-redshift ($z < 0.5$) pairs that have larger angular area and thus would yield fewer jet-aligned pairs via lower resolution radio imaging. Note that most of the lower-redshift galaxies follow the left-hand vertical track likely associated with star-forming galaxies.

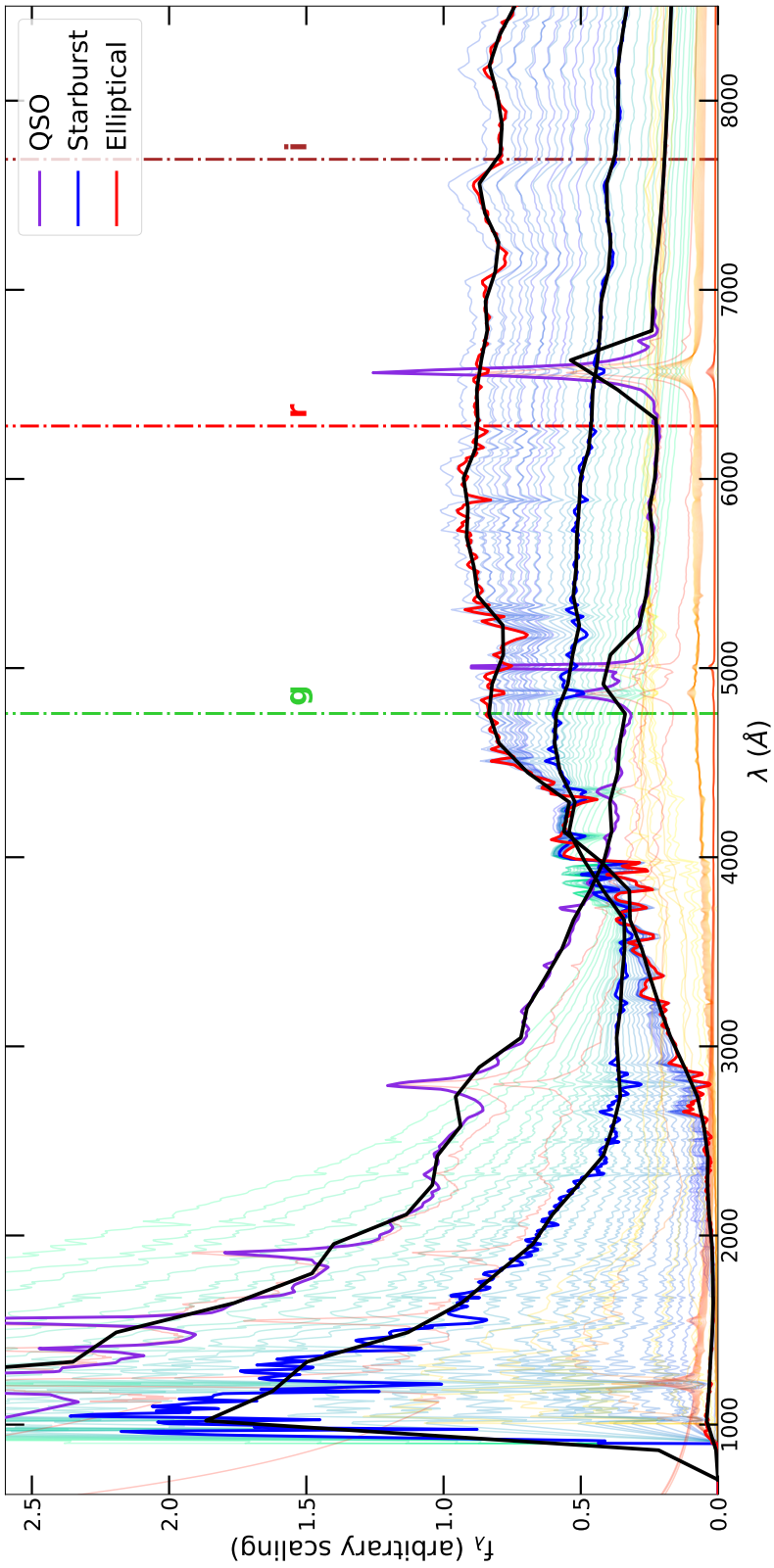

Figure 6.3. Spectral templates drawn from Ilbert et al. (2008) and Salvato et al. (2008). We show a wide range of early and late type galaxies, as well as QSOs. The colors for a given template are taken at the nominal locations of the bands marked by vertical dot-dashed lines, extracted from the black lines which are smoothed to resolutions of 200 Å. We redshift the templates and re-extract magnitudes to obtain the redshift evolutions shown in Figure 6.4.

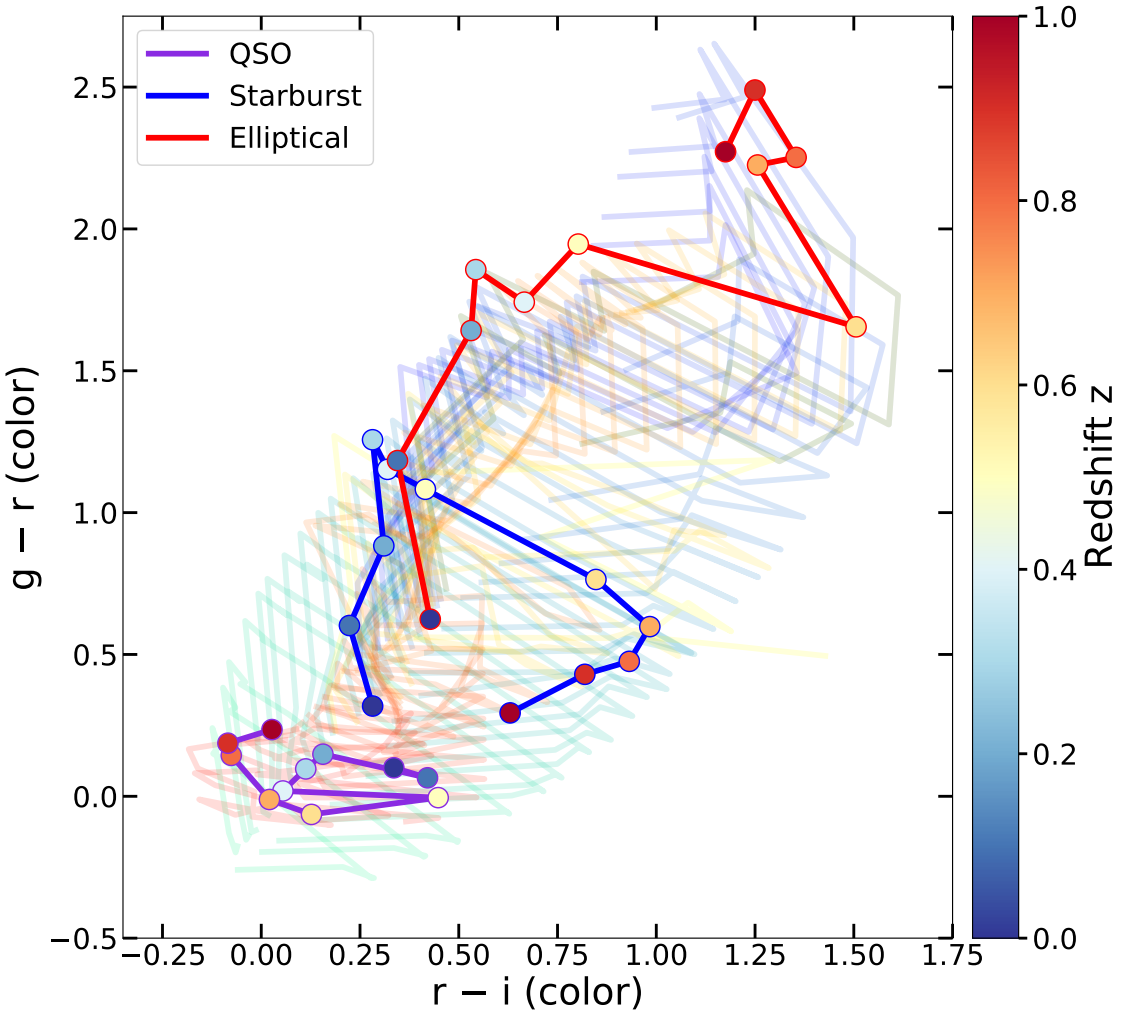

Figure 6.4. models of redshift evolution of the color-color space for different galaxy classes, at z intervals of 0.1. We highlight 3 distinct tracks (drawn from Figure 6.3) which show patterns of differing redshift dependence. QSO spectra are not particularly susceptible to changes in observed colors, while late-type galaxies show a strong dependence on redshift with an abrupt reddening at $z \sim 0.5$.

is a significant improvement over previous all-sky radio surveys, such as the Faint Images of the Radio Sky at Twenty cm (FIRST) survey, which only achieved angular resolution of 5″at a sensitivity of 150μJy/beam (Becker, White, and Helfand, 1995). The resolution of VLASS is sufficient to identify a substantial number of dAGNs at low-z with modest separations. For example, at a redshift of $z = 0.5$, VLASS should be able to resolve dAGN at physical separations down to ∼34 kpc. In order to resolve dAGNs at a scale of 10 kpc, the redshift limit for VLASS then becomes only z ∼1.8. While 33% of our kinematic pairs are below this redshift, two of these would not be resolved.

We can get a rough estimate of the number of sources expected in Stripe 82 from cross-matching VLASS targets with SDSS co-added images based on the matching results in Fu et al. (2015b). Of the 17,969 radio sources in the VS82 catalog, 62% were found to have optical matches. Of these, 83 pairs were found with reliable radio source separations within 5″, 52 of which were classified as Grade A and B, where 11 of these are below the angular resolution limit of VLASS. Assuming a similar rate of matching for the remaining area of Stripe 82 and taking into account the poorer angular resolution, we would thus expect an additional $\sim$ 90 such pairs to be found with VLASS. Given our final census of dAGNs, we might therefore expect to find 10 additional dAGN pairs using similar 0.3″radio imaging follow-up and optical spectroscopy.

Gordon et al. (2021) give first results for the whole area of VLASS using the quicklook image catalog produced after the second pass. They note that the quality of VLASS imaging products is well suited for a wide area search for dAGN, where AGN with radio lobes will be visible out to $z \sim 0.5$. Our suggested optical color cut would be a complimentary preselection

strategy to constrain the radio detections to this redshift, enabling an assessment of jet/lobe overlap with companion galaxies. The factor of ∼160 increase in area of the entire SDSS imaging survey over the VS82 region would yield an estimated >6,500 *resolvable* pairs designated as Grades A and B using our selection scheme. However, the coverage of SDSS outside Stripe 82 has ∼2 mag shallower observations compared to the co-added catalog of Jiang et al. (2014), lessening the number of optically faint detections. However, the r-band magnitude cut suggested above would still be well above this threshold, so we can estimate that the number of pairs that would be selected to be at low redshift. 25% of the grade A and B pairs would pass this cut, yielding ∼1600 new pairs from VLASS. If we ease the restriction so that only one galaxy in the pair needs to pass the cut, this number increases to ∼2500 new pairs. Again propagating this through the dAGN success rate of our sample, this upper limit should result in ∼300 dAGNs. This would be a substantial addition to the known dAGN population, effectively quadrupling it. Such a sample would finally make it possible to address the question of merger-induced synchronized accretion in a statistically rigorous fashion, making it a worthwhile endeavor for the astronomical community.

6.3 DAGN Duty Cycle

As ongoing work for the near future, we plan to calculate the duty cycle of dAGN activity. As we have discussed throughout this work, there are multiple channels through which AGN might be triggered. It is assumed that AGN in isolated galaxies accrete via stochastic processes in the absence of tidal torques from an ensuing merger. Stochastic accretion at a level given by the Eddington ratio (λ, as defined in §5.2) of $\log(\lambda) \sim -3.9$ results in an estimated ∼1% duty cycle for isolated AGN at $z < 0.5$ (Shankar, Weinberg,

and Miralda-Escudé, 2008). The rate of both SMBHs in a pair of merging galaxies being synchronously accreting stochastically is then this rate squared: 0.01%. We note that roughly half our kinematic pairs are at redshifts $z \geq 0.5$. Once we have calculated our observed duty cycle of synchronized black hole activity in mergers, we can compare against the expected rate to test whether the act of the merger does in fact play an important role in triggering AGN. Specifically, two non-stochastic effects might be at play. Merger-induced effects might facilitate the building of the central gas reservoir necessary to activate a SMBH. However, this need not lead to synchronized black hole accretion where the chance of one galaxy being activated is intrinsically linked to the fate of the companion galaxy. This latter scenario is encapsulated in the correlated AGN fraction, ξ (as defined in Fu et al., 2018), which converts single AGN in pairs to dAGN due to correlated activities. This fraction is zero in the event of random pairing (*i.e.*, chance simultaneous stochastic accretion in both galaxies in a pair).

To address the question of duty cycle and correlated dAGN, we must construct several fractions based on volume densities derived from our sample. The fraction of dual AGNs in our sample can be stated as:

$$f_{\rm d} = \frac{n_{\rm dAGN}}{n_{\rm pairs}}, \tag{6.1}$$

where the volume densities n are the number of dAGNs and galaxy pairs per Mpc^3 within the same comoving volume of the 92 deg^2 of the VS82 field. We can obtain a reasonable estimate for $n_{\rm dAGN}$ under the assumption that out of all of the grade A and B pairs identified from the ∼11,000 radio/optical galaxies in the area of the VS82 survey, we have rigorously identified nearly all dAGN systems down to the imposed magnitude limit. However, we must keep in mind that of the 21 kinematic pairs identified, we only have *VLA* follow-up observations for

17 systems. As was demonstrated above, this follow is crucial to refuting the possibility of overlapping jets which invalidate the evidence for dual AGN by radio-excess. This scenario may be the case for some of the remaining 4 systems without follow-up radio imaging, so we can scale the observed $n_{\rm dAGN}$ as $\frac{6}{17}\times 21$ to obtain a reasonable estimate for the complete number density of dAGNs in VS82.

Obtaining an estimate for $n_{\rm pairs}$ within the magnitude range of our sample requires knowledge of the luminosity function, $\Phi(\mathcal{M})$, where $\mathcal{M}$ is the absolute magnitude (in r-band, say) within the Petrosian radius. The number density of galaxies within the magnitude limit $\mathcal{M}_{\rm min} - \mathcal{M}_{\rm max}$ set by our sample of dAGNs is then:

$$n(\mathcal{M}_{\rm min}, \mathcal{M}_{\rm max}) = \int_{\mathcal{M}_{\rm min}}^{\mathcal{M}_{\rm max}} \Phi(\mathcal{M})\, d\mathcal{M}. \tag{6.2}$$

The luminosity function has been empirically determined for the highly spectroscopically complete Galaxy And Mass Assembly (GAMA) survey (Baldry et al., 2012), which serves as a useful analog for the VS82 region. However, this simplistic iteration of the luminosity function applies only to single field galaxies. Computing the volume density of pairs would thus require knowledge of the pair fraction (which itself depends on stellar mass since more massive galaxies are found in cluster environments) in addition to the volume density of galaxies (given by the luminosity function). Robotham et al. (2014) have addressed this complication using the GAMA-II sample. They determine an analytical form of the stellar mass function of close pairs (CP; with stellar masses M_1 and M_2) as a multiplicative single power law Schechter function:

$$\Phi_{\rm CP}(M_1, M_2) \equiv \frac{\partial^2 n}{\partial M_1 \partial M_2} = {\rm e}^{-(M_1+M_2)/M^*_{\rm CP}} \left[\phi^*_{\rm CP} \left(\frac{M_1}{M^*_{\rm CP}}\right)^{\alpha_{\rm CP}} \phi^*_{\rm CP} \left(\frac{M_2}{M^*_{\rm CP}}\right)^{\alpha_{\rm CP}}\right], \tag{6.3}$$

where $M^*_{\rm CP}$ is the Schechter function knee for the 2D close pair distribution, $\phi^*_{\rm CP}$ is the normalization, and $\alpha_{\rm CP}$ is the low-mass slope. The galaxy stellar mass function is analogous to the luminosity function since the luminosity of galaxies is related to the stellar mass via an assumed mass-to-light ratio (based on g and i photometric bands):

$$\log(M/L_i) = a + b(g - i), \tag{6.4}$$

where M is the stellar mass and L_i is the luminosity in solar units, and the fitted parameters a and b are determined empirically (Baldry et al., 2012). Robotham et al. (2014) report best-fit parameters from fitting the GAMA-II data within three dynamical ranges of projected separation of velocity separation. For our sample, the sensible choice is to use the parameters resulting from the fit assuming $r_{\rm sep}$=20 kpc/h and $v_{\rm sep}$= 500 km/s. These parameters are: $M^*_{\rm CP} = 10^{11.12}/{\rm M}_\odot$, $\phi^*_{\rm CP}$ = 0.0162 / $\rm h^3 Mpc^{-1}$, and $\alpha_{\rm CP}$ = -0.92 (Robotham et al., 2014). Plugging these into the close pair stellar mass function, we can then estimate $n_{\rm pairs}$.

To compute the duty cycle, we also need an analogous estimate for the fraction of *single* AGNs (sAGNs) in galaxy pairs for the VS82 region:

$$f_{\rm s} = \frac{n_{\rm sAGN}}{n_{\rm pairs}}. \tag{6.5}$$

At a glance, we might expect to similarly depend on the number of single AGNs in mergers uncovered by our Keck and VLA observations. But since all of the follow-up observations were of radio-preselected targets, our observed single AGNs are already biased to host radio-AGN. To obtain the general volume density of single AGNs in mergers, we can begin by calculating the fraction of galaxies in the parent sample that are in mergers. The parent sample here is the 92 $\rm deg^2$ area of the VS82 survey region. We can use the SDSS photometric

catalogs to find the number of galaxies in pairs (within $5''$ separation) with spectroscopic data from SDSS dr10 spectroscopic survey (with $\sim$30 kpc projected separation). We will implement additional criteria, such as a redshift cut matched to the range of our dAGN sample, and the r-band magnitude difference between the galaxies in a pair (to ensure that we select major mergers, in which galaxies tend to have similar magnitudes by the mass-to-light-ratio relation).

As noted by Fu et al. (2018), the SDSS spectroscopic targets suffer from incompleteness for the secondary components due to fiber collisions. While the primary galaxies in closely spaced pairs likely attain 98.6% spectroscopic completeness, only $\sim$30% of the secondary galaxies are likely covered through subsequent overlapping fields. Thus, the spectroscopic completeness for all paired galaxies in the SDSS survey is $\sim$64% ((98.6+30)/(100+100)). This incompleteness was not necessary to account for in the duty cycle calculation of Fu et al. (2015a), since all sources in their computation were drawn from SDSS spectra and thus suffered from the same spectroscopic incompleteness. The same is true here if we re-estimate $n_{\rm pairs}$ from the same parent sample. This is essentially the first steps of our original sample selection anyway, but with the added restrictions of data availability from the SDSS spectroscopic survey and our redshift and separation cuts. For reference, the three SDSS dAGNs studied in Fu et al. (2015a) had a redshift range of $0.005 < z < 0.2$, a range which yielded 13 AGNs (determined using BPT and radio-excess diagnostics) from the SDSS specobj catalog that met the matching pair-selection criteria. These 13 radio AGNs included the 3 dAGNs, such that $N_{\rm AGN} = N_{\rm sAGN} + N_{\rm dAGN}$. The corresponding selection for galaxy pairs yielded 215 optical pairs that need not have radio matches (which would likely correspond to radio AGN).

The general AGN duty cycle is then $N_{\rm AGN}/{\rm N}_{\rm pairs} = 13/215$ ∼6%, while the dAGN duty cycle is $N_{\rm dAGN}/N_{\rm AGN} = 3/13$ ∼23%. Over the same comoving volume of the VS82 region, the duty cycle for synchronized black hole accretion can be recast as: $\mathcal{F}_{\rm dAGN} = f_{\rm d}/(f_{\rm d} + f_{\rm s})$. Similarly, the duty cycle for AGN in general can be framed simply as: $\mathcal{F}_{\rm AGN} = f_{\rm d} + f_{\rm s}$. It is these duty cycles which we will compare against the predicted rate for stochastic fueling.

These corrected numbers of pair, single AGNs, and dAGNs will also allow us to estimate the lifetimes for single and synchronized AGN activity ($\tau_{\rm s}$ and $\tau_{\rm d}$, respectively). The dynamical friction timescale, $\tau_{\rm dyn}$, during which a major merger would be observable as a galaxy pair, can be used to estimate the AGN lifetimes via the Chandrasekhar formula (assuming typical values for separation, velocity separation, and stellar mass) (Foreman, Volonteri, and Dotti, 2009). Following Fu et al. (2015a), the corresponding timescales can be estimated as: $\tau_{\rm s} = \tau_{\rm dyn} \times \mathcal{F}_{\rm AGN} \times (1 + \mathcal{F}_{\rm dAGN})/2$, and $\tau_{\rm d} = \tau_{\rm dyn} \times \mathcal{F}_{\rm AGN} \times \mathcal{F}_{\rm dAGN}$. Once again as a reference, the values obtained using the sample in Fu et al. (2015a) corresponded to $\tau_{\rm s}$ ∼3.7 Myr and $\tau_{\rm d}$ ∼1.4 Myr. With twice the number of dAGNs in our now complete sample, we will be able to more securely compute these lifetimes. Lastly, we can use a similar procedure to that outlined in Fu et al. (2018) and Steffen et al. 2022 (*in prep.*) to delineate the relative contributions to dAGN fueling by merger-induced (which could instigate single and dual AGNs) and correlated AGN (ξ) effects. The combination of these effects on the number densities of dual and single AGNs results in a system of equations with an unknown parameter for merger-induced and correlated activity each. With our corrected fractions $f_{\rm s}$ and $f_{\rm d}$, we will be able to solve this system of equations for our sample to elucidate the degree to which these effects contribute. We can then finally compare these

values with predictions from merger simulations. Hydrodynamical simulations predict that a major merger at separations <10 kpc can be observed as a dual AGN ∼16% of the time (Wassenhove et al., 2012). Cosmological simulations using the Horizon-AGN simulation have also suggested that most dual AGNs can found at separations <30 kpc can be linked to ensuing galaxy mergers (Volonteri et al., 2021), which fits with the separations of all our dAGNs. Having corrected duty cycles for our sample will enable us to compare against the paradigm expected from simulations such as these.

CHAPTER 7

CONCLUSIONS

We now summarize the key findings of our rigorous multiwavelength analysis in search of dual AGN activity in merging galaxies. Throughout this text, we have studied in detail the majority of the remaining grade A and B sample of candidate dAGNs from Fu et al. (2015b). Optical spectroscopy has yielded well-constrained redshifts for the sample, and has revealed that of the 35 pairs observed overall, 21 are found to be kinematic pairs with consistent redshifts. The other 14 are projected pairs along the line of sight, and thus constitute isolated systems. Spectral fitting offers some indications of low ionization optical AGN activity. Many of the kinematic pairs are classified as LINERS and AGN/star-forming composite systems; however, we find that conclusive BPT classification for many of our pairs is significantly hampered by the high redshifts ($z \geq 0.47$) for over half of the sample. The low level of ionization is found by the WHAN analysis to be more accurately attributed to old stellar populations than AGN for most of the LINERs, while the composite systems are mostly verified as having strong AGN contribution. We use the Hα emission to calculate the SFRs, and project that the observed radio power is generally in excess by over 10$\times$ the expected value for star-formation alone, highly suggestive of AGN contribution to the radio flux for the bulk of our pairs.

We utilize higher resolution radio imaging to weed imposters where one radio jet may be superimposed on its companion galaxy, giving the false attribution of radio-excess in both. Our 6 GHz *VLA* radio imaging follow-up campaign of 17 kinematic pairs reveals

that 6 (4 previously known and 2 newly discovered) are indeed *bona fide* dual AGN systems with separate radio core emission. One of these pairs (2319+0038) is at a significantly higher redshift ($z \sim 0.9$), and is more widely separated than the others (sep$\sim$30 kpc). Most of the dAGNs show compact cores with spectral indices indicating synchrotron emission, likely from young small scale jets. We will subsequently calculate the duty cycle of dAGNs in our sample, correcting for observational biases, to test whether merger-induced or correlated black hole accretion is higher than predictions from models of stochastically triggered accretion. In our radio-selected sample, mergers do seem to play some role in triggering simultaneous black hole accretion, but predominantly at lower accretion levels consistent with radio mode LERGs.

At the very least, our radio-selected pairs suggest the presence of at least one AGN in each galaxy, whether by radio-excess, BPT class, MIR color, or radio imaging. We can thus conjecture that despite the elusiveness of observing simultaneous accretion, mergers make it consistently possible and likely that we would observe at least one AGN in the pair active at kiloparsec-scale separations. The remaining 11 kinematic pairs with radio follow-up show a mix of morphologies that suggest the presence of only one AGN in each system. Many pairs have obvious FR II radio lobes or extended FR I jets originating from one galaxy but are aligned with their companion galaxies which gives the false impression of two separate radio cores at lower angular resolution. This is another complication in the sample selection arising from the high redshift, and thus limited spatial resolution, of the kinematic pairs.

We therefore propose optical cuts for future wide-area surveys based on the lessons learned from our campaign, which should preferentially select galaxies at lower redshifts. A

cut at $r - i < 0.8$ preferentially selects galaxies below ~ 0.5 (corresponding to a separation of 34 kpc for our most closely spaced dual), which would enable complete BPT optical classification. An r-band magnitude cut at $m_r < 20.0$ would likely achieve a similar redshift selection and may be more accessible since it does not require data for two photometric bands. We add this pre-selection criterion to our sample selection strategy outlined in Fu et al. (2015b) to increase the success rate, with the expectation that it could yield a sizable population of dAGNs from future and ongoing radio surveys, as high as 300 new dAGNs from VLASS. In this way, the Stripe 82 field has served as a pilot study for such all-sky surveys, maximizing the future prospect of acquiring a much needed statistical sample of dAGNs while balancing the efficiency of a comprehensive and rigorous effort using state of the art multiwavelength follow-up techniques.

This work was supported in part by the National Science Foundation (NSF) grants AST-1614326 and AST-2103251.

BIBLIOGRAPHY

Abazajian, Kevork N. et al. (June 2009). "The Seventh Data Release of the Sloan Digital Sky Survey". In: 182.2, pp. 543–558. DOI: 10.1088/0067-0049/182/2/543. arXiv: 0812.0649 [astro-ph].

Ahn, Christopher P. et al. (Apr. 2014). "The Tenth Data Release of the Sloan Digital Sky Survey: First Spectroscopic Data from the SDSS-III Apache Point Observatory Galactic Evolution Experiment". In: 211.2, 17, p. 17. DOI: 10.1088/0067-0049/211/2/17. arXiv: 1307.7735 [astro-ph.IM].

Appenzeller, JImmo (2012). *Introduction to Astronomical Spectroscopy*. Cambridge University Press.

Baade, W. and R. Minkowski (Jan. 1954). "Identification of the Radio Sources in Cassiopeia, Cygnus A, and Puppis A." In: 119, p. 206. DOI: 10.1086/145812.

Balbus, Steven A. and John F. Hawley (July 1991). "A Powerful Local Shear Instability in Weakly Magnetized Disks. I. Linear Analysis". In: 376, p. 214. DOI: 10.1086/170270.

Baldry, I. K. et al. (Mar. 2012). "Galaxy And Mass Assembly (GAMA): the galaxy stellar mass function at z ¡ 0.06". In: 421.1, pp. 621–634. DOI: 10.1111/j.1365-2966.2012.20340.x. arXiv: 1111.5707 [astro-ph.CO].

Baldwin, J. A., M. M. Phillips, and R. Terlevich (Feb. 1981). "Classification parameters for the emission-line spectra of extragalactic objects." In: *Publications of the Astronomical Society of the Pacific* 93, pp. 5–19. DOI: 10.1086/130766.

Ballo, L. et al. (2004). "Arp 299: A Second Merging System with Two Active Nuclei?" In: *The Astrophysical Journal* 600.2, pp. 634–639. DOI: 10.1086/379887. URL: https://doi.org/10.1086/379887.

Bannikova, E. Yu et al. (May 2021). "Dynamical model of an obscuring clumpy torus in AGNs - I. Velocity and velocity dispersion maps for interpretation of ALMA observations". In: 503.1, pp. 1459–1472. DOI: 10.1093/mnras/stab468. arXiv: 2102.12130 [astro-ph.GA].

Bariuan, Luis Gabriel C. et al. (Jan. 2022). "The Fundamental Planes of Black Hole Activity for Radio-Loud and Radio-Quiet Quasars". In: *arXiv e-prints*, arXiv:2201.04666, arXiv:2201.04666. arXiv: 2201.04666 [astro-ph.HE].

Barnes, Joshua E. and Lars E. Hernquist (Apr. 1991). "Fueling Starburst Galaxies with Gas-rich Mergers". In: *Astrophysical Journal Letters* 370, p. L65. DOI: 10.1086/185978.

Becker, Robert H., Richard L. White, and David J. Helfand (Sept. 1995). "The FIRST Survey: Faint Images of the Radio Sky at Twenty Centimeters". In: 450, p. 559. DOI: 10.1086/176166.

Bell, Eric F. et al. (June 2004). "Nearly 5000 Distant Early-Type Galaxies in COMBO-17: A Red Sequence and Its Evolution since z~1". In: 608.2, pp. 752–767. DOI: 10.1086/420778. arXiv: astro-ph/0303394 [astro-ph].

Best, P. N. and T. M. Heckman (Apr. 2012). "On the fundamental dichotomy in the local radio-AGN population: accretion, evolution and host galaxy properties". In: *Monthly Notices of the Royal Astronomical Society* 421.2, pp. 1569–1582. DOI: 10.1111/j.1365-2966.2012.20414.x. arXiv: 1201.2397 [astro-ph.CO].

Bianchi, Stefano et al. (Mar. 2008). "Chandra unveils a binary active galactic nucleus in Mrk 463". In: *Monthly Notices of the Royal Astronomical Society* 386.1, pp. 105–110. ISSN: 0035-8711. DOI: 10.1111/j.1365-2966.2008.13078.x. eprint: https://academic.oup.com/mnras/article-pdf/386/1/105/2995475/mnras0386-0105.pdf. URL: https://doi.org/10.1111/j.1365-2966.2008.13078.x.

Blandford, R. D. and M. J. Rees (Dec. 1974). "A "twin-exhaust" model for double radio sources." In: 169, pp. 395–415. DOI: 10.1093/mnras/169.3.395.

Blandford, R. D. and R. L. Znajek (May 1977). "Electromagnetic extraction of energy from Kerr black holes." In: 179, pp. 433–456. DOI: 10.1093/mnras/179.3.433.

Blecha, Laura, Abraham Loeb, and Ramesh Narayan (Jan. 2013). "Double-peaked narrow-line signatures of dual supermassive black holes in galaxy merger simulations". In: *Monthly Notices of the Royal Astronomical Society* 429.3, pp. 2594–2616. ISSN: 0035-8711. DOI: 10.1093/mnras/sts533. eprint: https://academic.oup.com/mnras/article-pdf/429/3/2594/3286393/sts533.pdf. URL: https://doi.org/10.1093/mnras/sts533.

Blecha, Laura et al. (Oct. 2012). "Constraints on the nature of CID-42: recoil kick or supermassive black hole pair?" In: *Monthly Notices of the Royal Astronomical Society* 428.2, pp. 1341–1350. ISSN: 0035-8711. DOI: 10.1093/mnras/sts114. eprint: https://academic.oup.com/mnras/article-pdf/428/2/1341/3232851/sts114.pdf. URL: https://doi.org/10.1093/mnras/sts114.

Bondi, M. et al. (2016). "Unveiling the radio counterparts of two binary AGN candidates: J1108+0659 and J1131-0204". In: *Astronomy and Astrophysics* 588, A102. DOI: 10.1051/0004-6361/201528021. URL: https://doi.org/10.1051/0004-6361/201528021.

Brassington, Nicola J., Trevor J. Ponman, and Andrew M. Read (May 2007). "The Chandra view of galaxy mergers". In: *Monthly Notices of the Royal Astronomical Society* 377.4, pp. 1439–1456. ISSN: 0035-8711. DOI: 10.1111/j.1365-2966.2007.11763.x. eprint: https://academic.oup.com/mnras/article-pdf/377/4/1439/3792838/mnras0377-1439.pdf. URL: https://doi.org/10.1111/j.1365-2966.2007.11763.x.

Burbidge, E. Margaret (Jan. 1967). "Quasi-Stellar Objects". In: 5, p. 399. DOI: 10.1146/annurev.aa.05.090167.002151.

Buton, C. et al. (Jan. 2013). "Atmospheric extinction properties above Mauna Kea from the Nearby SuperNova Factory spectro-photometric data set". In: *Annual Review of Astronomy and Astrophysics* 549, A8, A8. DOI: 10.1051/0004-6361/201219834. arXiv: 1210.2619 [astro-ph.IM].

Buttiglione, S. et al. (2010). "An optical spectroscopic survey of the 3CR sample of radio galaxies with z< 0.3* - II. Spectroscopic classes and accretion modes in radio-loud AGN". In: *A&A* 509, A6. DOI: 10.1051/0004-6361/200913290. URL: https://doi.org/10.1051/0004-6361/200913290.

Calzetti, Daniela et al. (Apr. 2000). "The Dust Content and Opacity of Actively Star-forming Galaxies". In: *Astrophysical Journal* 533.2, pp. 682–695. DOI: 10.1086/308692. arXiv: astro-ph/9911459 [astro-ph].

Capelo, Pedro R. and Massimo Dotti (Nov. 2016a). "Shocks and angular momentum flips: a different path to feeding the nuclear regions of merging galaxies". In: *Monthly Notices of the Royal Astronomical Society* 465.3, pp. 2643–2653. ISSN: 0035-8711. DOI: 10.1093/mnras/stw2872. eprint: https://academic.oup.com/mnras/article-pdf/465/3/2643/8420196/stw2872.pdf. URL: https://doi.org/10.1093/mnras/stw2872.

— (Nov. 2016b). "Shocks and angular momentum flips: a different path to feeding the nuclear regions of merging galaxies". In: *Monthly Notices of the Royal Astronomical Society* 465.3, pp. 2643–2653. ISSN: 0035-8711. DOI: 10.1093/mnras/stw2872. eprint: https://academic.oup.com/mnras/article-pdf/465/3/2643/8420196/stw2872.pdf. URL: https://doi.org/10.1093/mnras/stw2872.

Capelo, Pedro R. et al. (Aug. 2017). "A survey of dual active galactic nuclei in simulations of galaxy mergers: frequency and properties". In: 469.4, pp. 4437–4454. DOI: 10.1093/mnras/stx1067. arXiv: 1611.09244 [astro-ph.GA].

Cappellari, Michele and Eric Emsellem (Feb. 2004). "Parametric Recovery of Line-of-Sight Velocity Distributions from Absorption-Line Spectra of Galaxies via Penalized Likelihood". In: *Publications of the Astronomical Society of the Pacific* 116.816, pp. 138–147. DOI: 10.1086/381875. arXiv: astro-ph/0312201 [astro-ph].

Cardelli, Jason A., Geoffrey C. Clayton, and John S. Mathis (Oct. 1989). "The Relationship between Infrared, Optical, and Ultraviolet Extinction". In: *Astrophysical Journal* 345, p. 245. DOI: 10.1086/167900.

Cavagnolo, K. W. et al. (Sept. 2010). "A Relationship Between AGN Jet Power and Radio Power". In: *Astrophysical Journal* 720.2, pp. 1066–1072. DOI: 10.1088/0004-637X/720/2/1066. arXiv: 1006.5699 [astro-ph.CO].

Cenarro, A. J. et al. (Sept. 2001). "Empirical calibration of the near-infrared Ca ii triplet - I. The stellar library and index definition". In: 326.3, pp. 959–980. DOI: 10.1046/j.1365-8711.2001.04688.x. arXiv: astro-ph/0109157 [astro-ph].

Cid Fernandes, R. et al. (May 2011). "A comprehensive classification of galaxies in the Sloan Digital Sky Survey: how to tell true from fake AGN?" In: *Monthly Notices of the Royal Astronomical Society* 413.3, pp. 1687–1699. DOI: 10.1111/j.1365-2966.2011.18244.x. arXiv: 1012.4426 [astro-ph.CO].

Comerford, Julia M. et al. (June 2009). "Inspiralling Supermassive Black Holes: A New Signpost for Galaxy Mergers". In: *Astrophysical Journal* 698.1, pp. 956–965. DOI: 10.1088/0004-637X/698/1/956. arXiv: 0810.3235 [astro-ph].

Comerford, Julia M. et al. (2011). "CHANDRA OBSERVATIONS OF A 1.9 kpc SEPARATION DOUBLE X-RAY SOURCE IN A CANDIDATE DUAL ACTIVE GALACTIC NUCLEUS GALAXY AT z = 0.16". In: *The Astrophysical Journal* 737.1, p. L19. DOI: 10.1088/2041-8205/737/1/l19. URL: https://doi.org/10.1088/2041-8205/737/1/l19.

Comerford, Julia M. et al. (2015). "MERGER-DRIVEN FUELING OF ACTIVE GALACTIC NUCLEI: SIX DUAL AND OF AGNs DISCOVERED WITHCHANDRAANDHUBBLE SPACE TELESCOPEOBSERVATIONS". In: *The Astrophysical Journal* 806.2, p. 219. DOI: 10.1088/0004-637x/806/2/219. URL: https://doi.org/10.1088/0004-637x/806/2/219.

Condon, J. J. (Feb. 1997). "Errors in Elliptical Gaussian Fits". In: *Publications of the Astronomical Society of the Pacific* 109, pp. 166–172. DOI: 10.1086/133871.

Condon, James J. and Scott M. Ransom (2016). *Essential Radio Astronomy*.

Connor, Thomas et al. (Dec. 2019). "X-Ray Observations of a z $\sim$ 6.2 Quasar/Galaxy Merger". In: 887.2, 171, p. 171. DOI: 10.3847/1538-4357/ab5585. arXiv: 1909.08619 [astro-ph.GA].

De Rosa, Alessandra et al. (Dec. 2019). "The quest for dual and binary supermassive black holes: A multi-messenger view". In: 86, 101525, p. 101525. DOI: 10.1016/j.newar.2020.101525. arXiv: 2001.06293 [astro-ph.GA].

Deane, R. P. et al. (2014). "A close-pair binary in a distant triple supermassive black hole system". In: *Nature* 511.7507, pp. 57–60. DOI: 10.1038/nature13454. URL: https://doi.org/10.1038/nature13454.

Di Matteo, Tiziana, Volker Springel, and Lars Hernquist (Feb. 2005). "Energy input from quasars regulates the growth and activity of black holes and their host galaxies". In: *Nature* 433.7026, pp. 604–607. DOI: 10.1038/nature03335. arXiv: astro-ph/0502199 [astro-ph].

Ellison, Sara L. et al. (Dec. 2011). "Galaxy pairs in the Sloan Digital Sky Survey – IV. Interactions trigger active galactic nuclei". In: *Monthly Notices of the Royal Astronomical Society* 418.3, pp. 2043–2053. ISSN: 0035-8711. DOI: 10.1111/j.1365-2966.2011.19624.x. eprint: https://academic.oup.com/mnras/article-pdf/418/3/2043/18449261/mnras0418-2043.pdf. URL: https://doi.org/10.1111/j.1365-2966.2011.19624.x.

Ellison, Sara L. et al. (May 2017). "Discovery of a dual active galactic nucleus with 8 kpc separation". In: *Monthly Notices of the Royal Astronomical Society: Letters* 470.1, pp. L49–L53. ISSN: 1745-3925. DOI: 10.1093/mnrasl/slx076. eprint: https://academic.oup.com/mnrasl/article-pdf/470/1/L49/17722036/slx076.pdf. URL: https://doi.org/10.1093/mnrasl/slx076.

Fabbiano, G. et al. (Sept. 2011). "A close nuclear black-hole pair in the spiral galaxy NGC3393". In: *Nature* 477.7365, pp. 431–434. DOI: 10.1038/nature10364. arXiv: 1109.0483 [astro-ph.CO].

Falcke, H., E. Körding, and S. Markoff (Feb. 2004). "A scheme to unify low-power accreting black holes. Jet-dominated accretion flows and the radio/X-ray correlation". In: 414, pp. 895–903. DOI: 10.1051/0004-6361:20031683. arXiv: astro-ph/0305335 [astro-ph].

Fanaroff, B. L. and J. M. Riley (May 1974). "The morphology of extragalactic radio sources of high and low luminosity". In: *Monthly Notices of the Royal Astronomical Society* 167, 31P–36P. DOI: 10.1093/mnras/167.1.31P.

Fath, Edward Arthur (Jan. 1909). "The spectra of some spiral nebulae and globular star clusters". In: *Lick Observatory Bulletin* 149, pp. 71–77. DOI: 10.5479/ADS/bib/1909LicOB.5.71F.

Foord, Adi et al. (Mar. 2020). "A Second Look at 12 Candidate Dual AGNs Using BAYMAX". In: 892.1, 29, p. 29. DOI: 10.3847/1538-4357/ab72fa. arXiv: 2002.01033 [astro-ph.HE].

Foreman, G., M. Volonteri, and M. Dotti (Mar. 2009). "Double Quasars: Probes of Black Hole Scaling Relationships and Merger Scenarios". In: 693.2, pp. 1554–1562. DOI: 10.1088/0004-637X/693/2/1554. arXiv: 0812.1569 [astro-ph].

Frank, Juhan, Andrew King, and Derek J. Raine (2002). *Accretion Power in Astrophysics: Third Edition*. Cambridge University Press.

Fu, Hai et al. (Oct. 2011a). "A Kiloparsec-scale Binary Active Galactic Nucleus Confirmed by the Expanded Very Large Array". In: *Astrophysical Journal Letters* 740.2, L44, p. L44. DOI: 10.1088/2041-8205/740/2/L44. arXiv: 1109.0008 [astro-ph.CO].

Fu, Hai et al. (June 2011b). "Mergers in Double-peaked [O III] Active Galactic Nuclei". In: *Astrophysical Journal* 733.2, 103, p. 103. DOI: 10.1088/0004-637X/733/2/103. arXiv: 1009.0767 [astro-ph.CO].

Fu, Hai et al. (2011). "THE NATURE OF DOUBLE-PEAKED [O III] ACTIVE GALACTIC NUCLEI". In: *The Astrophysical Journal* 745.1, p. 67. DOI: 10.1088/0004-637x/745/1/67. URL: https://doi.org/10.1088/0004-637x/745/1/67.

Fu, Hai et al. (Dec. 2015a). "Binary Active Galactic Nuclei in Stripe 82: Constraints on Synchronized Black Hole Accretion in Major Mergers". In: *Astrophysical Journal Letters* 815.1, L6, p. L6. DOI: 10.1088/2041-8205/815/1/L6. arXiv: 1511.03283 [astro-ph.GA].

Fu, Hai et al. (Jan. 2015b). "Radio-selected Binary Active Galactic Nuclei from the Very Large Array Stripe 82 Survey". In: *Astrophysical Journal* 799.1, 72, p. 72. DOI: 10.1088/0004-637X/799/1/72. arXiv: 1411.0685 [astro-ph.GA].

Fu, Hai et al. (2018). "SDSS-IV MaNGA: Galaxy Pair Fraction and Correlated Active Galactic Nuclei". In: *The Astrophysical Journal* 856.2, p. 93. DOI: 10.3847/1538-4357/aab364. URL: https://doi.org/10.3847/1538-4357/aab364.

Gallo, Elena et al. (Aug. 2005). "A dark jet dominates the power output of the stellar black hole Cygnus X-1". In: 436.7052, pp. 819–821. DOI: 10.1038/nature03879. arXiv: astro-ph/0508228 [astro-ph].

Genzel, R., D. Hollenbach, and C. H. Townes (May 1994). "The nucleus of our Galaxy". In: *Reports on Progress in Physics* 57.5, pp. 417–479. DOI: 10.1088/0034-4885/57/5/001.

Gerke, Brian F. et al. (May 2007). "The DEEP2 Galaxy Redshift Survey: AEGIS Observations of a Dual AGN at z = 0.7". In: *Astrophysical Journal Letters* 660.1, pp. L23–L26. DOI: 10.1086/517968. arXiv: astro-ph/0608380 [astro-ph].

Gordon, Yjan A. et al. (2021). "A Quick Look at the 3 GHz Radio Sky. I. Source Statistics from the Very Large Array Sky Survey". In: *The Astrophysical Journal Supplement Series* 255.2, p. 30. DOI: 10.3847/1538-4365/ac05c0. URL: https://doi.org/10.3847/1538-4365/ac05c0.

Goulding, Andy D. et al. (July 2019). "Discovery of a Close-separation Binary Quasar at the Heart of a z $\sim$ 0.2 Merging Galaxy and Its Implications for Low-frequency Gravitational Waves". In: 879.2, L21, p. L21. DOI: 10.3847/2041-8213/ab2a14. arXiv: 1907.03757 [astro-ph.GA].

Greenstein, Jesse L. and Maarten Schmidt (July 1964). "The Quasi-Stellar Radio Sources 3C 48 and 3C 273." In: 140, p. 1. DOI: 10.1086/147889.

Gross, Arran C. et al. (2019). "X-Ray Properties of Radio-selected Dual Active Galactic Nuclei". In: *The Astrophysical Journal* 883.1, p. 50. DOI: 10.3847/1538-4357/ab3795. URL: https://doi.org/10.3847/1538-4357/ab3795.

Haardt, Francesco and Laura Maraschi (Aug. 1993). "X-Ray Spectra from Two-Phase Accretion Disks". In: *Astrophysical Journal* 413, p. 507. DOI: 10.1086/173020.

Heckman, T. M. (July 1980). "An Optical and Radio Survey of the Nuclei of Bright Galaxies - Activity in the Normal Galactic Nuclei". In: 87, p. 152.

Heckman, Timothy M. and Philip N. Best (Aug. 2014). "The Coevolution of Galaxies and Supermassive Black Holes: Insights from Surveys of the Contemporary Universe". In: 52, pp. 589–660. DOI: 10.1146/annurev-astro-081913-035722. arXiv: 1403.4620 [astro-ph.GA].

Heckman, Timothy M. et al. (2004). "Present-Day Growth of Black Holes and Bulges: The Sloan Digital Sky Survey Perspective". In: *The Astrophysical Journal* 613.1, pp. 109–118. DOI: 10.1086/422872. URL: https://doi.org/10.1086/422872.

Hernquist, Lars and J. Christopher Mihos (July 1995). "Excitation of Activity in Galaxies by Minor Mergers". In: *Astrophysical Journal* 448, p. 41. DOI: 10.1086/175940. arXiv: astro-ph/9501090 [astro-ph].

Hine, R. G. and M. S. Longair (July 1979). "Optical spectra of 3CR radio galaxies." In: 188, pp. 111–130. DOI: 10.1093/mnras/188.1.111.

Ho, L. C. (Sept. 2008). "Nuclear activity in nearby galaxies." In: *Annual Review of Astronomy and Astrophysics* 46, pp. 475–539. DOI: 10.1146/annurev.astro.45.051806.110546. arXiv: 0803.2268 [astro-ph].

Hodge, J. A. et al. (July 2011). "High-resolution Very Large Array Imaging of Sloan Digital Sky Survey Stripe 82 at 1.4 GHz". In: *Astronomical Journal* 142.1, 3, p. 3. DOI: 10.1088/0004-6256/142/1/3. arXiv: 1103.5749 [astro-ph.CO].

Hopkins, Philip F., Dale D. Kocevski, and Kevin Bundy (Sept. 2014). "Do we expect most AGN to live in discs?" In: *Monthly Notices of the Royal Astronomical Society* 445.1, pp. 823–834. ISSN: 0035-8711. DOI: 10.1093/mnras/stu1736. eprint: https://academic.oup.com/mnras/article-pdf/445/1/823/18472985/stu1736.pdf. URL: https://doi.org/10.1093/mnras/stu1736.

Hopkins, Philip F. et al. (2005). "A Physical Model for the Origin of Quasar Lifetimes". In: *The Astrophysical Journal* 625.2, pp. L71–L74. DOI: 10.1086/431146. URL: https://doi.org/10.1086/431146.

Hopkins, Philip F. et al. (Mar. 2006). "A Unified, Merger-driven Model of the Origin of Starbursts, Quasars, the Cosmic X-Ray Background, Supermassive Black Holes, and Galaxy Spheroids". In: *Astrophysical Journal Letters* 163.1, pp. 1–49. DOI: 10.1086/499298. arXiv: astro-ph/0506398 [astro-ph].

Hou, Meicun, Zhiyuan Li, and Xin Liu (Sept. 2020). "A Chandra X-Ray Survey of Optically Selected AGN Pairs". In: 900.1, 79, p. 79. DOI: 10.3847/1538-4357/aba4a7. arXiv: 2001.10686 [astro-ph.GA].

Hou, Meicun et al. (2019). "Active Galactic Nucleus Pairs from the Sloan Digital Sky Survey. III. Chandra X-Ray Observations Unveil Obscured Double Nuclei". In: *The Astrophysical Journal* 882.1, p. 41. DOI: 10.3847/1538-4357/ab3225. URL: https://doi.org/10.3847/1538-4357/ab3225.

Husemann, B. et al. (July 2020). "Revisiting dual AGN candidates with spatially resolved LBT spectroscopy. The impact of spillover light contamination". In: 639, A117, A117. DOI: 10.1051/0004-6361/202037988. arXiv: 2006.01846 [astro-ph.GA].

Ilbert, O. et al. (2008). "COSMOS PHOTOMETRIC REDSHIFTS WITH 30-BANDS FOR 2-deg2". In: *The Astrophysical Journal* 690.2, pp. 1236–1249. DOI: 10.1088/0004-637x/690/2/1236. URL: https://doi.org/10.1088/0004-637x/690/2/1236.

Imanishi, Masatoshi et al. (Mar. 2020). "Subaru Infrared Adaptive Optics-assisted High-spatial-resolution Imaging Search for Luminous Dual Active Galactic Nuclei in Nearby Ultraluminous Infrared Galaxies". In: 891.2, 140, p. 140. DOI: 10.3847/1538-4357/ab733e. arXiv: 2002.04046 [astro-ph.GA].

Iwasawa, K. et al. (Aug. 2020). "A Compton-thick nucleus in the dual active galactic nuclei of Mrk 266". In: 640, A95, A95. DOI: 10.1051/0004-6361/202038513. arXiv: 2007.03258 [astro-ph.GA].

Jaffe, Walter et al. (Mar. 1996). "The Nuclear Disk of NGC 4261: Hubble Space Telescope Images and Ground-based Spectra". In: 460, p. 214. DOI: 10.1086/176963.

Jarrett, T. H. et al. (2011). "THESPITZER-WISESURVEY OF THE ECLIPTIC POLES". In: *The Astrophysical Journal* 735.2, p. 112. DOI: 10.1088/0004-637x/735/2/112. URL: https://doi.org/10.1088/0004-637x/735/2/112.

Jiang, Linhua et al. (2014). "THE SLOAN DIGITAL SKY SURVEY STRIPE 82 IMAGING DATA: DEPTH-OPTIMIZED CO-ADDS OVER 300 deg 2 IN FIVE FILTERS". In: *The Astrophysical Journal Supplement Series* 213.1, p. 12. DOI: 10.1088/0067-0049/213/1/12. URL: https://doi.org/10.1088/0067-0049/213/1/12.

Junkkarinen, V. et al. (Mar. 2001). "LBQS 0103-2753: A 0.3" Binary Quasar". In: *Astrophysical Journal Letters* 549.2, pp. L155–L159. DOI: 10.1086/319173. arXiv: astro-ph/0102501 [astro-ph].

Justham, Stephen and Kevin Schawinski (June 2012). "Another thread in the tapestry of stellar feedback: X-ray binaries". In: *Monthly Notices of the Royal Astronomical Society* 423.2, pp. 1641–1651. ISSN: 0035-8711. DOI: 10.1111/j.1365-2966.2012.20985.x. eprint: https://academic.oup.com/mnras/article-pdf/423/2/1641/2888564/mnras0423-1641.pdf. URL: https://doi.org/10.1111/j.1365-2966.2012.20985.x.

Kauffmann, Guinevere and Timothy M. Heckman (July 2009). "Feast and Famine: regulation of black hole growth in low-redshift galaxies". In: *Monthly Notices of the Royal Astronomical Society* 397.1, pp. 135–147. ISSN: 0035-8711. DOI: 10.1111/j.1365-2966.2009.14960.x. eprint: https://academic.oup.com/mnras/article-pdf/397/1/135/18431103/mnras0397-0135.pdf. URL: https://doi.org/10.1111/j.1365-2966.2009.14960.x.

Kauffmann, Guinevere et al. (Dec. 2003). "The host galaxies of active galactic nuclei". In: *Monthly Notices of the Royal Astronomical Society* 346.4, pp. 1055–1077. DOI: 10.1111/j.1365-2966.2003.07154.x. arXiv: astro-ph/0304239 [astro-ph].

Kellermann, K. I. et al. (Oct. 1989). "VLA Observations of Objects in the Palomar Bright Quasar Survey". In: 98, p. 1195. DOI: 10.1086/115207.

Kewley, L. J. et al. (July 2001). "Theoretical Modeling of Starburst Galaxies". In: *Astrophysical Journal* 556.1, pp. 121–140. DOI: 10.1086/321545. arXiv: astro-ph/0106324 [astro-ph].

Kewley, Lisa J. et al. (Nov. 2006). "The host galaxies and classification of active galactic nuclei". In: *Monthly Notices of the Royal Astronomical Society* 372.3, pp. 961–976. DOI: 10.1111/j.1365-2966.2006.10859.x. arXiv: astro-ph/0605681 [astro-ph].

Khachikian, E. Y. and D. W. Weedman (Sept. 1974). "An atlas of Seyfert galaxies." In: 192, pp. 581–589. DOI: 10.1086/153093.

Kim, D. C. et al. (Nov. 2020). "Dual AGN Candidates with Double-peaked [O III] Lines Matching that of Confirmed Dual AGNs". In: 904.1, 23, p. 23. DOI: 10.3847/1538-4357/abb9a0. arXiv: 2011.09961 [astro-ph.GA].

Kocevski, Dale D. et al. (2015). "ARE COMPTON-THICK AGNs THE MISSING LINK BETWEEN MERGERS AND BLACK HOLE GROWTH?" In: *The Astrophysical Journal* 814.2, p. 104. DOI: 10.1088/0004-637x/814/2/104. URL: https://doi.org/10.1088/0004-637x/814/2/104.

Komatsu, E. et al. (Feb. 2011). "Seven-year Wilkinson Microwave Anisotropy Probe (WMAP) Observations: Cosmological Interpretation". In: 192.2, 18, p. 18. DOI: 10.1088/0067-0049/192/2/18. arXiv: 1001.4538 [astro-ph.CO].

Komossa, S. et al. (Jan. 2003). "Discovery of a Binary Active Galactic Nucleus in the Ultraluminous Infrared Galaxy NGC 6240 Using Chandra". In: *Astrophysical Journal Letters* 582.1, pp. L15–L19. DOI: 10.1086/346145. arXiv: astro-ph/0212099 [astro-ph].

Kormendy, John and Luis C. Ho (2013). "Coevolution (Or Not) of Supermassive Black Holes and Host Galaxies". In: *Annual Review of Astronomy and Astrophysics* 51.1, pp. 511–653. DOI: 10.1146/annurev-astro-082708-101811. eprint: https://doi.org/10.1146/annurev-astro-082708-101811. URL: https://doi.org/10.1146/annurev-astro-082708-101811.

Koss, Michael et al. (2010). "MERGING AND CLUSTERING OF THE SWIFT BAT AGN SAMPLE". In: *The Astrophysical Journal* 716.2, pp. L125–L130. DOI: 10.1088/2041-8205/716/2/l125. URL: https://doi.org/10.1088/2041-8205/716/2/l125.

Koss, Michael et al. (2011). "CHANDRA DISCOVERY OF A BINARY ACTIVE GALACTIC NUCLEUS IN Mrk 739". In: *The Astrophysical Journal* 735.2, p. L42. DOI: 10.1088/2041-8205/735/2/l42. URL: https://doi.org/10.1088/2041-8205/735/2/l42.

Koss, Michael et al. (2012). "UNDERSTANDING DUAL ACTIVE GALACTIC NUCLEUS ACTIVATION IN THE NEARBY UNIVERSE". In: *The Astrophysical Journal* 746.2, p. L22. DOI: 10.1088/2041-8205/746/2/l22. URL: https://doi.org/10.1088/2041-8205/746/2/l22.

Koss, Michael J. et al. (2016). "NuSTAR RESOLVES THE FIRST DUAL AGN ABOVE 10 keV IN SWIFT J2028.52543". In: *The Astrophysical Journal* 824.1, p. L4. DOI: 10.3847/2041-8205/824/1/l4. URL: https://doi.org/10.3847/2041-8205/824/1/l4.

Lacy, M. et al. (2020). "The Karl G. Jansky Very Large Array Sky Survey (VLASS). Science Case and Survey Design". In: *Publications of the Astronomical Society of the Pacific*

132.1009, p. 035001. DOI: 10.1088/1538-3873/ab63eb. URL: https://doi.org/10.1088/1538-3873/ab63eb.

Laing, R. A. et al. (Jan. 1994). "Spectrophotometry of a Complete Sample of 3CR Radio Sources: Implications for Unified Models". In: *The Physics of Active Galaxies*. Ed. by Geoffrey V. Bicknell, Michael A. Dopita, and Peter J. Quinn. Vol. 54. Astronomical Society of the Pacific Conference Series, p. 201.

Lawrence, A. et al. (Aug. 2007). "The UKIRT Infrared Deep Sky Survey (UKIDSS)". In: 379.4, pp. 1599–1617. DOI: 10.1111/j.1365-2966.2007.12040.x. arXiv: astro-ph/0604426 [astro-ph].

Lawson, C. L. and R. J. Hanson (1974). *Solving least squares problems*. Englewood Cliffs, NJ: Prentice-Hall Series in Automatic Computation.

Li, Kunyang, David R. Ballantyne, and Tamara Bogdanović (Aug. 2021). "The Detectability of Kiloparsec-scale Dual Active Galactic Nuclei: The Impact of Galactic Structure and Black Hole Orbital Properties". In: *Astrophysical Journal* 916.2, 110, p. 110. DOI: 10.3847/1538-4357/ac06a0. arXiv: 2103.02862 [astro-ph.GA].

Liang, E. P. T. and R. H. Price (Nov. 1977). "Accretion disk coronae and Cygnus X-1." In: *Astrophysical Journal* 218, pp. 247–252. DOI: 10.1086/155677.

Liu, Ji-Feng et al. (2013). "Puzzling accretion onto a black hole in the ultraluminous X-ray source M 101 ULX-1". In: *Nature* 503.7477, pp. 500–503. DOI: 10.1038/nature12762. URL: https://doi.org/10.1038/nature12762.

Liu, Xin, Yue Shen, and Michael A. Strauss (2012). "ACTIVE GALACTIC NUCLEUS PAIRS FROM THE SLOAN DIGITAL SKY SURVEY. II. EVIDENCE FOR TIDALLY ENHANCED STAR FORMATION AND BLACK HOLE ACCRETION". In: *The Astrophysical Journal* 745.1, p. 94. DOI: 10.1088/0004-637x/745/1/94. URL: https://doi.org/10.1088/0004-637x/745/1/94.

Liu, Xin et al. (Jan. 2010). "Type 2 Active Galactic Nuclei with Double-Peaked [O III] Lines: Narrow-Line Region Kinematics or Merging Supermassive Black Hole Pairs?" In: *Astrophysical Journal* 708.1, pp. 427–434. DOI: 10.1088/0004-637X/708/1/427. arXiv: 0908.2426 [astro-ph.CO].

Liu, Xin et al. (2012). "CHANDRAX-RAY ANDHUBBLE SPACE TELESCOPEIMAGING OF OPTICALLY SELECTED KILOPARSEC-SCALE BINARY ACTIVE GALACTIC NUCLEI. I. NATURE OF THE NUCLEAR IONIZING SOURCES". In: *The Astrophysical Journal* 762.2, p. 110. DOI: 10.1088/0004-637x/762/2/110. URL: https://doi.org/10.1088/0004-637x/762/2/110.

Liu, Xin et al. (July 2018a). "Hubble Space Telescope Wide Field Camera 3 Identifies an r_p = 1 Kpc Dual Active Galactic Nucleus in the Minor Galaxy Merger SDSS J0924+0510 at z = 0.1495". In: *Astrophysical Journal* 862.1, 29, p. 29. DOI: 10.3847/1538-4357/aac9cb. arXiv: 1712.01866 [astro-ph.GA].

Liu, Xin et al. (Feb. 2018b). "Very Long Baseline Array Imaging of Type-2 Seyferts with Double-peaked Narrow Emission Lines: Searches for Sub-kpc Dual AGNs and Jet-powered Outflows". In: *Astrophysical Journal* 854.2, 169, p. 169. DOI: 10.3847/1538-4357/aaab47. arXiv: 1709.03561 [astro-ph.GA].

Lynden-Bell, D. (Aug. 1969). "Galactic Nuclei as Collapsed Old Quasars". In: 223.5207, pp. 690–694. DOI: 10.1038/223690a0.

Markwardt, C. B. (Sept. 2009). "Non-linear Least-squares Fitting in IDL with MPFIT". In: *Astronomical Data Analysis Software and Systems XVIII*. Ed. by D. A. Bohlender, D. Durand, and P. Dowler. Vol. 411. Astronomical Society of the Pacific Conference Series, p. 251. arXiv: 0902.2850 [astro-ph.IM].

Martini, Paul (Jan. 2004). "QSO Lifetimes". In: *Coevolution of Black Holes and Galaxies*. Ed. by Luis C. Ho, p. 169. arXiv: astro-ph/0304009 [astro-ph].

Mazzarella, J. M. et al. (2012). "INVESTIGATION OF DUAL ACTIVE NUCLEI, OUTFLOWS, SHOCK-HEATED GAS, AND YOUNG STAR CLUSTERS IN MARKARIAN 266". In: *The Astronomical Journal* 144.5, p. 125. DOI: 10.1088/0004-6256/144/5/125. URL: https://doi.org/10.1088/0004-6256/144/5/125.

McConnell, Nicholas J. and Chung-Pei Ma (Feb. 2013). "Revisiting the Scaling Relations of Black Hole Masses and Host Galaxy Properties". In: 764.2, 184, p. 184. DOI: 10.1088/0004-637X/764/2/184. arXiv: 1211.2816 [astro-ph.CO].

McGurk, R. C. et al. (Sept. 2011). "Spatially Resolved Spectroscopy of SDSS J0952+2552: A Confirmed Dual Active Galactic Nucleus". In: *Astrophysical Journal Letters* 738.1, L2, p. L2. DOI: 10.1088/2041-8205/738/1/L2. arXiv: 1107.2651 [astro-ph.CO].

Merloni, Andrea, Sebastian Heinz, and Tiziana Di Matteo (2005). "A Fundamental Plane of Black Hole Activity: Pushing Forward the Unification Scheme". In: *Astrophysics and Space Science* 300.1, pp. 45–53. DOI: 10.1007/s10509-005-1183-x. URL: https://doi.org/10.1007/s10509-005-1183-x.

Müller-Sánchez, F. et al. (2015). "THE ORIGIN OF DOUBLE-PEAKED NARROW LINES IN ACTIVE GALACTIC NUCLEI. I. VERY LARGE ARRAY DETECTIONS OF DUAL AGNs AND AGN OUTFLOWS". In: *The Astrophysical Journal* 813.2, p. 103. DOI: 10.1088/0004-637x/813/2/103. URL: https://doi.org/10.1088/0004-637x/813/2/103.

Murphy, E. J. et al. (Aug. 2011). "Calibrating Extinction-free Star Formation Rate Diagnostics with 33 GHz Free-free Emission in NGC 6946". In: *Astrophysical Journal* 737.2, 67, p. 67. DOI: 10.1088/0004-637X/737/2/67. arXiv: 1105.4877 [astro-ph.CO].

Narayan, Ramesh and Insu Yi (June 1994). "Advection-dominated Accretion: A Self-similar Solution". In: 428, p. L13. DOI: 10.1086/187381. arXiv: astro-ph/9403052 [astro-ph].

Netzer, Hagai (2013). *The Physics and Evolution of Active Galactic Nuclei*. Cambridge University Press.

Norman, C. and J. Silk (Mar. 1983). "The dynamics and fueling of active nuclei". In: *Astrophysical Journal* 266, pp. 502–515. DOI: 10.1086/160798.

O'Dea, Christopher P. and D. J. Saikia (Dec. 2021). "Compact steep-spectrum and peaked-spectrum radio sources". In: 29.1, 3, p. 3. DOI: 10.1007/s00159-021-00131-w. arXiv: 2009.02750 [astro-ph.GA].

O'Dell, S. L. (Feb. 1986). "The optical continuum emission of active galactic nuclei". In: 98, pp. 140–147. DOI: 10.1086/131735.

Oke, J. B. et al. (Apr. 1995). "The Keck Low-Resolution Imaging Spectrometer". In: *Publications of the Astronomical Society of the Pacific* 107, p. 375. DOI: 10.1086/133562.

Osterbrock, Donald E. and Gary J. Ferland (2006). *Astrophysics of gaseous nebulae and active galactic nuclei*. 2nd. ed. Sausalito, CA: University Science Books.

Owen, F. N. et al. (July 1985). "VLA observations of the multiple jet galaxy 3C 75." In: *Astrophysical Journal Letters* 294, pp. L85–L88. DOI: 10.1086/184514.

Perley, Daniel A. (Aug. 2019). "Fully Automated Reduction of Longslit Spectroscopy with the Low Resolution Imaging Spectrometer at the Keck Observatory". In: *Publications of the Astronomical Society of the Pacific* 131.1002, p. 084503. DOI: 10.1088/1538-3873/ab215d. arXiv: 1903.07629 [astro-ph.IM].

Perley, R. A. and B. J. Butler (Feb. 2013). "An Accurate Flux Density Scale from 1 to 50 GHz". In: *Astrophysical Journal Letters* 204.2, 19, p. 19. DOI: 10.1088/0067-0049/204/2/19. arXiv: 1211.1300 [astro-ph.IM].

Peters, Christina M. et al. (Oct. 2015). "Quasar Classification Using Color and Variability". In: 811.2, 95, p. 95. DOI: 10.1088/0004-637X/811/2/95. arXiv: 1508.04121 [astro-ph.GA].

Peterson, Bradley M. and Amri Wandel (Aug. 1999). "Keplerian Motion of Broad-Line Region Gas as Evidence for Supermassive Black Holes in Active Galactic Nuclei". In: 521.2, pp. L95–L98. DOI: 10.1086/312190. arXiv: astro-ph/9905382 [astro-ph].

Pfeifle, Ryan W. et al. (Oct. 2019). "A Triple AGN in a Mid-infrared Selected Late-stage Galaxy Merger". In: 883.2, 167, p. 167. DOI: 10.3847/1538-4357/ab3a9b. arXiv: 1908.01732 [astro-ph.GA].

Pierce, J. C. S. et al. (Feb. 2022). "Do AGN triggering mechanisms vary with radio power? - II. The importance of mergers as a function of radio power and optical luminosity". In: 510.1, pp. 1163–1183. DOI: 10.1093/mnras/stab3231. arXiv: 2111.03075 [astro-ph.GA].

Pillepich, Annalisa et al. (Dec. 2017). "First results from the IllustrisTNG simulations: the stellar mass content of groups and clusters of galaxies". In: *Monthly Notices of the Royal Astronomical Society* 475.1, pp. 648–675. ISSN: 0035-8711. DOI: 10.1093/mnras/stx3112. eprint: https://academic.oup.com/mnras/article-pdf/475/1/648/23534158/stx3112.pdf. URL: https://doi.org/10.1093/mnras/stx3112.

Polletta, M. et al. (July 2007). "Spectral Energy Distributions of Hard X-Ray Selected Active Galactic Nuclei in the XMM-Newton Medium Deep Survey". In: 663.1, pp. 81–102. DOI: 10.1086/518113. arXiv: astro-ph/0703255 [astro-ph].

Pringle, J. E. (Oct. 1976). "Thermal instabilities in accretion discs." In: 177, pp. 65–71. DOI: 10.1093/mnras/177.1.65.

Ptak, A. et al. (2015). "A FOCUSED, HARD X-RAY LOOK AT ARP 299 WITHNuSTAR". In: *The Astrophysical Journal* 800.2, p. 104. DOI: 10.1088/0004-637x/800/2/104. URL: https://doi.org/10.1088/0004-637x/800/2/104.

Richards, Gordon T. et al. (June 2002). "Spectroscopic Target Selection in the Sloan Digital Sky Survey: The Quasar Sample". In: 123.6, pp. 2945–2975. DOI: 10.1086/340187. arXiv: astro-ph/0202251 [astro-ph].

Robotham, A. S. G. et al. (Nov. 2014). "Galaxy And Mass Assembly (GAMA): galaxy close pairs, mergers and the future fate of stellar mass". In: 444.4, pp. 3986–4008. DOI: 10.1093/mnras/stu1604. arXiv: 1408.1476 [astro-ph.GA].

Rodriguez-Gomez, Vicente et al. (Feb. 2016). "The stellar mass assembly of galaxies in the Illustris simulation: growth by mergers and the spatial distribution of accreted stars". In: *Monthly Notices of the Royal Astronomical Society* 458.3, pp. 2371–2390. ISSN:

0035-8711. DOI: 10.1093/mnras/stw456. eprint: https://academic.oup.com/mnras/article-pdf/458/3/2371/8005964/stw456.pdf. URL: https://doi.org/10.1093/mnras/stw456.

Rosario, D. J. et al. (2011). "ADAPTIVE OPTICS IMAGING OF QUASI-STELLAR OBJECTS WITH DOUBLE-PEAKED NARROW LINES: ARE THEY DUAL ACTIVE GALACTIC NUCLEI?" In: *The Astrophysical Journal* 739.1, p. 44. DOI: 10.1088/0004-637x/739/1/44. URL: https://doi.org/10.1088/0004-637x/739/1/44.

Rosas-Guevara, Yetli M. et al. (Feb. 2019). "The abundances and properties of Dual AGN and their host galaxies in the EAGLE simulations". In: *Monthly Notices of the Royal Astronomical Society* 483.2, pp. 2712–2720. DOI: 10.1093/mnras/sty3251. arXiv: 1805.01479 [astro-ph.GA].

Roy, Namrata et al. (Dec. 2021). "Radio Morphology of Red Geysers". In: 922.2, 230, p. 230. DOI: 10.3847/1538-4357/ac24a0. arXiv: 2109.02609 [astro-ph.GA].

Salpeter, E. E. (Aug. 1964). "Accretion of Interstellar Matter by Massive Objects." In: *Astrophysical Journal* 140, pp. 796–800. DOI: 10.1086/147973.

Salvato, M. et al. (2008). "PHOTOMETRIC REDSHIFT AND CLASSIFICATION FOR THEXMM-COSMOS SOURCES". In: *The Astrophysical Journal* 690.2, pp. 1250–1263. DOI: 10.1088/0004-637x/690/2/1250. URL: https://doi.org/10.1088/0004-637x/690/2/1250.

Sánchez-Blázquez, P. et al. (Sept. 2006). "Medium-resolution Isaac Newton Telescope library of empirical spectra". In: 371.2, pp. 703–718. DOI: 10.1111/j.1365-2966.2006.10699.x. arXiv: astro-ph/0607009 [astro-ph].

Sarzi, Marc et al. (Mar. 2006). "The SAURON project - V. Integral-field emission-line kinematics of 48 elliptical and lenticular galaxies". In: 366.4, pp. 1151–1200. DOI: 10.1111/j.1365-2966.2005.09839.x. arXiv: astro-ph/0511307 [astro-ph].

Satyapal, Shobita et al. (May 2014). "Galaxy pairs in the Sloan Digital Sky Survey – IX. Merger-induced AGN activity as traced by the Wide-field Infrared Survey Explorer". In: *Monthly Notices of the Royal Astronomical Society* 441.2, pp. 1297–1304. ISSN: 0035-8711. DOI: 10.1093/mnras/stu650. eprint: https://academic.oup.com/mnras/article-pdf/441/2/1297/3713056/stu650.pdf. URL: https://doi.org/10.1093/mnras/stu650.

Satyapal, Shobita et al. (Oct. 2017). "Buried AGNs in Advanced Mergers: Mid-infrared Color Selection as a Dual AGN Candidate Finder". In: *Astrophysical Journal* 848.2, 126, p. 126. DOI: 10.3847/1538-4357/aa88ca. arXiv: 1707.03921 [astro-ph.GA].

Schawinski, Kevin et al. (Nov. 2007). "Observational evidence for AGN feedback in early-type galaxies". In: *Monthly Notices of the Royal Astronomical Society* 382.4, pp. 1415–1431. ISSN: 0035-8711. DOI: 10.1111/j.1365-2966.2007.12487.x. eprint: https://academic.oup.com/mnras/article-pdf/382/4/1415/3940026/mnras0382-1415.pdf. URL: https://doi.org/10.1111/j.1365-2966.2007.12487.x.

Schmidt, M. (Mar. 1963). "3C 273 : A Star-Like Object with Large Red-Shift". In: 197.4872, p. 1040. DOI: 10.1038/1971040a0.

Seyfert, Carl K. (Jan. 1943). "Nuclear Emission in Spiral Nebulae." In: 97, p. 28. DOI: 10.1086/144488.

Shakura, N. I. and R. A. Sunyaev (Jan. 1973). "Black holes in binary systems. Observational appearance." In: *AAP* 24, pp. 337–355.

Shankar, Francesco, David H. Weinberg, and Jordi Miralda-Escudé (2008). "SELF-CONSISTENT MODELS OF THE AGN AND BLACK HOLE POPULATIONS: DUTY CYCLES, ACCRETION RATES, AND THE MEAN RADIATIVE EFFICIENCY". In: *The Astrophysical Journal* 690.1, pp. 20–41. DOI: 10.1088/0004-637x/690/1/20. URL: https://doi.org/10.1088/0004-637x/690/1/20.

Shen, Yue et al. (Jan. 2021). "A hidden population of high-redshift double quasars unveiled by astrometry". In: *Nature Astronomy* 5, pp. 569–574. DOI: 10.1038/s41550-021-01323-1. arXiv: 2105.03298 [astro-ph.GA].

Shields, G. A. (July 1974). "X-ray ionization and the helium abundance in 3C 120." In: 191, pp. 309–316. DOI: 10.1086/152969.

Siemiginowska, Aneta et al. (Nov. 1995). "Testing Models for the Quasar Big Blue Bump via Color-Color Diagrams". In: 454, p. 77. DOI: 10.1086/176467.

Singha, M. et al. (Sept. 2021). "Ionized Gas Outflows in Low-excitation Radio Galaxies Are Radiation Driven". In: 918.2, 65, p. 65. DOI: 10.3847/1538-4357/ac06c7. arXiv: 2106.02086 [astro-ph.GA].

Slipher, V. M. (Jan. 1917). "The spectrum and velocity of the nebula N.G.C. 1068 (M 77)". In: *Lowell Observatory Bulletin* 3, pp. 59–62.

Smith, K. L. et al. (June 2010). "A Search for Binary Active Galactic Nuclei: Double-peaked [O III] AGNs in the Sloan Digital Sky Survey". In: *Astrophysical Journal* 716.1, pp. 866–877. DOI: 10.1088/0004-637X/716/1/866. arXiv: 0908.1998 [astro-ph.CO].

Stockton, Alan et al. (2004). "Two Active Nuclei in 3C 294". In: *The Astrophysical Journal* 600.2, pp. 626–633. DOI: 10.1086/380096. URL: https://doi.org/10.1086/380096.

Storchi-Bergmann, Thaisa and Allan Schnorr-Müller (2019). "Observational constraints on the feeding of supermassive black holes". In: *Nature Astronomy* 3.1, pp. 48–61. DOI: 10.1038/s41550-018-0611-0. URL: https://doi.org/10.1038/s41550-018-0611-0.

Teng, Stacy H. et al. (2012). "CHANDRAOBSERVATIONS OF GALAXY ZOO MERGERS: FREQUENCY OF BINARY ACTIVE NUCLEI IN MASSIVE MERGERS". In: *The Astrophysical Journal* 753.2, p. 165. DOI: 10.1088/0004-637x/753/2/165. URL: https://doi.org/10.1088/0004-637x/753/2/165.

Thomas, D. et al. (May 2013). "Stellar velocity dispersions and emission line properties of SDSS-III/BOSS galaxies". In: 431.2, pp. 1383–1397. DOI: 10.1093/mnras/stt261. arXiv: 1207.6115 [astro-ph.CO].

Tingay, S. J. and R. B. Wayth (June 2011). "A VLBA Search for Binary Black Holes in Active Galactic Nuclei with Double-peaked Optical Emission Line Spectra". In: *Astronomical Journal* 141.6, 174, p. 174. DOI: 10.1088/0004-6256/141/6/174. arXiv: 1103.2597 [astro-ph.CO].

Torrey, Paul et al. (Dec. 2012). "Moving-mesh cosmology: properties of gas discs". In: *Monthly Notices of the Royal Astronomical Society* 427.3, pp. 2224–2238. ISSN: 0035-8711. DOI: 10.1111/j.1365-2966.2012.22082.x. eprint: https://academic.

oup.com/mnras/article-pdf/427/3/2224/3841802/427-3-2224.pdf. URL: https://doi.org/10.1111/j.1365-2966.2012.22082.x.

Tubín, Dusán et al. (Apr. 2021). "The Complex Gaseous and Stellar Environments of the Nearby Dual Active Galactic Nucleus Mrk 739". In: 911.2, 100, p. 100. DOI: 10.3847/1538-4357/abedba. arXiv: 2103.12180 [astro-ph.GA].

Urry, C. Megan and Paolo Padovani (Sept. 1995). "Unified Schemes for Radio-Loud Active Galactic Nuclei". In: *Publications of the Astronomical Society of the Pacific* 107, p. 803. DOI: 10.1086/133630. arXiv: astro-ph/9506063 [astro-ph].

Ursini, F. et al. (Dec. 2020). "Estimating the size of X-ray lamppost coronae in active galactic nuclei". In: 644, A132, A132. DOI: 10.1051/0004-6361/202039158. arXiv: 2010.07166 [astro-ph.HE].

Valdes, Francisco et al. (June 2004). "The Indo-US Library of Coudé Feed Stellar Spectra". In: 152.2, pp. 251–259. DOI: 10.1086/386343. arXiv: astro-ph/0402435 [astro-ph].

van der Marel, Roeland P. and Marijn Franx (Apr. 1993). "A New Method for the Identification of Non-Gaussian Line Profiles in Elliptical Galaxies". In: 407, p. 525. DOI: 10.1086/172534.

Vazdekis, A. et al. (July 2012). "MIUSCAT: extended MILES spectral coverage – I. Stellar population synthesis models". In: *Monthly Notices of the Royal Astronomical Society* 424.1, pp. 157–171. ISSN: 0035-8711. DOI: 10.1111/j.1365-2966.2012.21179.x. eprint: https://academic.oup.com/mnras/article-pdf/424/1/157/3260738/mnras0424-0157.pdf. URL: https://doi.org/10.1111/j.1365-2966.2012.21179.x.

Villforth, C. et al. (Apr. 2014). "Morphologies of z $\sim$ 0.7 AGN host galaxies in CANDELS: no trend of merger incidence with AGN luminosity". In: 439.4, pp. 3342–3356. DOI: 10.1093/mnras/stu173. arXiv: 1401.5477 [astro-ph.GA].

Volonteri, Marta et al. (Dec. 2021). "Dual AGN in the Horizon-AGN simulation and their link to galaxy and massive black hole mergers, with an excursus on multiple AGN". In: *arXiv e-prints*, arXiv:2112.07193, arXiv:2112.07193. arXiv: 2112.07193 [astro-ph.GA].

Wang, Jian-Min et al. (Nov. 2009). "Active Galactic Nuclei with Double-Peaked Narrow Lines: Are they Dual Active Galactic Nuclei?" In: *Astrophysical Journal Letters* 705.1, pp. L76–L80. DOI: 10.1088/0004-637X/705/1/L76. arXiv: 0910.0580 [astro-ph.CO].

Wassenhove, Sandor Van et al. (2012). "OBSERVABILITY OF DUAL ACTIVE GALACTIC NUCLEI IN MERGING GALAXIES". In: *The Astrophysical Journal* 748.1, p. L7. DOI: 10.1088/2041-8205/748/1/l7. URL: https://doi.org/10.1088/2041-8205/748/1/l7.

Wright, Edward L. et al. (Dec. 2010). "The Wide-field Infrared Survey Explorer (WISE): Mission Description and Initial On-orbit Performance". In: 140.6, pp. 1868–1881. DOI: 10.1088/0004-6256/140/6/1868. arXiv: 1008.0031 [astro-ph.IM].

Wrobel, J. M., R. C. Walker, and H. Fu (2014). "EVIDENCE FROM THE VERY LONG BASELINE ARRAY THAT J1502SE/SW ARE DOUBLE HOTSPOTS, NOT A SUPERMASSIVE BINARY BLACK HOLE". In: *The Astrophysical Journal* 792.1,

p. L8. DOI: 10.1088/2041-8205/792/1/l8. URL: https://doi.org/10.1088/2041-8205/792/1/l8.

Xu, Chun, Mario Livio, and Stefi Baum (Sept. 1999). "Radio-loud and Radio-quiet Active Galactic Nuclei". In: 118.3, pp. 1169–1176. DOI: 10.1086/301007. arXiv: astro-ph/9905322 [astro-ph].

Yong, Suk Yee, Rachel L. Webster, and Anthea L. King (Mar. 2016). "Black Hole Mass Estimation: How Good is the Virial Estimate?" In: 33, e009, e009. DOI: 10.1017/pasa.2016.8. arXiv: 1602.04672 [astro-ph.GA].

Yuan, F. et al. (2002). "NGC 4258: A jet-dominated low-luminosity AGN?" In: *Astronomy and Astrophysics* 391.1, pp. 139–148. DOI: 10.1051/0004-6361:20020817. URL: https://doi.org/10.1051/0004-6361:20020817.

Yue, Minghao et al. (2021). "A Candidate Kiloparsec-scale Quasar Pair at z = 5.66". In: *The Astrophysical Journal Letters* 921.2, p. L27. DOI: 10.3847/2041-8213/ac31a9. URL: https://doi.org/10.3847/2041-8213/ac31a9.

Yun, Min S., Naveen A. Reddy, and J. J. Condon (June 2001). "Radio Properties of Infrared-selected Galaxies in the IRAS 2 Jy Sample". In: *Astrophysical Journal* 554.2, pp. 803–822. DOI: 10.1086/323145. arXiv: astro-ph/0102154 [astro-ph].

Zhang, Yang-Wei et al. (Dec. 2021a). "A Systematic Search for Dual Active Galactic Nuclei in Merging Galaxies (ASTRO-DARING) II: First Results from Long-slit Spectroscopic Observations". In: 162.6, 289, p. 289. DOI: 10.3847/1538-3881/ac2deb. arXiv: 2111.00635 [astro-ph.GA].

— (Dec. 2021b). "A Systematic Search for Dual AGNs in Merging Galaxies (Astro-daring): III: Results from the SDSS Spectroscopic Surveys". In: 162.6, 276, p. 276. DOI: 10.3847/1538-3881/ac1ce7. arXiv: 2111.00636 [astro-ph.GA].

Zhao, Yulin et al. (Jan. 2022). "The Relation between Morphological Asymmetry and Nuclear Activity in Low-redshift Galaxies". In: 925.1, 70, p. 70. DOI: 10.3847/1538-4357/ac375b. arXiv: 2111.03558 [astro-ph.GA].

Zheng, X. Z. et al. (Dec. 2009). "Observational Constraints on the Co-Evolution of Supermassive Black Holes and Galaxies". In: 707.2, pp. 1566–1577. DOI: 10.1088/0004-637X/707/2/1566. arXiv: 0911.0005 [astro-ph.CO].

APPENDIX A

ANALYSIS OF THE PROJECTED PAIRS

Throughout the main text, we have selectively shown only the relevant data that are germane to the discussion of dual AGN. This primary requirement of the main sample was that galaxies must be shown to be within kinematic pairs as evidence of an ensuing or ongoing galactic merger.

The subsample of projected pairs (*i.e.*, those which appear to spatially proximate on the sky but are actually separated by cosmic distances along the line of sight) have thus far been neglected in our discussion, since they represent isolated galaxies. They are, however, quite interesting in their own right. Most do indeed show evidence of AGN via radio-excess (via Hβ), although the same caveat applies here even more so than for the kinematic pairs. The higher redshift of the projected pairs sample would likely prevent conclusively resolving structures between the two galaxies in a pair, and so we would expect higher frequency of radio jet/lobe overlap between the two.

We note that only five of the 28 projected pairs galaxies have results from spectral fitting, mostly due to the high redshift. In fact, as noted in the text, one galaxy is so high redshift that there is no overlap with its de-redshifted spectrum and the SSP templates. None of the fitted galaxies shows conclusive evidence of BPT Seyfert or LINER type AGN activity, although 4/5 are composite types, and three of these are categorized as strong AGN by the WHAN diagram ruling out older stellar populations. Interestingly, all galaxies with detected [O III] emission are found to be radio-loud. Lastly, the pairs in 2242+0030,

2308+0025, and 2318+0045 are found to to host IR AGN by the color cut of Satyapal et al. (2017). In particular, we remind the reader that 230858.75+002531.4 was found to be a broad line (Type I) QSO, and so it is not surprising that it could be responsible for the IR signature in its pair; however, the presence of broad lines immediately rules out the possibility that the central source is heavily obscured by the dust emitting the IR signature, so we must be viewing the source at an appreciable inclination angle to be able to observe both the optical and IR emission.

The isolated host galaxies of the projected pairs are found to have a similar range of stellar masses to the kinematic pairs. The lack of [O III] measurements prevents Eddington ratio estimates for 10 of the galaxies. The remainder appear to have Eddington ratios that are on average higher than the kinematic pairs, apparently approaching the Eddington limit. This comparison is not particularly meaningful, however, since the majority of these isolated galaxies may not even contain an active AGN.

We give the corresponding optical-derived data for the projected pairs, in the same format as was done for the kinematic pairs, in Tables A.1, A.2, A.3.

Table A.1. Emission Line Properties of the Projected Pairs

Optical Designation J2000 (1)	z (2)	log([O III]/Hβ) (3)	log([N II]/Hα) (4)	log([S II]/Hα) (5)	log([O I]/Hα) (6)	$L_{\mathrm{H}\alpha}$ log(erg s^{-1}) (7)	$W_{\mathrm{H}\alpha}$ log(Å) (8)	$L_{[\mathrm{O\ III}]}$ log(erg s^{-1}) (9)	$P^{\mathrm{int}}_{1.4\ \mathrm{GHz}}$ log(W Hz^{-1}) (10)
011156.52−000017.3	0.253	-0.19 ± ...	-0.24 ± ...	0.1 ± ...	-0.43 ± ...	39.4	0.3 ± ...	38.7	24.9
011613.73+005807.3	1.052	1.48 ± ...	...± ...	...± ...	...± ...	...	...± ...	41.9	25.5
011613.77+005801.9	0.9402	-0.96 ± ...	...± ...	...± ...	...± ...	...	...± ...	39.4	25.0
012050.37−004656.6	0.834	...± ...	...± ...	...± ...	...± ...	...	...± ...	...	24.5
012050.55−004658.4	0.4824	0.01 ± ...	...± ...	...± ...	...± ...	...	...± ...	40.0	24.2
013505.88+011908.4	0.7842	...± ...	...± ...	...± ...	...± ...	...	...± ...	...	24.4
013505.89+011911.5	0.357	-0.38 ± ...	...± ...	...± ...	...± ...	...	...± ...	40.5	24.0
014457.10−004216.6	0.6535	...± ...	...± ...	...± ...	...± ...	...	...± ...	...	24.8
014457.17−004218.8	0.3193	-0.35 ± ...	-0.4 ± ...	...± ...	-1.69 ± ...	41.7	1.5 ± ...	40.6	24.3
221331.60+004834.6	0.812	...± ...	...± ...	...± ...	...± ...	...	...± ...	...	25.2
221331.87+004836.1	0.9068	...± ...	...± ...	...± ...	...± ...	...	...± ...	...	25.3
221806.92+004515.9	1.0988	...± ...	...± ...	...± ...	...± ...	...	...± ...	...	25.5
221806.98+004517.9	0.836	...± ...	...± ...	...± ...	...± ...	...	...± ...	...	25.2
224204.25+003029.4	0.7621	0.55 ± ...	...± ...	...± ...	...± ...	...	...± ...	41.3	24.4
224204.45+003028.1	0.5104	-0.01 ± ...	-0.38 ± ...	-0.61 ± ...	-1.3 ± ...	42.3	2.2 ± ...	41.5	23.9
225002.04+001131.9	0.988	...± ...	...± ...	...± ...	...± ...	...	...± ...	...	24.9
225002.10+001136.3	0.5295	0.31 ± ...	...± ...	...± ...	...± ...	...	...± ...	39.9	24.0
230223.28−000301.2	0.3105	0.03 ± ...	-0.36 ± ...	-0.18 ± ...	-1.23 ± ...	40.4	1.1 ± ...	39.6	24.1
230223.46−000259.4	0.545	0.38 ± ...	...± ...	...± ...	...± ...	40.5	0.2 ± ...	40.3	24.4
230453.04−010946.6	0.7448	0.63 ± ...	...± ...	...± ...	...± ...	...	...± ...	41.3	24.9
230453.13−010945.5	1.4339	...± ...	...± ...	...± ...	...± ...	...	...± ...	...	25.7
230559.17+002409.0	0.556	-0.03 ± ...	...± ...	...± ...	...± ...	...	...± ...	40.9	24.0
230559.19+002407.4	0.345	-0.27 ± ...	...± ...	...± ...	-1.2 ± ...	41.2	1.5 ± ...	40.5	23.9
230858.68+002527.8	0.941	...± ...	...± ...	...± ...	...± ...	...	...± ...	...	24.7
231843.30+004527.2	0.2744	0.2 ± ...	-0.48 ± ...	-0.65 ± ...	-1.83 ± ...	40.8	1.6 ± ...	39.9	23.2
231843.55+004525.0	0.9587	0.53 ± ...	...± ...	...± ...	...± ...	...	...± ...	42.3	25.3

Every two rows is a pair (with the exception of 0111−0000 and 2308+0025), and sources are sorted in ascending R.A. (1) J2000 coordinate of the optical source; (2) redshift; (3)−(6) logarithmic emission line ratios and 1σ errors; (7) logarithmic Hα luminosity, corrected for reddening; (8) logarithmic Hα equivalent width and 1σ error; (9) logarithmic [O III] luminosity, corrected for reddening; (10) logarithmic radio power computed from integrated source flux at 1.4 GHz.

Table A.2. Classifications of Single Galaxies Projected Pairs

Optical Designation J2000 (1)	BPT1 class (2)	BPT2 class (3)	BPT3 class (4)	Radio Excess (5)	Radio Loud (6)	MIR color (7)	Mode (8)
011156.52−000017.3	Comp	LINER	LINER	Y	Y	N	L
011613.73+005807.3	...	...	...	<	Y	N	H
011613.77+005801.9	...	...	...	<	Y	N	L
012050.37−004656.6	...	...	...	N	N	N	...
012050.55−004658.4	...	...	...	<	Y	N	L
013505.88+011908.4	...	...	...	<	N	N	...
013505.89+011911.5	...	...	...	<	Y	N	L
014457.10−004216.6	...	...	...	<	Y	N	L
014457.17−004218.8	SF	...	SF	Y	Y	N	L
221331.60+004834.6	...	...	...	<	N	N	...
221331.87+004836.1	...	...	...	N	N	N	...
221806.92+004515.9	...	...	...	N	N	N	...
221806.98+004517.9	...	...	...	N	N	N	...
224204.25+003029.4	...	...	...	<	Y	Y	L
224204.45+003028.1	Comp	SF	SF	Y	N	Y	L
225002.04+001131.9	...	...	...	N	N	N	...
225002.10+001136.3	...	...	...	<	Y	N	L
230223.28−000301.2	Comp	LINER	SF	Y	Y	N	L
230223.46−000259.4	...	...	...	Y	Y	N	L
230453.04−010946.6	...	...	...	<	Y	N	H
230453.13−010945.5	...	...	...	N	N	N	...
230559.17+002409.0	...	...	...	<	Y	N	L
230559.19+002407.4	...	...	SF	Y	Y	N	L
230858.68+002527.8	...	...	...	N	N	Y	...
231843.30+004527.2	Comp	SF	SF	Y	Y	Y	H
231843.55+004525.0	...	...	...	<	Y	Y	H

Every two rows is a pair (with the exception of 0111−0000 and 2308+0025), and sources are sorted in ascending R.A. (1) J2000 coordinate of the optical source; (2) − (4) BPT diagnostic classifications (in order of Figures 2.3, 2.4, 2.5); (5) Radio excess determined via Hα SFR (< denotes excess via Hβ); (6) Radio loudness determined via $L_{[OIII]}$; (7) mid-IR color AGN status based on criteria of Satyapal et al. (2017); (8) mode of AGN activity (HERG/LERG).

Table A.3. Derived Optical Properties of Single Galaxies in Projected Pairs

Optical Designation J2000 (4)	$M_\star$ $\log(M_\odot)$ (5)	$\sigma_\star$ (km(1)	$M_{\rm BH}$ (2)	$\log(\lambda)$ (3)
011156.52−000017.3	10.0	395.48	7.5	-1.1
011613.73+005807.3	11.4	310.5	9.2	-1.8
011613.77+005801.9	8.7	657.17	6.1	0.4
012050.37−004656.6	10.9	800.0	8.5	...
012050.55−004658.4	11.3	221.79	9.0	-3.0
013505.88+011908.4	10.9	203.22	8.6	...
013505.89+011911.5	11.9	275.64	9.7	-3.5
014457.10−004216.6	11.9	206.99	9.7	-3.4
014457.17−004218.8	10.9	77.32	8.6	-2.3
221331.60+004834.6	10.5	400.0	8.1	...
221331.87+004836.1	11.7	368.74	9.5	...
221806.92+004515.9	11.6	141.34	9.3	...
221806.98+004517.9	10.3	160.89	7.8	...
224204.25+003029.4	11.8	260.95	9.7	-2.8
224204.45+003028.1	10.3	226.3	7.9	-0.9
225002.04+001131.9	11.7	301.18	9.5	...
225002.10+001136.3	10.1	10.32	7.7	-1.8
230223.28−000301.2	9.6	88.51	7.1	-1.2
230223.46−000259.4	11.5	254.75	9.3	-3.1
230453.04−010946.6	9.6	150.0	7.1	-0.2
230453.13−010945.5	11.5	251.21	9.3	...
230559.17+002409.0	11.7	184.44	9.5	-3.1
230559.19+002407.4	9.9	19.26	7.4	-1.2
230858.68+002527.8	10.5	10.62	8.1	...
231843.30+004527.2	9.3	200.26	6.7	-1.1
231843.55+004525.0	11.4	238.43	9.2	-1.4

Every two rows is a pair (with the exception of 0111−0000 and 2308+0025), and sources are sorted in ascending R.A. (1) J2000 coordinate of the optical source; (2) merger component or isolated galaxy in a projected pair; (3) total stellar mass measured from modeling the optical spectrum with simple stellar populations; (4) intrinsic stellar velocity dispersion of the stellar populations, where the higher resolution SDSS spectra are marked with * (LRIS has a maximum resolution of $\sim$200 km s^{-1}, so we do not report values below this); (5) black hole mass inferred from the $M_{\rm BH} - M_\star$ relation of Kormendy and Ho (2013), which has an intrinsic scatter of $\sim$0.29 dex; (6) Eddington ratio, $\lambda = (L_{\rm rad} + L_{\rm mech})/L_{\rm Edd}$.

APPENDIX B

SPECTROSCOPIC FIGURES

In this appendix, we show the spectra for all of our galaxy pairs. For each galaxy pair in our sample, we give two sets of figures. We first show the optical spectra reduction and redshift estimate multi-panel figures. The structure of these plots is as follows: we show: **Top left:** the optical image with sources labeled A and B. The slit is overlaid (dashed green lines) with the gray arrow indicating orientation of the slit. **Top right:** 2D optical spectra. LRIS acquires data separately for the blue (upper panel) and red regions of the spectrum (lower panel). Source A and B are labeled as the lower and upper extracted regions, respectively. We show the extraction regions with dashed lines which follow the polynomial terms given by the trace. We also indicate useful "landmark" spectral features. The brightness is rescaled arbitrarily for readability. **Bottom:** the 1D spectra for each extracted source in the pair before flux calibration. Emission and absorption lines are indicated with blue and red vertical lines, respectively, to estimate redshift. Strong telluric bands are shown as green shaded regions. At this point in the pipeline, the blue and red sides of the spectra are still separated.

In the captions of these diagnostic plots, we give details of what features led us to our redshift estimate. This is done for the spectra that have quality flags in Table 2.2, indicating lower S/N data.

We also show the spectral fitting plots for each source. The two individual sources which could not be fit are shown using a flux-calibrated plot that is not fitted.

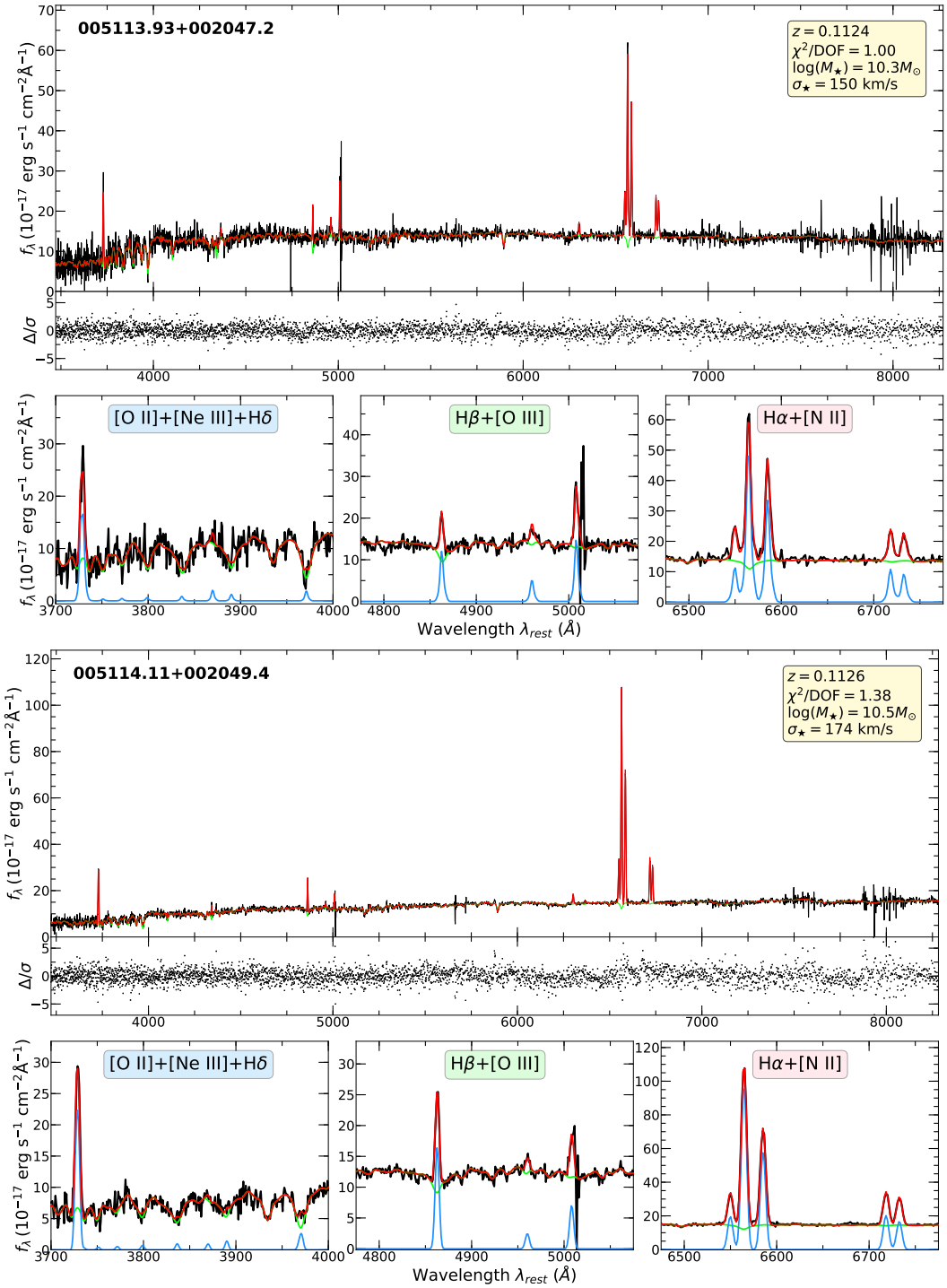

Figure B.1. 0051+0020

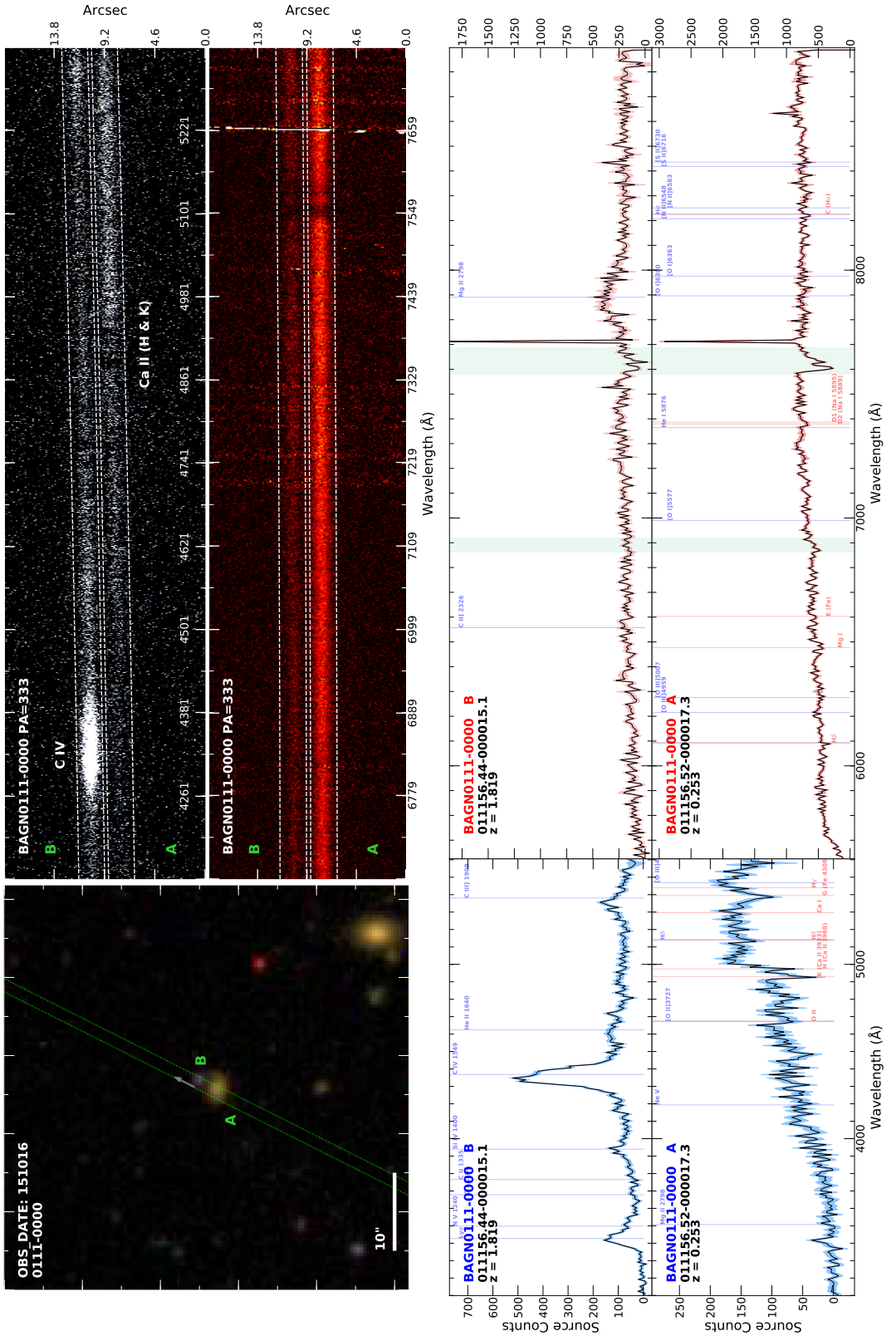

Figure B.2. 0111−0000

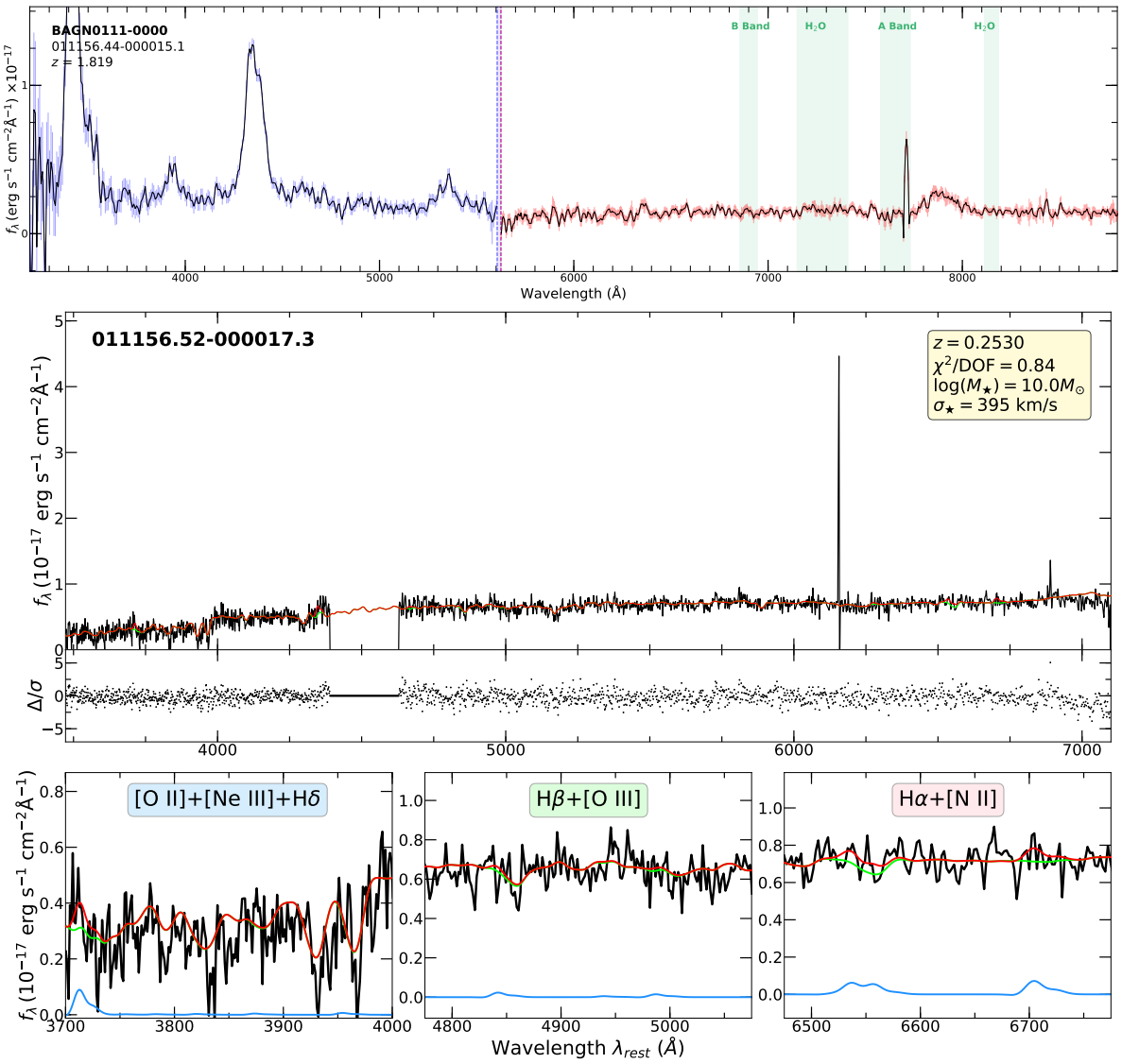

Figure B.3. 0111−0000

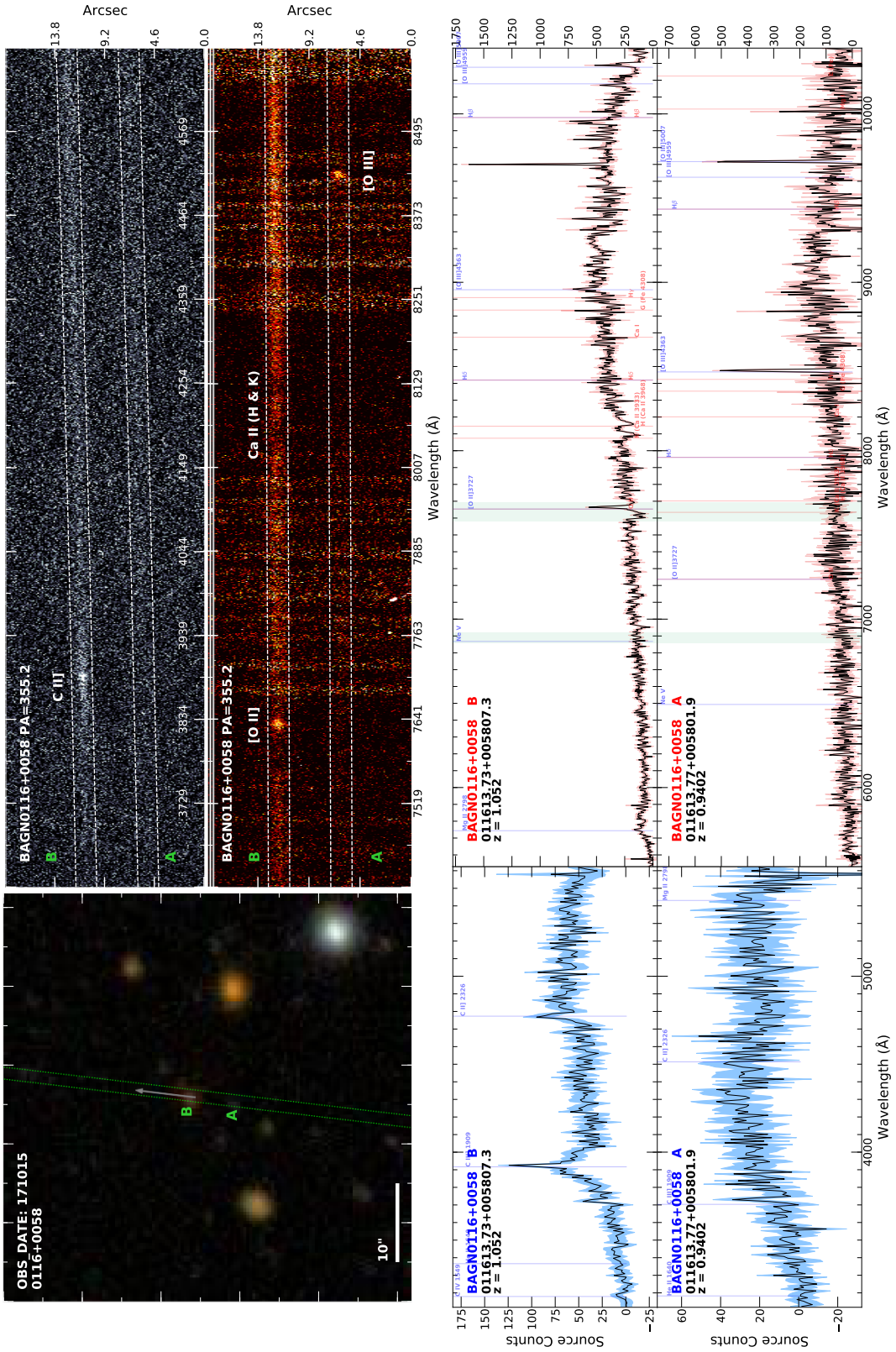

Figure B.4. 0116+0058

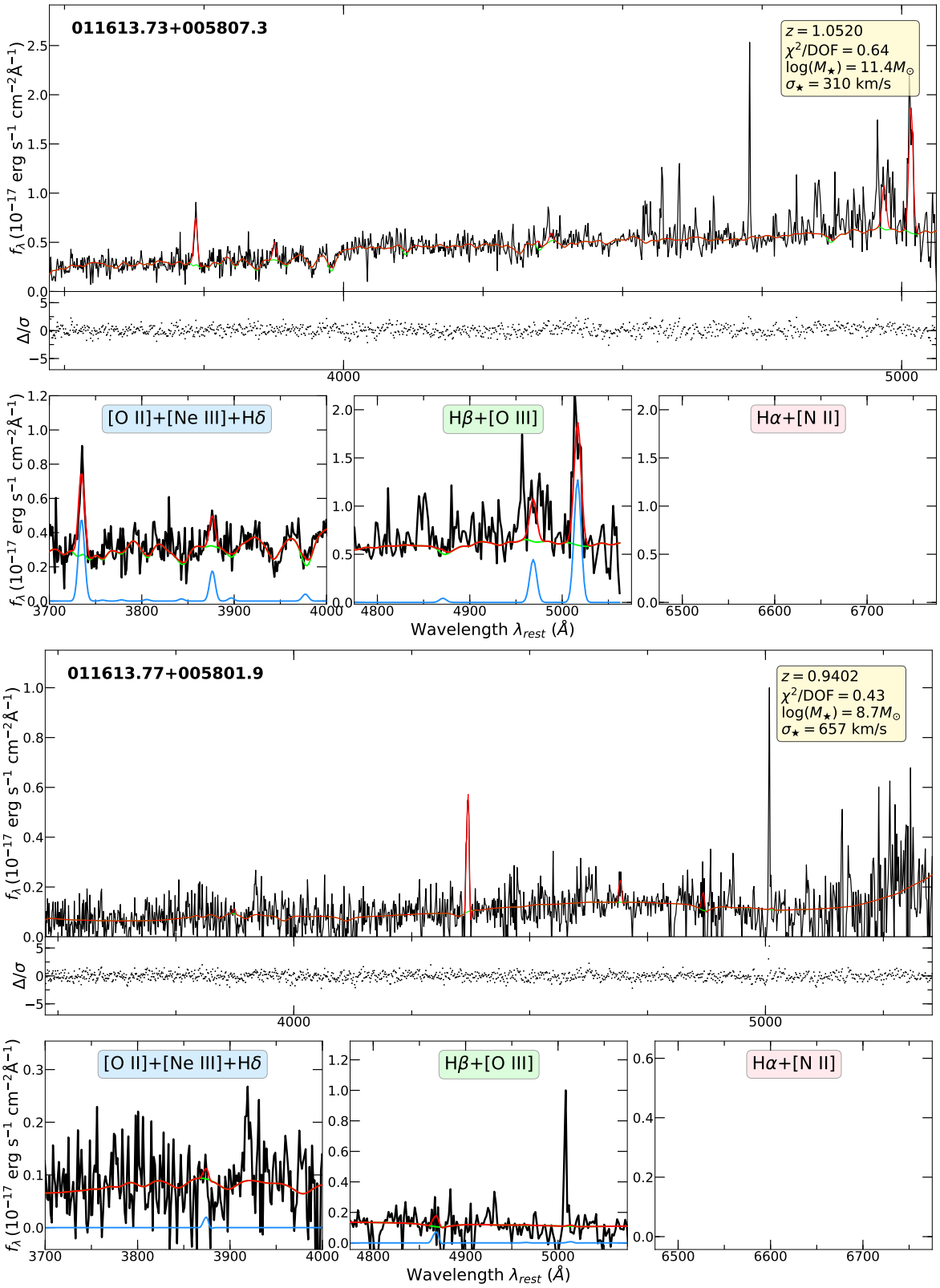

Figure B.5. 0116+0058

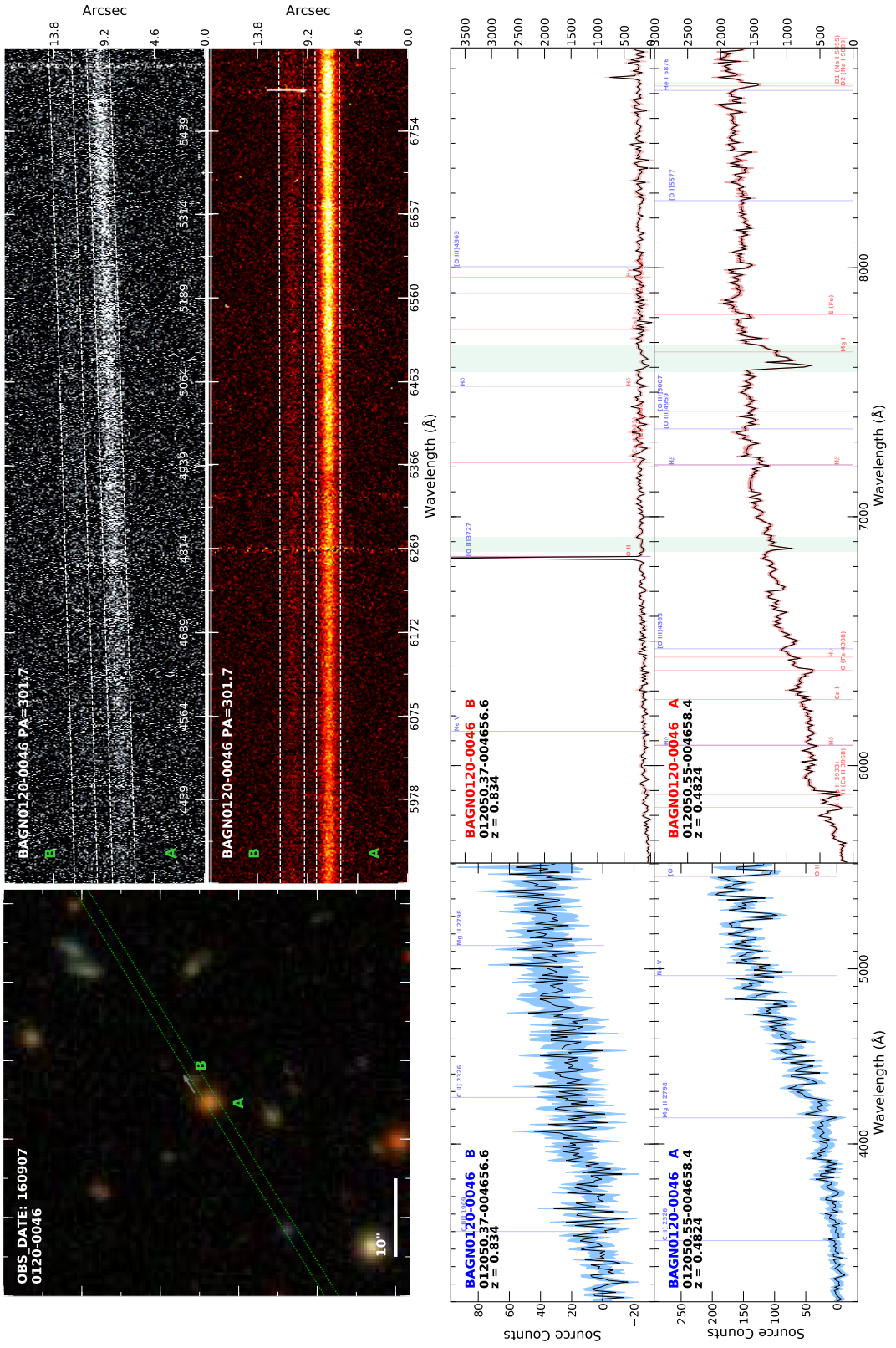

Figure B.6. 0120−0046

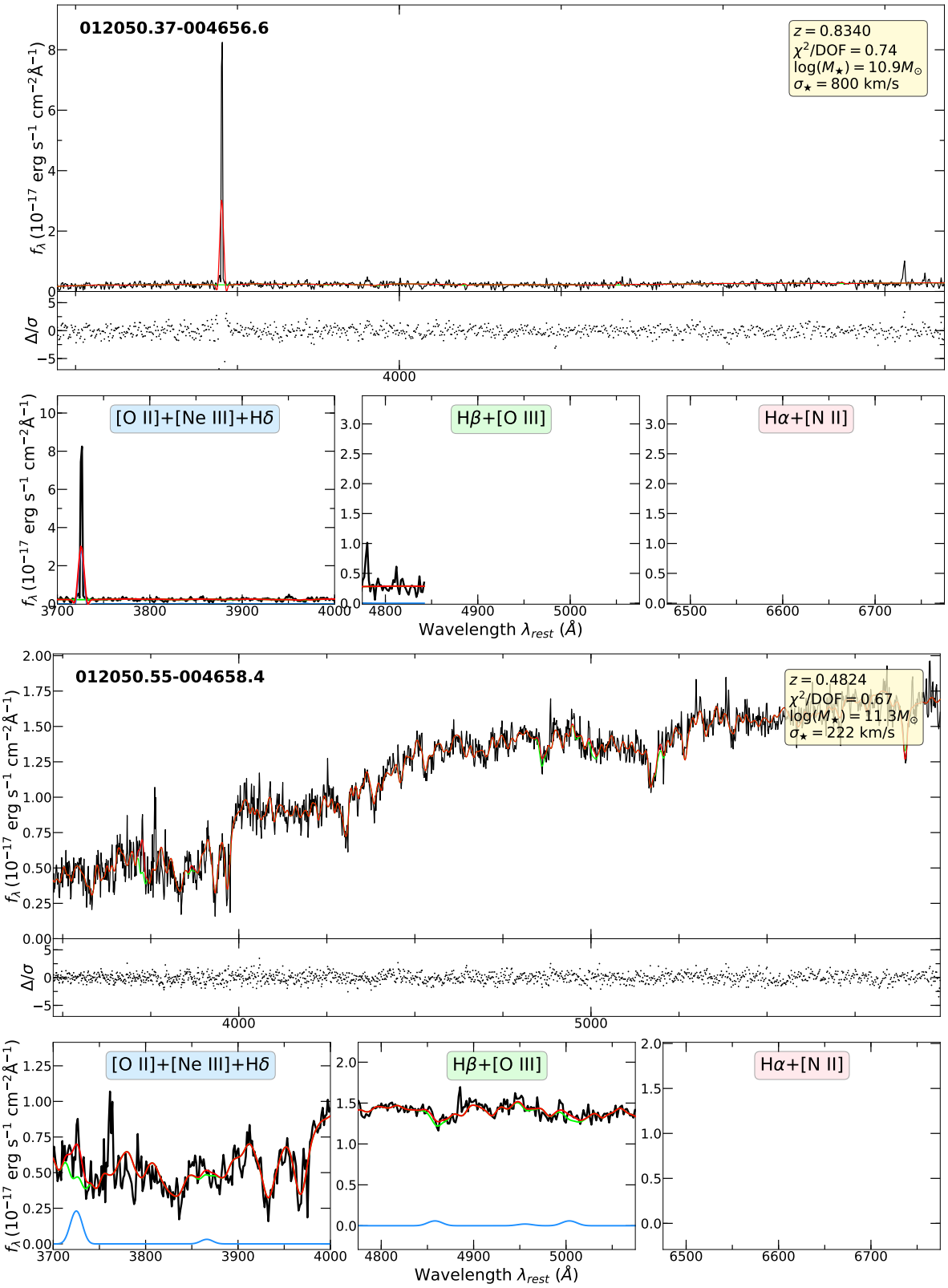

Figure B.7. 0120−0046

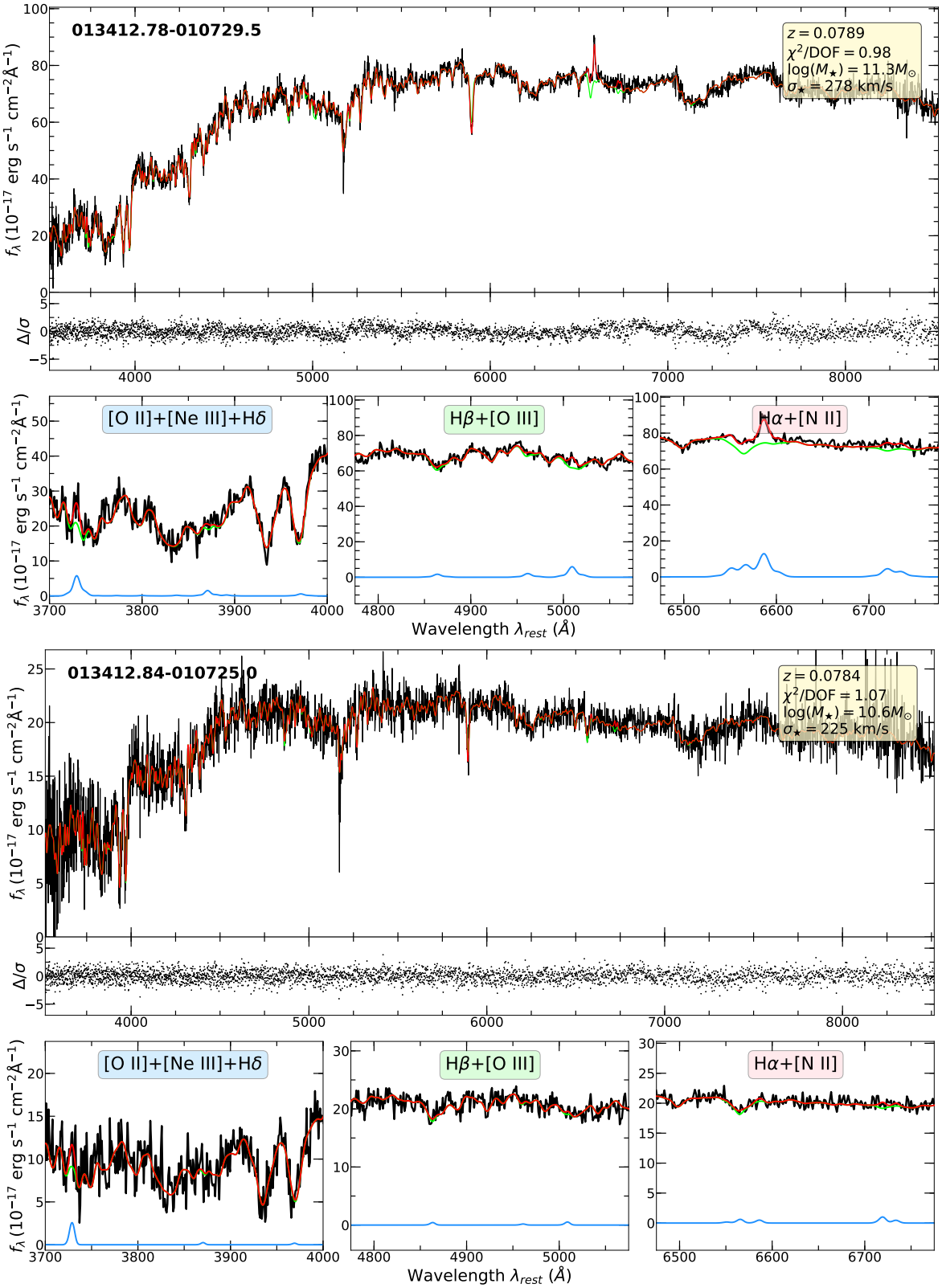

Figure B.8. 0134−0107

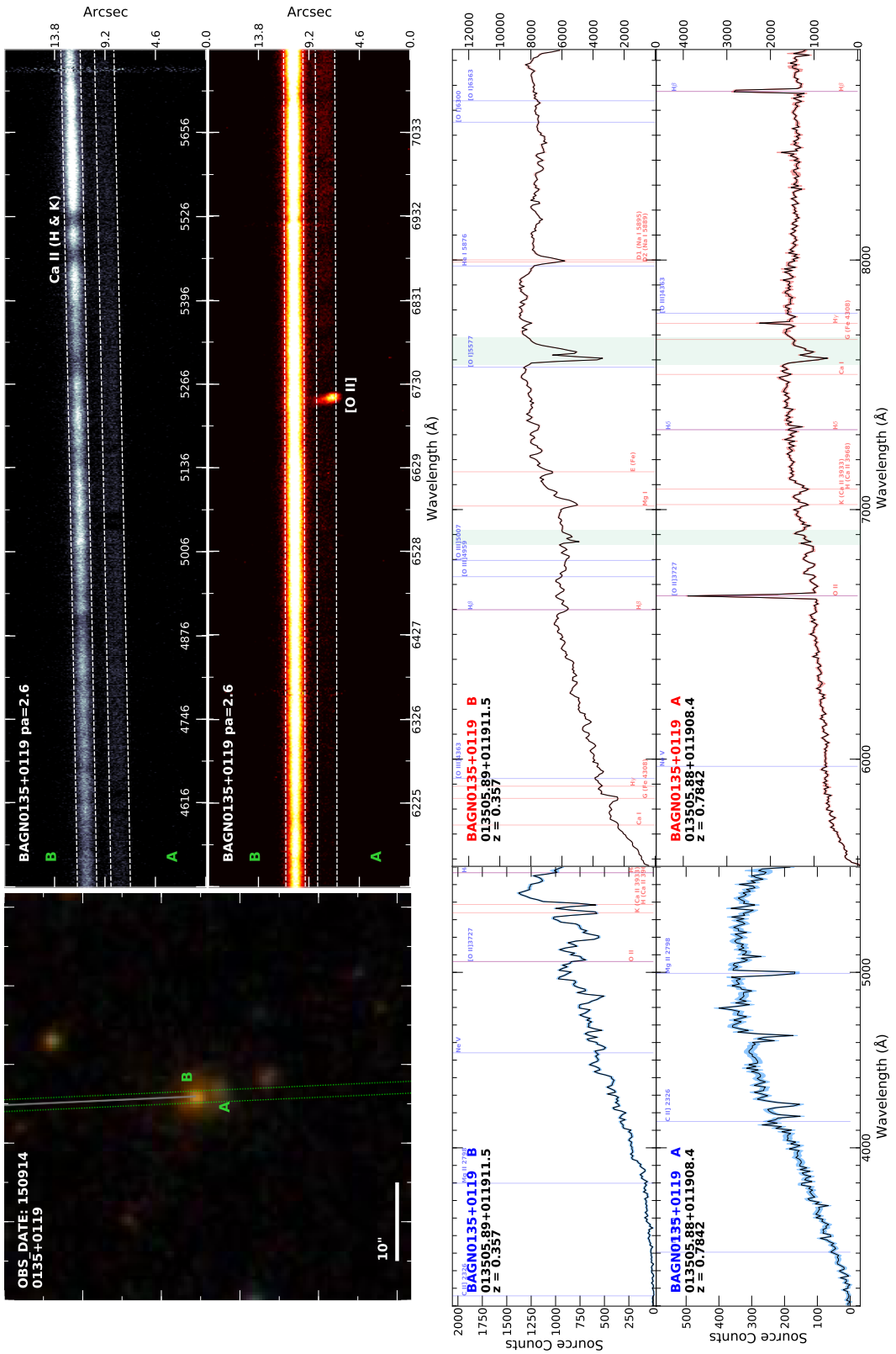

Figure B.9. 0135+0119

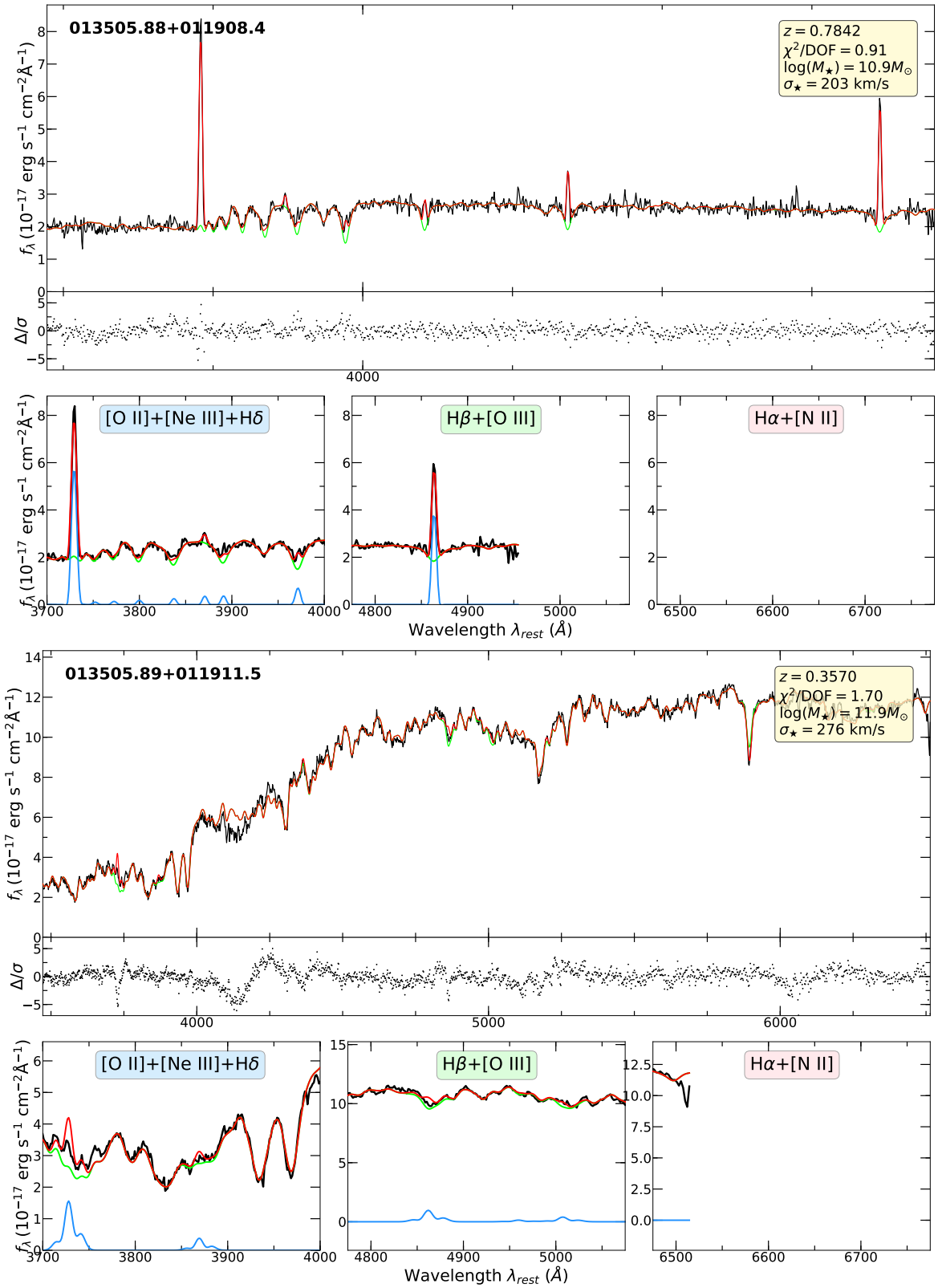

Figure B.10. 0135+0119

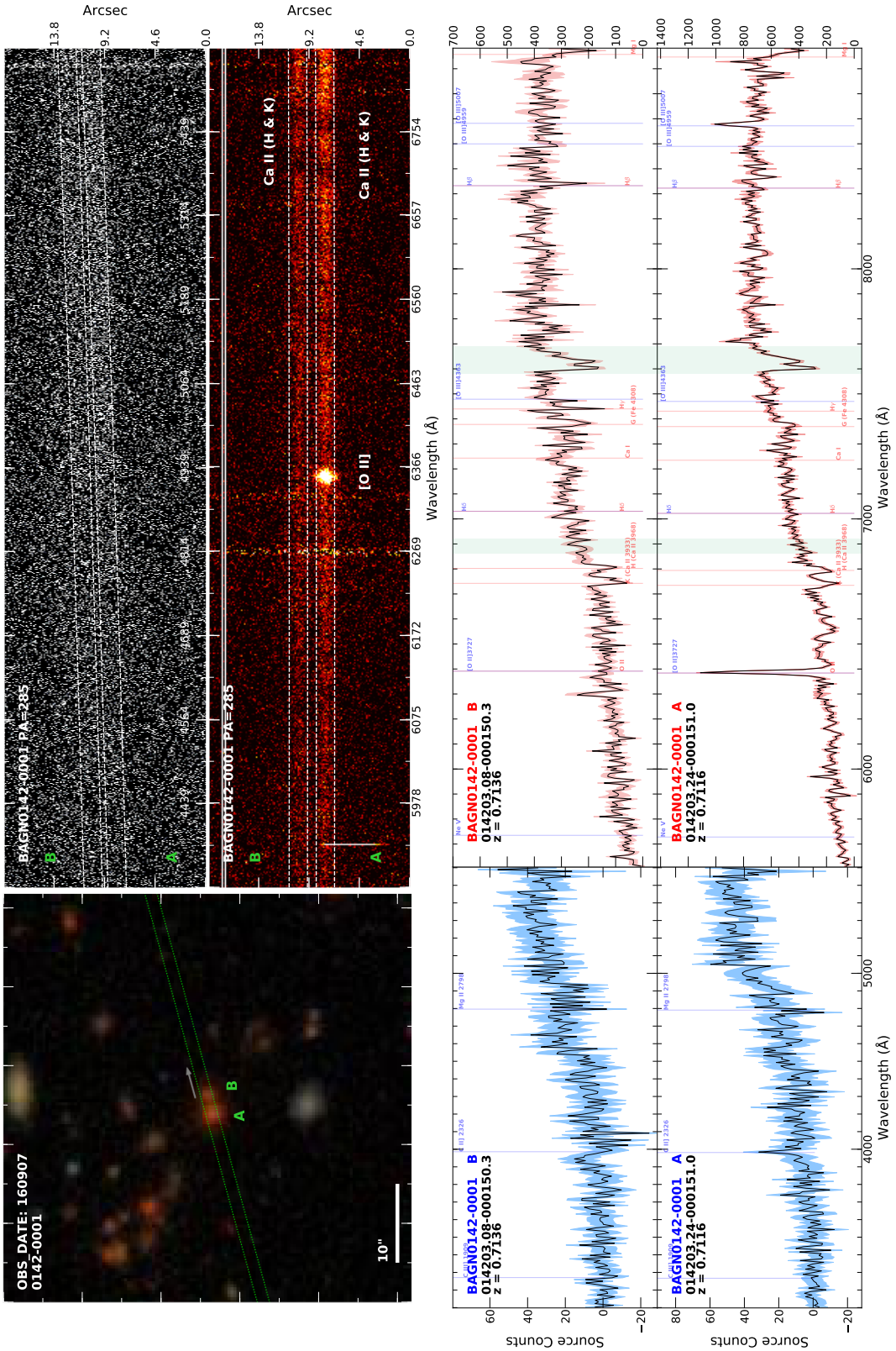

Figure B.11. 0142−0001

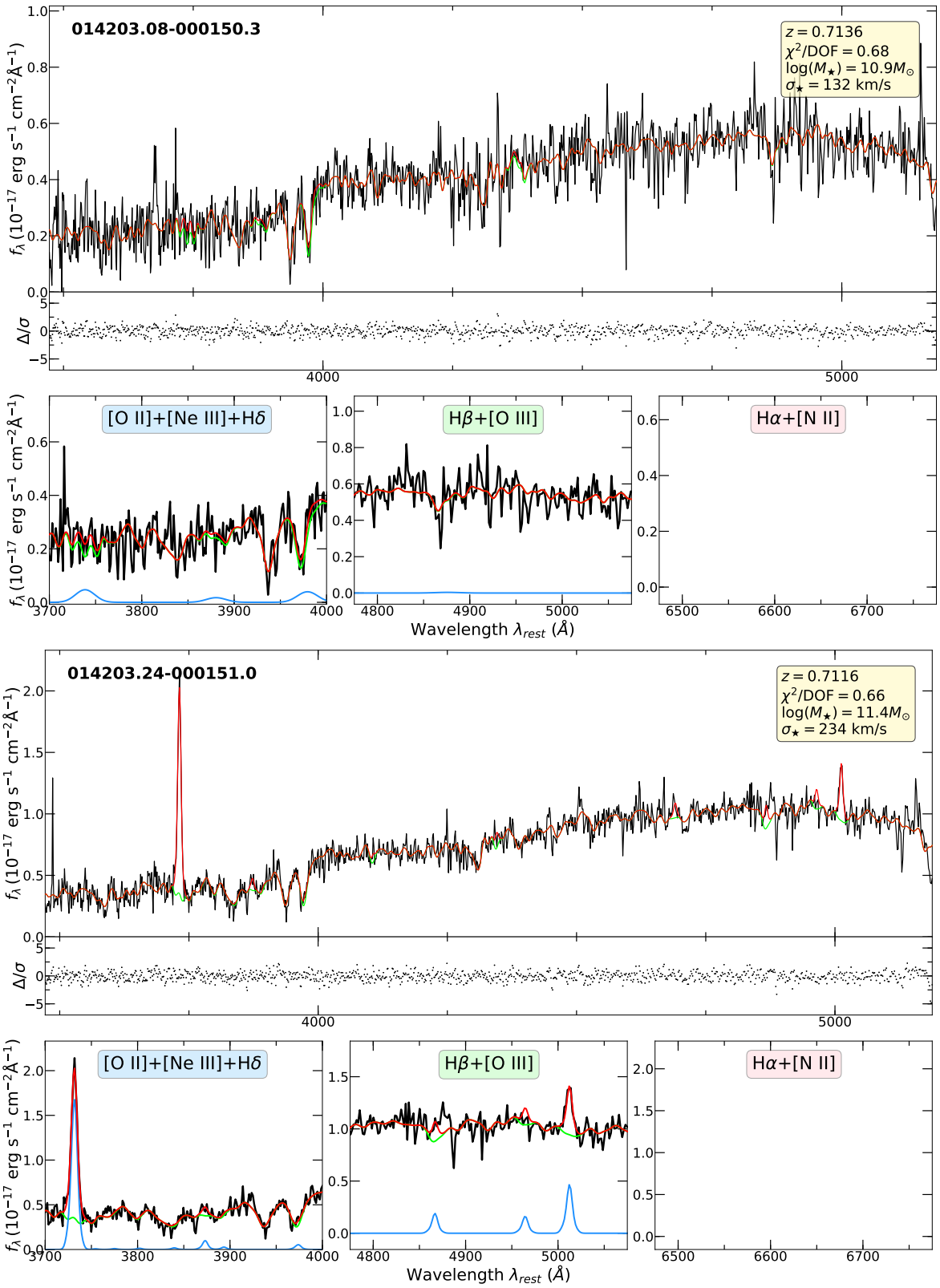

Figure B.12. 0142−0001

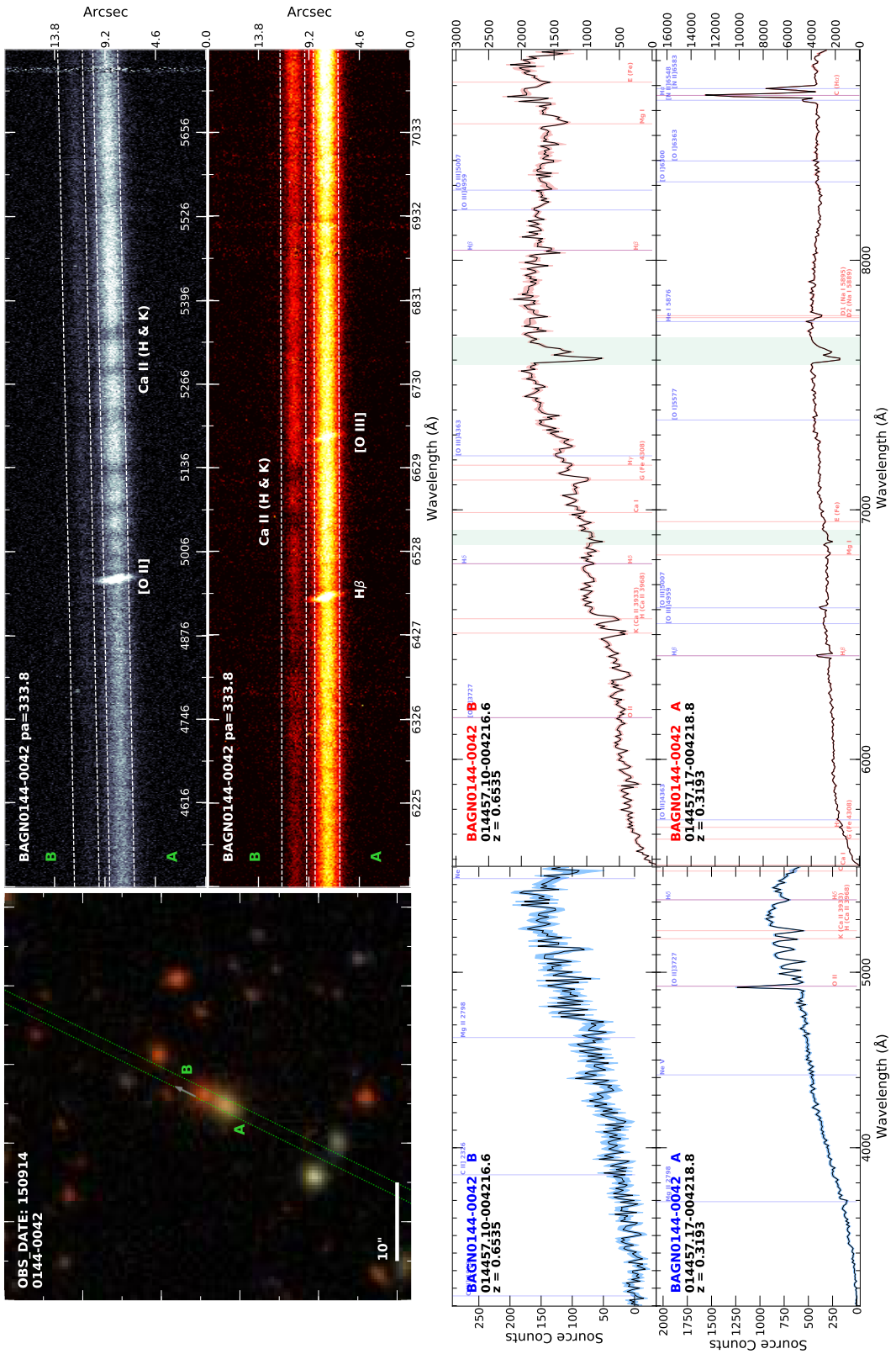

Figure B.13. 0144−0042

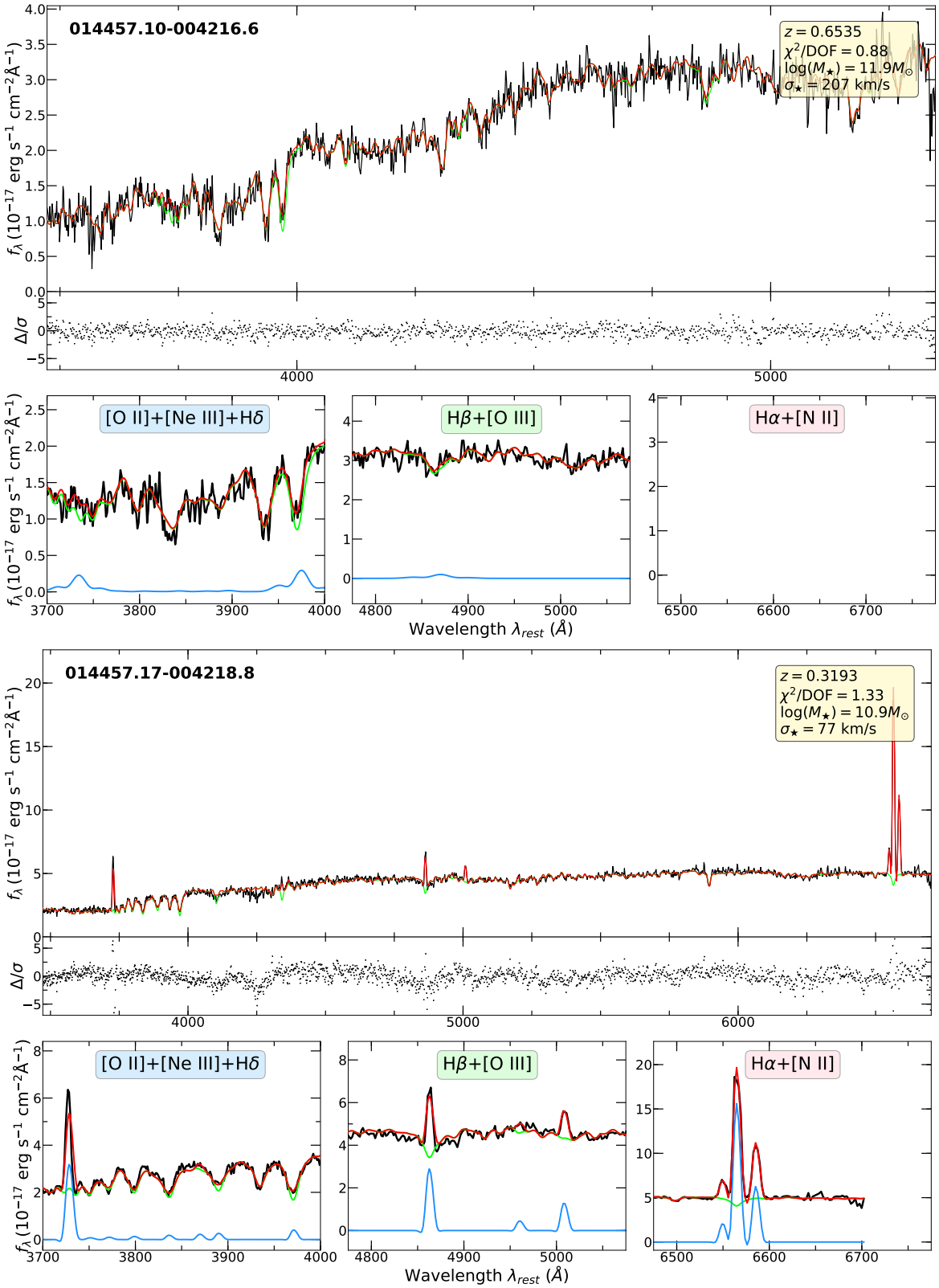

Figure B.14. 0144−0042

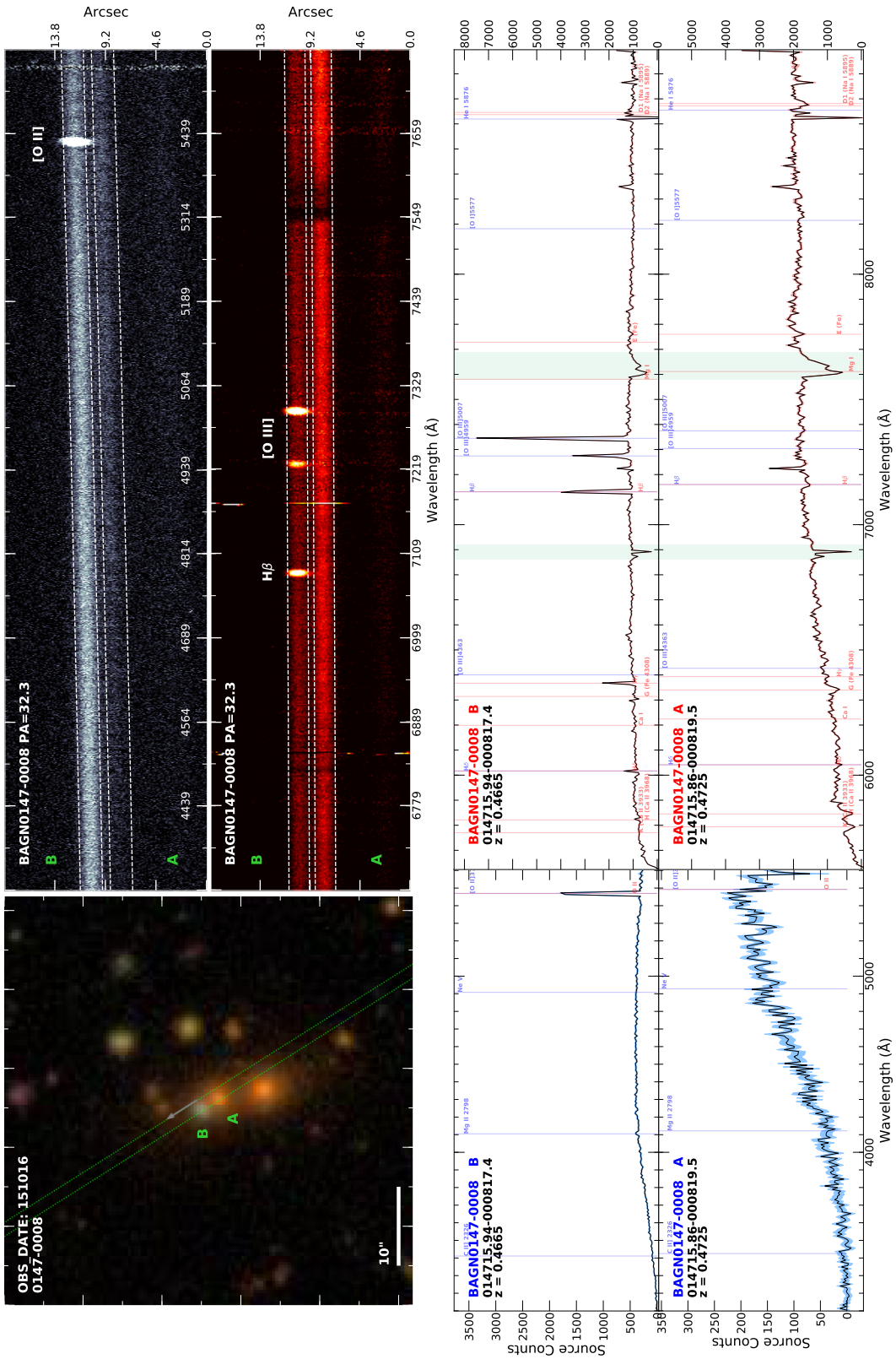

Figure B.15. 0147−0008

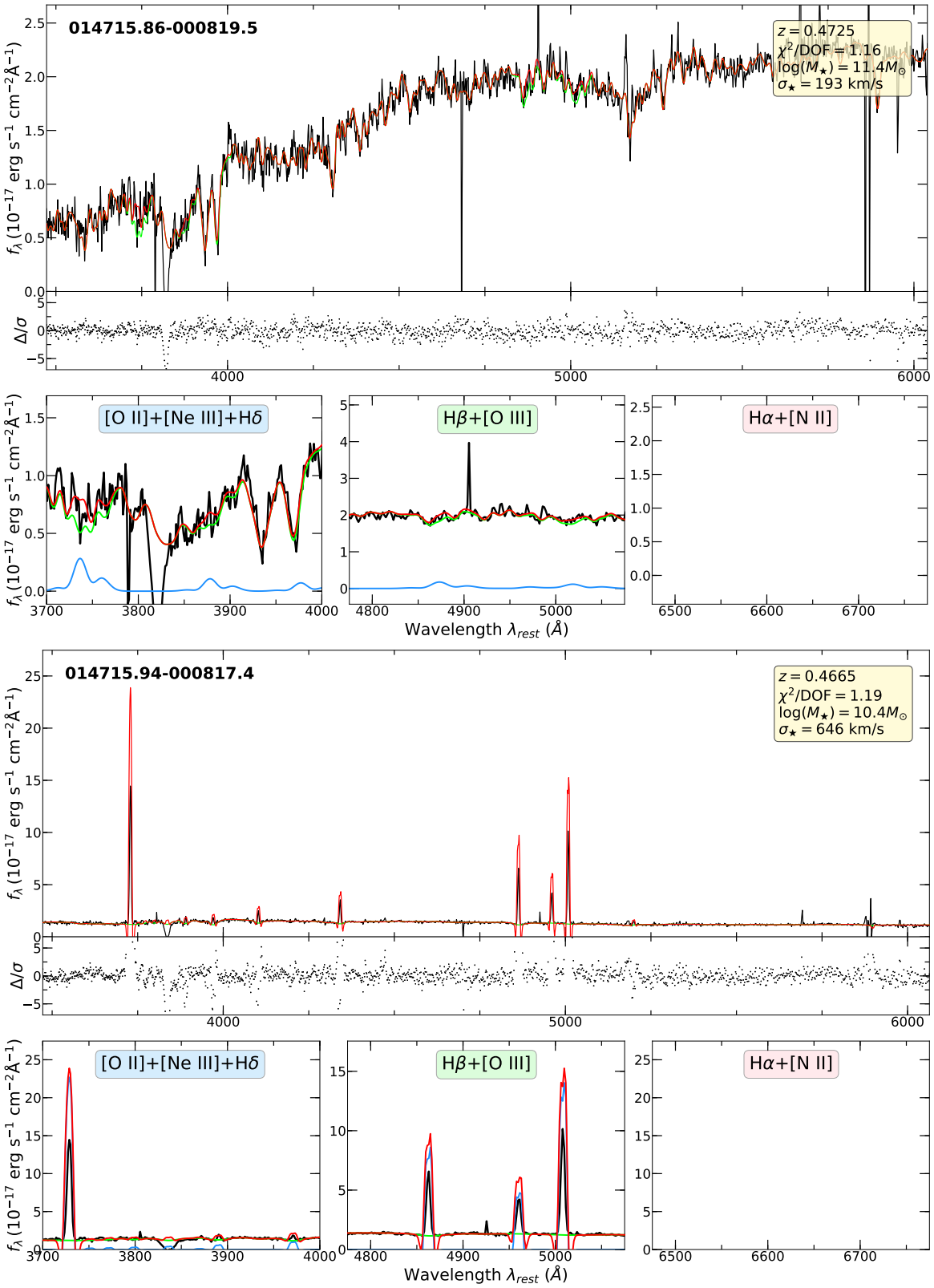

Figure B.16. 0147−0008

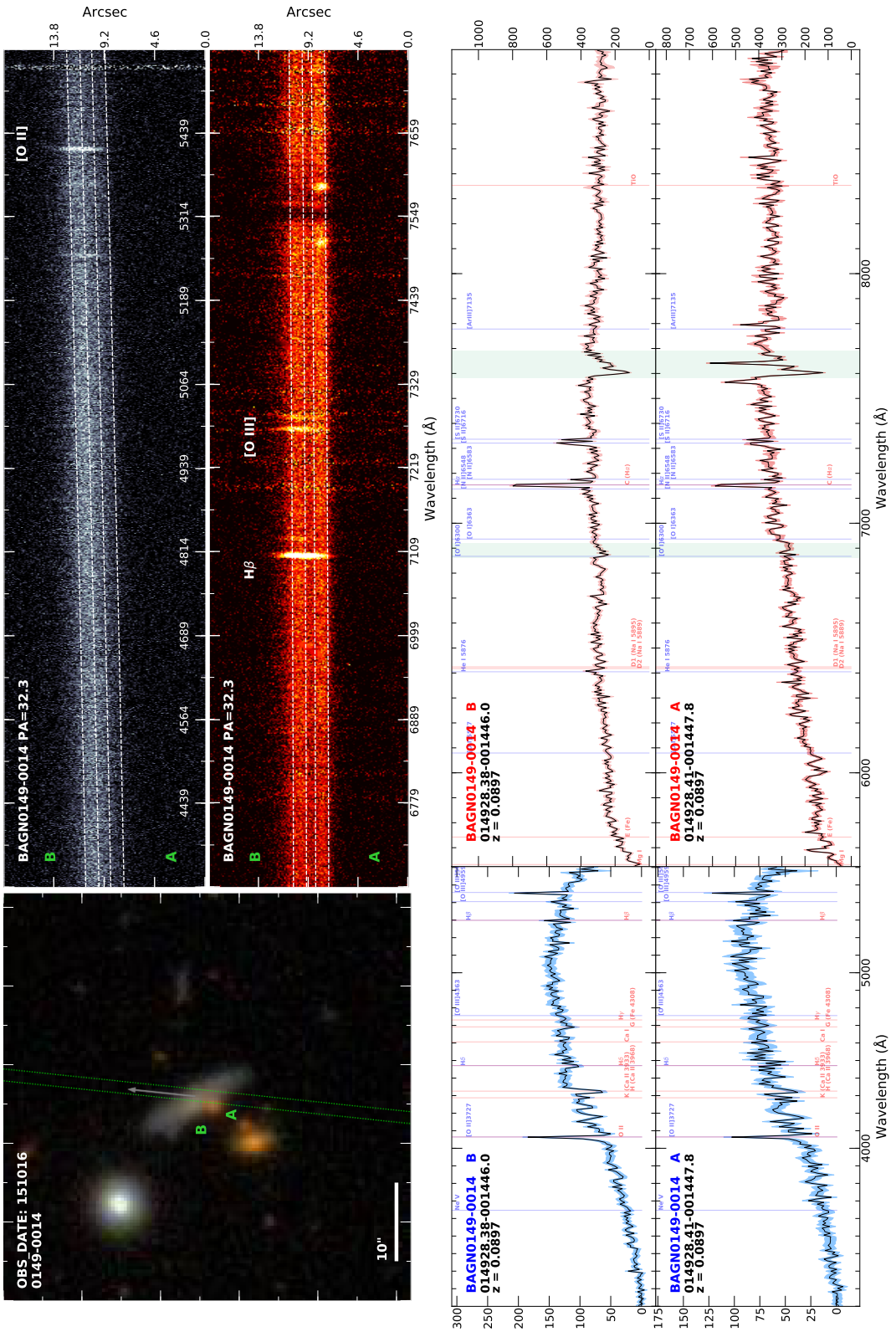

Figure B.17. 0149−0014. This pair required template matching to obtain a redshift estimate. However, we were able to find clear indications of the [N II] and [S II] lines for both objects.

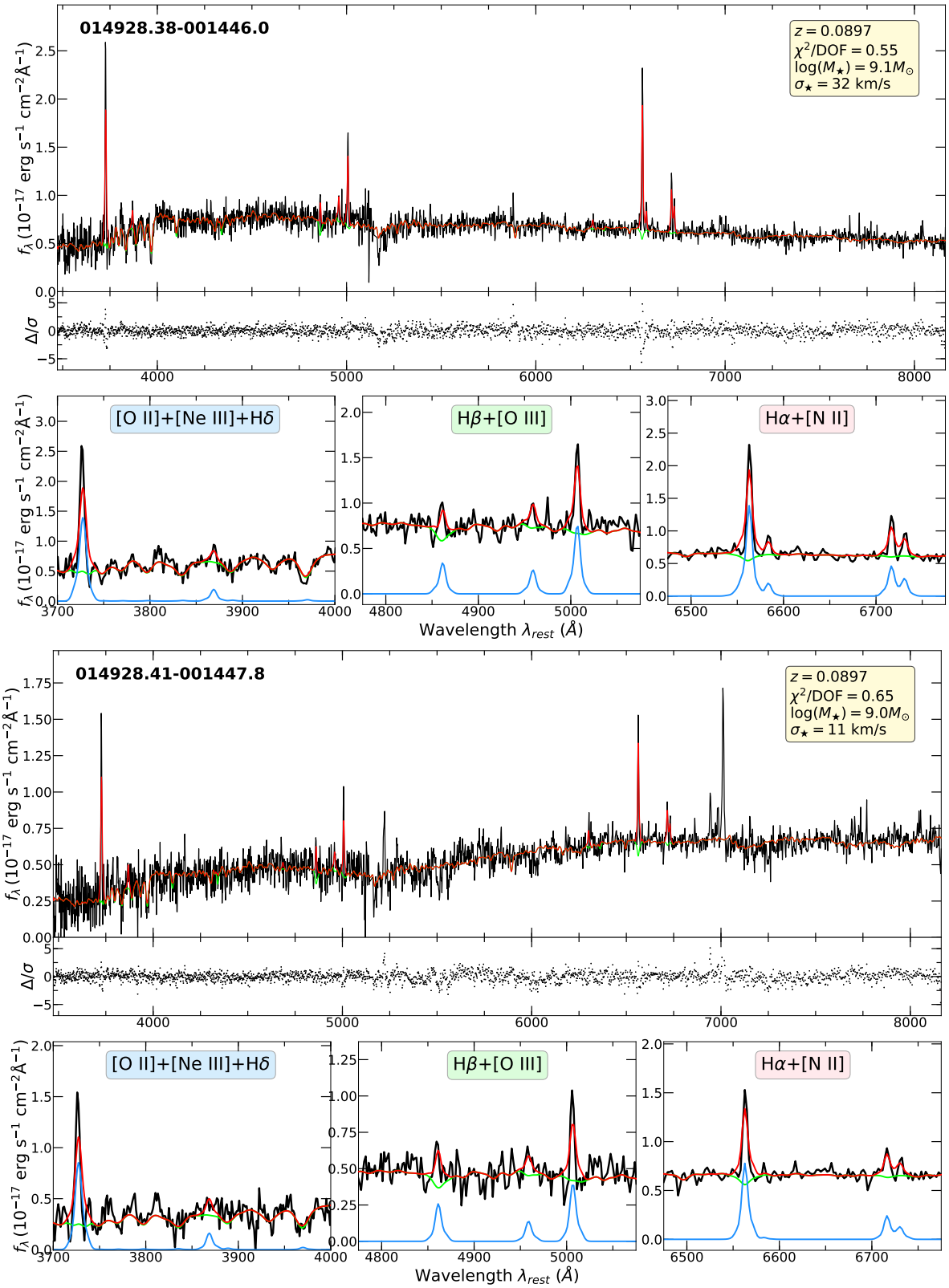

Figure B.18. 0149−0014

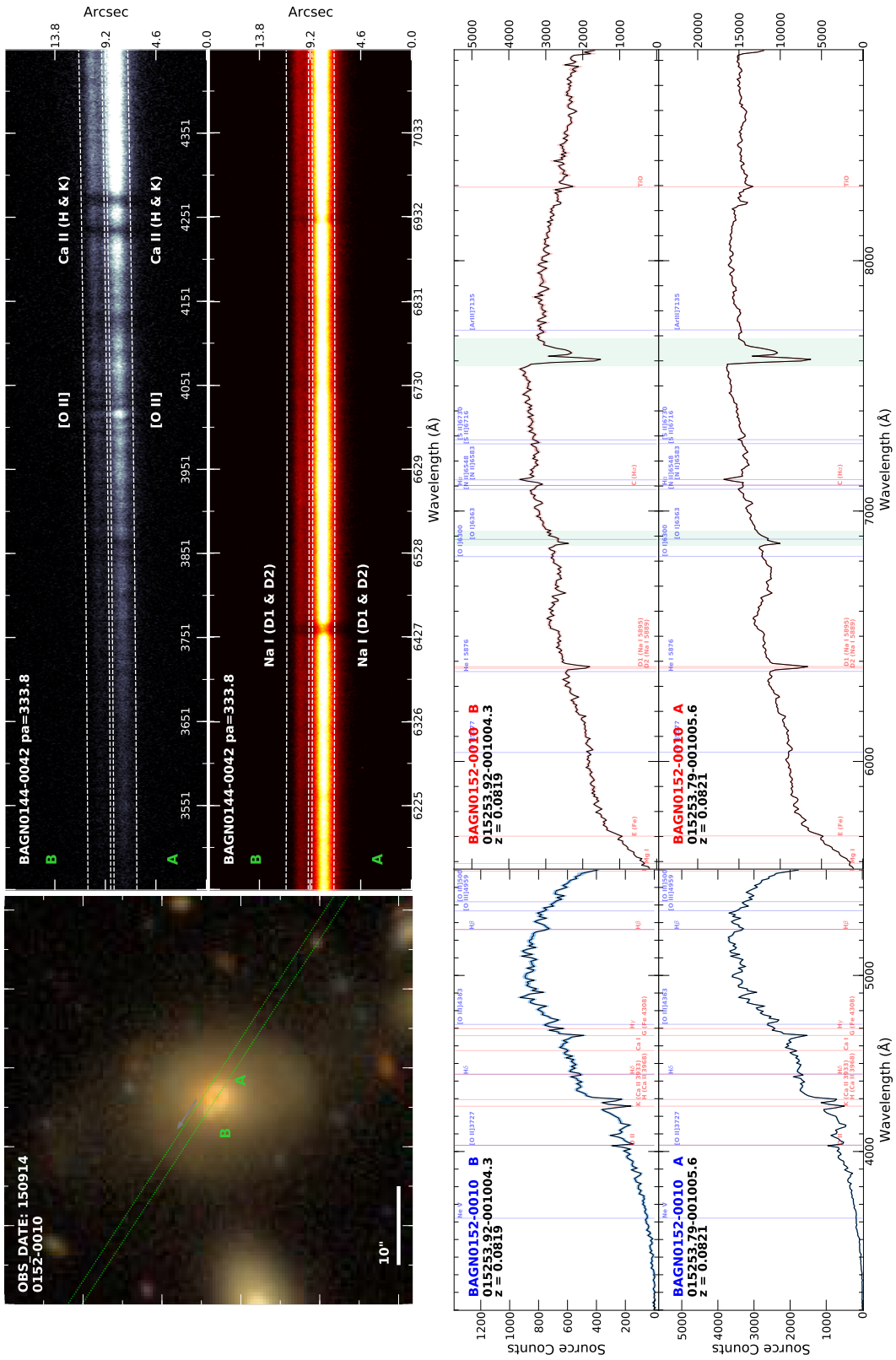

Figure B.19. 0152−0010

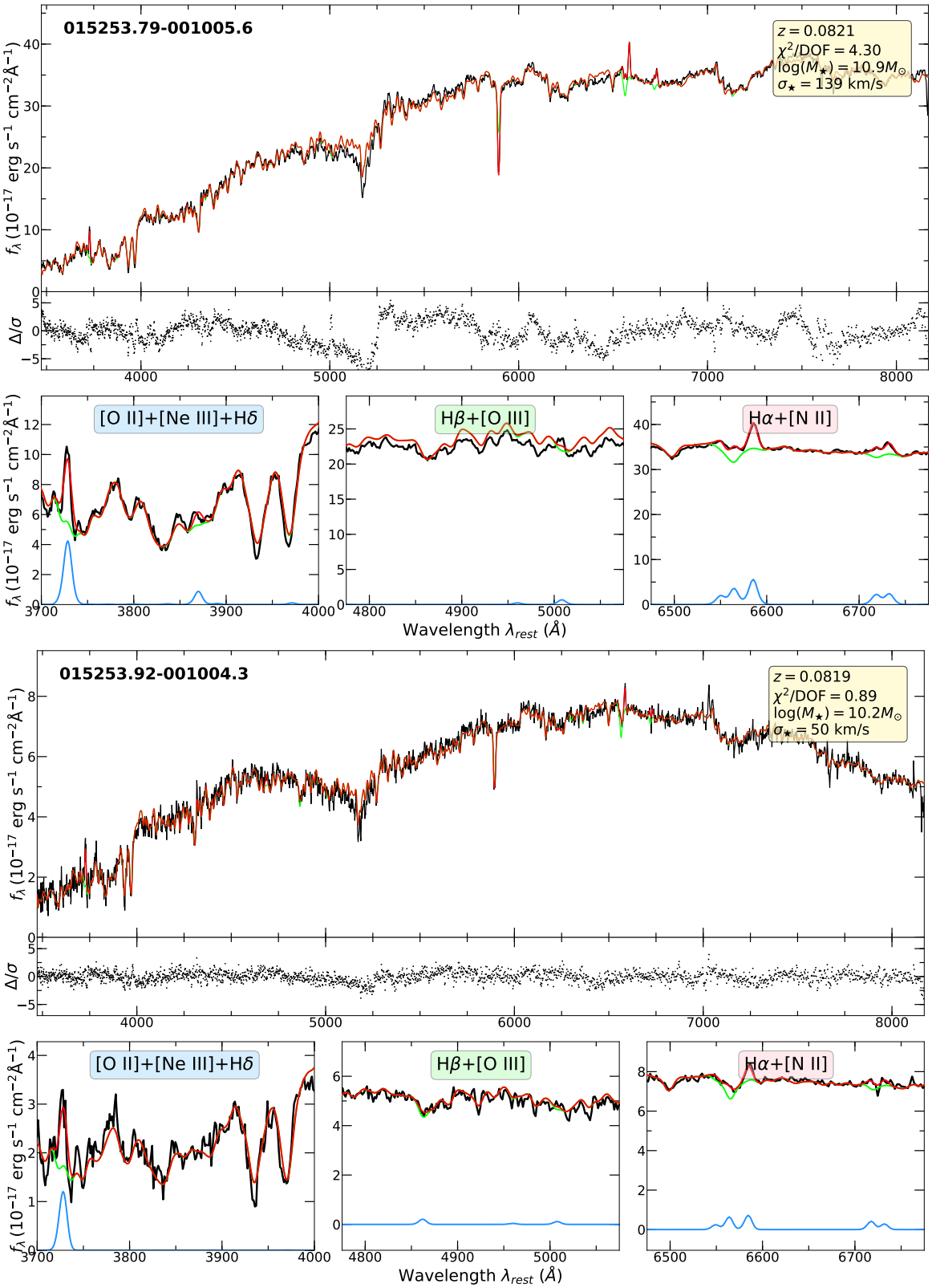

Figure B.20. 0152−0010

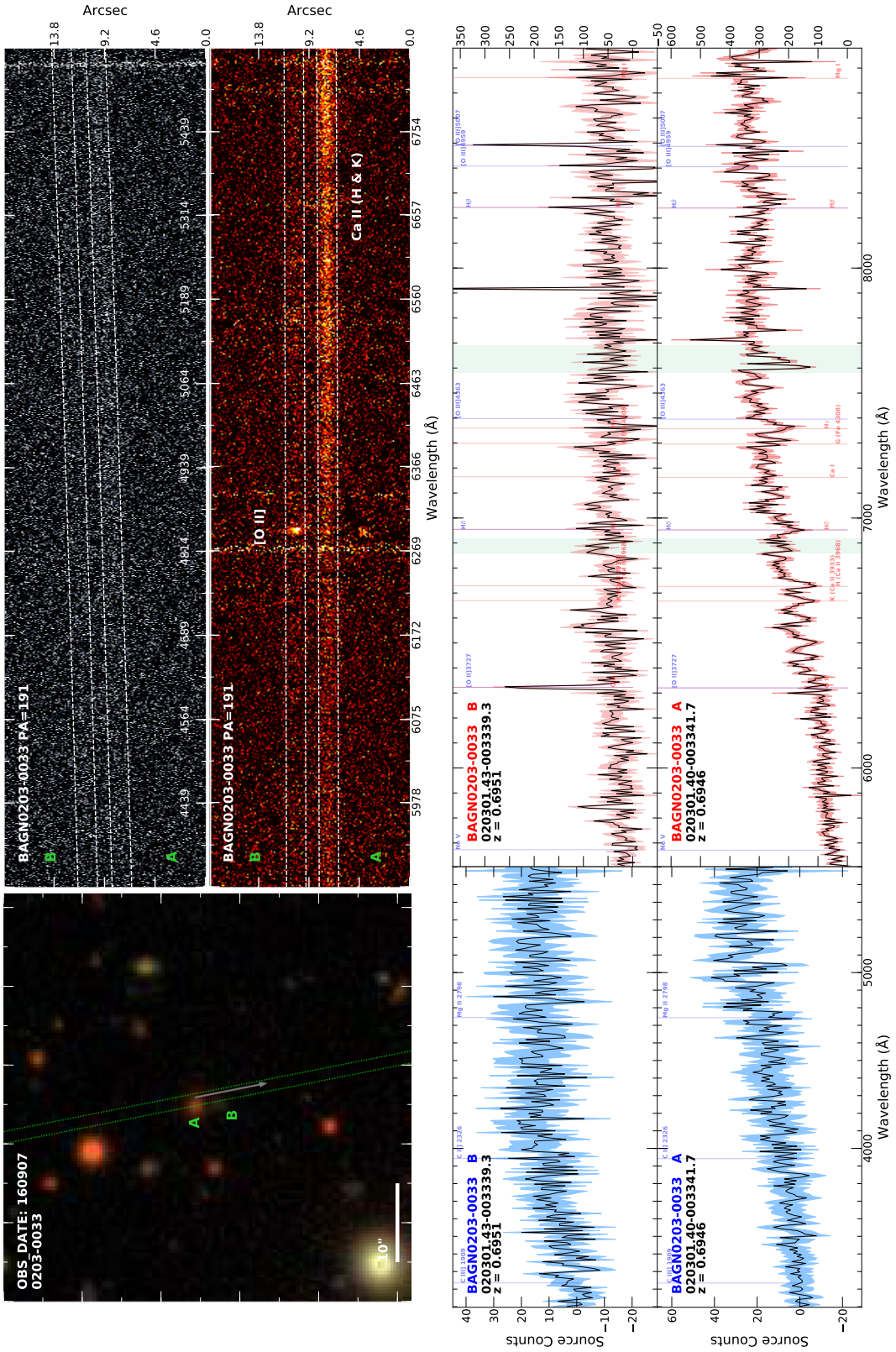

Figure B.21. 0203−0033

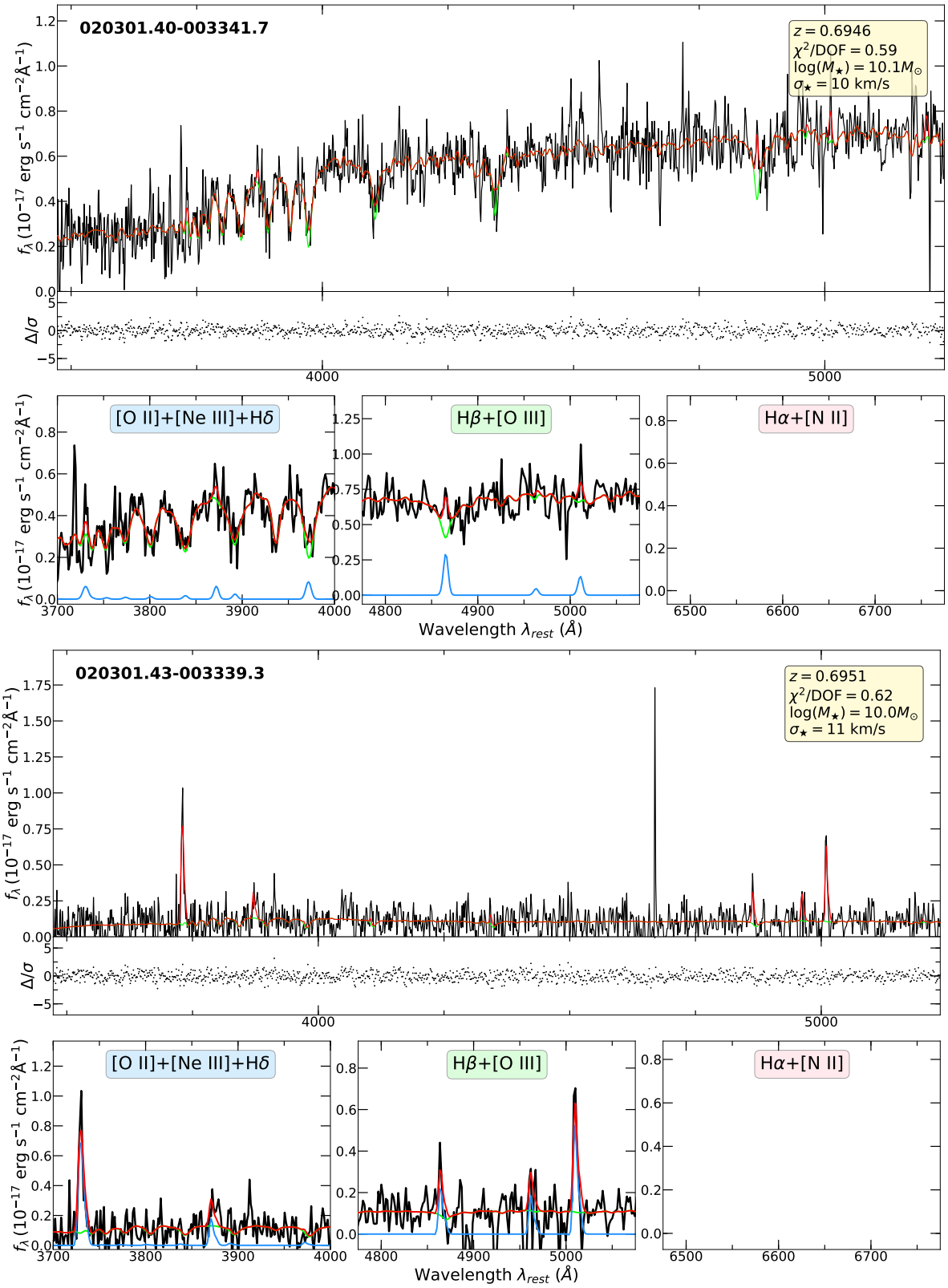

Figure B.22. 0203−0033

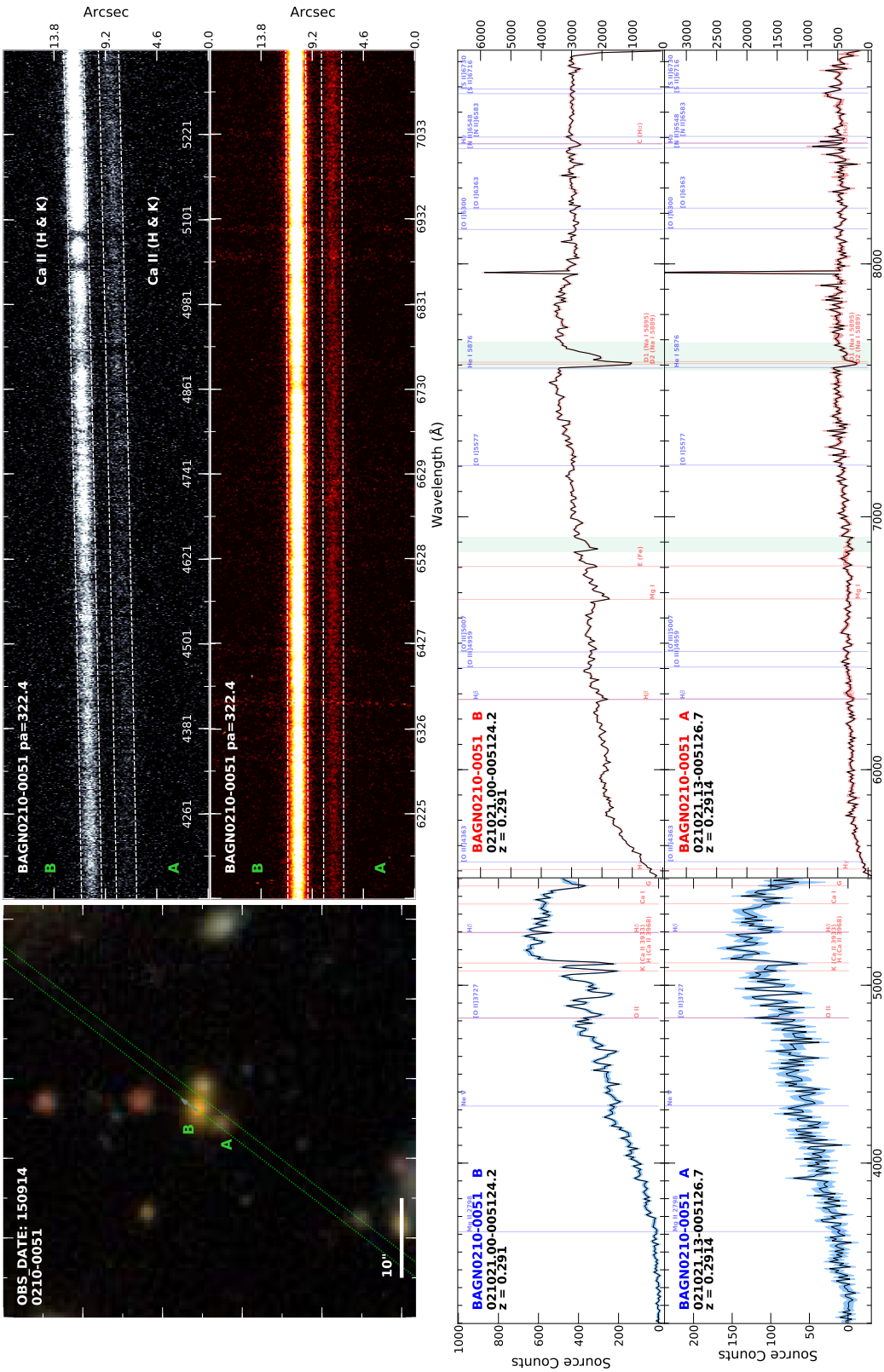

Figure B.23. 0210−0051. This pair required template matching to obtain a redshift estimate. However, we were able to find unambiguous matches of the Ca II H and K absorption features for both objects.

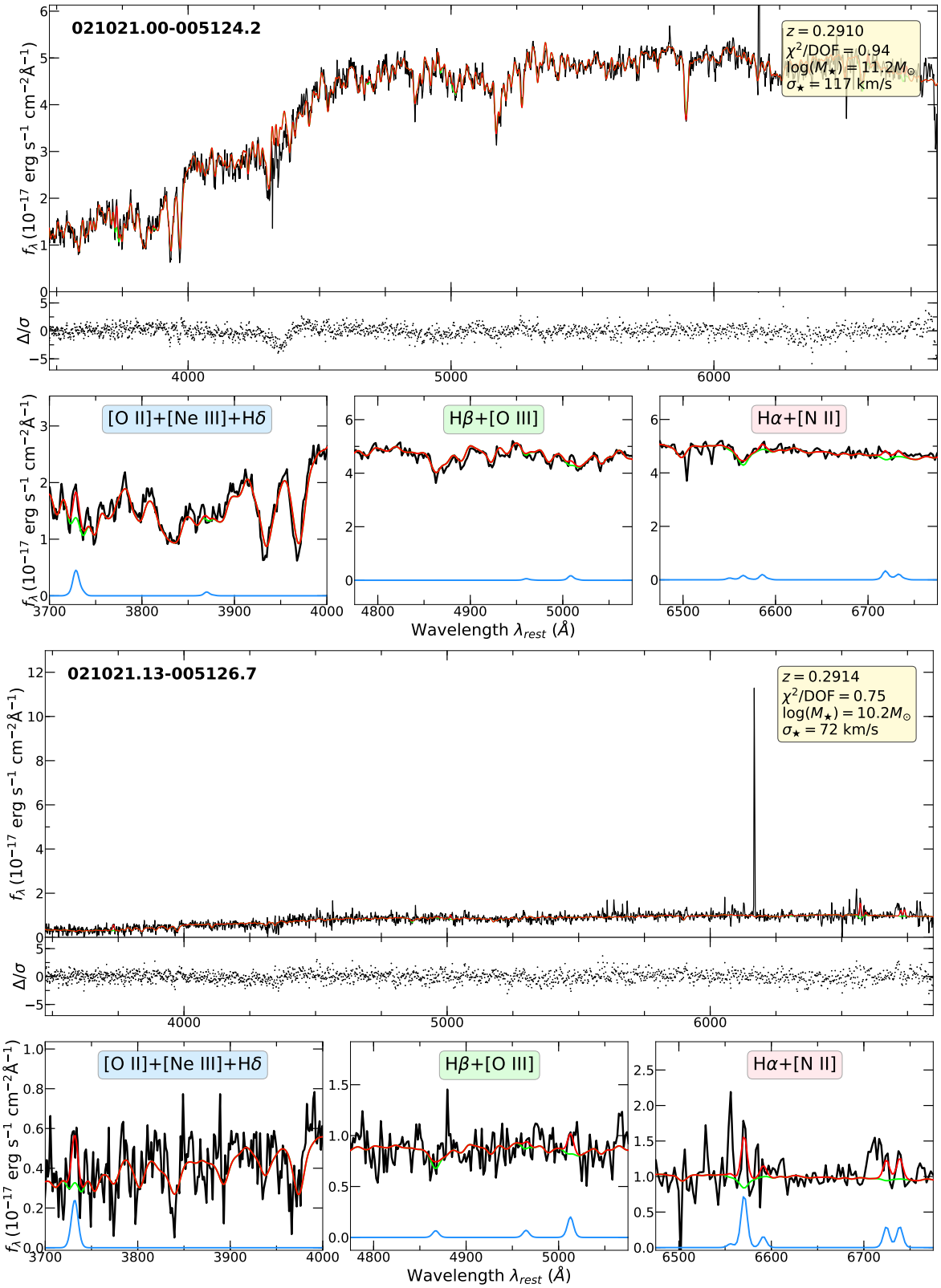

Figure B.24. 0210−0051

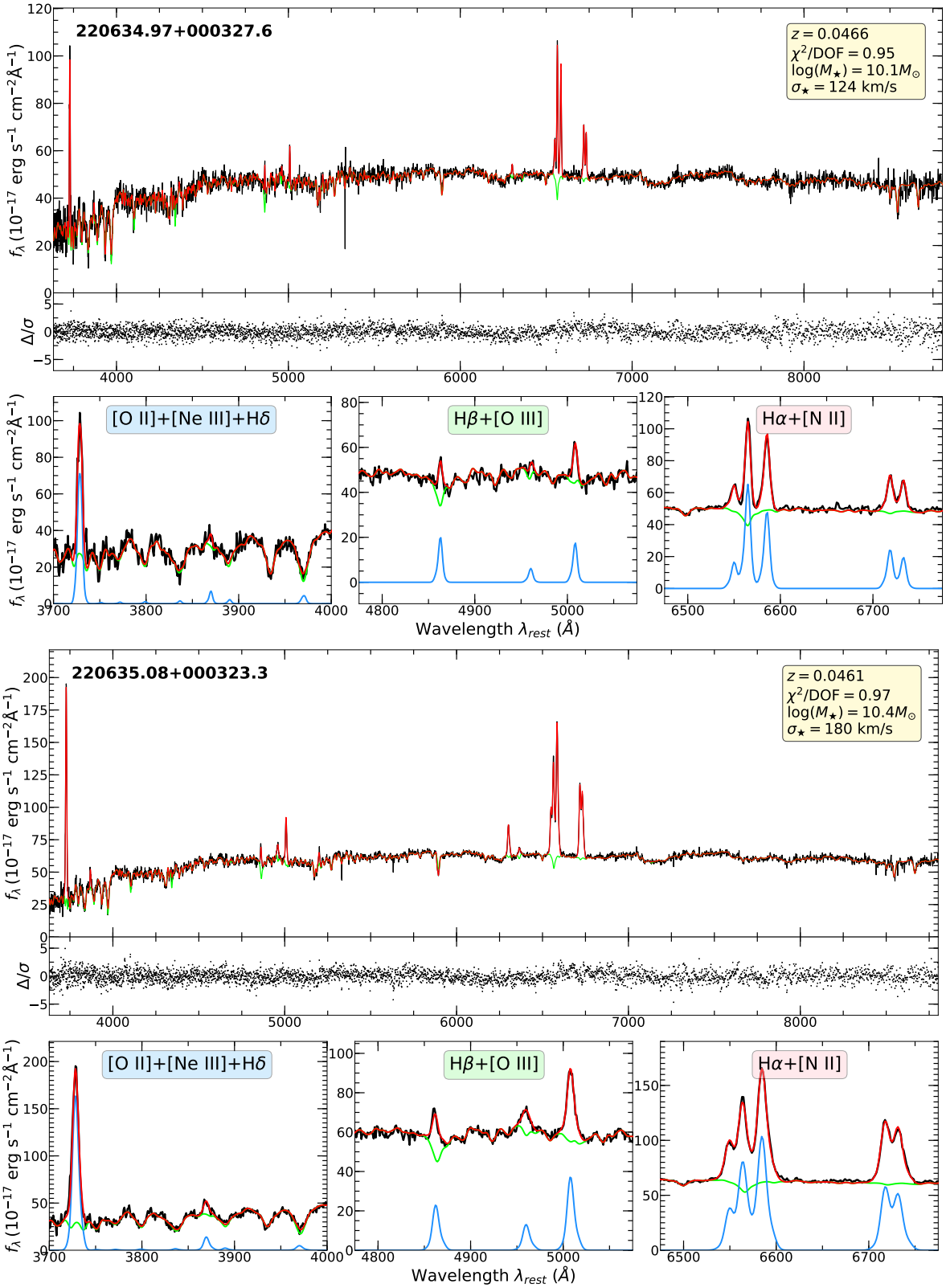

Figure B.25. 2206+0003

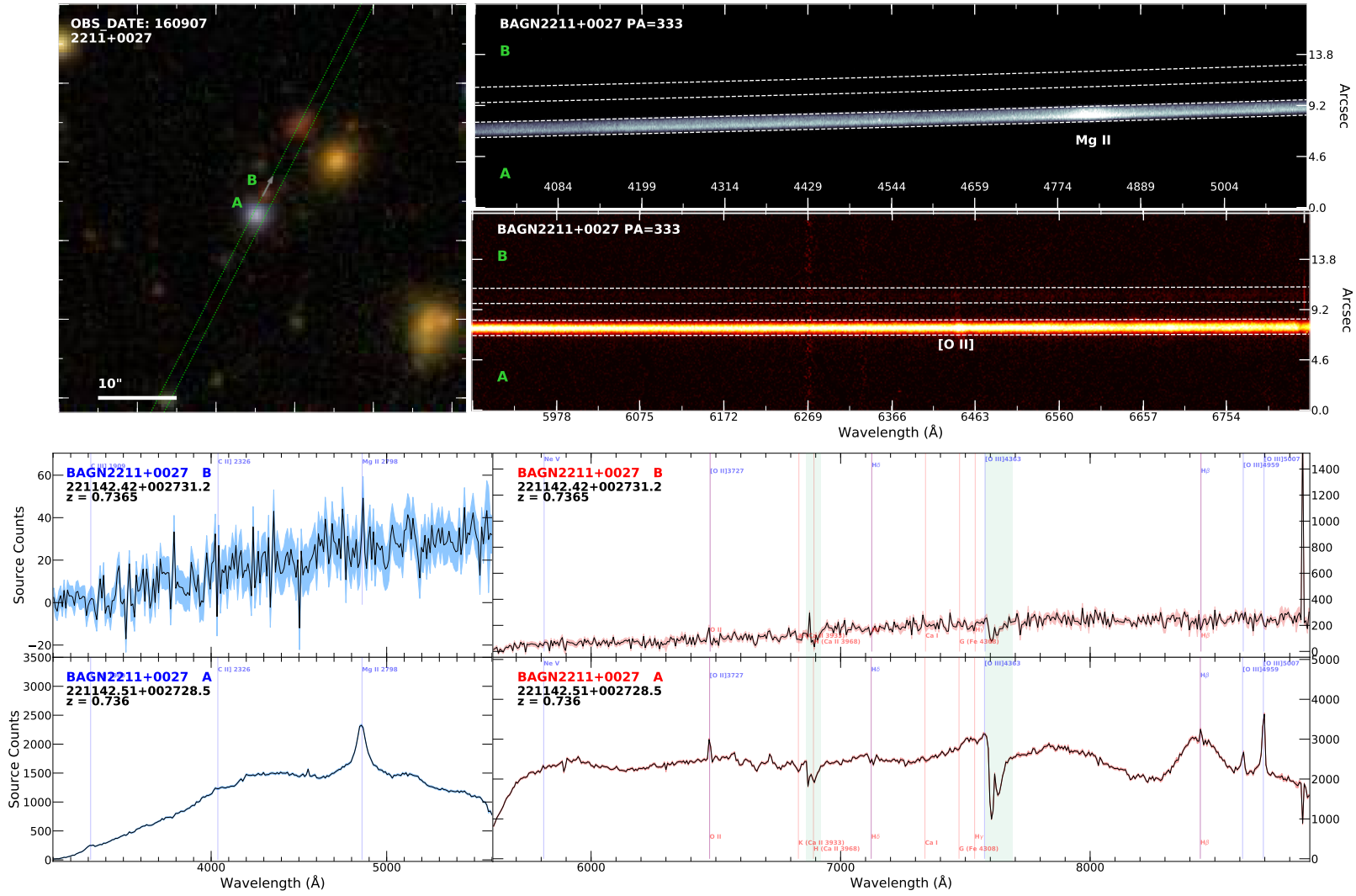

Figure B.26. 2211+0027. This pair required template matching to obtain a redshift estimate. This pair was trickier than most. The upper source shows indications of the Ca II H and K absorption, while the lower source has evidence the [O III] emission lines around a broadened Hβ.

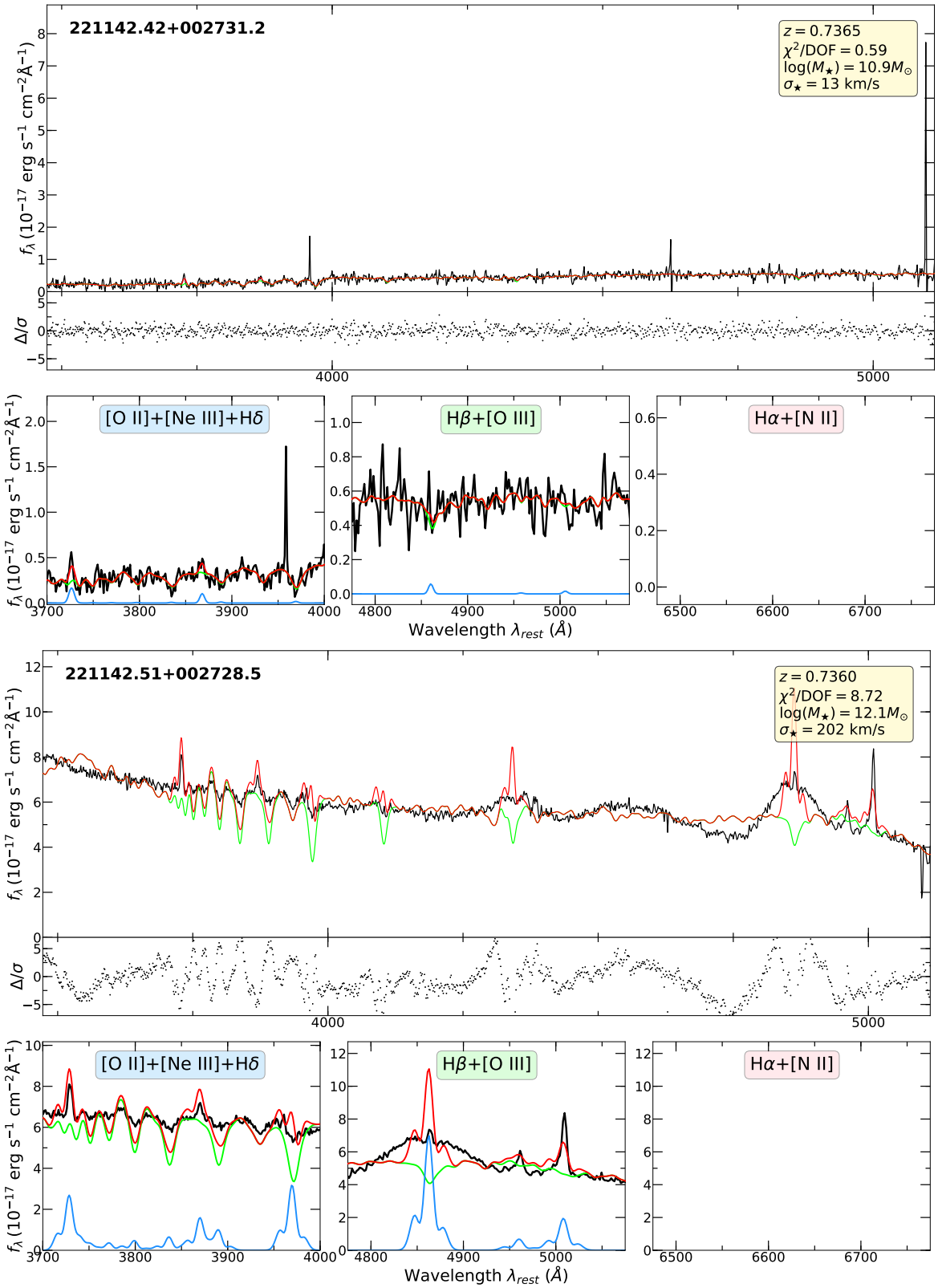

Figure B.27. 2211+0027

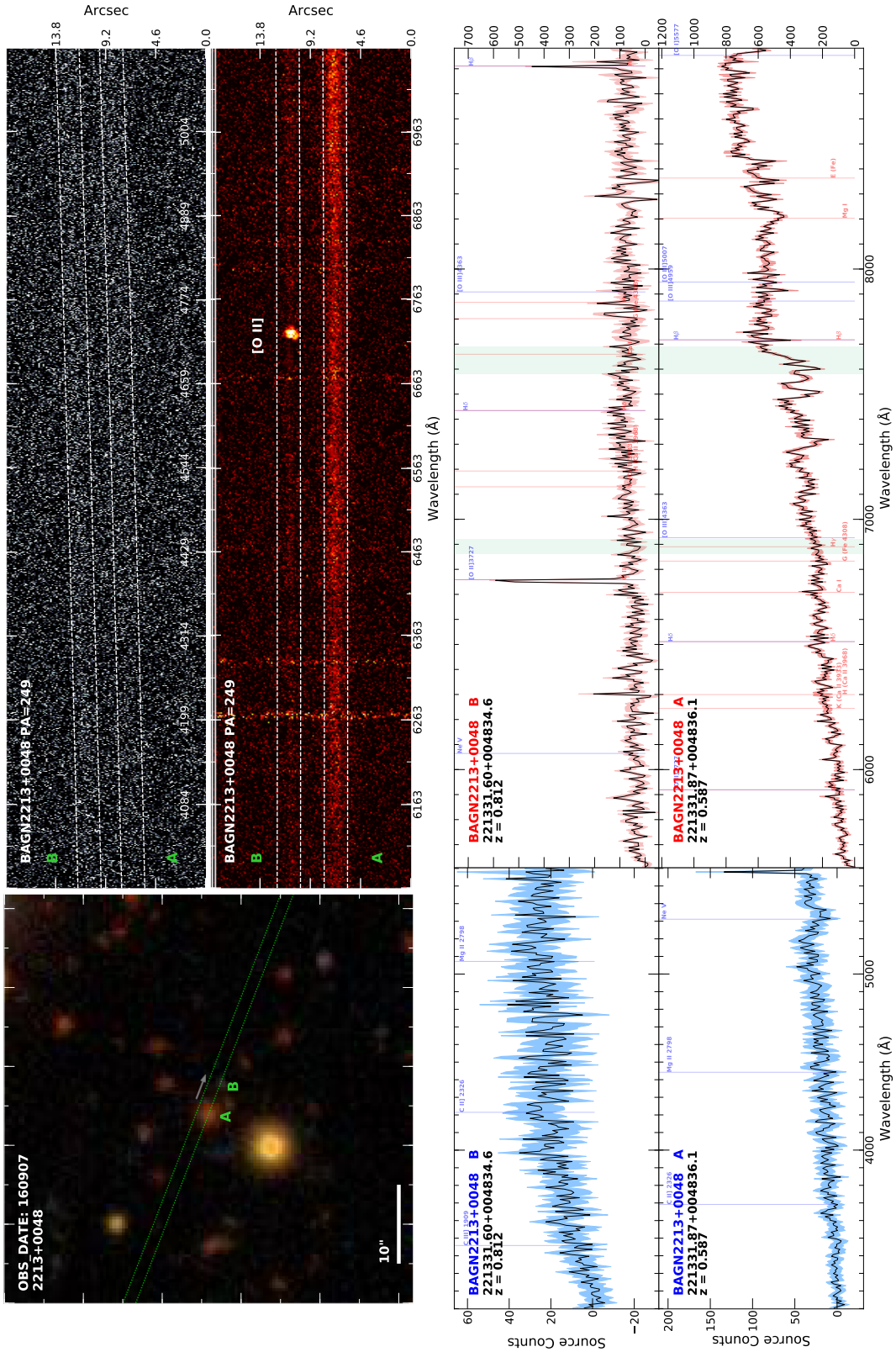

Figure B.28. 2213+0048. This pair required template matching to obtain a redshift estimate. These spectra are very low S/N, with a low amplitude pattern showing through. We were able to match the positions of O II and Bβ for the upper source. The lower source's redshift is less certain, although the region around the Ca II absorption features matched up with templates.

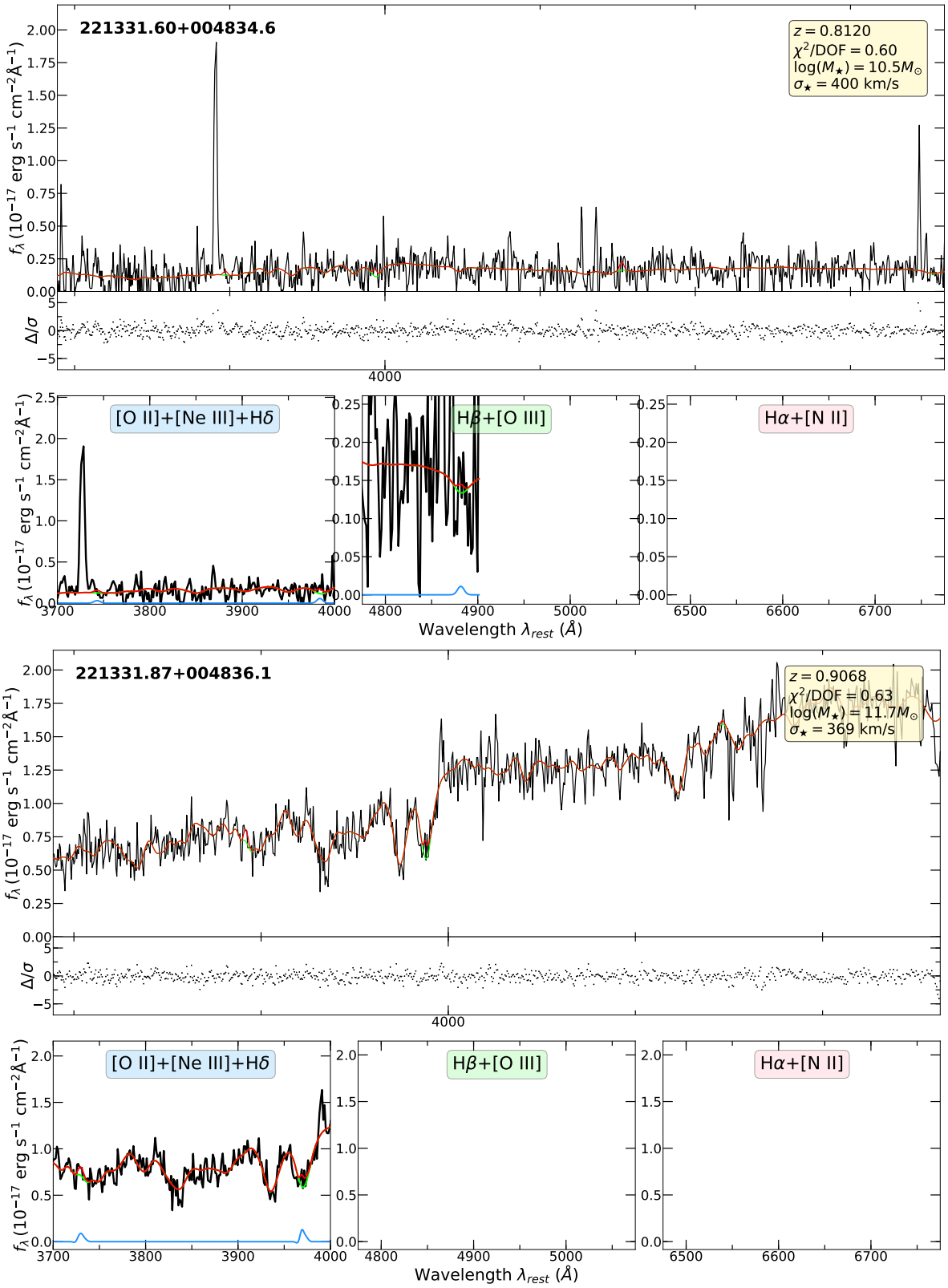

Figure B.29. 2213+0048

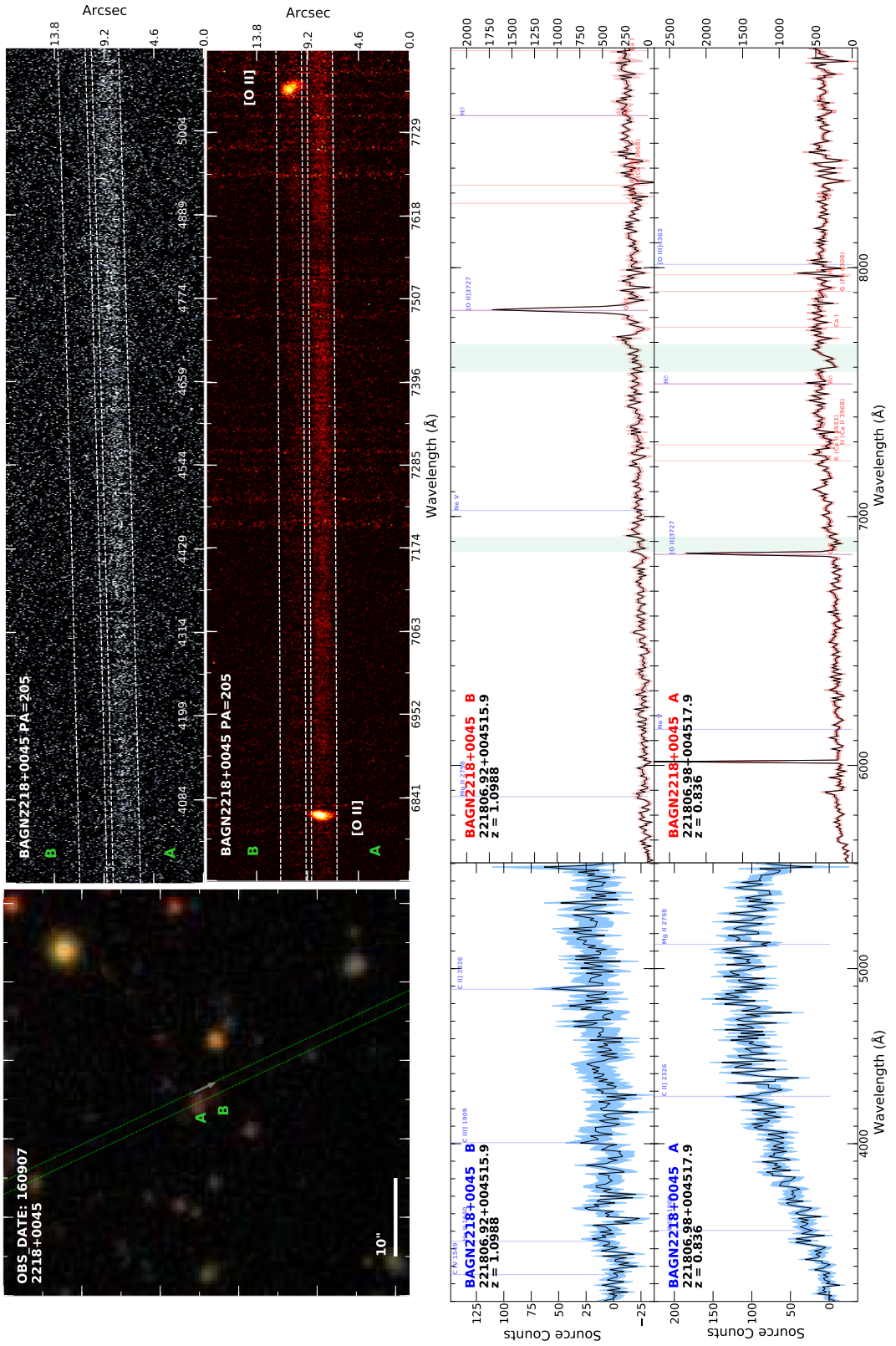

Figure B.30. 2218+0045

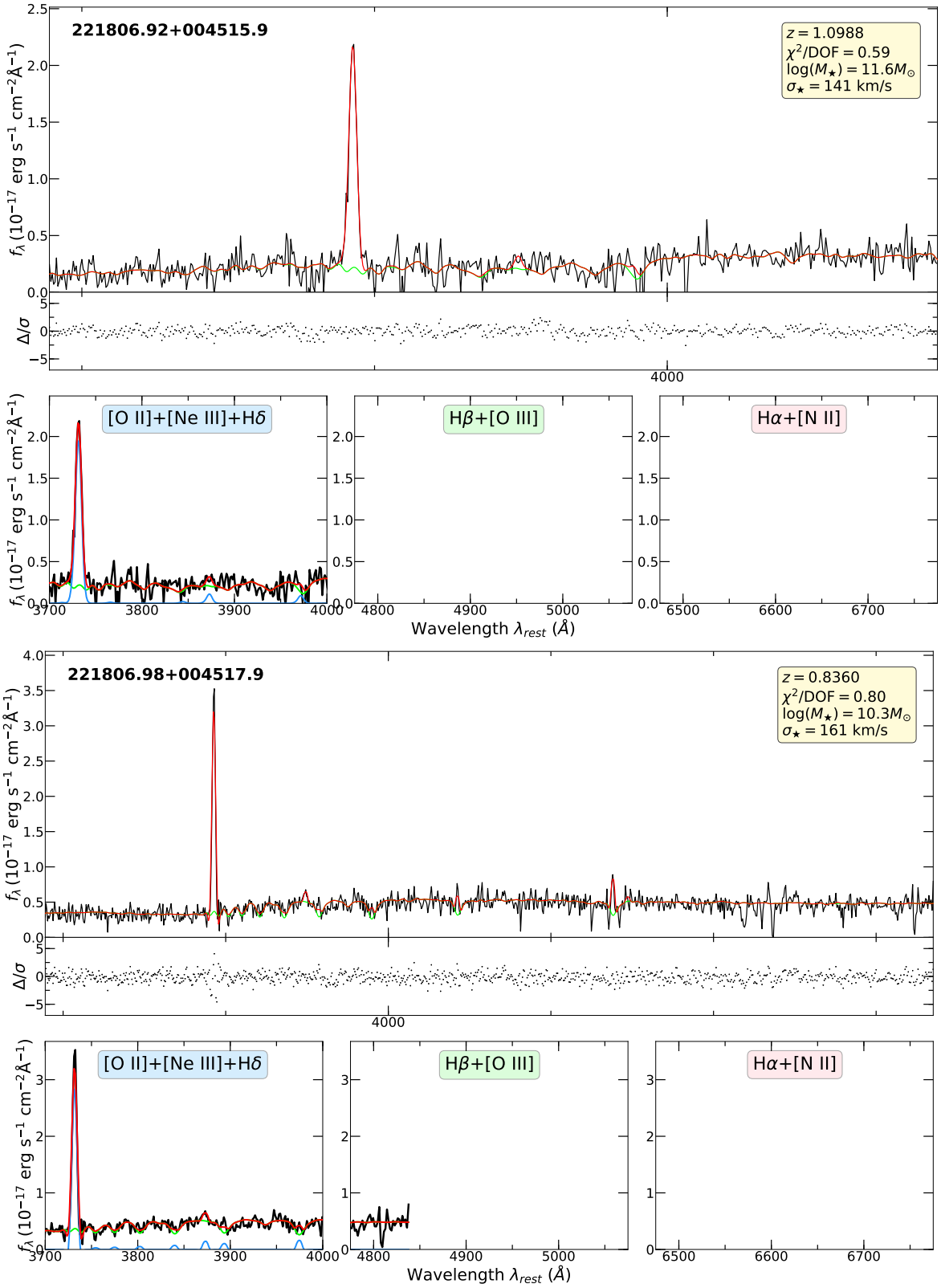

Figure B.31. 2218+0045

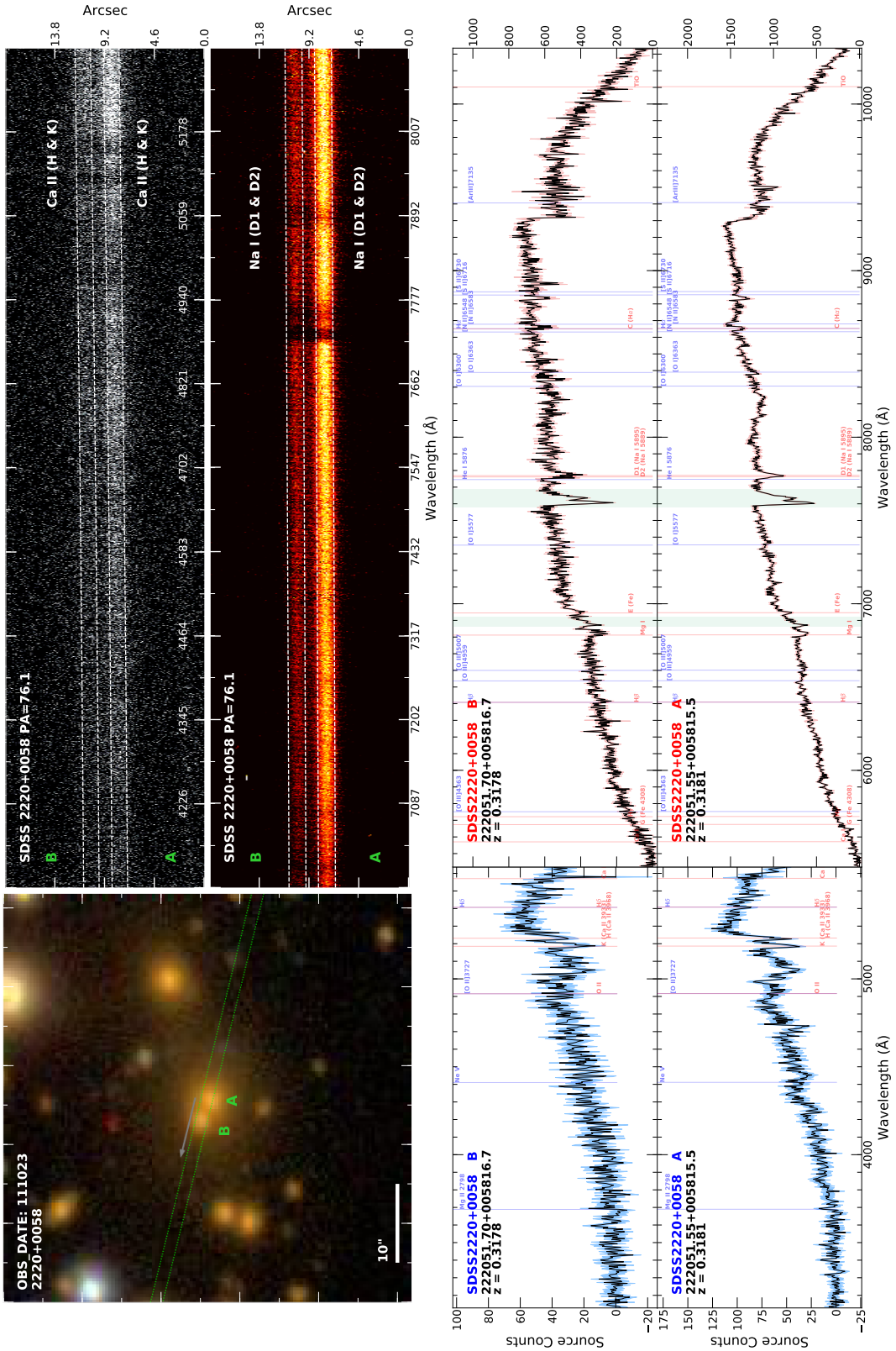

Figure B.32. 2220+0058

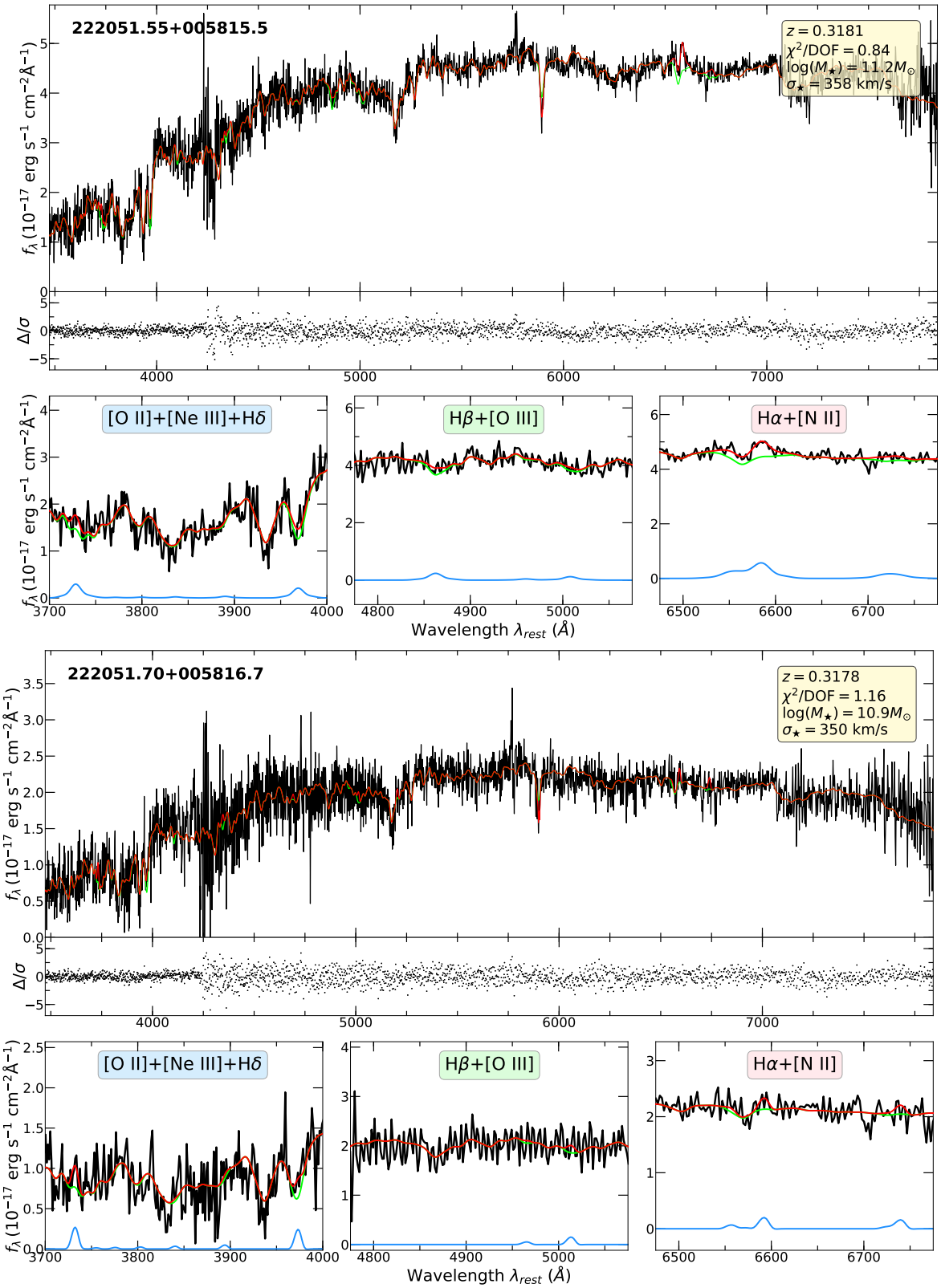

Figure B.33. 2220+0058

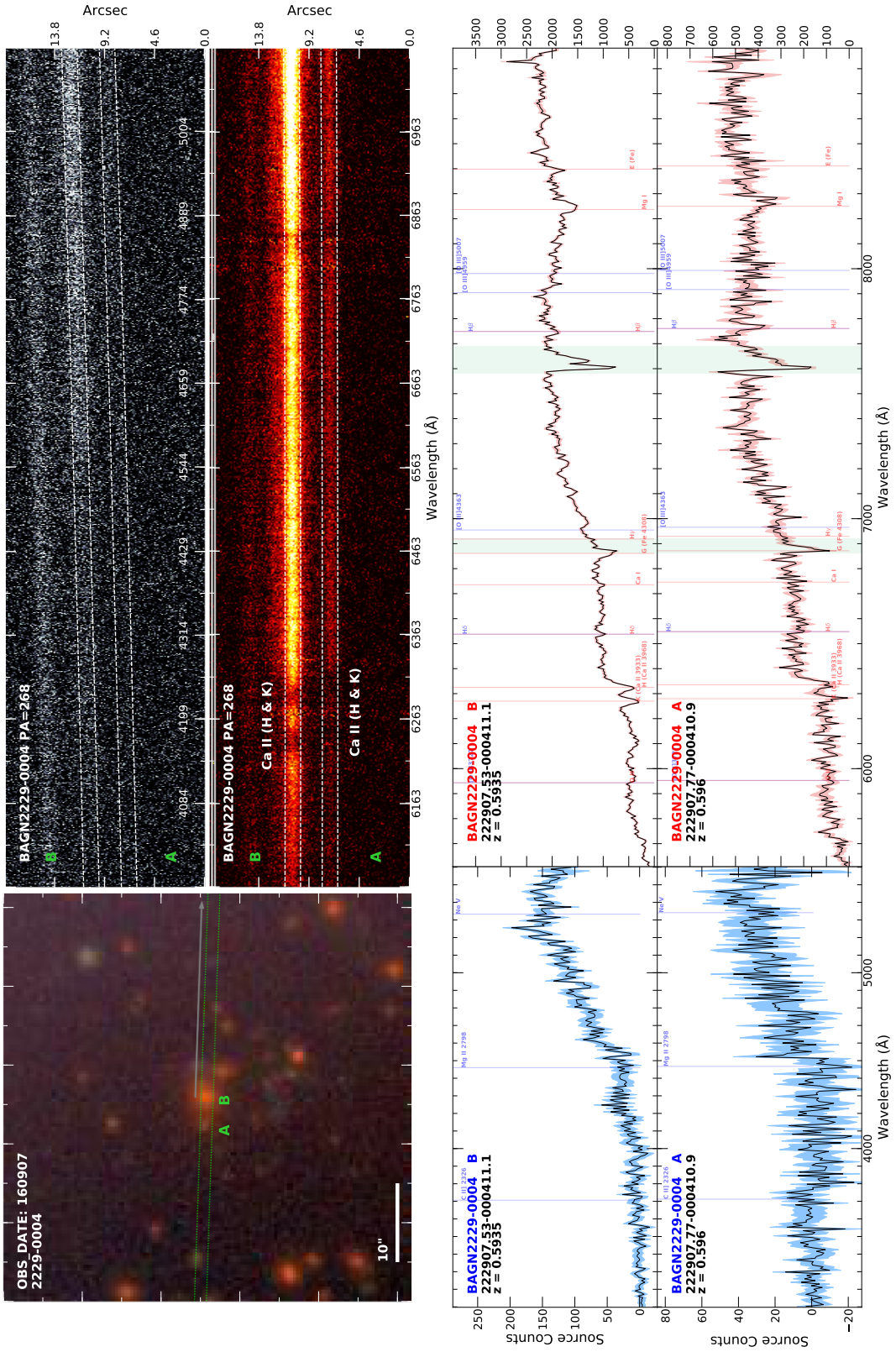

Figure B.34. 2229−0004

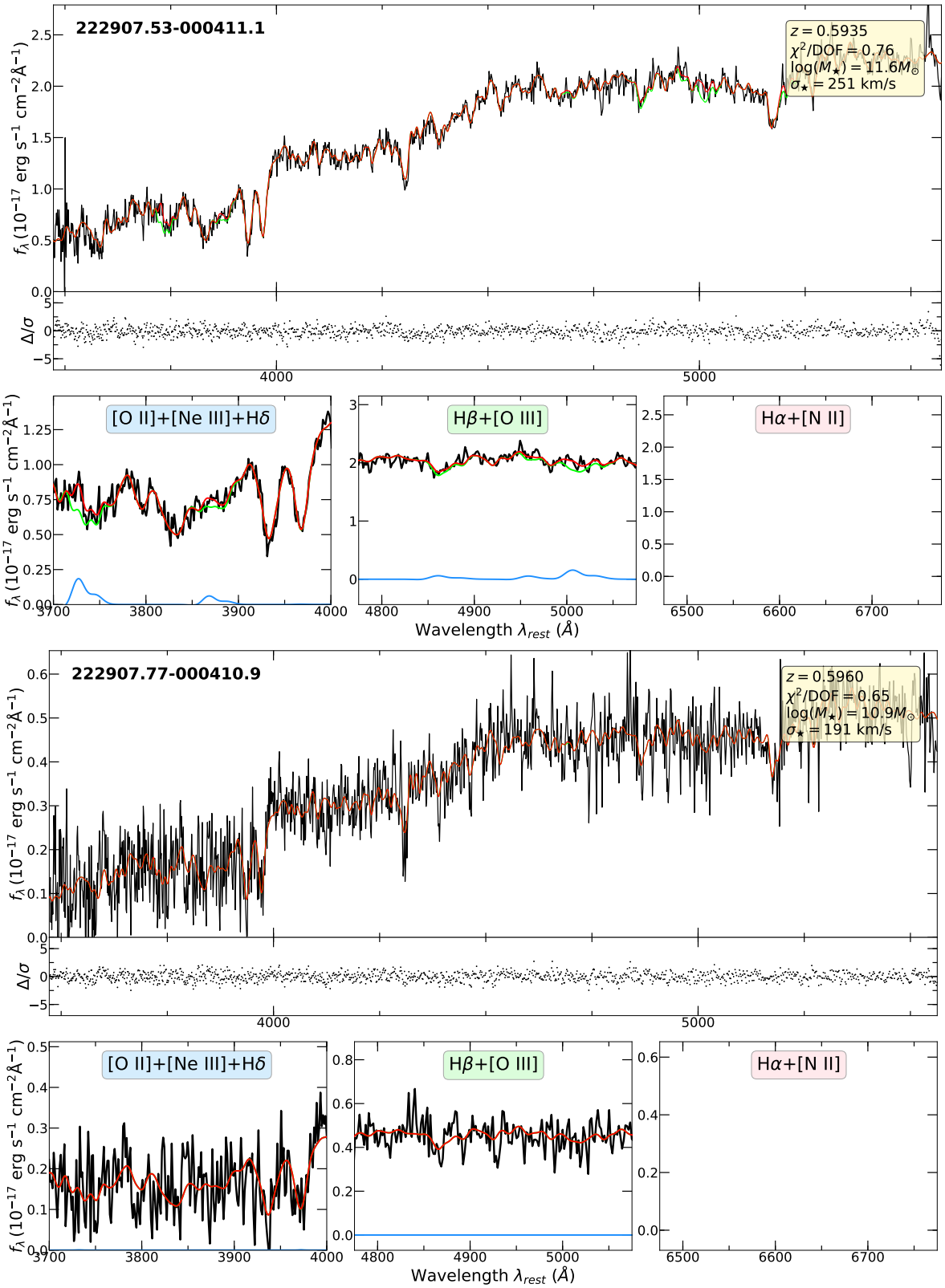

Figure B.35. 2229−0004

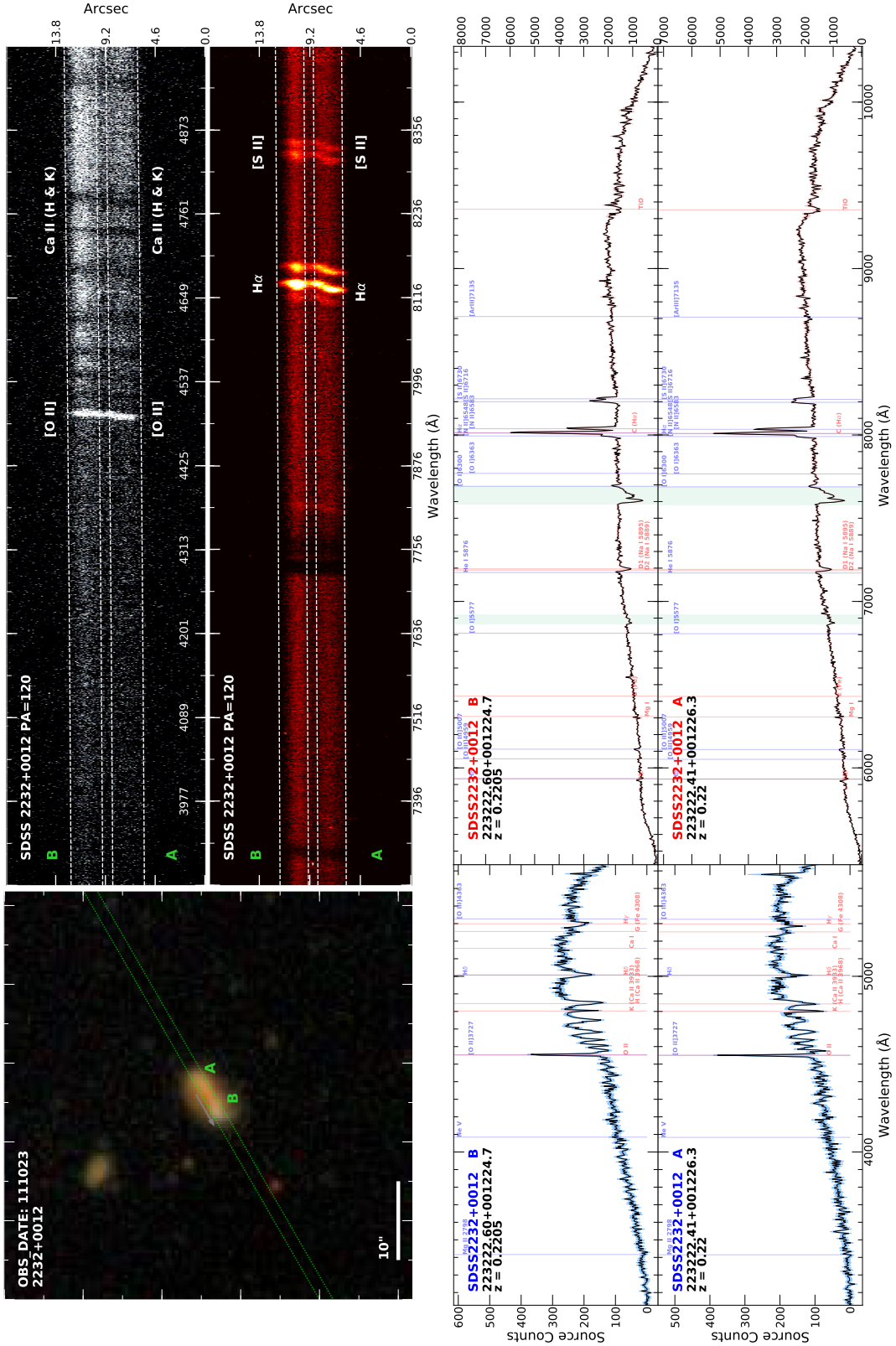

Figure B.36. 2232+0012

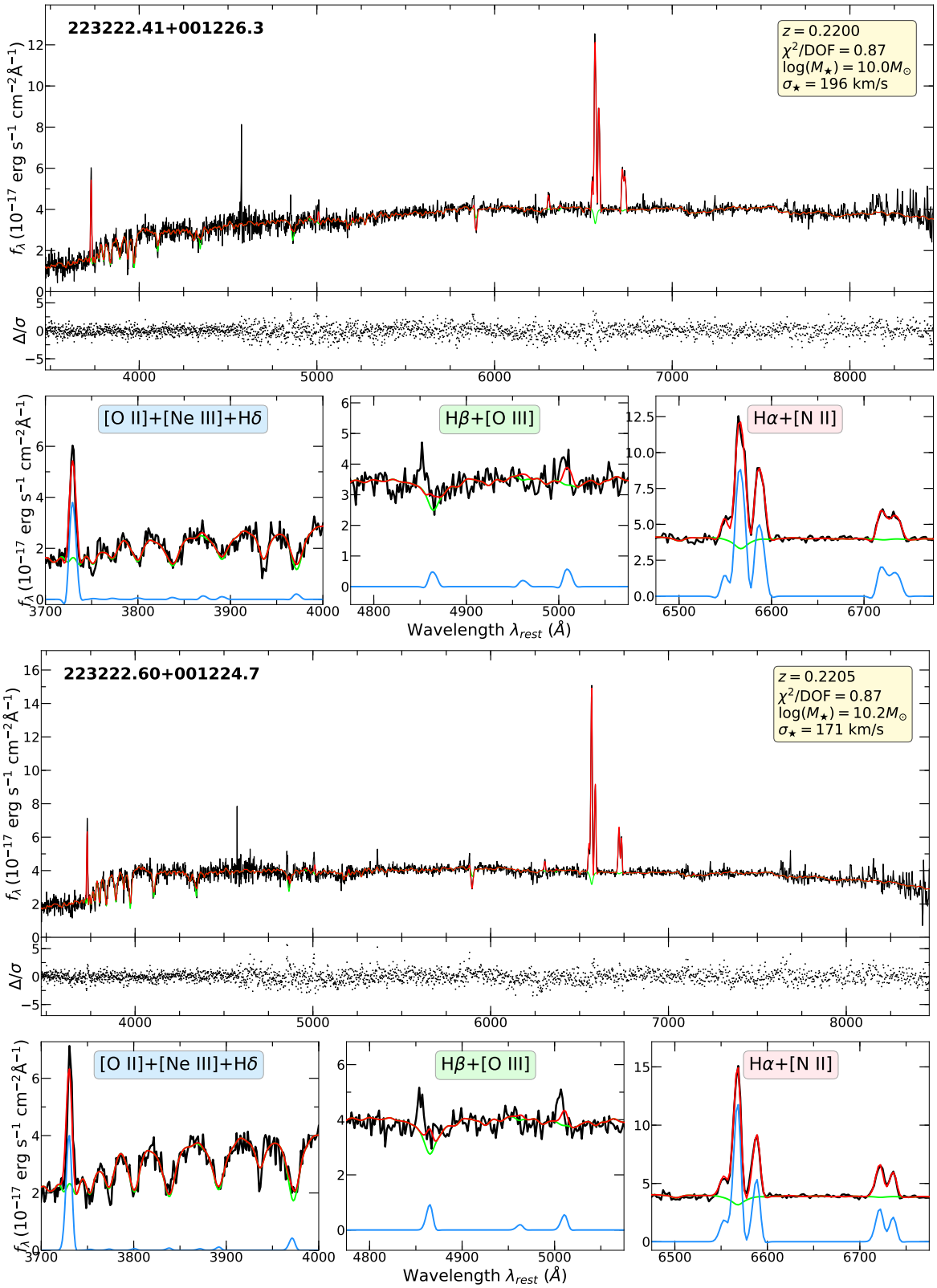

Figure B.37. 2232+0012

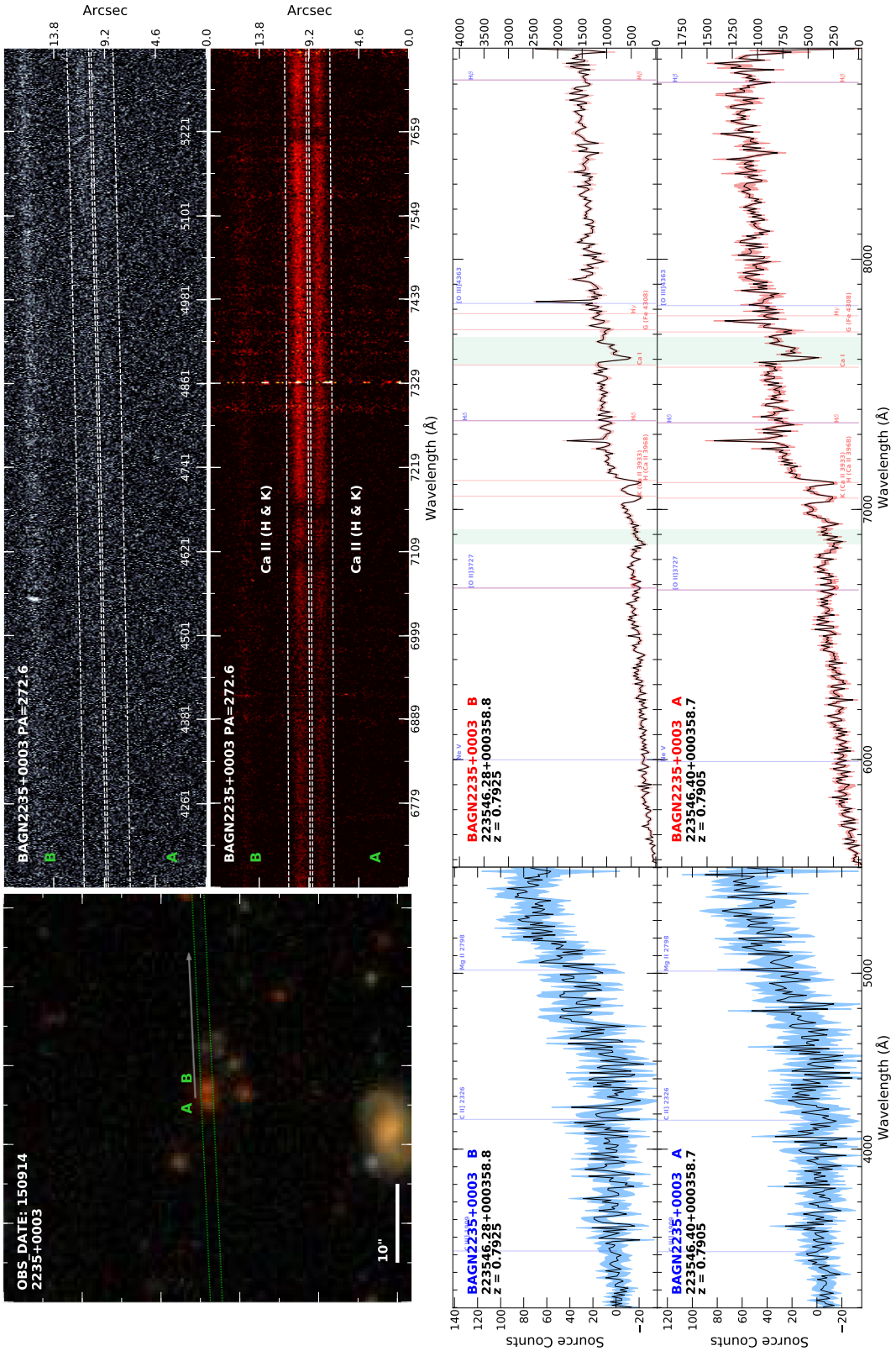

Figure B.38. 2235+0003

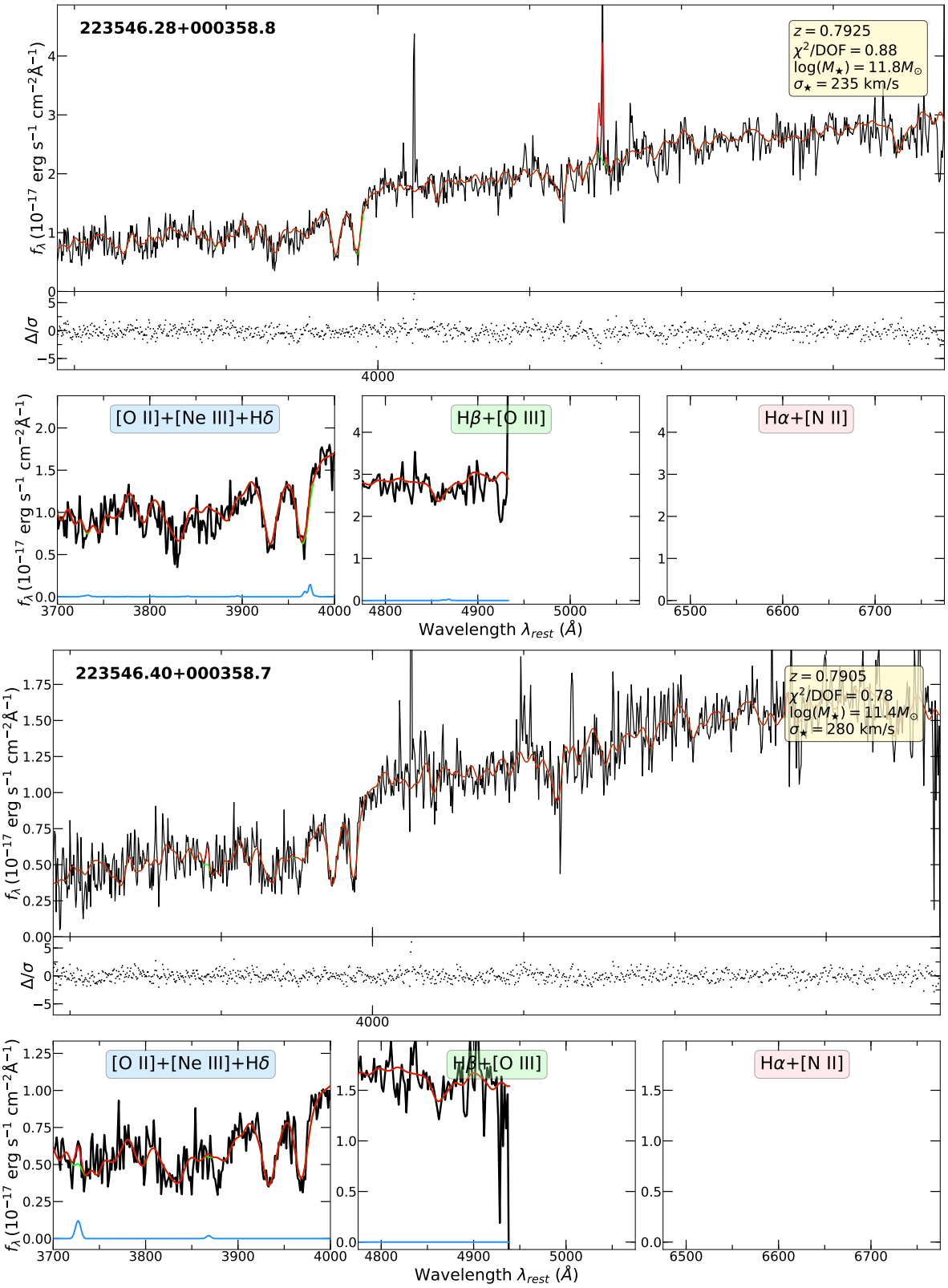

Figure B.39. 2235+0003

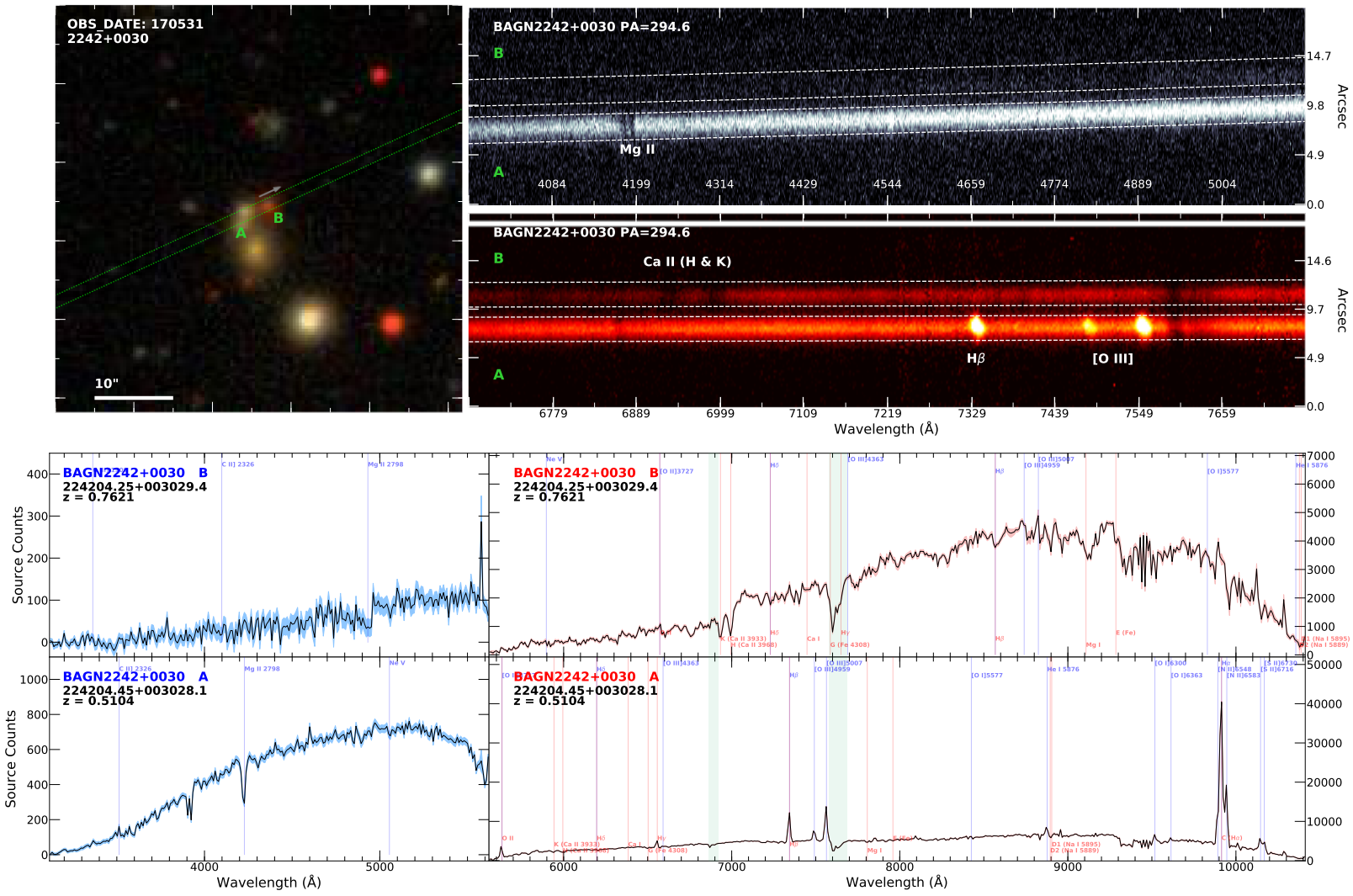

Figure B.40. 2242+0030. This pair required template matching to obtain a redshift estimate. The red side has lingering issues of imperfect sky-subtraction and cosmics that make it difficult to disentangle the true emission features. The Ca II and Mg I absorption features led to a redshift estimate. The lower source shows an unambiguous Hβ and [O III] complex.

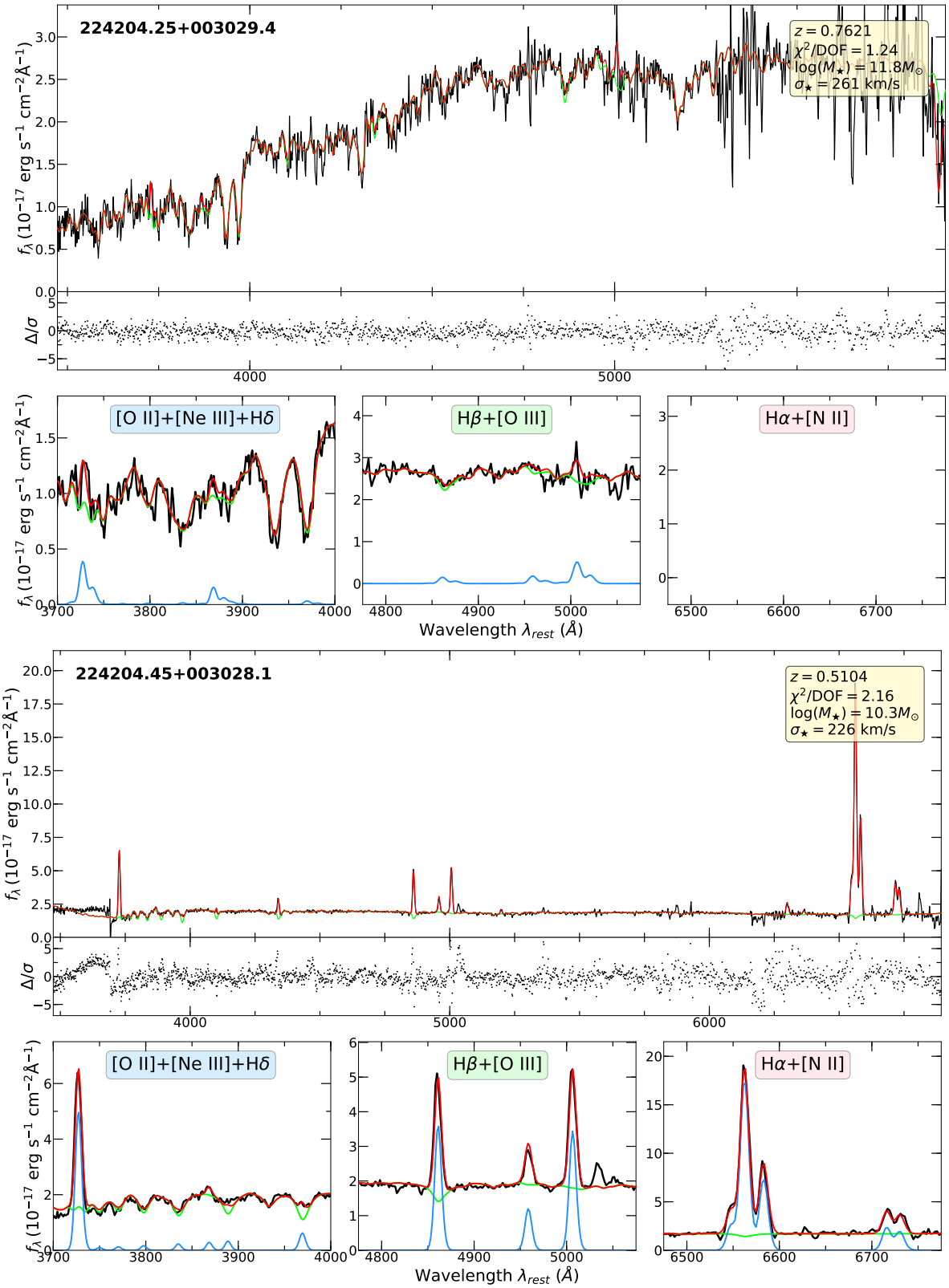

Figure B.41. 2242+0030

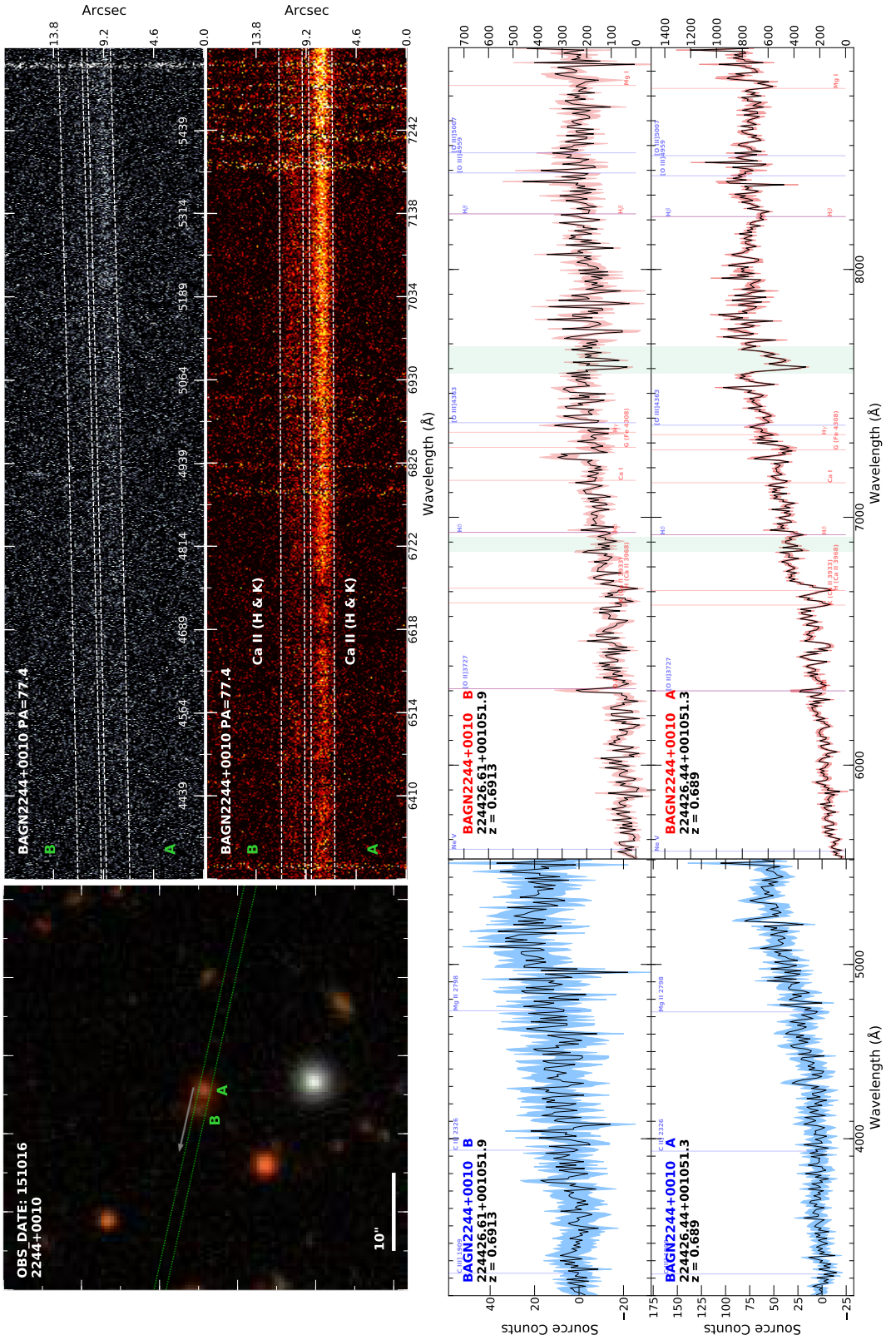

Figure B.42. 2244+0010

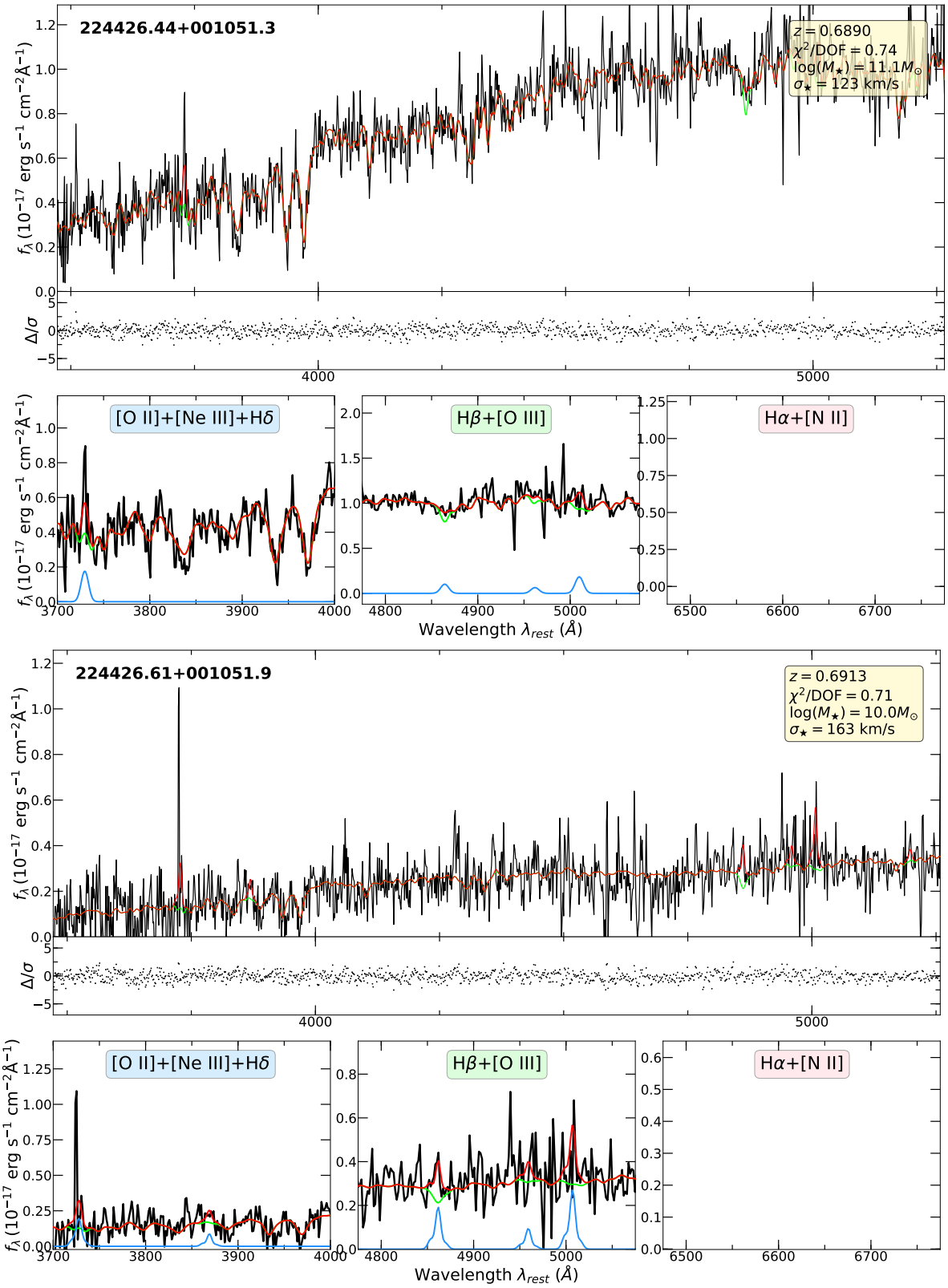

Figure B.43. 2244+0010

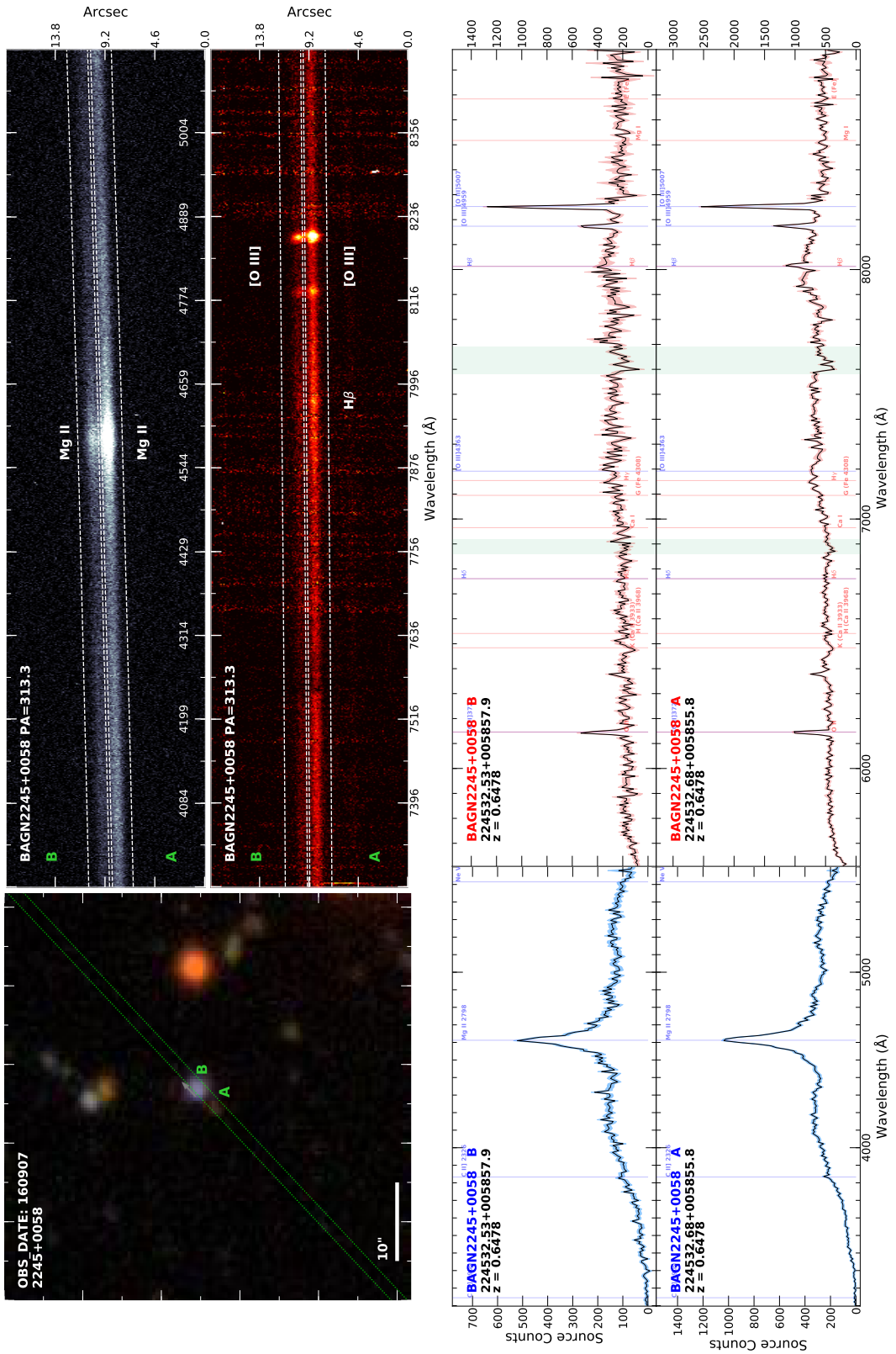

Figure B.44. 2245+0058

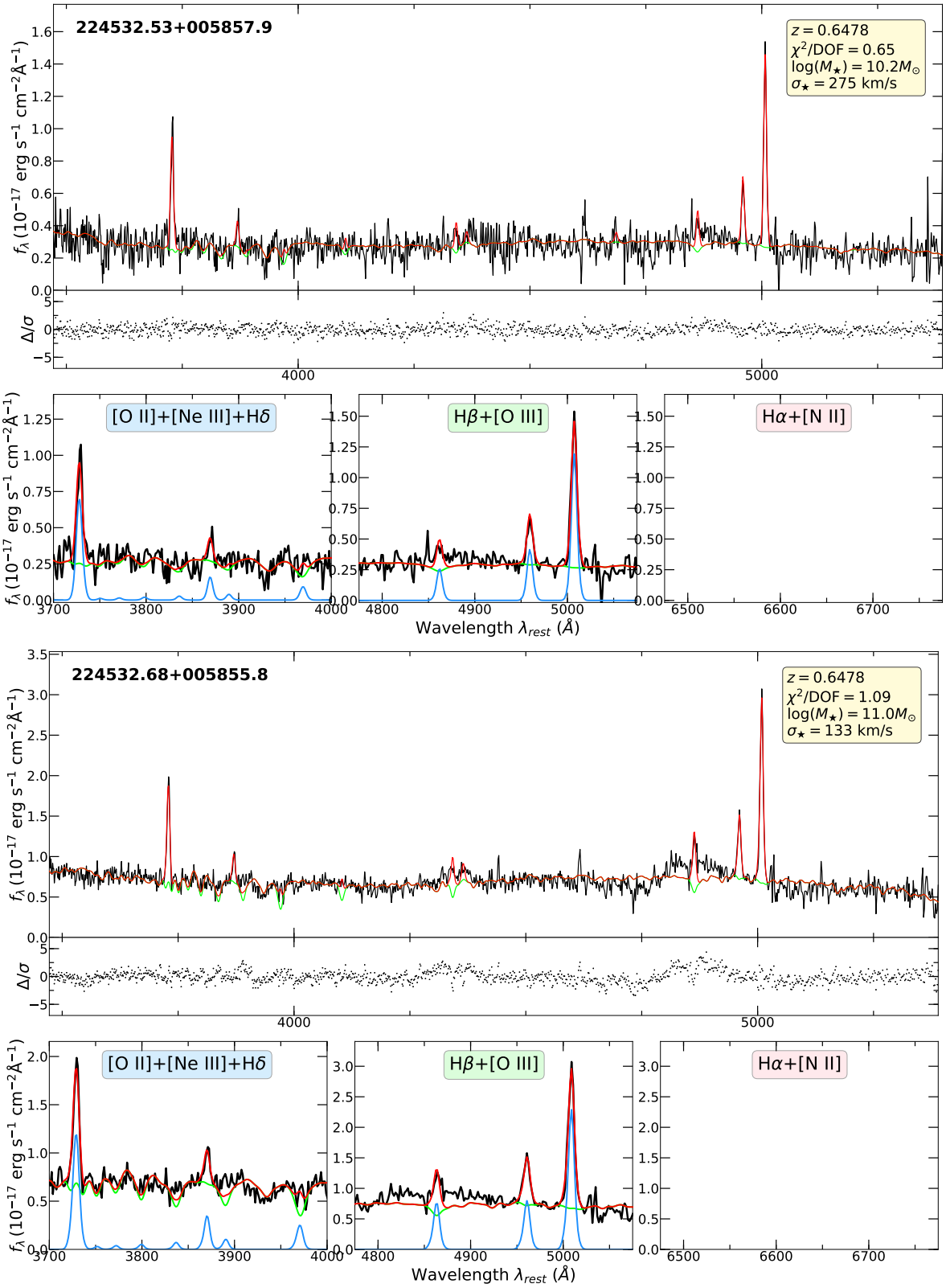

Figure B.45. 2245+0058

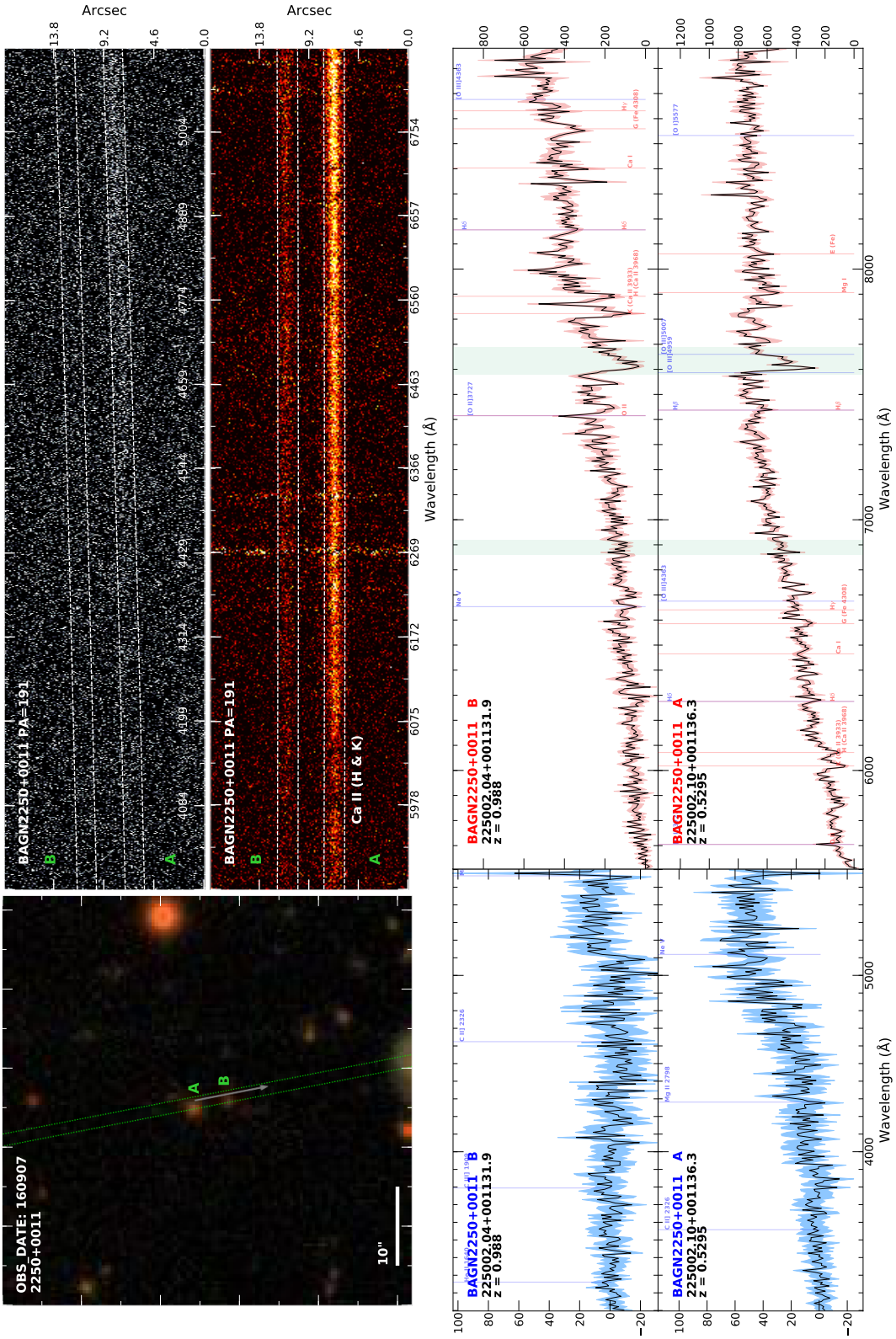

Figure B.46. 2250+0011. This pair required template matching to obtain a redshift estimate. However, we were able to find clear indications of the Ca II absorption lines for both objects.

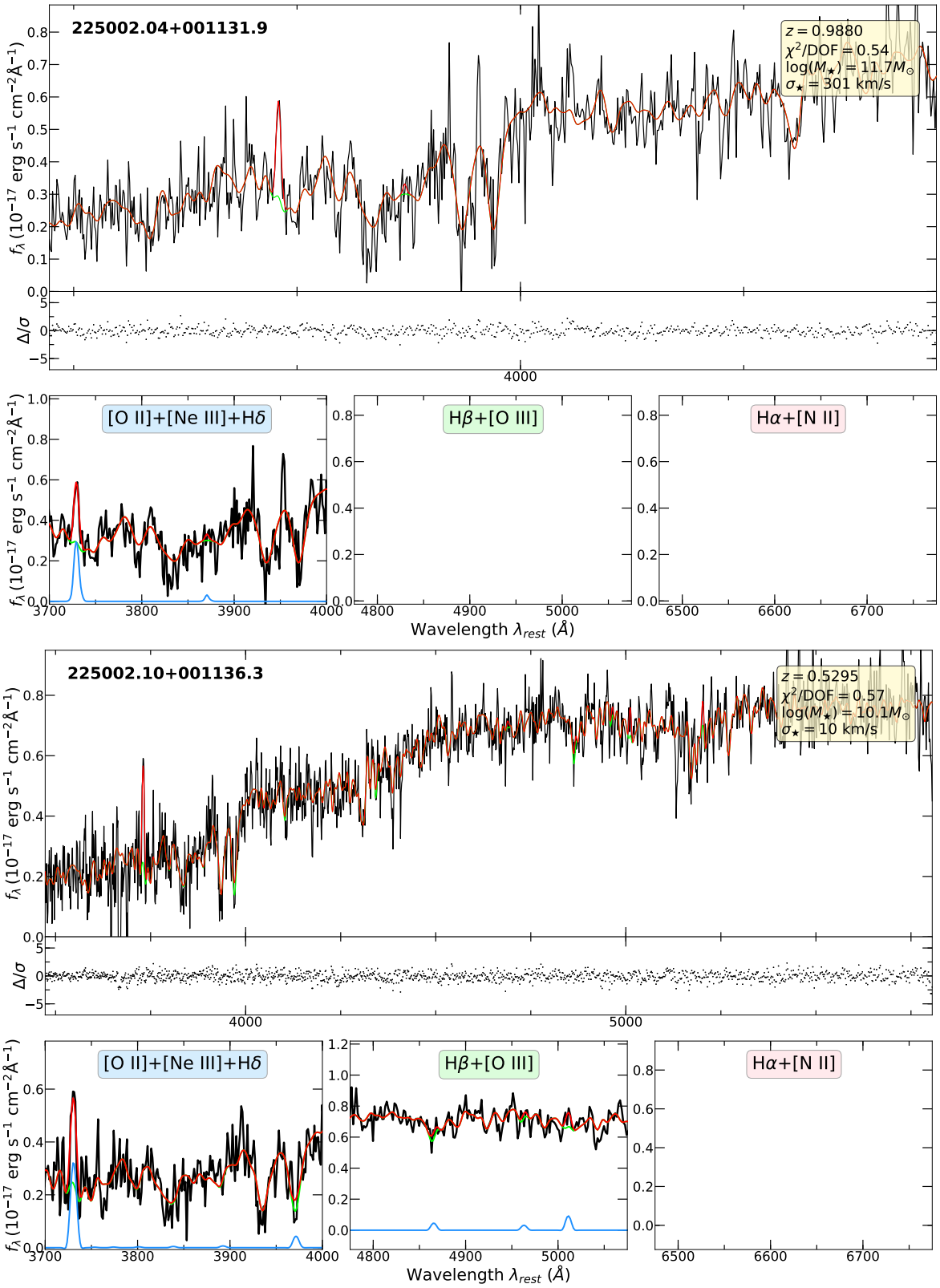

Figure B.47. 2250+0011

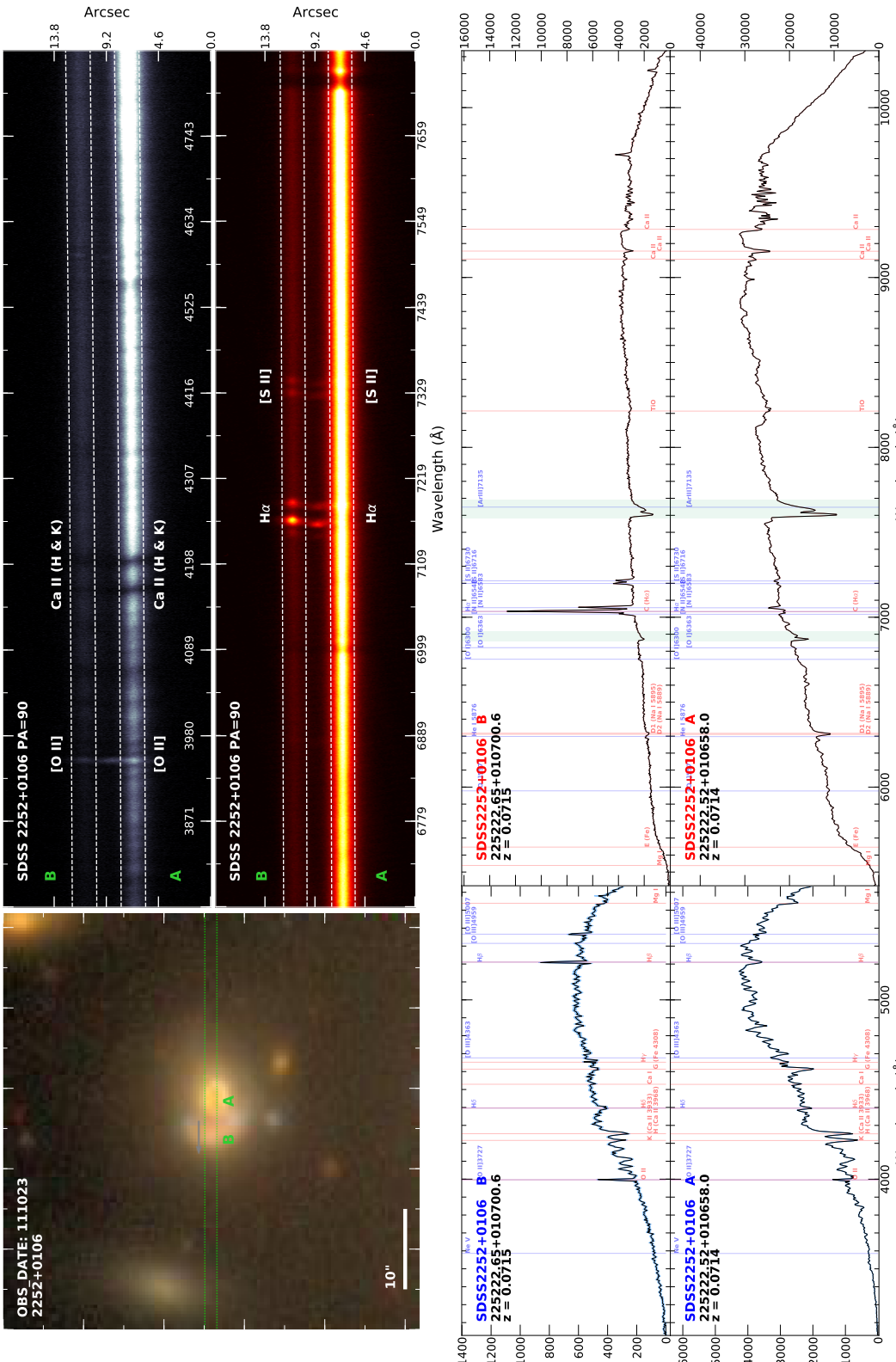

Figure B.48. 2252+0106. We note that this pair was considered grade D in the original sample selection, but shows clear evidence of a merger.

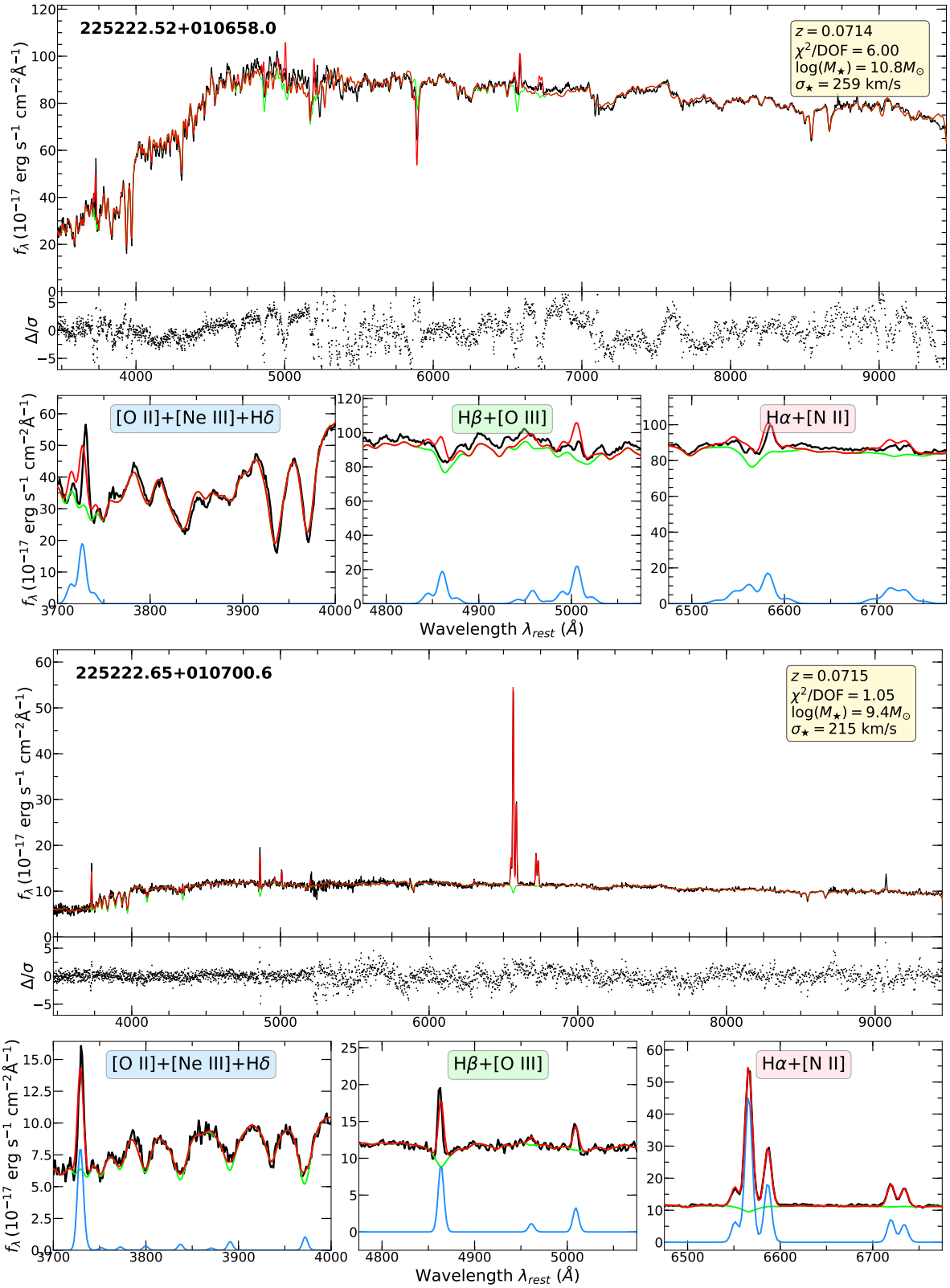

Figure B.49. 2252+0106

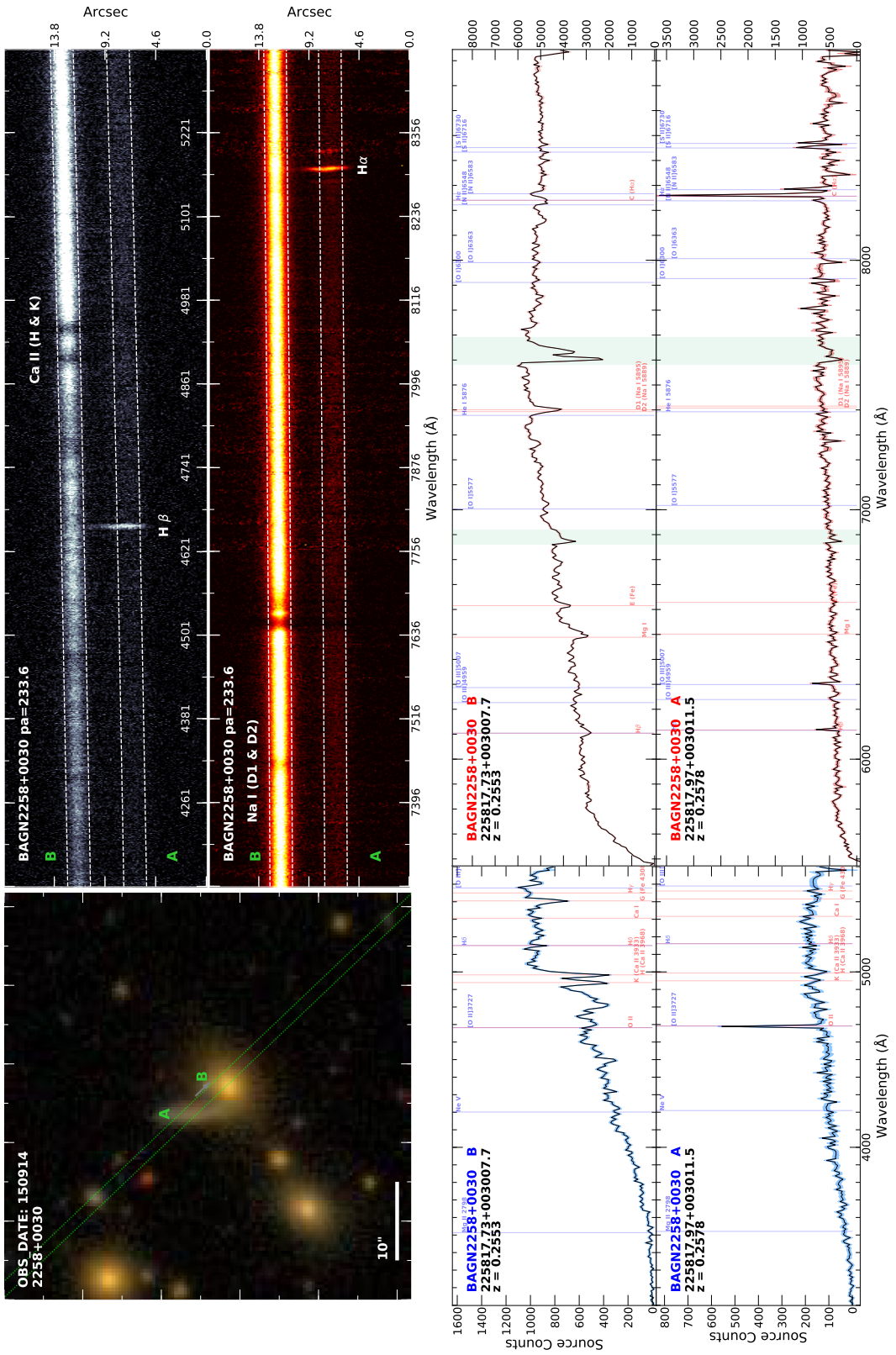

Figure B.50. 2258+0030

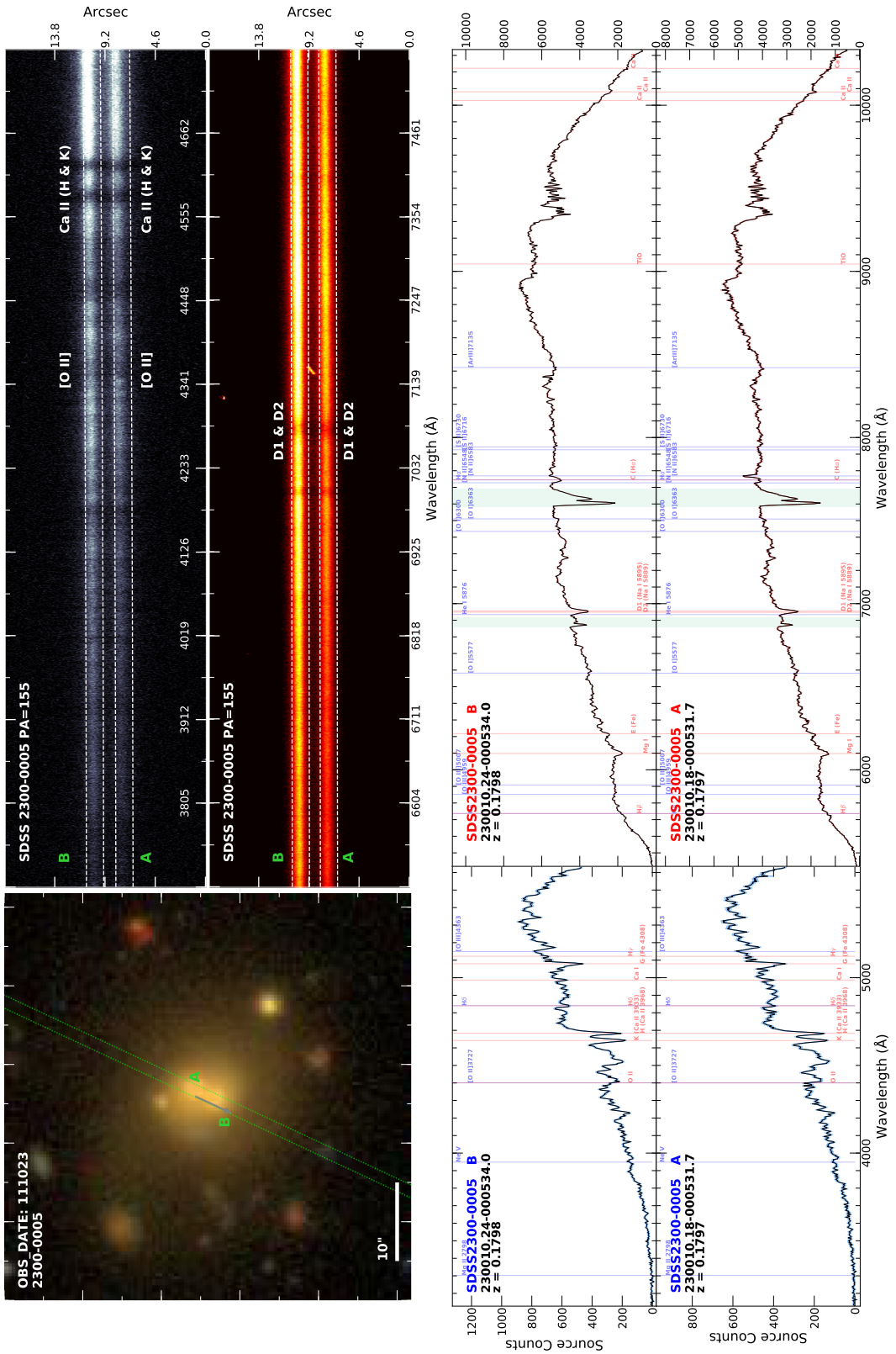

Figure B.52. 2300-0005

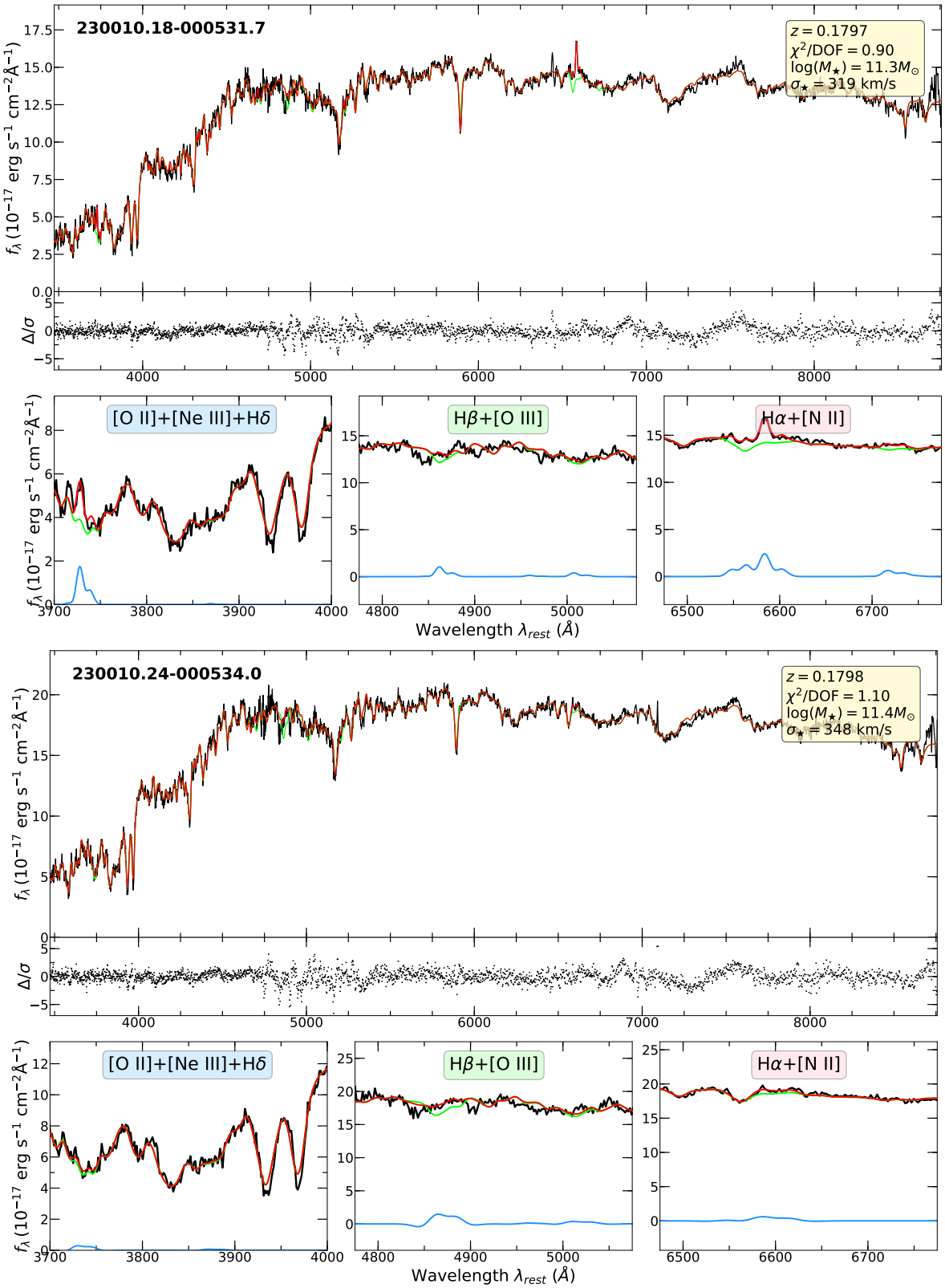

Figure B.53. 2300-0005

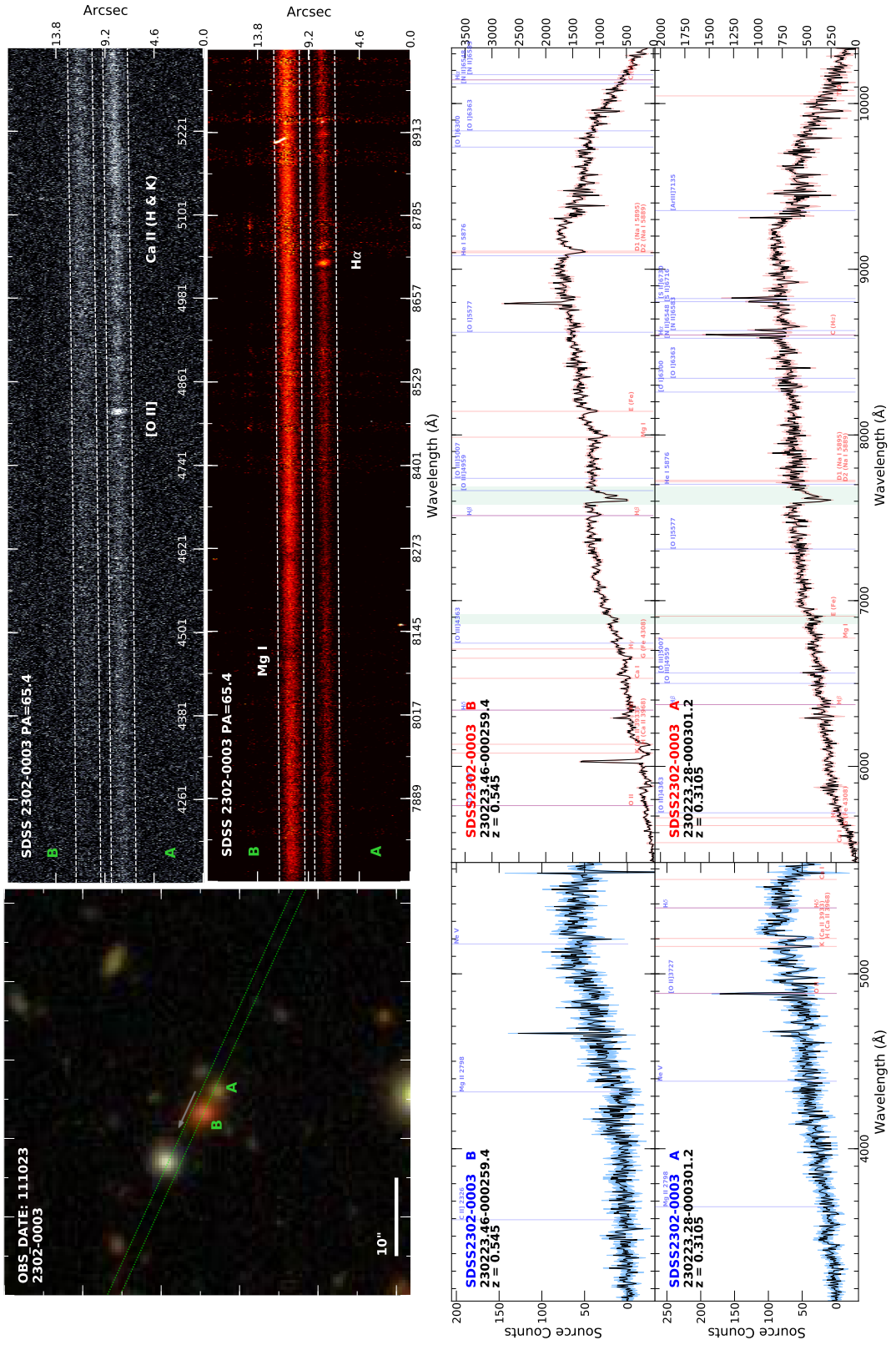

Figure B.54. 2302−0003

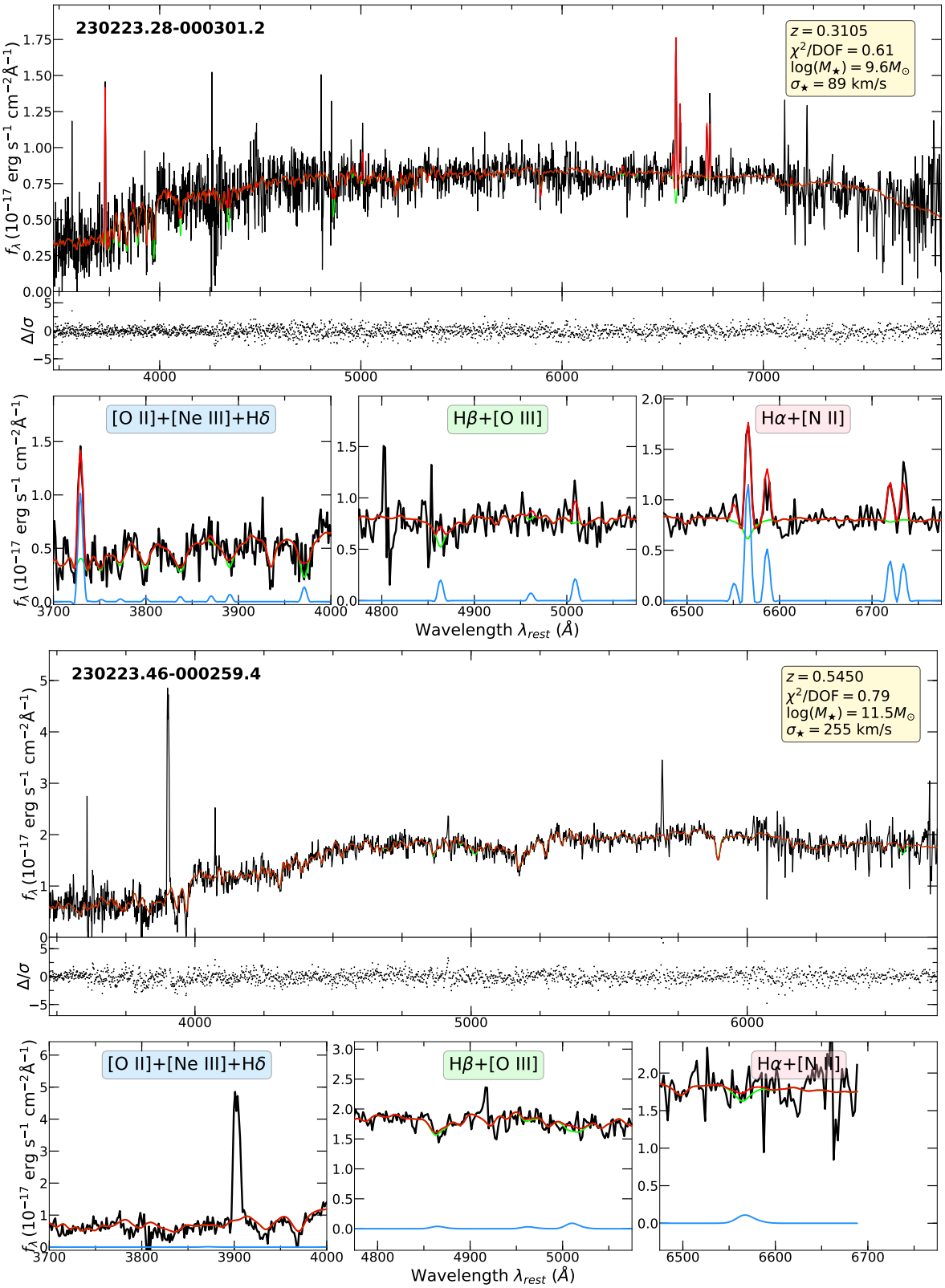

Figure B.55. 2302−0003

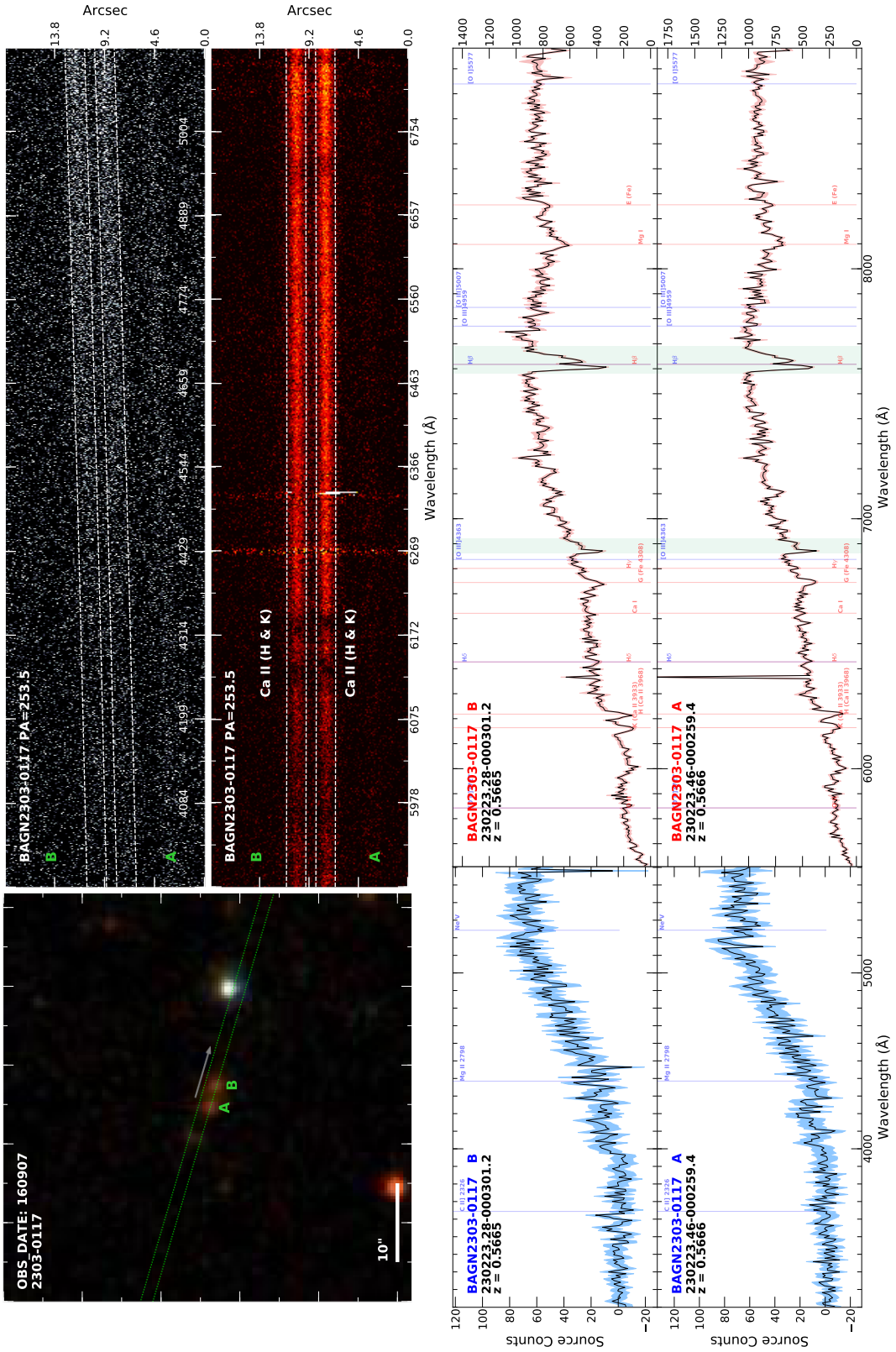

Figure B.56. 2303−0117

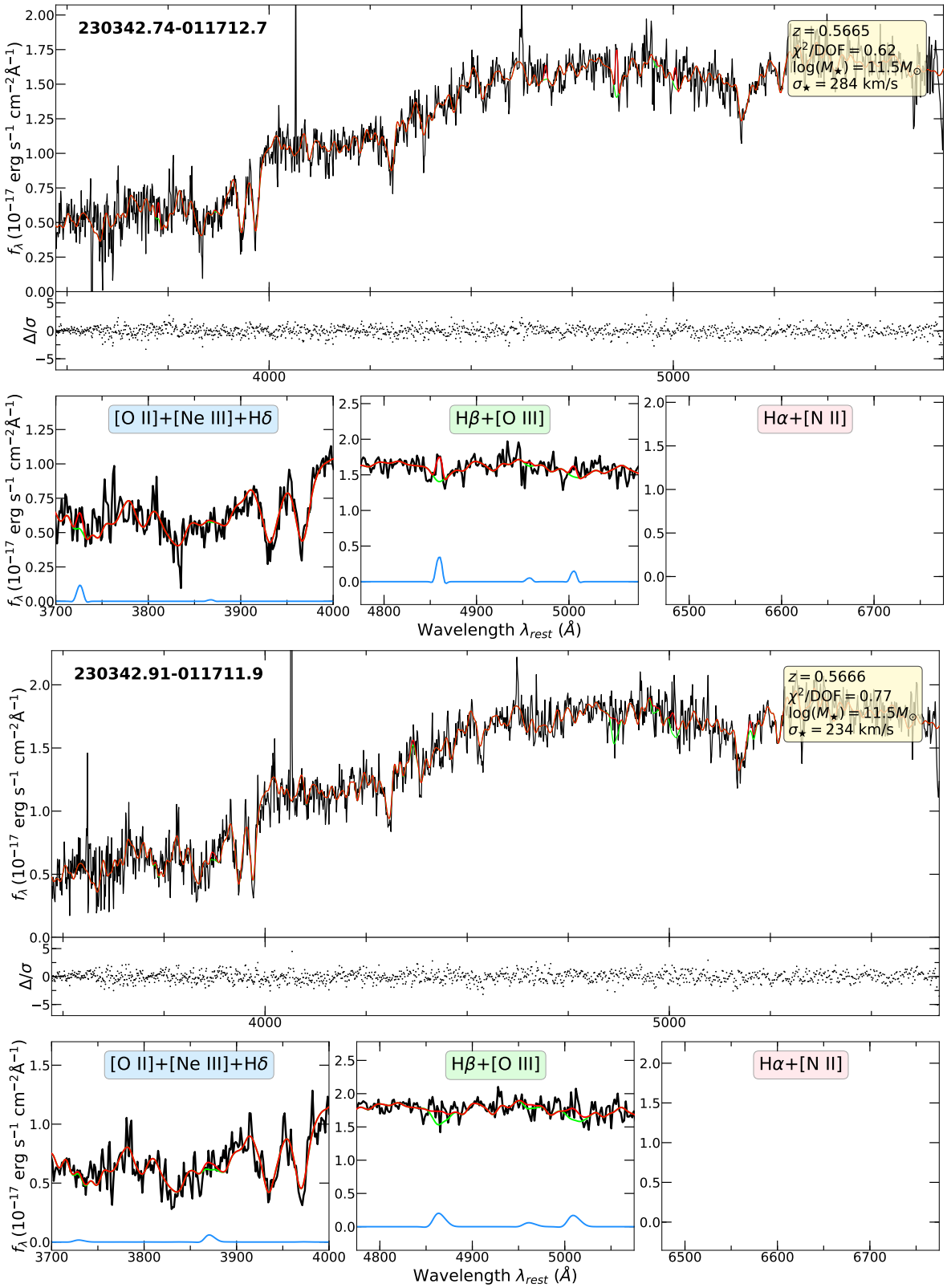

Figure B.57. 2303−0117

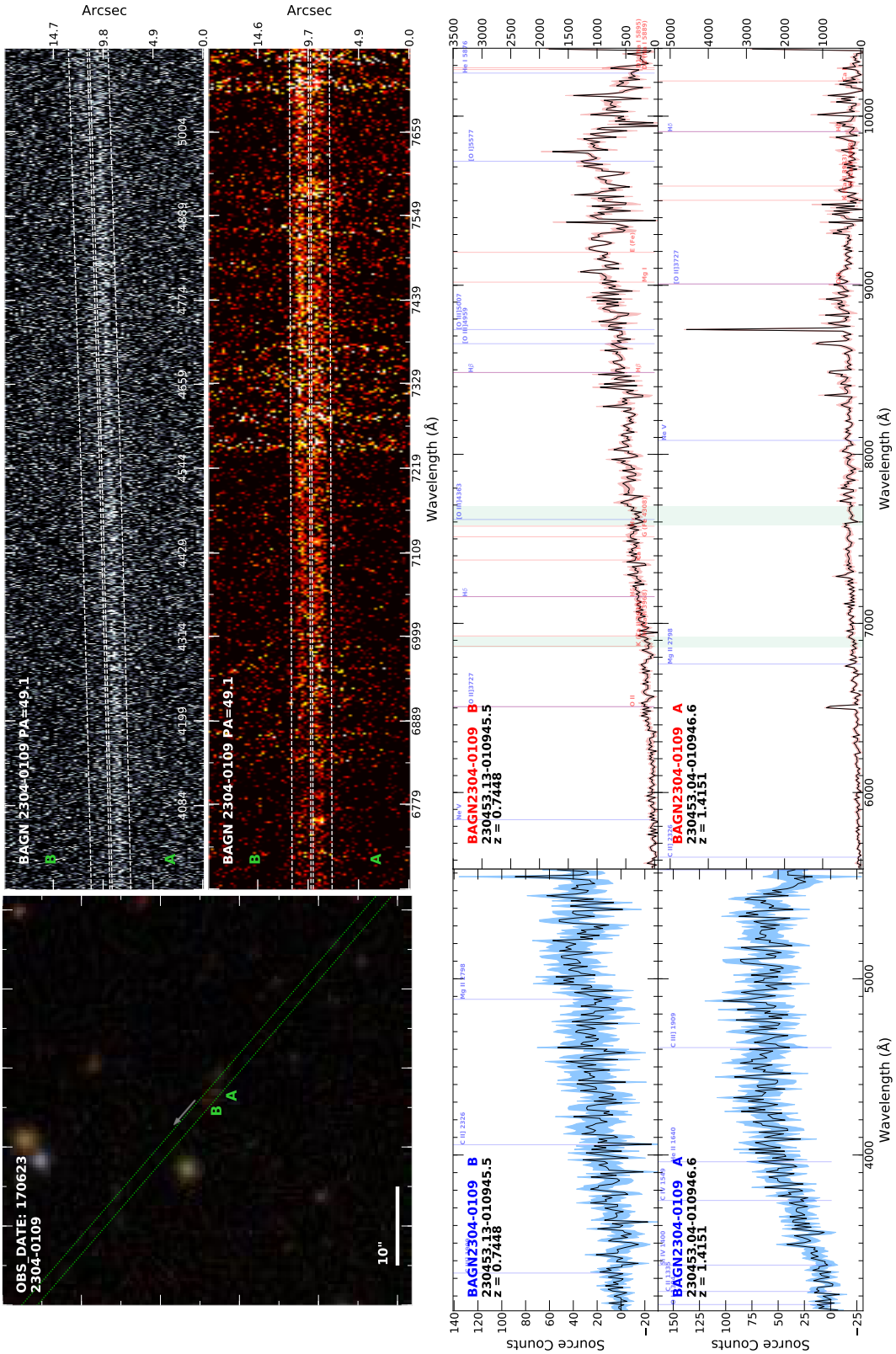

Figure B.58. 2304−0109. This pair required template matching to obtain a redshift estimate. However, we were able to find clear indications of the [O III] and Ca II lines for both objects.

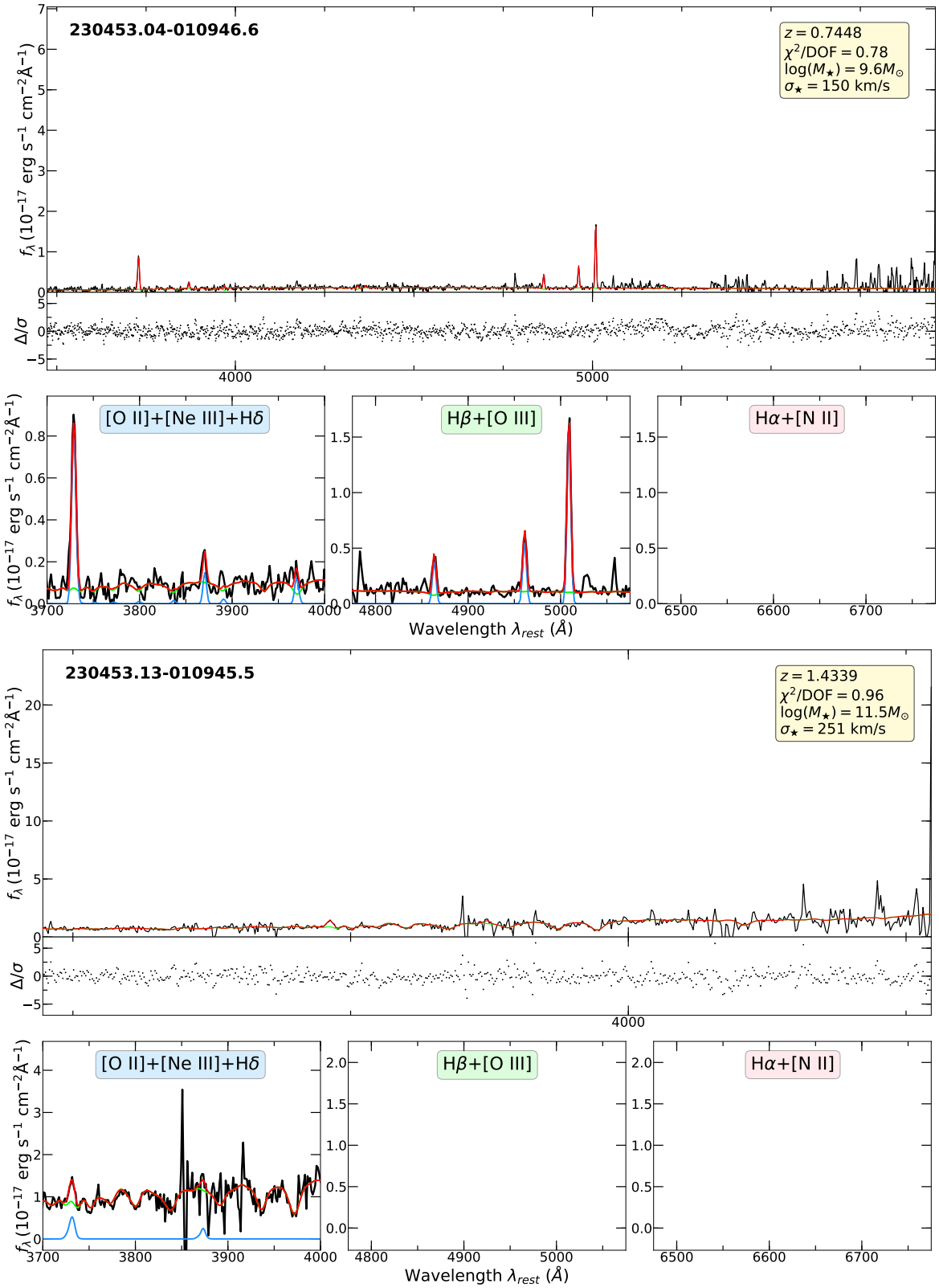

Figure B.59. 2304−0109

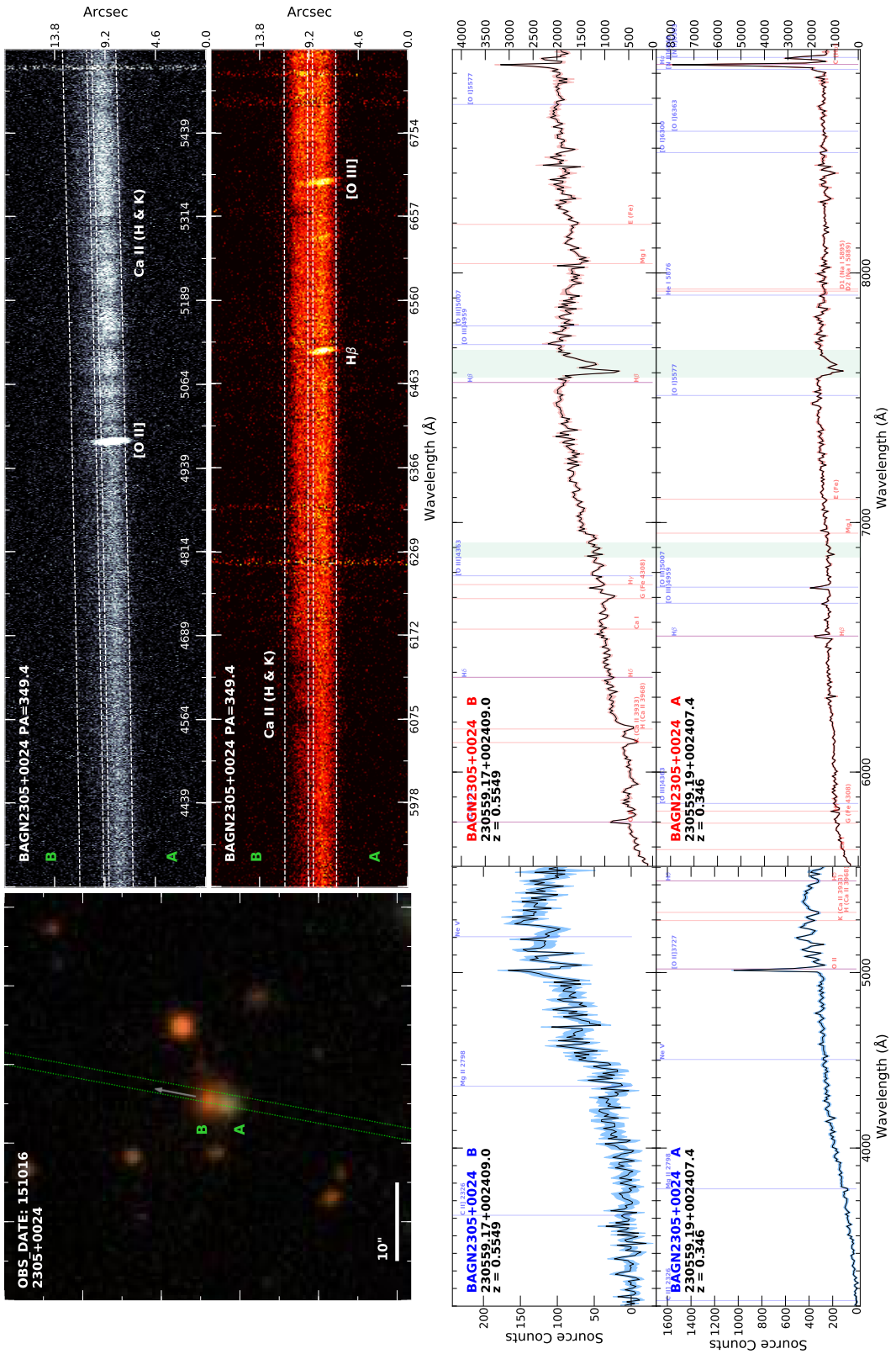

Figure B.60. 2305+0024

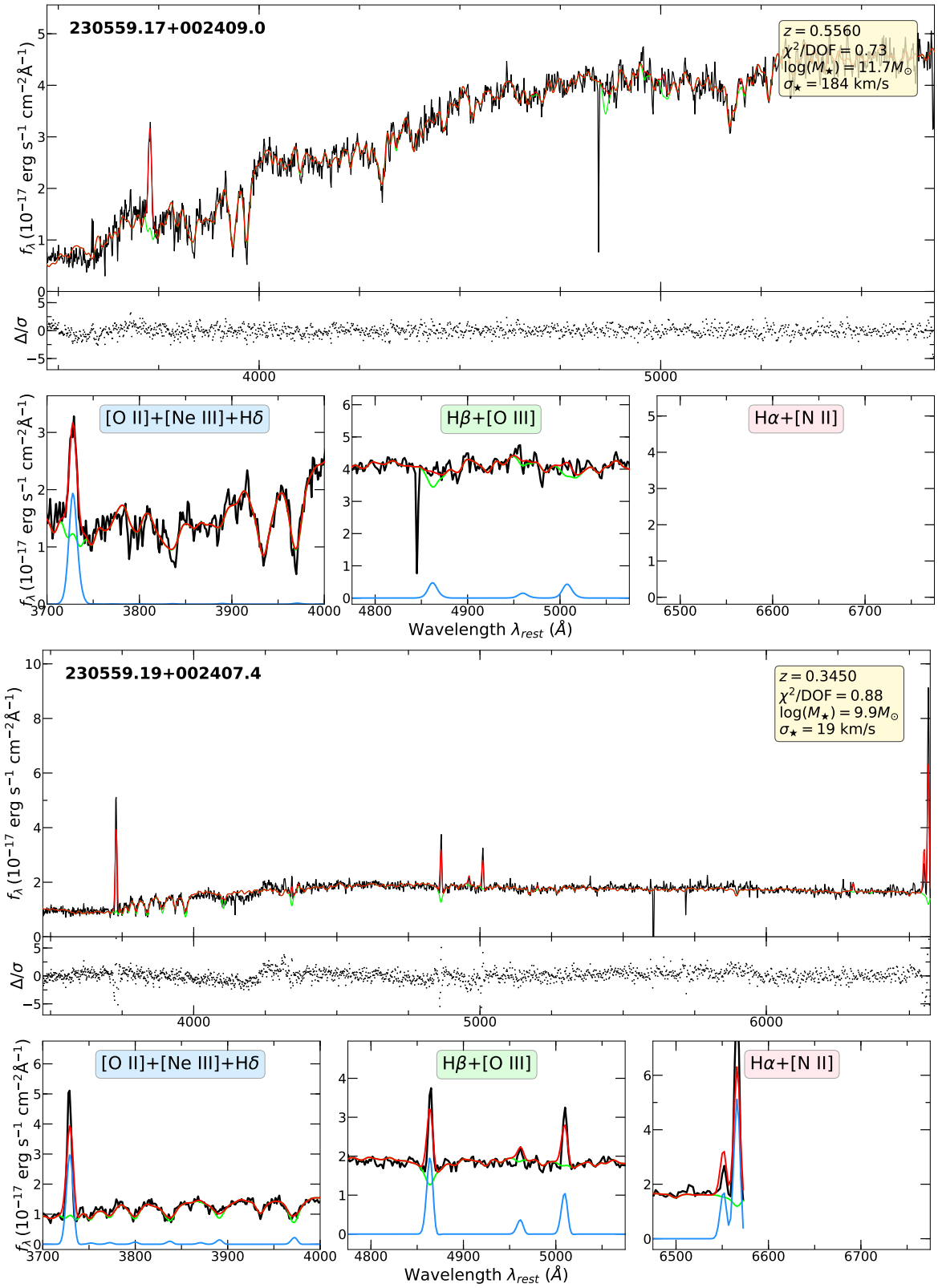

Figure B.61. 2305+0024

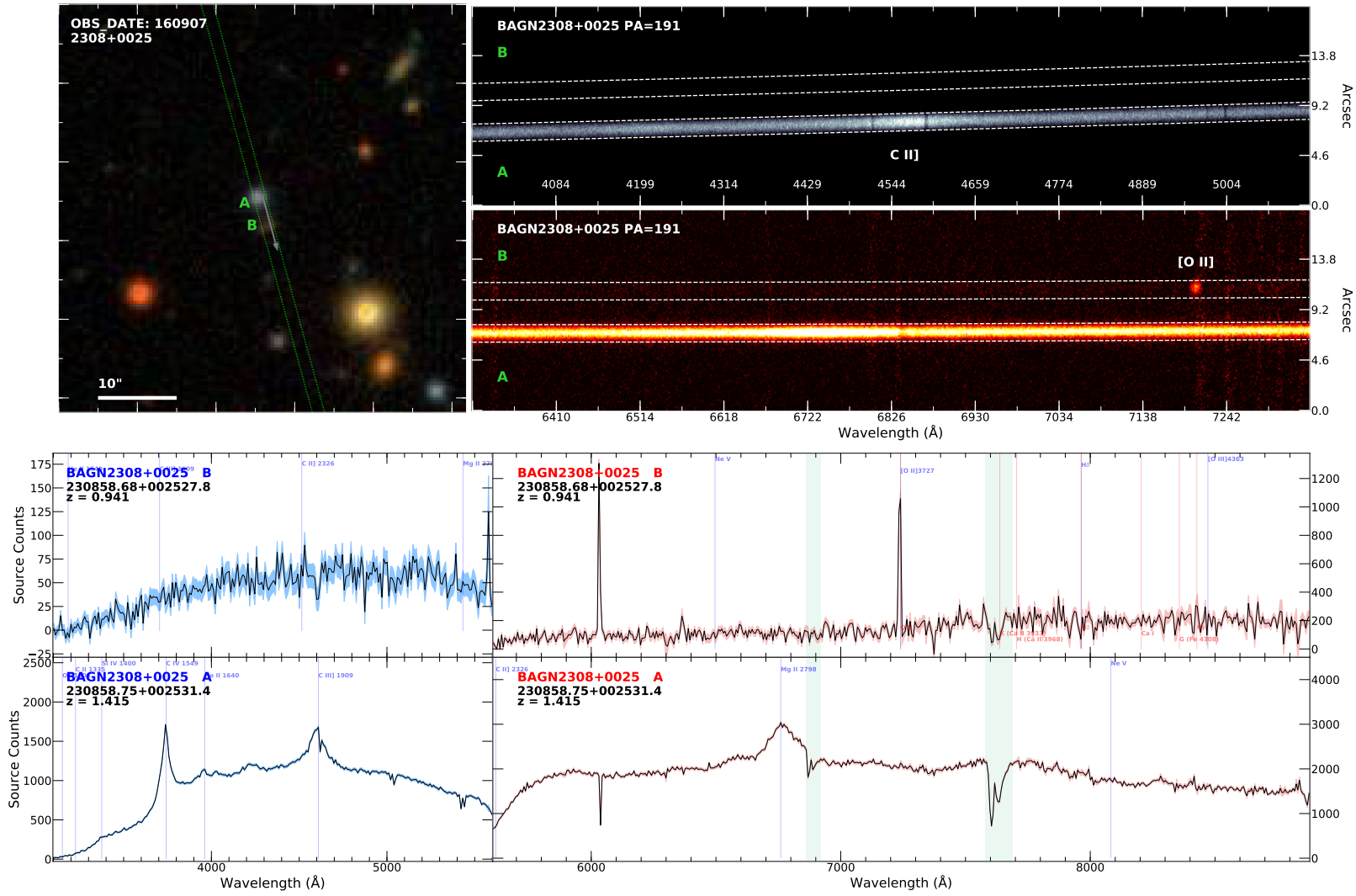

Figure B.62. 2308+0025. This pair required template matching to obtain a redshift estimate. Despite an uncleaned cosmic, we were able to identify the O II emission in the upper source. The lower source is an unambiguous broad line QSO at high redshift.

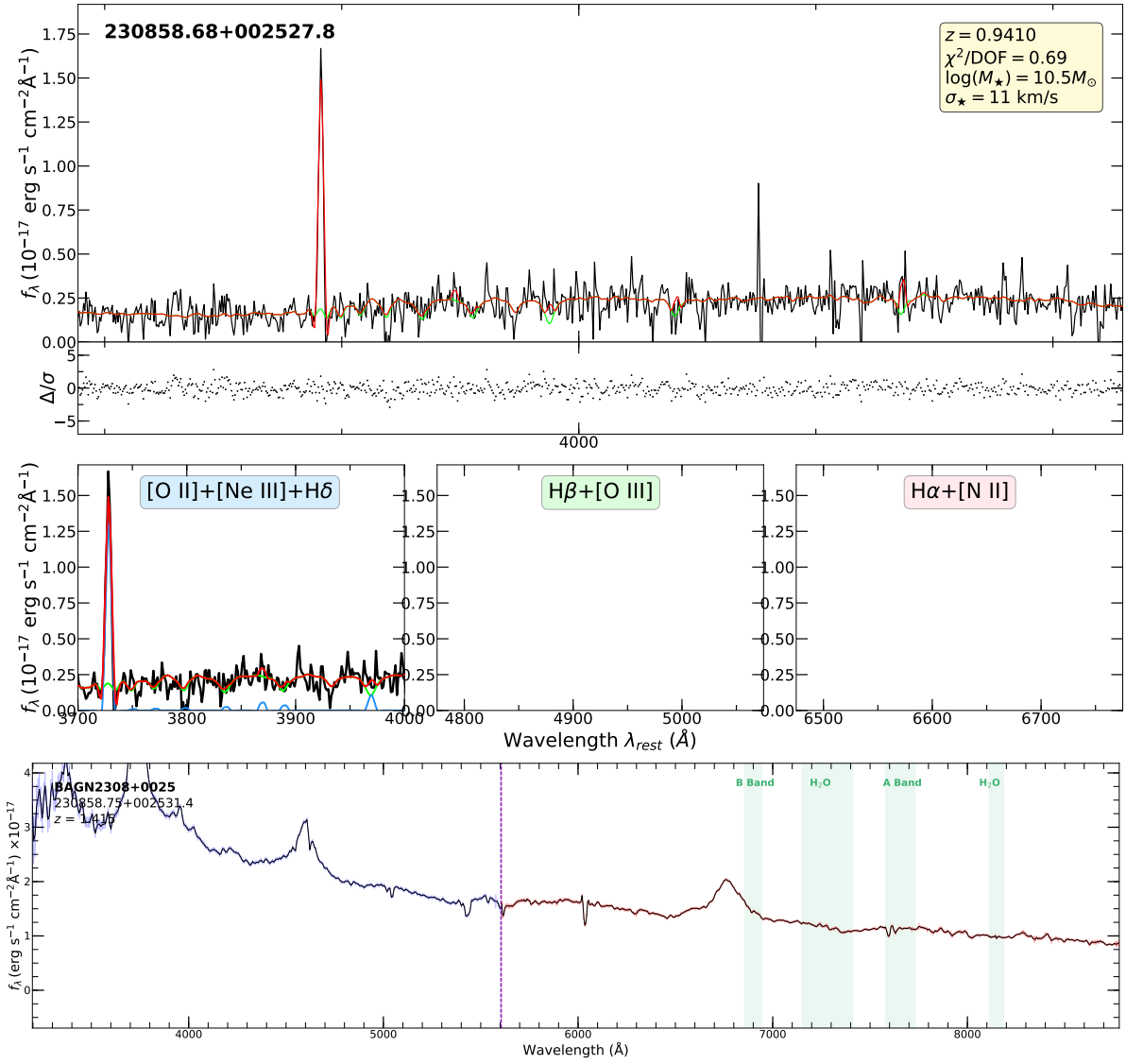

Figure B.63. 2308+0025

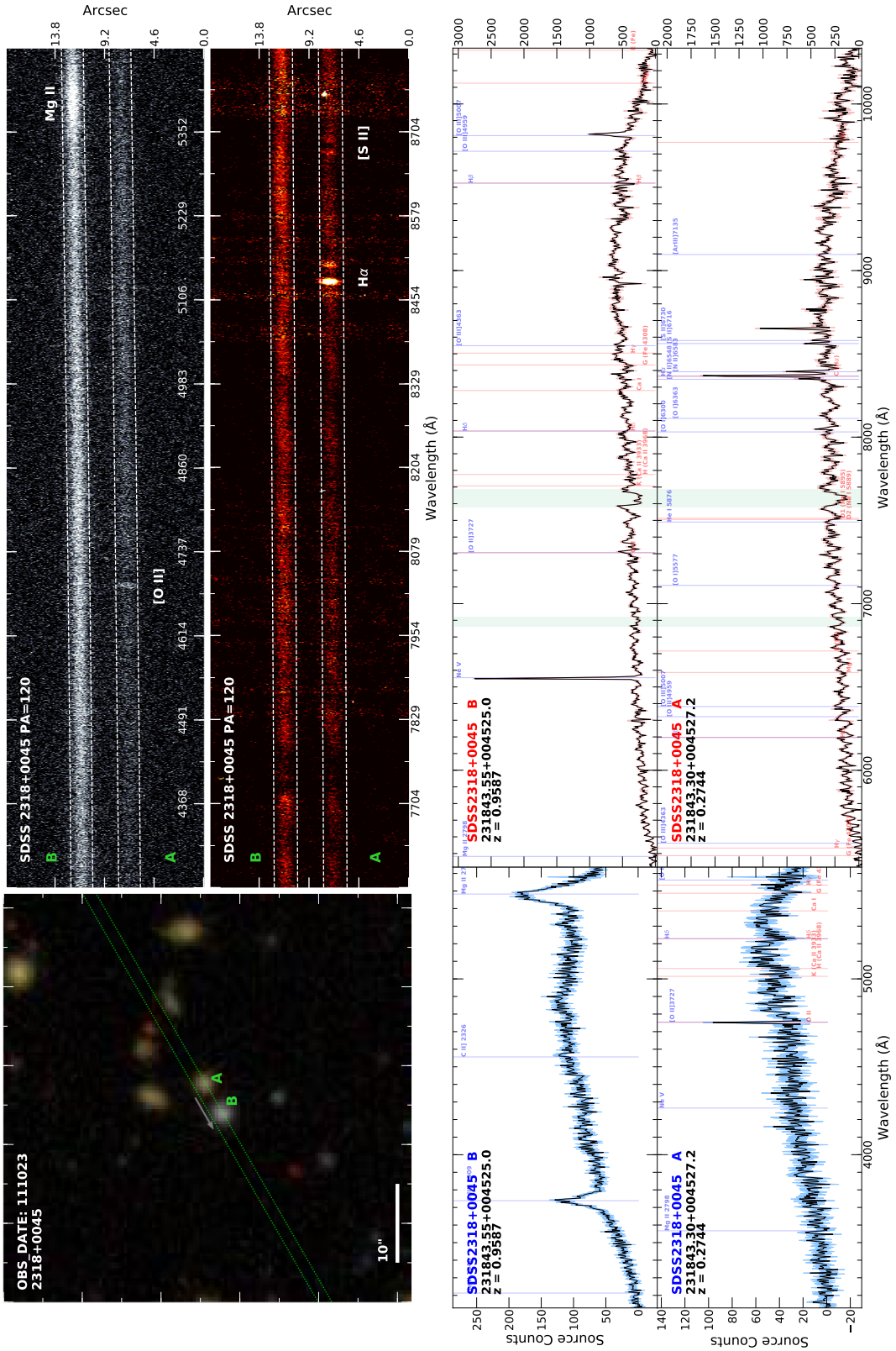

Figure B.64. 2318+0045

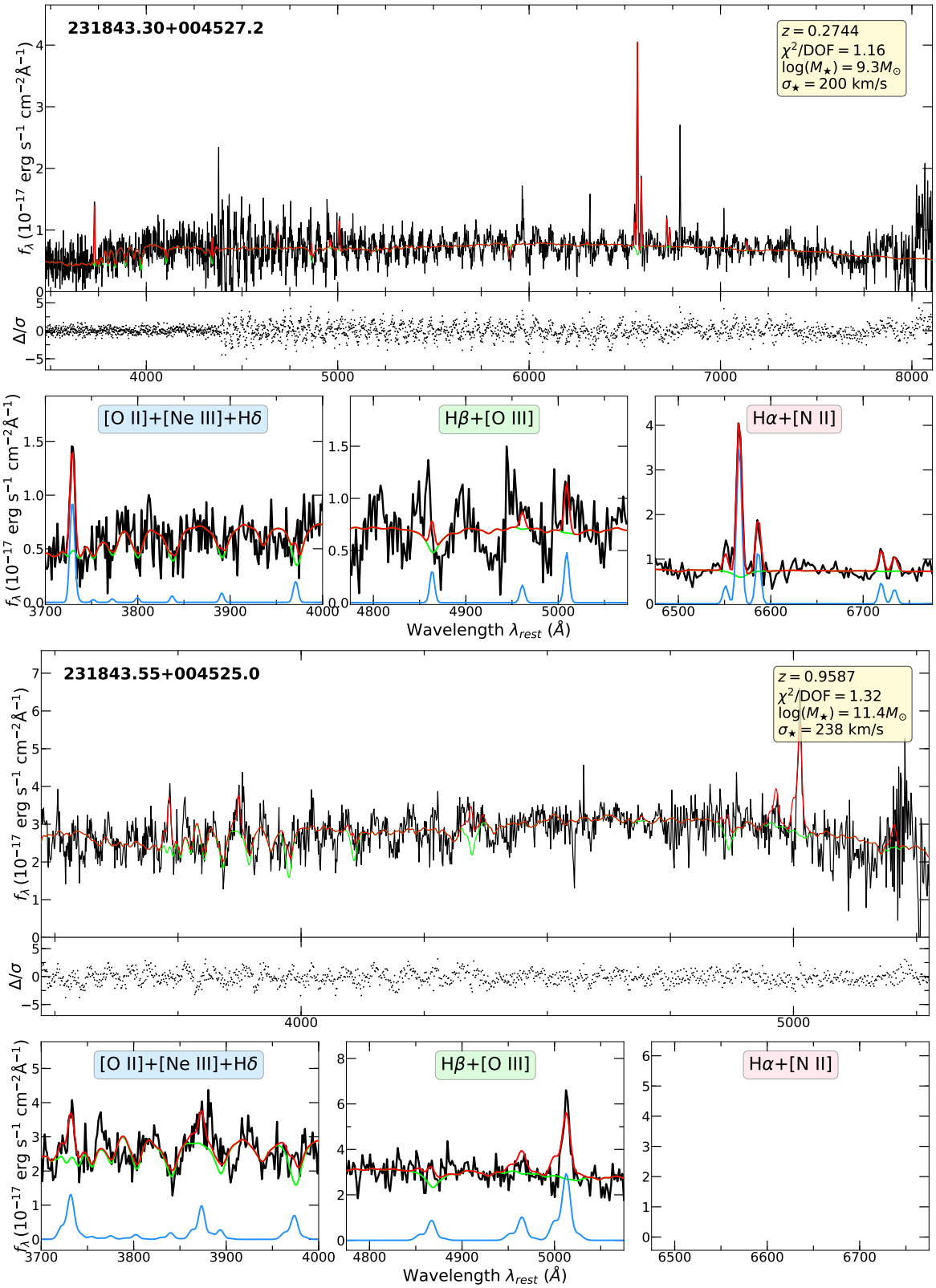

Figure B.65. 2318+0045

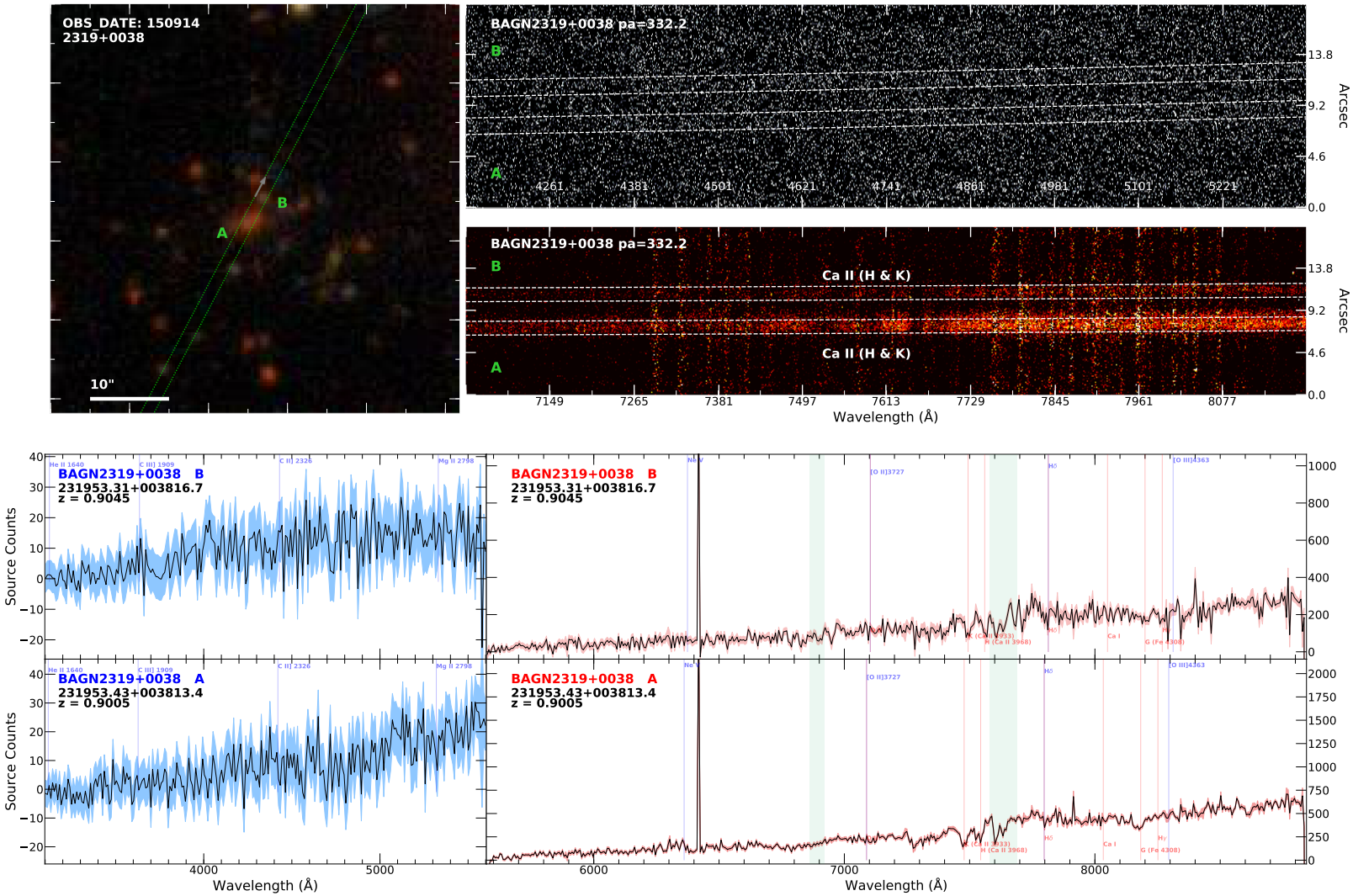

Figure B.66. 2319+0038. This pair required template matching to obtain a redshift estimate. An uncleaned cosmic is clearly visible in the 2D spectrum, and thus ignored. We find very convincing matches for the Ca II absorption features.

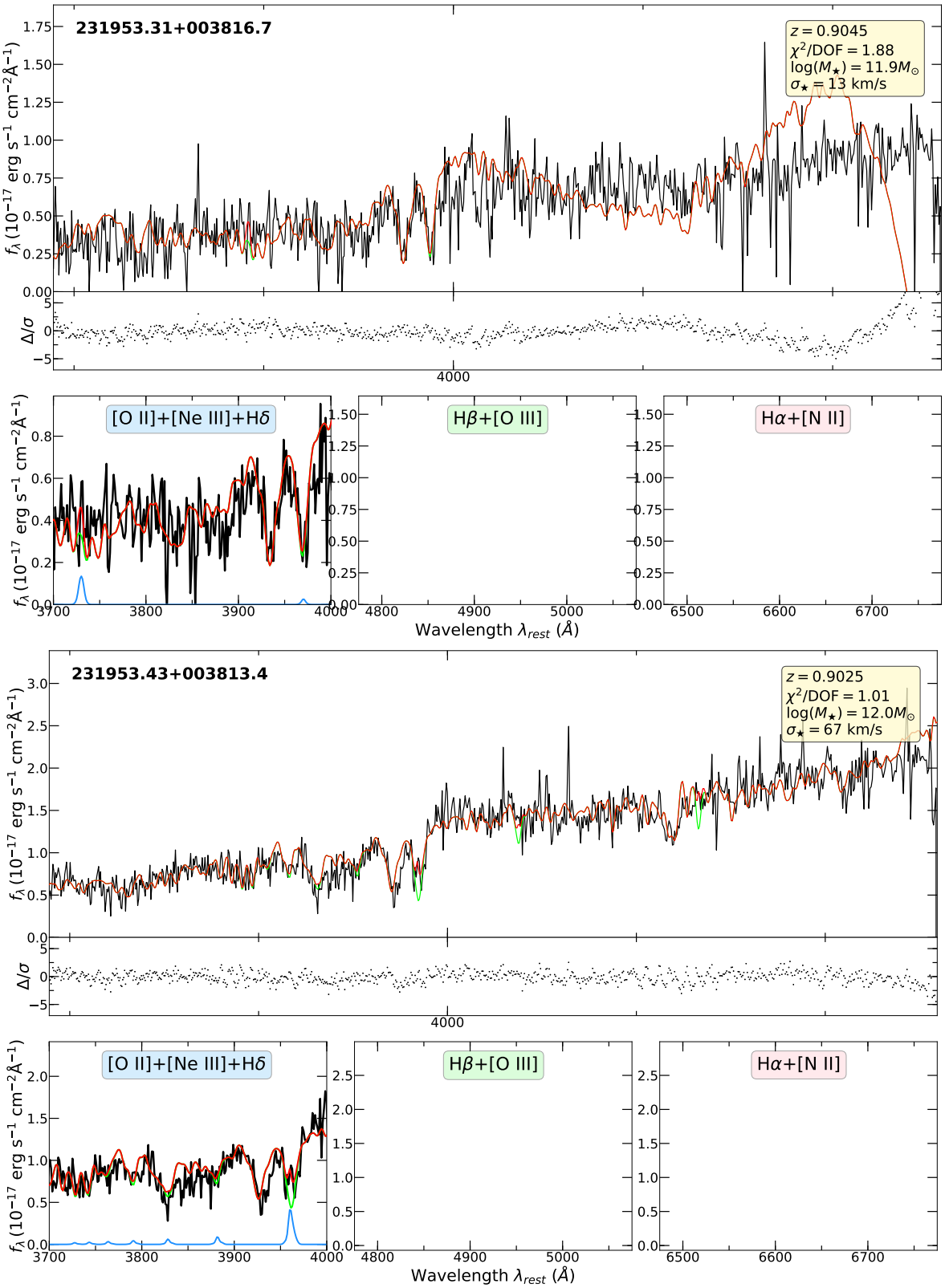

Figure B.67. 2319+0038